IAHR AIRH

Supported by Spain Water and IWHR, China

IAHR 2017

37th IAHR WORLD CONGRESS

13-18 August, 2017

Kuala Lumpur, Malaysia

SPECIAL SESSION

IAHR AIRH

Supported by Spain Water and IWHR, China

IAHR 2017

37th IAHR WORLD CONGRESS

13-18 August, 2017

Kuala Lumpur, Malaysia

TRANSIENTS IN PIPES

Lead Speaker: Silvia Meniconi

Proceedings of the 37th IAHR World Congress
August 13 – 18, 2017, Kuala Lumpur, Malaysia

MECHANISMS THAT LEAD TO THE OCCURRENCE OF VIOLENT GEYSERS IN STORMWATER AND COMBINED SEWER SYSTEMS

ARTURO S. LEON[(1)]

[(1)] Department of Civil and Environmental Engineering, University of Houston, Houston, United States,
aleon3@uh.edu

ABSTRACT

Supported with laboratory observations, this paper describes the mechanisms that lead to violent eruptions in stormwater and combined sewer systems. This is the first time that violent eruptions have been produced in a laboratory setting. Each geyser produced consists of a few consecutive violent eruptions within a time frame of a few seconds with heights that may exceed 30 m, measured from the top of the dropshaft. These characteristics resemble those geysers that occurred in actual stormwater and combined sewer systems.

Keywords: Combined sewer system; geyser; stormwater; transient; violent eruption.

1 INTRODUCTION

Geysers have been studied over three decades in terms of water phase only or air-water interaction (Guo and Song, 1991; Vasconcelos, 2005; Lewis, 2011; Wright et al., 2011). Even though geysers were studied for a relatively long time, their violent behavior was neither reproduced experimentally nor numerically. In particular, it is not clear how to predict a large geyser height as observed in actual stormwater and combined sewer systems. For instance, for a geyser eruption to rise a height of 20 meters, the velocity of the gas-liquid mixture at the manhole exit would be about 20.4 m/s [$w = (2gH)^{0.5}$ where H is the eruption height]. Also, it is not clear the reasons for consecutive eruptions, where the second or third eruption is typically the strongest in terms of height and velocity. Hence, it can be inferred that the processes that lead to the occurrence of violent geysers are not yet well understood. The motivation of this article is to, based on laboratory observations, describe the mechanisms that lead to violent geysers in stormwater and combined sewer systems. The present conference paper is a summary of part of the material in Leon (2017). For an in-depth discussion on the mechanisms that lead to the occurrence of violent geysers in stormwater and combined sewer systems, the reader is referred to Leon (2017).

2 MECHANISMS FOR GEYSERING IN STORMWATER AND COMBINED SEWER SYSTEMS

On average, each laboratory geyser event consisted of a few consecutive violent eruptions (3 to 8 eruptions) within a time frame of a few seconds (e.g., 2 to 10 seconds) with heights that may exceed 30 m. The violent eruptions produced resemble the characteristics of those that occurred in actual stormwater and combined sewer systems. For details of the experimental work, the reader is referred to Leon et al. (2016). The laboratory observations are summarized in schematics (Figure 1.1-1.6), video snapshots for vertical pipe (Figure 2), video snapshots for horizontal pipe (Figure 3), and data of pressure transducers (Figure 4-6). Nine pressure transducers were used in the visualization experiments. The location of pressure transducers 2 to 8 are presented in Figure 7. Pressure transducer 1 was located at the top of the upstream tank (see complete experimental setup in Leon et al., 2016). For clarity, the pressure head traces for transducers 3, 5 and 7 are omitted in Figure 5 and 6. The main mechanisms that lead to geysering can be summarized as follows:

i. A large air pocket, which is formed during the filling of near-horizontal tunnels (Vasconcelos, 2005), approaches the dropshaft. This can be observed in Figure 1.1 and 3.
ii. The large air pocket enters the dropshaft and rises due to buoyancy. The front of the air pocket, which resembles the classical Taylor bubble, occupies almost the entire cross-sectional area of the dropshaft. The tail of the air pocket ascending in the dropshaft is highly turbulent with a near homogenous mixture of air and water with great content of void fraction. In a similar way to the classical Taylor bubble, as the air pocket ascends, a significant amount of liquid that is on top of the air pocket is carried upwards and a portion of the water falls on the sides of the pocket (e.g., film flow). This can be observed in Figure 1.2 and 2.
iii. When the Taylor-like bubble reaches the top of the dropshaft, most of the water that is on top of the air pocket is spilled (Figure 1.3).
iv. As water is quickly lost due to spilling, the hydrostatic pressure in the dropshaft is rapidly reduced, which accelerates the air entering the dropshaft. The rapid acceleration of air leads to a weak eruption from the dropshaft (Figure 1.4). Subsequently, the rapid increase in air velocity in the horizontal pipe results in the Kelvin-Helmholtz (KH) instability that transforms the initial stratified flow

regime (Figure 3) to wavy and, eventually, slug flow, which is a series of liquid plugs (slugs) separated by relatively large air pockets. The liquid slugs have some entrained air. The aforementioned wavy air interfaces and slugs can be observed in snapshots 3 to 24 in Figure 3. During this process, the flow in the dropshaft is highly mixed and turbulent (see Figure 2).

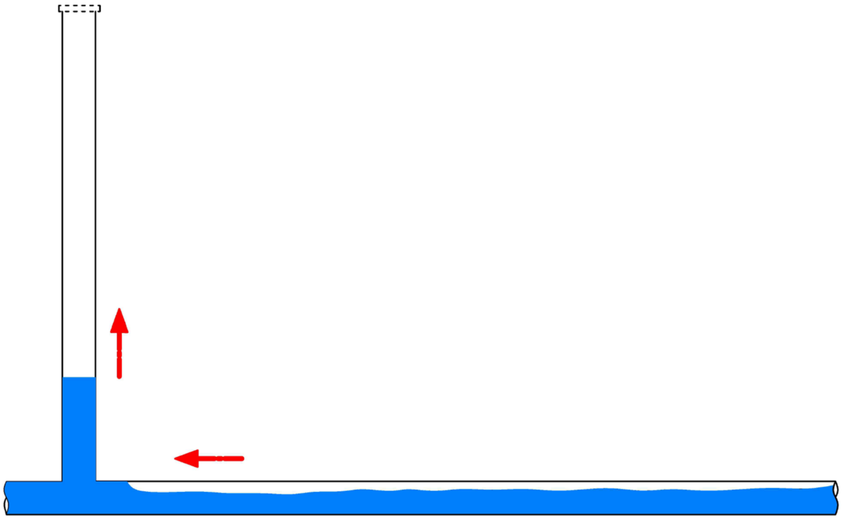

Figure 1.1. Air pocket approaching dropshaft.

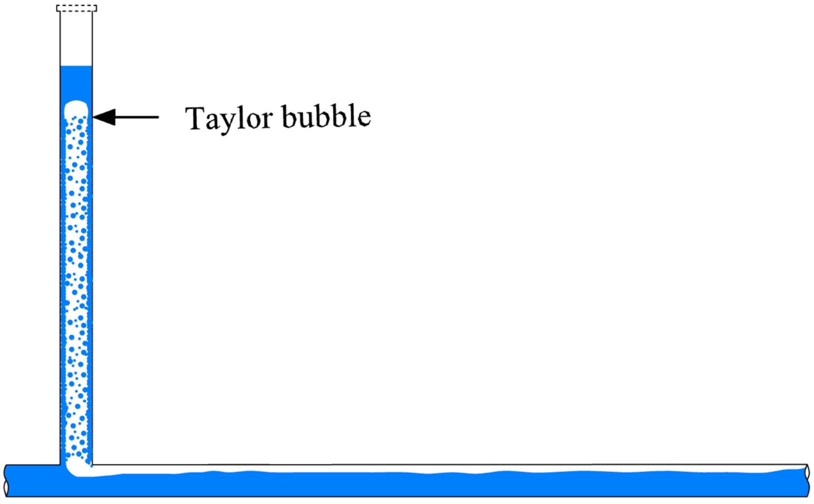

Figure 1.2. Rising of Taylor-like bubble.

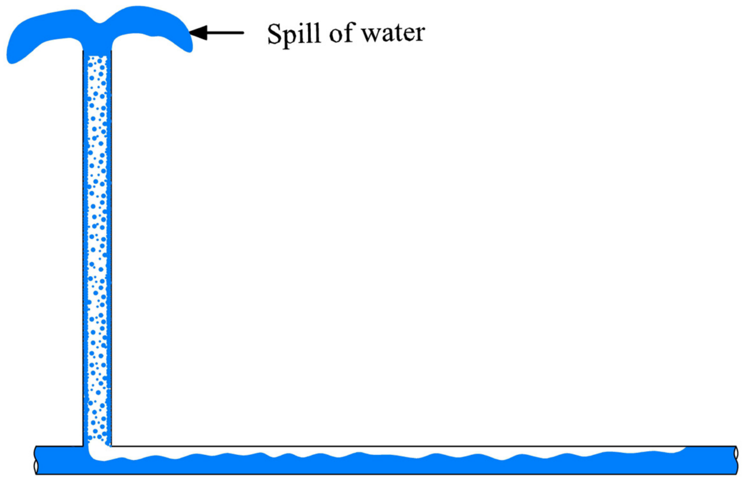

Figure 1.3. Water spill and acceleration of air pocket in horizontal pipe.

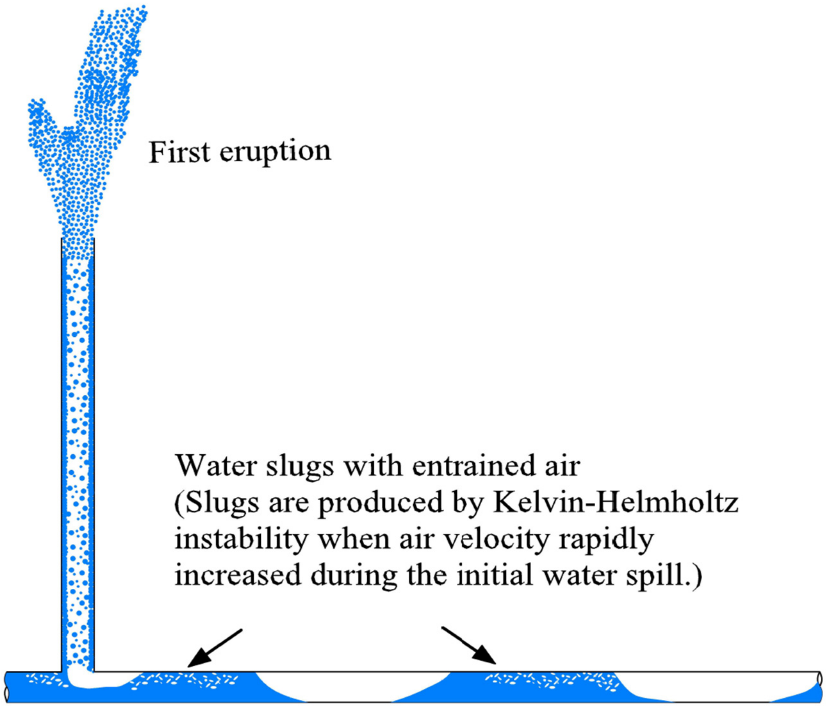

Figure 1.4. First eruption and formation of liquid slugs.

v. Once the slugs are formed in the horizontal pipe, they are violently propelled into the dropshaft right after a sudden drop of pressure in the dropshaft (e.g., after the previous eruption). During this process, new slugs can be formed in the horizontal pipe. The slugs in the horizontal pipe are propelled in bursts, each of which may result in a new eruption. The propelling of liquid slugs is activated whenever a significant pressure gradient between the horizontal pipe and the dropshaft is attained. Note in Figure 4-6 that geyser eruptions (e.g., large pressure fluctuations at transducer 9), are preceded by large pressure gradients between the horizontal pipe (e.g., transducers 4 and 6) and the dropshaft (e.g., transducer 8). Note also in Figure 4-6 that the pressures located downstream of the dropshaft (transducers 6 and 7) have significant fluctuations around the mean pressure. Note also in Figure 6 that the pressure trace at transducer 8 follows a similar pressure oscillation pattern to that of transducer 6, although with a slight delay. This means that pressure transients in the horizontal pipe are propagated to the dropshaft, and hence, pressure transients can also have an impact on geyser eruptions. In particular, large pressure gradients may be developed between the horizontal pipe and the dropshaft due to pressure transients. Note also in Figure 6 that the pressure head at transducer 2 decays slowly and it is not significantly affected by the pressure head oscillations at transducer 8. This is because of the discontinuity produced by the slugs, which block the uniform release of air from the horizontal pipe. The slow decay of pressure head in the horizontal pipe, due to the slugs, provides the pressure to still achieve significant pressure gradients (between the horizontal pipe and dropshaft) after the first geyser eruption. It is worth mentioning that the liquid slugs supply the water for the eruptions. Overall, the second or third geyser has the largest intensity in terms of height (Figure 1.5).

vi. After the second or third eruption, there may be a few more eruptions, however as water is lost in the dropshaft and the horizontal pipe around the dropshaft is depressurized, the geysering is terminated (Figure 1.6). On average, we observed between 3 to 8 eruptions in a time frame of 2 to 10 seconds. After the eruptions are terminated, the water depth at rest in the horizontal pipe is between 10% to 50% of the pipe diameter. The violent propelling of slugs was reported in various studies of two-phase flows (Wallis and Dodson 1973; Grotjahn and Mewes, 2007).

The author's laboratory experiments were performed using air as the gas. In addition to air that is entrapped in near-horizontal tunnels and that is transported to the dropshaft, it is argued that, in a similar way to the degassing pipes in Lakes Nyos and Monoun (Leon, 2016), geysering can be enhanced by exsolution of dissolved gases (Halbwachs et al., 2004). A sewer system contains a mixture of toxic and non-toxic gases that can be present at various levels depending upon the source (Hutter, 1993; Viana et al., 2007). For instance, ammonia, which is widely used in fertilizers, is present in large amounts in stormwater and combined sewer systems. Some of the gases, such as ammonia, are easily absorbed in water. Ledig (1924) has shown that ammonia is absorbed in water at least 100 times faster than carbon dioxide. In most cases, it is likely that dissolved gases are below saturation, however they can be exsolved when the air pocket moves bottom water upward to the point where dissolved gas pressure exceeds local hydrostatic pressure. The role of exsolution of dissolved gases on geyser intensity is not part of the present study.

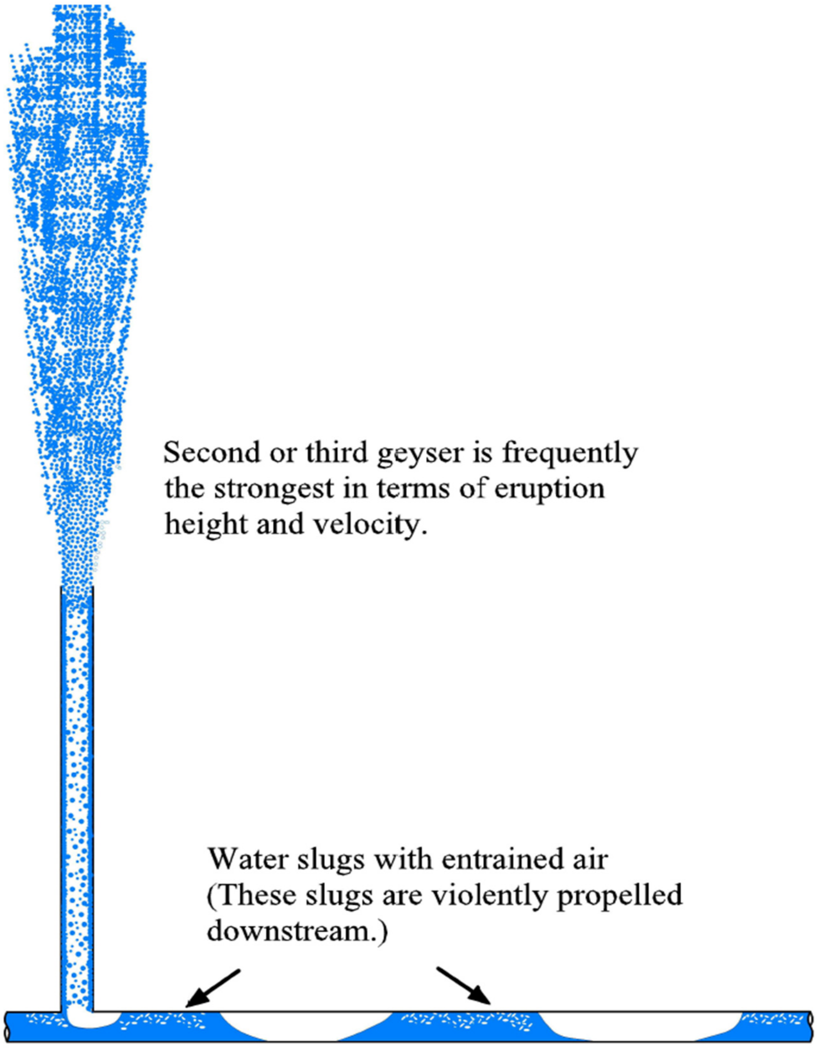

Figure 1.5. Successive eruptions as a result of blowout of slugs.

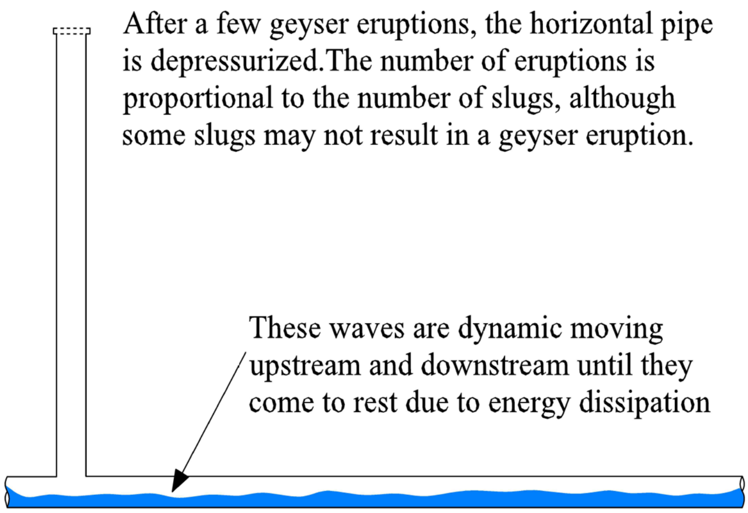

Figure 1.6. Depressurization and propagation of waves in the horizontal pipe.

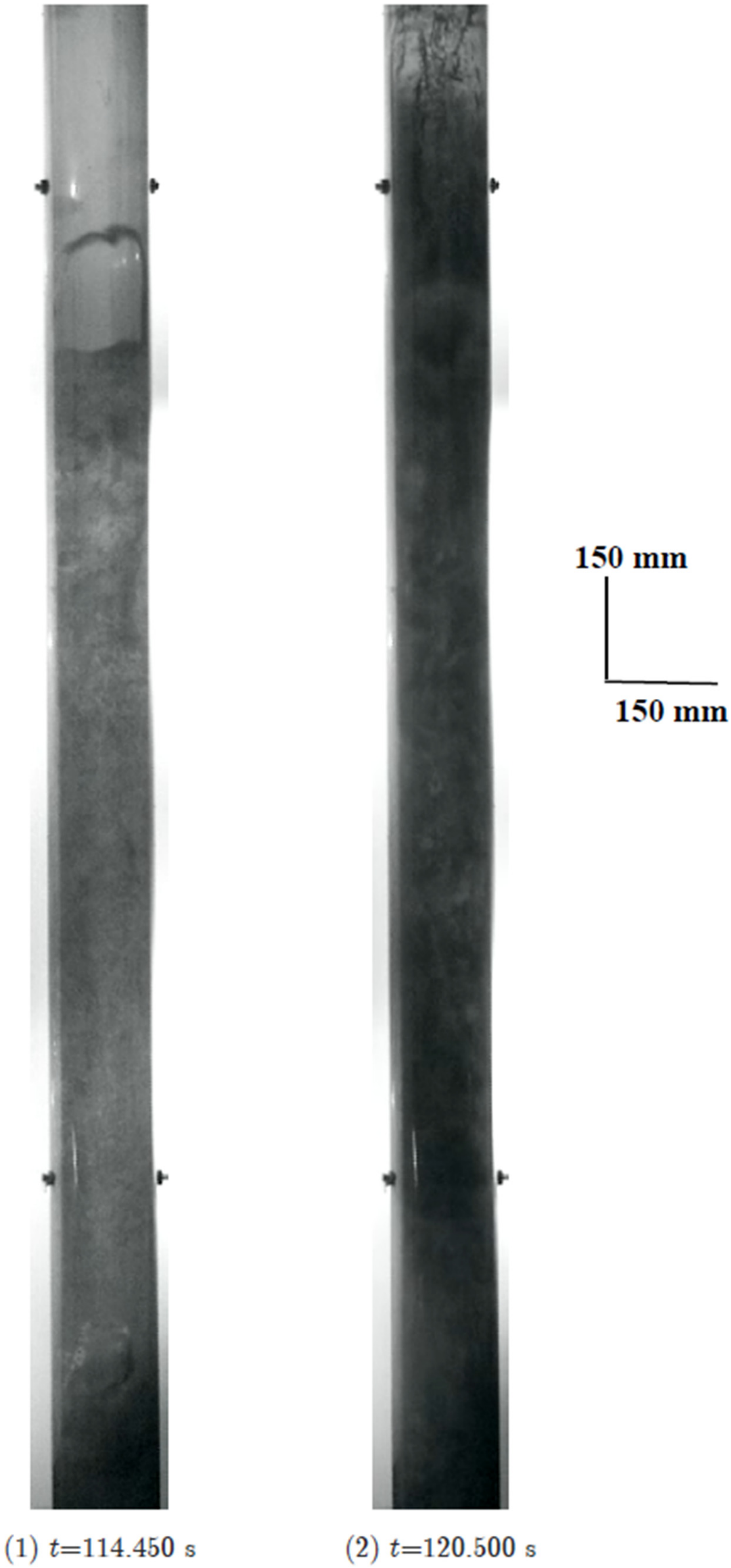

Figure 2. Flow snapshots in the experimental vertical pipe at various times.

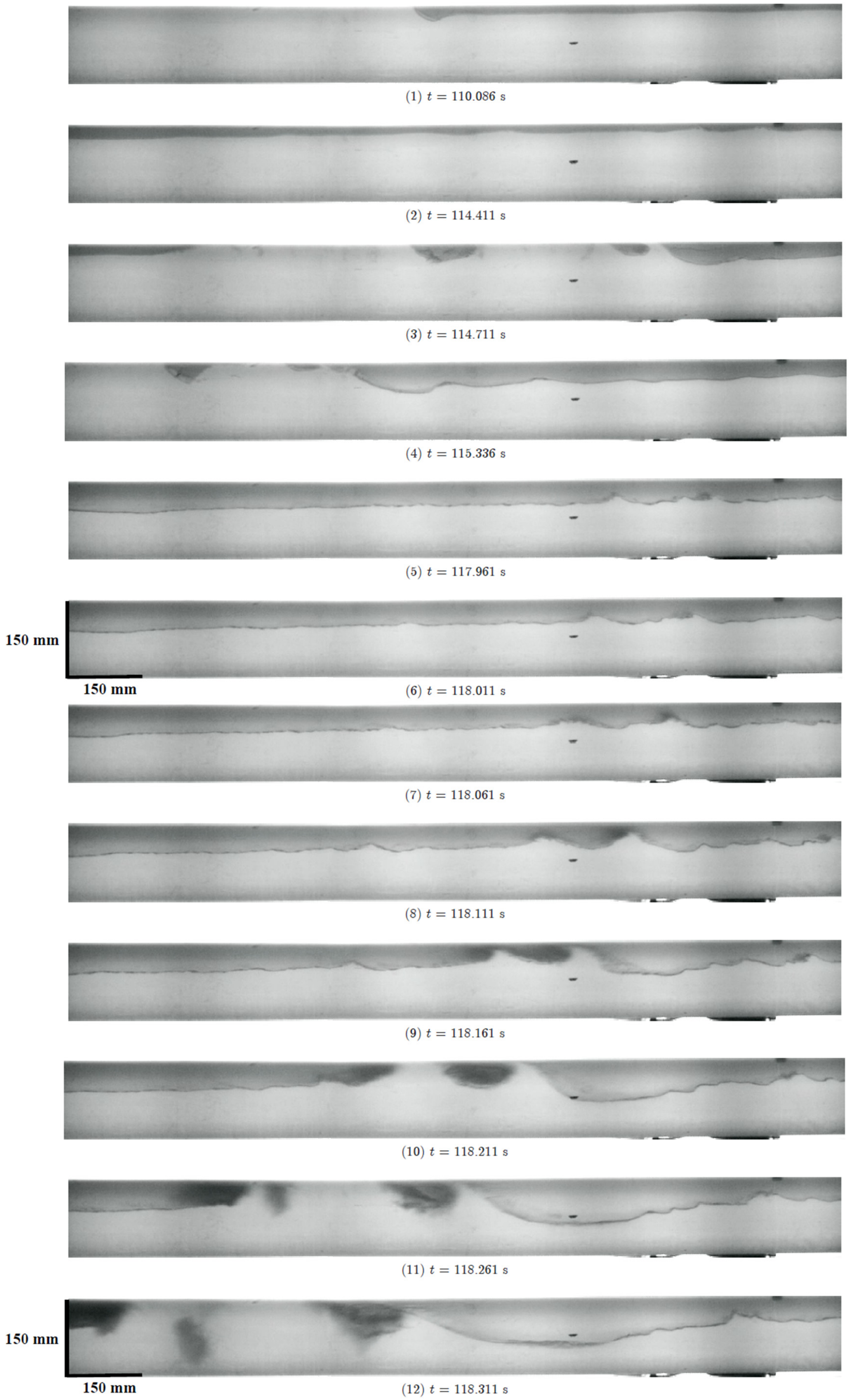

Figure 3. Flow snapshots in the experimental horizontal pipe at various times.

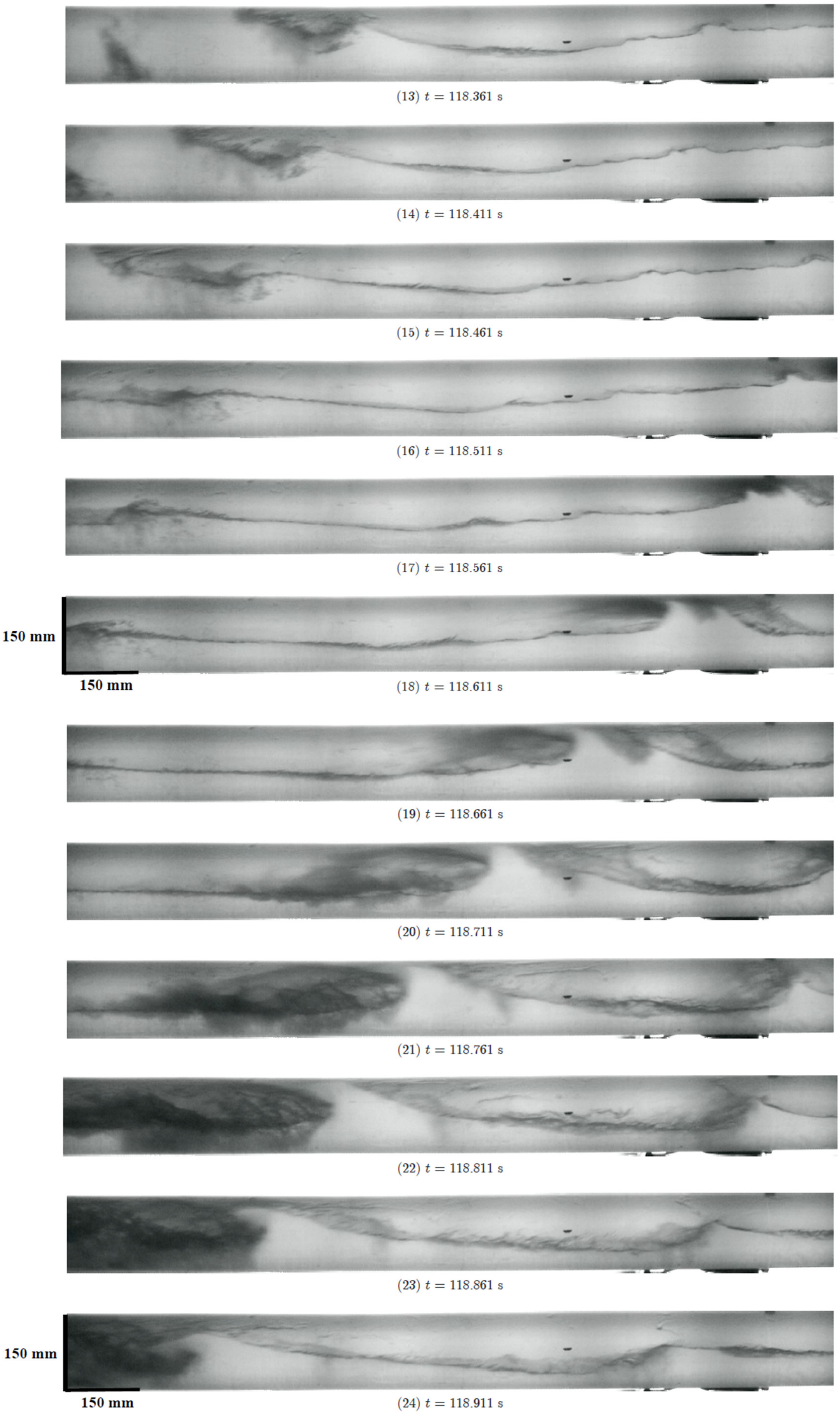

(13) $t = 118.361$ s

(14) $t = 118.411$ s

(15) $t = 118.461$ s

(16) $t = 118.511$ s

(17) $t = 118.561$ s

(18) $t = 118.611$ s

(19) $t = 118.661$ s

(20) $t = 118.711$ s

(21) $t = 118.761$ s

(22) $t = 118.811$ s

(23) $t = 118.861$ s

(24) $t = 118.911$ s

Figure 3. Flow snapshots in the experimental horizontal pipe at various times (Cont.).

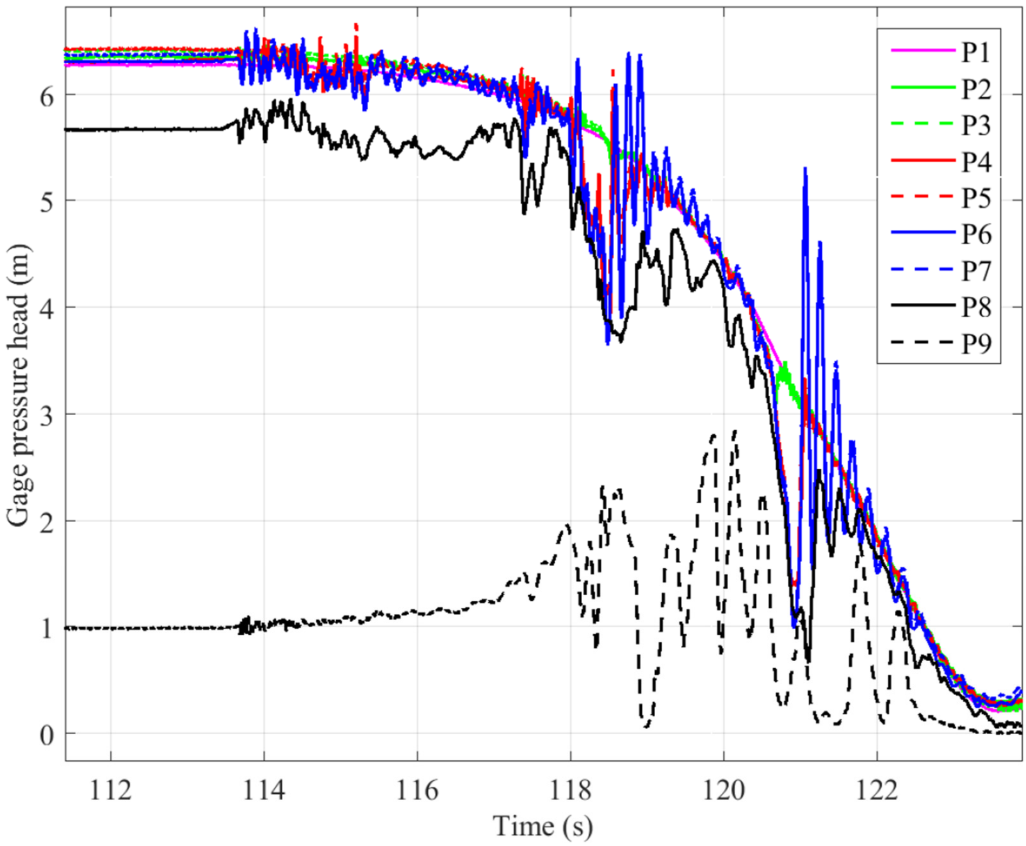

Figure 4. Example of pressure heads recorded in a geyser experiment (dropshaft height = 6 m).

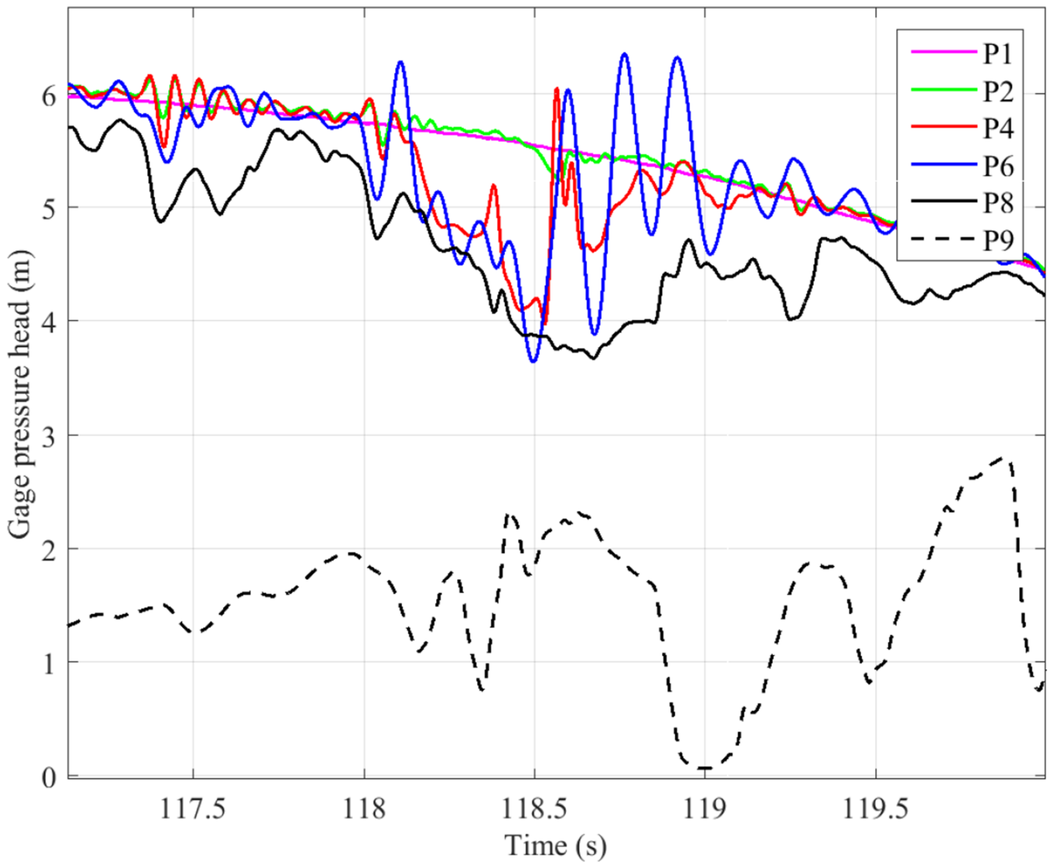

Figure 5. First zoom-in of Figure 4.

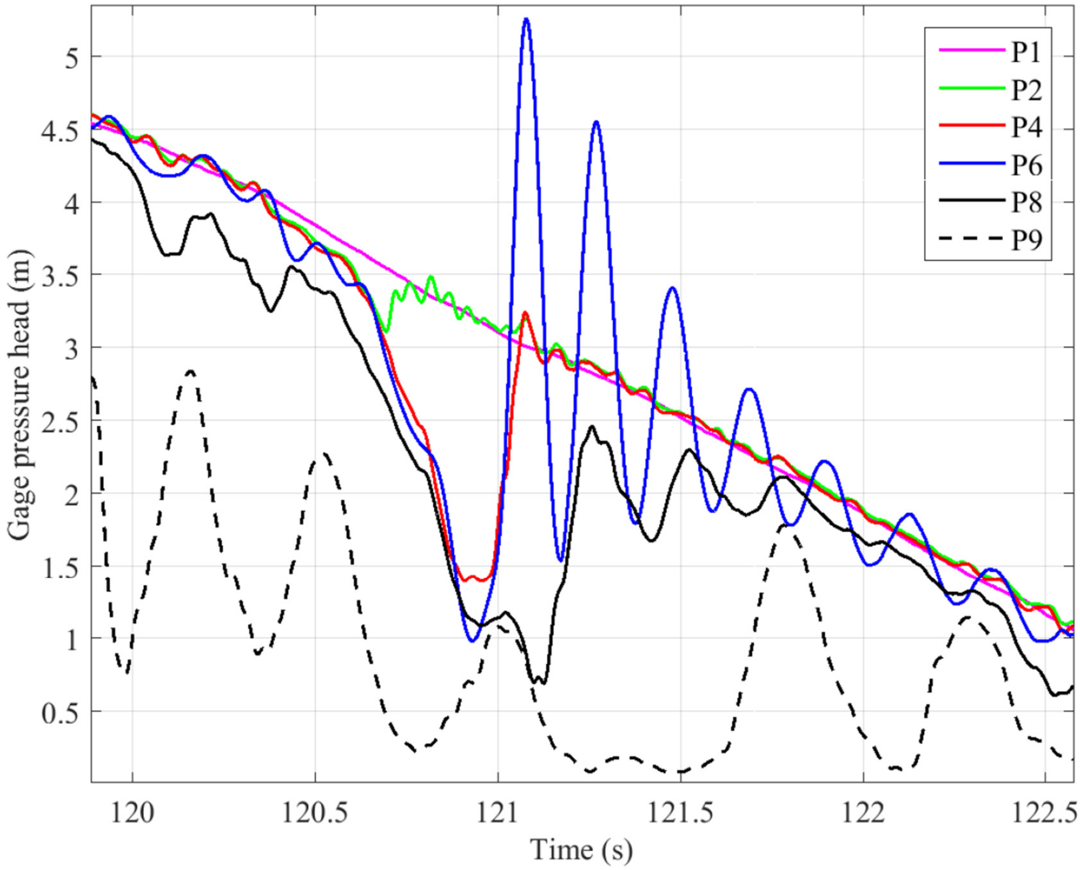

Figure 6. Second zoom-in of Figure 4.

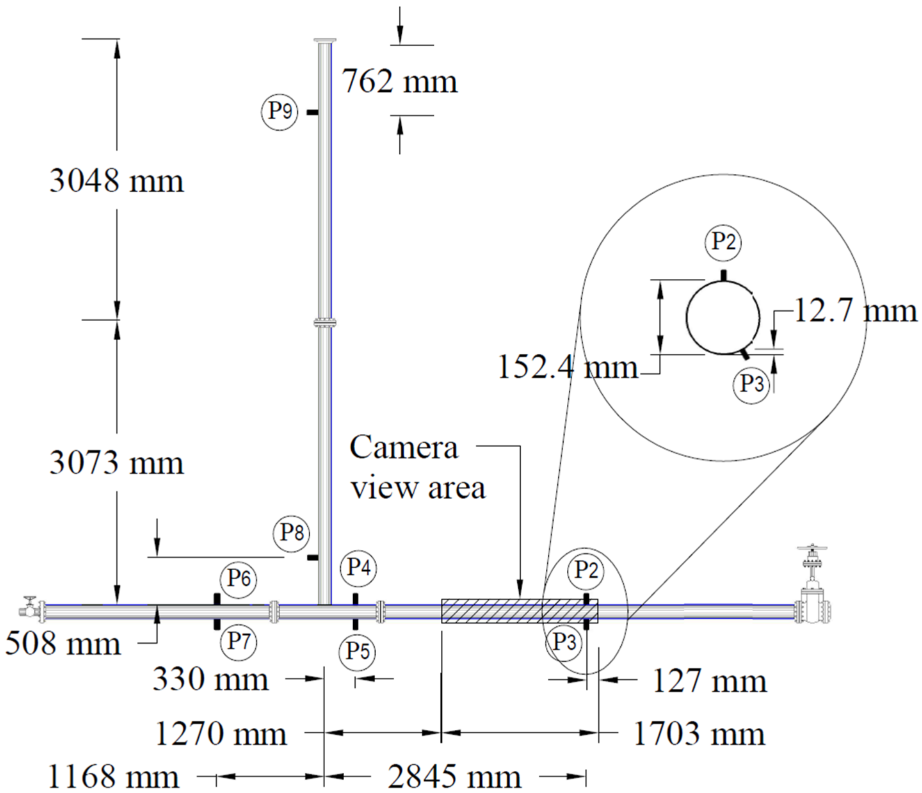

Figure 7. Location of pressure sensors for visualization experiments (Not To Scale).

3 CONCLUSIONS

Based on laboratory observations, this paper describes the mechanisms that lead to violent geysers in vertical shafts. This is the first time that violent eruptions have been produced in a laboratory setting. Each geyser produced consists of a few consecutive violent eruptions within a time frame of a few seconds with heights that may exceed 30 m, measured from the top of the dropshaft. These characteristics resemble those geysers that occurred in actual stormwater and combined sewer systems.

ACKNOWLEDGEMENTS

The author gratefully acknowledges the financial support of the U.S. Environmental Protection Agency under Grant number R835187. This manuscript has not been formally reviewed by EPA. The views expressed are solely those of the authors. EPA does not endorse any products or commercial services mentioned.

REFERENCES

Grotjahn, K. & Mewes, D. (2007). Transient Behaviour of Two-Phase Slug Flow in Horizontal Pipes. In *Transient Phenomena in Multiphase and Multicomponent Systems*, 103–118.

Guo, Q. & Song, C.S.S. (1991). Hydrodynamics under Transient Conditions. *Journal of Hydraulic Eng*ineering, 117, 1042-1055.

Halbwachs, M., Sabroux, J.C., Grangeon, J., Kayser, G. & Tochon-Danguy, J.C. (2004). Degassing The “Killer Lakes” Nyos and Monoun, Cameroon. *Eos*, 85, 281.

Hutter, G.M. (1993). Reference data sheet on sewer gas(es). Available:http://www.meridianeng.com/Reference%20Data%20Sheet%20on%20Sewer%20Gases.pdf [Accessed 01/02/2017].

Ledig, P.G. (1924). Absorption of Carbon Dioxide and Ammonia from Gas Bubbles. *Journal of Industrial and Engineering Chemistry*, 16, 1231–1233.

Leon, A.S. (2016). Mathematical Models for Quantifying Eruption Velocity in Degassing Pipes Based on Exsolution of a Single Gas and Simultaneous Exsolution Of Multiple Gases. *Journal of volcanology and geothermal research*, 323, 72-79.

Leon, A.S. (2017). Mechanisms that Lead to Violent Geysers in Vertical Shafts. *Journal of Hydraulic Research* (under review).

Leon, A.S., Elayeb, I. & Tang, Y. (2016). An Experimental Study on Violent Geysers in Vertical Shafts. *Journal of Hydraulic Engineering* (under review).

Lewis, J.M. (2011). A Physical Investigation of Air/Water Interactions Leading to Geyser Events in Rapid Filling Pipelines. *Ph.D. thesis*, University of Michigan.

Vasconcelos, J.G. (2005). Dynamic Approach to the Description of Flow Regime Transition in Stormwater Systems. *Ph.D. thesis*, University of Michigan.

Viana, P., Yin, K., Zhao, X. & Rockne, K. (2007). Modeling and Control of Gas Ebullition in Capped Sediments. In *Proceedings of the 4th International Conference on Remediation of Contaminated Sediments,* 22–25. Columbus, OH, USA: Battelle Press.

Wallis, G.B. & Dodson, J.E. (1973). The Onset of Slugging in Horizontal Stratified Air-Water Flow. *International Journal of Multiphase Flow*, 1, 173-193.

Wright, S., Lewis, J. & Vasconcelos, J. (2011). Geysering in Rapidly Filling Storm-Water Tunnels. *Journal of Hydraulic Eng*ineering, 137, 112–115.

THE EFFECT OF WAVE SPEED AND PUMP SPECIFIC SPEED ON TRANSIENT PRESSURES SIMULATIONS

RUBEN NERELLA[(1)] & VENKATA RATHNAM ERVA[(2)]

[(1)] Department of Civil Engineering, PACE Institute of Technology and Sciences, Ongole, India,
[(2)] Department of Civil Engineering, National Institute of Technology, Warangal, India,
ruben_n@pace.ac.in; evr@nitw.ac.in

ABSTRACT

Pumping mains that are conveying large quantity of water from lower elevation to higher elevations over long distance may experience undesirable water hammer pressures and are also referred to as hydraulic transients. They may arise due to abrupt operations like sudden opening or closing of valves or power failure to pump in pumping mains. Unplanned power tripping generates water hammer pressure that may fluctuates from minimum pressures or vacuum pressures to maximum transient pressures. Liquid column separation is the phenomena which may occur in a pumping mains when the pressure head decreases to vapour pressure of the flowing liquid and this analysis is important for planning transient mitigation devices. This paper presents a study on numerical simulation of water hammer with column separation events. A case study of pumping main of JCR Devadula Lift Irrigation Project, Telangana, India is presented. Discrete vapour cavitation model (DVCM) was applied to simulate the transient pressures in pumping mains for pump trip scenario. The effect of wave speed (500-1200m/s) and specific speed of the pump (17-52) on the developed transient pressures were investigated. The water hammer equations were solved using Method of Characteristics (MOC) approach. The effect of unsteady friction was neglected. Then, discrete vapour cavity equations were incorporated at each computational grid (node) to simulate cavitation locations, along delivery length of pumping main. The results show that when the specific speed of the pump increases, the minimum pressure head near pump delivery increased and cavitation event does not occur. Similarly, the maximum pressure head decreases as the specific speed increases. Moreover, results show that the maximum transient's pressures heads are increasing and minimum pressures are decreasing for higher value of wave speeds.

Keywords: Fluid Transients; wave speed; pumping main; specific speed; liquid column separation.

1 INTRODUCTION

Transient flow analysis is very important for the design and commissioning of water pumping systems. Simulation of transient pressure heads (positive and negative) for pump trip scenario and planning suitable surge mitigation devices in the transmission mains is a great challenge for hydraulic engineers. Pipe collapse, joint movements, extreme vibration and excessive noise may occur from negative transient pressure conditions. When pressure in the system drops to vapour pressure of the liquid at a given temperature, vapourous cavitation and water column separation occurs (Davis, 2004). This can create vapour bubbles or cavities near pump valve or check valve, knee points or elevated points in the pipe system. Due to dynamics in the pipe system, these cavities may collapse and the pressures generated after the collapse are very high and these high positive pressures can be so high that the pipe may burst if sufficient wall thickness is not provided for pipes (Chaudhry, 1979; Ramos et al., 2005).

Cavitation phenomenon is very high in transmissions mains as compared to distribution systems due to the absence of branch networks, take-off's and loop networks which attenuate or reduces the transient pressure wave created by a disturbance (Izquierdo and Iglesias, 2004). The use of large diameter pipes, and high discharge transmission mains in present day water demand driven scenario further increased the need to study the cavitation phenomenon. (Ruben, 2017). Much theoretical and experimental analysis have been done in the realm of cavitation and water column separation which was first identified by Joukowsky in the early twentieth century (Bergant et al., 2006; Ghidaoui et al., 2005). The intensity of water column separation and its associated pressure spikes resulted by rapid closure of a reservoir-pipe-valve system was studied and analysed by three numerical models namely, discrete vapour cavity model (DVCM), discrete gas cavity model (DGCM) and generalized interface vapour cavity model (Bergant and Simpson, 1999). They claimed that DVCM involves simple algorithm and takes smaller computational time compared to more complex and still in development stage GIVCM model. The results show that DVCM generates accurate results when the number of reaches is restricted. A laboratory test was conducted and the numerical prediction of pressure changes during water hammer with liquid column separation by DVCM were compared with experimental results (Adamkowski and Lewandowski, 2012). In their experiment, visualization of cavities and its associated pressures were observed not only at the vicinity of shutoff valve but along some discrete points of the pipeline. A small difference between laboratory and experimental values may be accounted for not considering unsteady friction in the model was pointed out. However, it is worthy to mention that the first two pressure waves generated by DVCM with steady friction and DVCM with unsteady friction shows no difference. As for practical design aspect, the first or second pressure head is very important in design of pipe diameter, thickness etc. They concluded that DVCM with steady friction can also be used for field systems.

Numerical prediction of water hammer and column separation with DVCM and GIVCM approach for imaginary pump-pipeline was analysed (Sadafi et al., 2012). In their study, the effect of various hydraulic and geometric parameters like pipe diameter, pump-motor inertia and specific speed were investigated. A simple reservoir pipe valve was numerically simulated by DVCM during rapid filling of the system (Malekpour and Karney, 2014). The major findings showed that the knee points are prone to the occurrence of water column separation and that the magnitude of the resultant over pressures depends on the geometrical and hydraulic characteristics of the profile. In the literature for many years, it was confirmed from the investigations that specific speed (N_s) can affect the characteristics of the pump (Aydar et al., 2009; Rohani and Afshar, 2010). A practical method to prevent column separation in sewage pumping system was studied by increasing the specific speed of the pump (Yang, 2001). All the aforementioned studies on cavitation have focused on simple reservoir-pipe-valve systems and a simple pump-pipeline profiles (laboratory test apparatus) using DVCM. Many studies on hydraulic transients caused from power failure to pumps can be found in Thorley and Faithfull (1992), Ramos et al. (2005), Lingireddy and Wood (1998), Ulanicki et al. (2008), Jedral et al. (2002).

The main objective of this research is to study the effect of wave speed and pump specific speed on the generated transient pressures using discrete vapour cavitation model.

2 MATHEMATICAL MODELING

The water hammer equations that describe the water-gas mixture flow are the equations of motion and continuity as in Eq. [1] – [2] (Chaudhry, 1979):

$$\mathrm{gA}\frac{\partial \mathrm{H}}{\partial \mathrm{t}} + \mathrm{a}^2\frac{\partial \mathrm{Q}}{\partial \mathrm{x}} = 0 \qquad [1]$$

$$\mathrm{gA}\frac{\partial \mathrm{H}}{\partial \mathrm{x}} + \frac{\partial \mathrm{Q}}{\partial \mathrm{t}} + \mathrm{f}\frac{\mathrm{Q}|\mathrm{Q}|}{2\mathrm{DA}} = 0 \qquad [2]$$

where **H**, **t**, **a** and **g** are the piezometric pressure head, time, wave speed of liquid, and gravitational acceleration, respectively, and A, Q, x, t and D are the pipe area, discharge, distance, Darcy- Weisbach friction factor and inner diameter of pipe respectively. The wave speed or celerity in Eq. [3] for water considering the elastic behaviour of the pipe wall is given by (Wylie and Streeter, 1978):

$$\mathrm{a} = \sqrt{\frac{\frac{\mathrm{K}}{\rho}}{1+\left(\frac{\mathrm{K}}{\mathrm{E}}\right)\left(\frac{\mathrm{D}}{\mathrm{e}}\right)}} \qquad [3]$$

where K = bulk modulus of elasticity of the fluid, ρ = mass density of the fluid, E = Young's modulus of elasticity of the pipe, and e = pipe-wall thickness. Eq. [3] can be applied to various problems that includes major transmission pipelines like water distribution systems, pressurized and sewerage mains and natural gas pipelines. The pipe constraint or anchoring constraint is not considered in the calculation of wave speed.

2.1 Discrete vapour cavity model (DVCM)

In DVCM model, a vapour cavity can form in computational grids (Figure 1) and the head should be set to saturated vapour pressure head as described in Eq. [4] (Sadafi, et al., 2012). The widely-accepted method of characteristics (MOC) was used to solve Eq. [1] – [2]. Using this method, the governing partial differential equations are converted into ordinary differential equations. These equations are also called compatibility equations, Eq. [5] – [6] which are valid along the characteristic lines in distance (x) and time (t) plane. The compatibility equations are numerically integrated to arrive for unknowns of H and Q at time t.

$$\mathrm{H}_{abs} = H_{abs}^{V} \qquad [4]$$

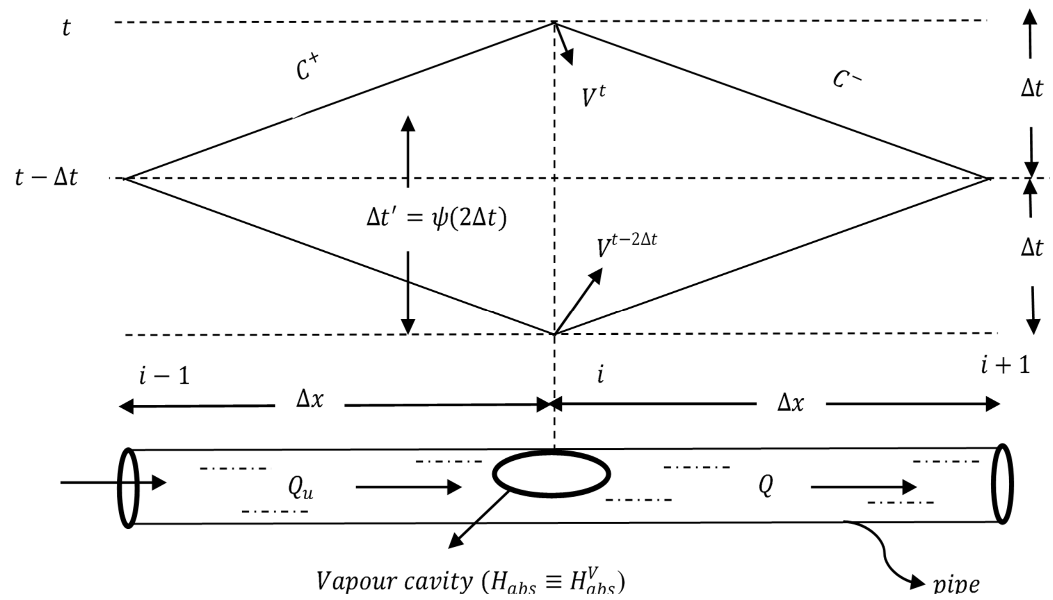

Figure 1. Grid Computation in DVCM (Source: Ruben, 2017).

Along the C+characteristic line ($\Delta x/\Delta t = +a$):

$$gA\left(H_{i,t} - H_{i-1,t_0}\right) + a\left((Q_u)_{i,t} - Q_{i-1,t_0}\right) + \frac{f\Delta x}{2gDA^2}(Q_u)_{i,t}\left|Q_{i-1,t_0}\right| = 0 \qquad [5]$$

Along the C- characteristic line ($\Delta x/\Delta t = a -$):

$$A\left(H_{i,t} - H_{i+1,t_0}\right) + a\left((Q)_{i,t} - (Q_u)_{i+1,t_0}\right) + \frac{f\Delta x}{2gDA^2}Q_{i,t}\left|(Q_u)_{i+1,t_0}\right| = 0 \qquad [6]$$

The variation of discharge in the system can be simulated at i^{th} computational node by assigning upstream discharge as $(Q_u)_i$ and downstream discharge as (Q_i) to include discrete vapour cavity model. In conventional MOC model, they are made equal and identical i.e. $Q_u \equiv Q$. Conversely in discrete vapour model, $Q_u \not\equiv Q$ at points where liquid becomes vapour. After coupling Eq. [5] – [6] with different boundary conditions like, pipe junction, pumps, valves, and surge protection devices, numerically prediction and calculations were performed by time-marching from a given initial condition. The staggered grid along with rectangular was used to get the unknown values at computation grids (Figure.1). The continuity equation, Eq. [7] is required to solve for differential flows at computation nodes to quantify formation of vapour volumes.

$$\frac{dV_v^*}{\partial t} = Q_u - Q \qquad [7]$$

Eq. [7] must be integrated to be used in DVCM model. The integration yields Eq. [8]:

$$V^{n+1} = V^{n-1} + \{\psi(Q^{n+1} - Q_u^{n+1}) + (1-\psi)(Q^{n-1} - Q_u^{n-1})\}2\Delta t \qquad [8]$$

where V^{n+1}, V^{n-1} are the vapour volumes at the new time and $2\Delta t$ earlier repectively and ψ is a weighting factor ($\psi = \Delta t'/2\Delta t$) used in time direction as shown in (Figure 1). This factor is used to control numerical oscillations. The values for ψ between 0 and 0.5 produces unstable results and ψ=1 does not produce any numerical oscillations. In all simulation, ψ was taken as 1.

3 RESULTS AND DISCUSSIONS

The details of the pump – pipe line system of reach-1 of J.C.R Devadula lift irrigation project (Figure 2) are as follows: length of transmission main= 38252m, diameter of pipe = 3m, pipe material is mild steel, pipe wall thickness e=16mm, bulk modulus of elasticity of water K =2.19GPa, Modulus of elasticity of mild steel E =210GPa, and Poisson's coefficient of the mild steel ν =0.3. The wave speed (a) was estimated as 877m/s by using Eq. [3]. The discharge in the pipe line was 14m^3/s. This pumping station consists of two pumps (Reduced Level or low water level=+71m) installed in parallel and have the following rated parameters: Rated discharge: Q_R=7m^3/s, Rated head: H_R=131m, Rated rotational speed: N_R=500RPM, Pump Inertia: I=14730 kg.m^2 and Rated efficiency: η_R=0.91. The pump's specific speed can be calculated as in Eq. [9]. (Chaudhry, 1979).

$$N_s = \frac{N_R\sqrt{Q_R}}{H_R^{0.75}} \quad [9]$$

where subscript R represents the rated condition and all of the units are in the SI system. The pipe was divided into 200 reaches. Cavities are expected to form at points where pressure drops to vapour pressure of the liquid in the pipeline. In this section, the influences of two parameters, including specific speed of the pump and pressure wave speed on the calculated pressure heads at pump location were studied.

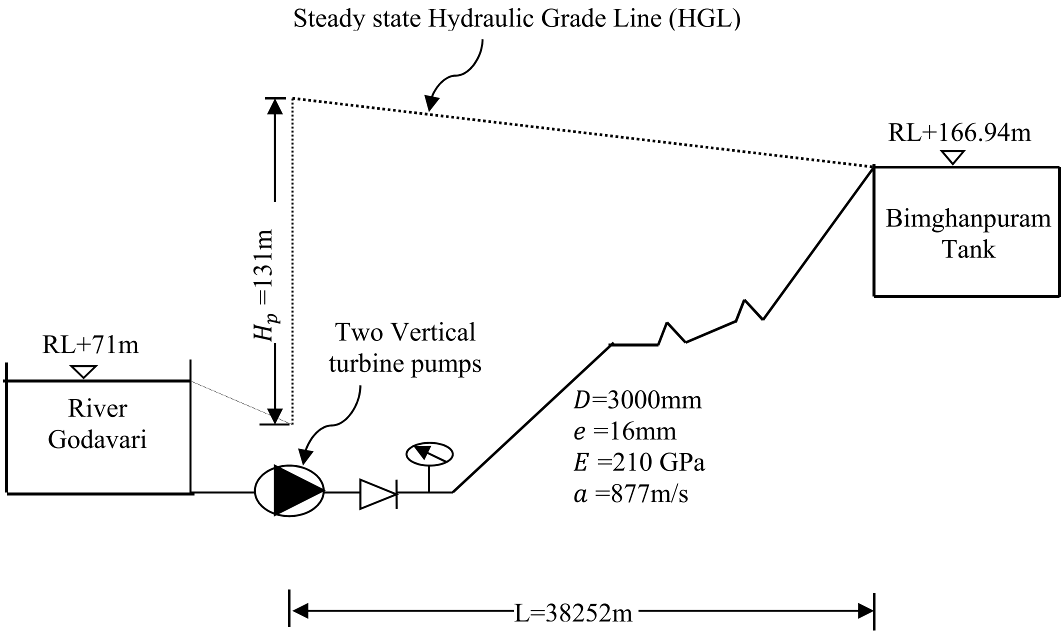

Figure 2. Schematic sketch of JCR Devadula Lift Irrigation Project (Source: Ruben, 2017).

3.1 Influence of specific speed

In this section, two alternative pumps with the specific speeds of 17 and 52 in addition to the main rated specific speed of 35 were numerically studied using the current DVCM method. The obtained results are shown in Figure 3. The minimum pressure heads for the specific speed of 17,35 and 52 were 21m, 23m and 16 m, respectively. The results indicate that when the specific speed increases, the minimum pressure head after pump failure increases. The minimum value may not reach the saturated vapour head, as was observed for all specific speeds. Thus, no cavities are expected to form in these two cases. In contrast, the peak pressure head declines as the specific speed increases. The maximum pressure heads for the specific speed of 17 and 52 were 239 and 215 m, respectively, both of which were less than the peak head of 227m when the specific speed of the pump was 35. Thus, as the specific speed of the pump increases, the peak pressure head in the period of reverse flow decreases.

Due to high negative pressure heads along the pipeline, the cavitation with column separation at appropriate locations are shown in Figure 4. Table 1 shows the total cavity volumes formed along the length of the pipe line for three different specific speeds. Thus, as the specific speed of the pump increases, the vapour volumes decreases which indicates the decrease in negative pressures/column separation (Ruben, 2017).

Table 1: Vapour volumes along the length of the pipeline.

	Specific speed (Ns)		
	17	35	52
Vapour volumes (m^3)	890	870	843

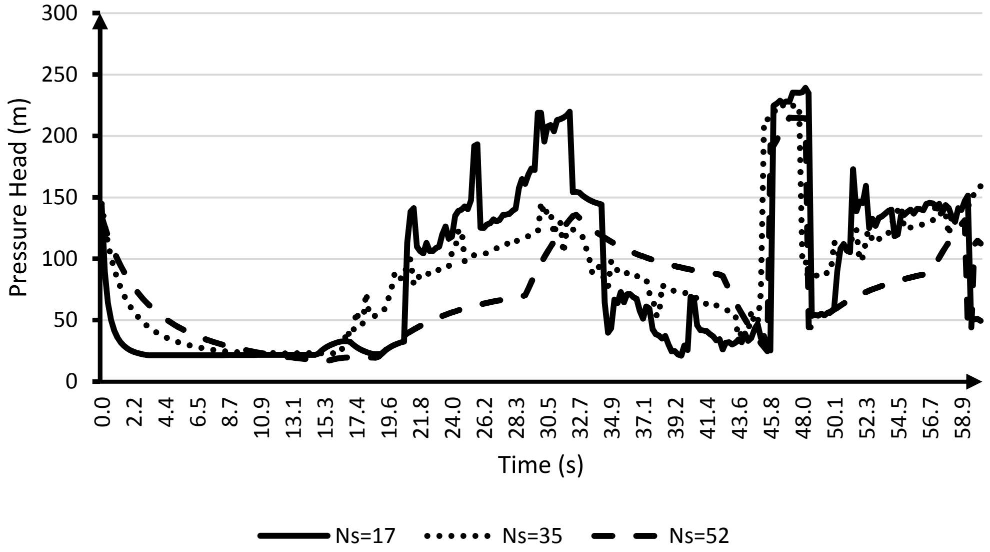

Figure 3. Pressure head vs. time at pump location.

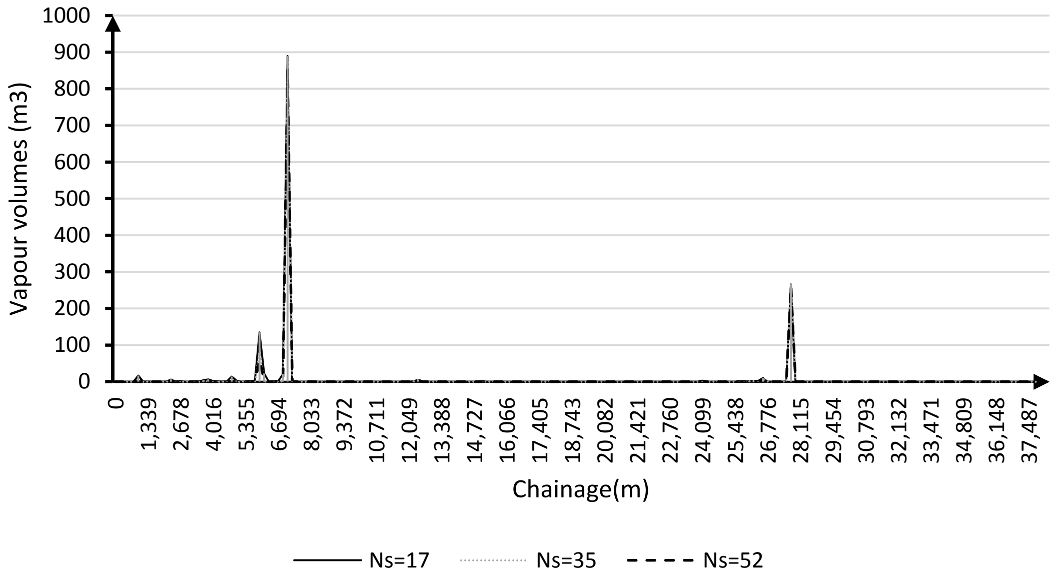

Figure 4. Vapour volume formation along the length of pipelines for different specific speeds.

3.2 Influence of wave speed

The water hammer wave speed derived from the continuity equation and is a function of Bulk modulus of elasticity of the fluid, pipe radius, thickness, e, and young's modulus of elasticity, E. Eq. [3] can be applied to various problems that includes major transmission pipelines like water distribution systems, pressurized and sewerage mains and natural gas pipelines.

For each design parameter, as in this case, the wave speed, a high and a low parametric value were considered based on practical considerations. In a given parametric run, a single design parameter is varied from its value in the reference case while keeping the magnitude of all other variables identical to those of the reference case. Keeping the specific speed of the pump constant, the influence of different wave speeds i.e. 500m/s and 1200m/s in addition to the min wave speed i.e. 877m/s, were numerically simulated and are shown in Figure 5(a) – (c). The maximum pressure heads for different wave speeds viz. 500m/s, 877m/s, and 1200m/s were 193.67m, 226.9m and 259.2m respectively. Thus, as the wave speed increases, the peak pressure heads increases (Ruben, 2017).

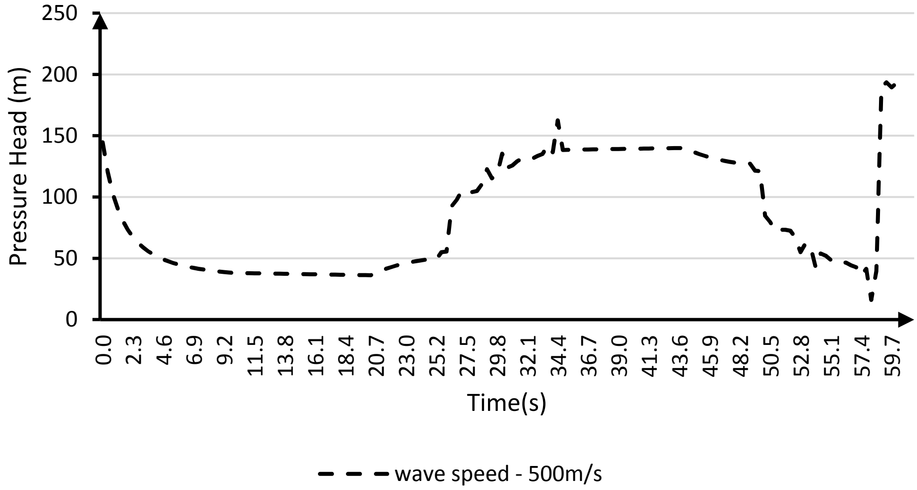

(a)

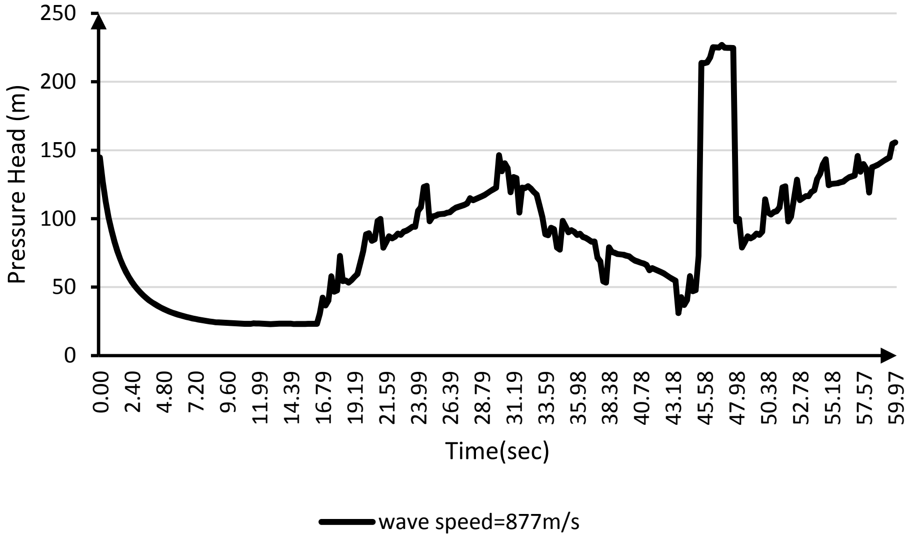

(b)

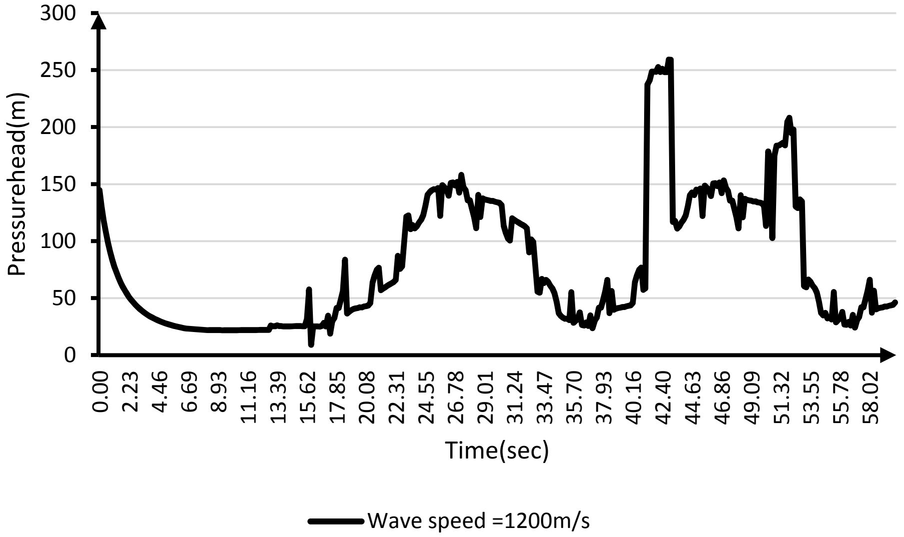

(c)

Figure 5. Effect of the wave speed (for constant Ns=35) by DVCM model.

4 CONCLUSIONS

In this research, water hammer with column separation events in the raising main due to power failure to pumps were investigated using discrete vapour cavity model (DVCM). The DVCM model uses the method of characteristic approach. The effect of wave speed (500m/s, 877m/s, and 1200m/s) and pump specific speed (17rpm, 35rpm, and 52 rpm) on the generated transient pressure heads were numerically simulated. It is observed that as specific speed of the pump increases, the peak pressure head decreases. Besides, as the wave speed increases, the pressure head increases as well. It can be stated that cavitation and liquid column separation events can be prevented if higher specific speeds pumps and low wave speed flexible piping system are selected for water conveyance purpose.

REFERENCES

Adamkowski, A. & Lewandowski, M. (2012). Investigation of Hydraulic Transients in a Pipeline with Column Separation. *Journal of Hydraulic Engineering*, 138(11), 935-944.

Aydar, E., Ilikan, A.N. & Sen, M., (2009). Experimental Investigation of the Complete Characterisitcs of Roto Dynamic Pumps. Colorado USA, *Proceedings of the ASME 2009 Fluids Engineering Division*.

Bergant, A. & Simpson, A.R. (1999). Pipeline Column Seperationflow Regimes. *Journal of Hydraulic Engineering*, 125(8), 835-848.

Bergant, A., Simpson, A. & Tijsseling, A. (2006). Water Hammer with Column Separation: A Historical Review. *Journal of Fluids and Structures*, Volume 22, 135-171.

Chaudhry, H.M. (1979). *Applied Hydraulic Transients*. Newyork: Van Nostrand Reighnhold Company.

Davis, A. (2004). Hydraulic Transients in Transmission and Distribution Systems. *Urban Water Journal*, 1(2), 157-166.

Ghidaoui, M.S., Zhao, M., McInnis, D.A. & Axworthy, D.H. (2005). A Review Ofwater Hammer Theory and Practice. *Applied Mechanics Reviews*, Volume 58, 49-76.

Izquierdo, J. & Iglesias, P.L. (2004). Mathematical Modelling of Hydraulic Transients in Complex Systems. *Math. Comput. Modell.*, 39(4), 529–540.

Jedral, W.A., Karaśkiewicz, K.J. & Hamid, A.S. (2002). Dimensionless Characteristics of Pumps With Specific Speeds, *J. Fluids Eng,* 124(2), 546-550.

Lingireddy, S. & Wood, D.J. (1998). Improved Operation Of Water Distribution Systems Using Variable-Speed Pumps. *J. Energy Eng.*, 124(3), 90–102

Malekpour, A. & Karney, B.W. (2014). Profile-Induced Column Separation and Rejoining During Rapid Pipeline Filling. *Journal of Hydraulic Engineering*, 140(11), 1-12.

Ramos, H., Almeida, A.B., Borga, A. & Anderson, A. (2005). Simulation of Severe Hydraulic Transient Conditions in Hydro and Pump Systems. *Water Resour.*, 26(2), 7–16.

Rohani, M. & Afshar, M.H. (2010). Simulation of Transient Flow Caused by Pump Failure: Point-Implicit Method of Characteristics. *Ann. Nucl. Energy*, 37(12), 1742–1750.

Ruben, N. (2017) Analysis of Hydraulic Transients in Water Conveyance Pumping Systems Using Discrete Vapour Cavitation Model. *PhD. Thesis*, National Institute of Technology Warangal, India

Sadafi, M.H., Riasi, A. & Nourbakhsh, S.A. (2012). Cavitating Flow During Water Hammer Using Generalized Interface Vaporous Cavitation Model. *Journal of fluids and structures*, Volume 34, 190-201.

Thorley, A.R.D. & Faithfull, E.M. (1992). Inertias of Pumps and Their Driving Motors. *Proc., Int. Conf. on Unsteady Flow and Fluid Transients*, R. Bettess and J. Watts, eds., Balkema, Rotterdam, Netherlands, 285–289.

Ulanicki, B., Kahler, J. & Coulbeck, B. (2008). Modeling The Efficiency and Power Characteristics of a Pump Group. *J. Water Resour. Plann. Manage.*, 134(1), 88–93.

Wylie, B.E. & Streeter, V.L. (1978). *Fluid Transients*. s.l.:McGraw-Hill Inc..

Yang, K.-l. (2001). Practical Method to Prevent Liquid Column Seperation. *Journal of Hydraulic Engineering*, 127(7), 620-623.

DYNAMICS OF FRICTIONAL WATER HAMMER - THEORY AND FIELD TESTS

JIM C. P. LIOU[(1)], BRUNO BRUNONE[(2)] & SILVIA MENICONI[(3)]

[(1)] Department of Civil Engineering, University of Idaho, Moscow, Idaho, USA,
liou@uidaho.edu
[(2,3)] Department of Civil and Environmental Engineering, University of Perugia, Italy,
bruno.brunone@unipg.it; silvia.meniconi@unipg.it

ABSTRACT

Consider a pipeline that supplies water to a constant-head reservoir. Subsequent to a sudden inlet flow stoppage there is an immediate Allievi-Joukowsky head drop at the inlet. This is followed by a period of line drafting during which a more gradual but sustained head drop continues for a 2 L/a seconds where L = length of the pipeline and a = water hammer wave speed of the water-pipeline system. The inlet head at 2 L/a seconds is the lowest of the entire water hammer episode and is of interest in certain applications. Because friction affects water hammer in a complicated way, quantification of line drafting is usually accomplished through numerical solution of the governing equations for one-dimensional transient flow. This study presents an analytical method to obtain the head at the inlet as a function of time for 2 L/a seconds after the flow stoppage. An equation to directly compute the minimum head at the pipeline inlet is also presented. The validity of the analytical results is evaluated by six sets of measured data on pump shutdown transients in a steel rising water main of Recanati, Italy.

Keywords: Analytical approximation; field data; friction; line drafting; water hammer.

1 INTRODUCTION

For transients in pipelines caused by the closure of an inlet valve, friction attenuates the amplitude of water hammer wave fronts and causes line drafting. The latter is a sustained pressure drop behind the wave front. For cross-country oil pipelines and long water transmission mains, the pressure at the inlet is usually very high in order to overcome the great frictional head loss of the pipeline. The initial sudden pressure drop due to valve closure may not bring the inlet pressure down to the negative range immediately, but line drafting may just do that a short while later. This is so because the sustained pressure drop can be very significant relative to the initial sudden pressure drop. Line drafting may lead to vapor cavity formation or even column separation. The subsequent vapor cavity collapse or column rejoining can create sudden pressure rises that threatens the integrity of pipelines. Because of the nonlinearity of the friction term in the governing equations of water hammer, satisfactory explanation and analytical quantification of line drafting are not available in the literature.

For a highly frictional pipeline where the length is large and/or the diameter small, the effective closure time of a discharge valve is much shorter than its physical closure time (Liou and Wylie, 2016). The same is true for closing a valve at the inlet of a pipeline. For such pipelines, line drafting can be analyzed in terms of an instantaneous closure of an inlet valve or an imposed sudden flow stoppage at the inlet. Figures 1 and 2 contrast the inlet valve closure transients with and without friction.

Depicted in Figure 1 is the water hammer without friction, with H_U = head at the reservoir end, H_V = head at the valve end, V_0 = steady state discharge velocity, V = velocity immediately behind the wave front, a = wave speed, t = time and dt = a time increment. The head and velocity profiles at t (solid lines) and $t + dt$ (dotted lines) are indicated. The profiles represent the head and velocity waves of water hammer. The initial hydraulic grade line (HGL) is horizontal. The head drop at the closed valve propagates downstream un-attenuated. The velocity behind the head wave is stopped completely. Before the waves are reflected back to the valve, the head at the closed valve remains constant and equals the steady state head mins the head drop due to stopping the initial velocity at the pipe inlet.

Depicted in Figure 2 is the water hammer with friction. The head wave attenuates as it travels downstream. The velocity is not stopped fully by the passage of the head wave. Subsequent to the initial sudden water hammer head drop, there is a sustained head drop behind the wave front as more and more fluid is drafted away from the closed end. This sustained head drop is reversed when the wave reflected from the downstream reservoir arrives at the pipeline inlet. Although numerically solving the governing equations can quantify the sustained head drop, an analytical solution is much more convenient and presents a more complete picture. Such an analytical solution will be presented elsewhere. This paper uses a set of field data to evaluate the validity of the analytical solution.

  / ISSN 1562-6865 (Online) - ISSN 1063-7710 (Print)

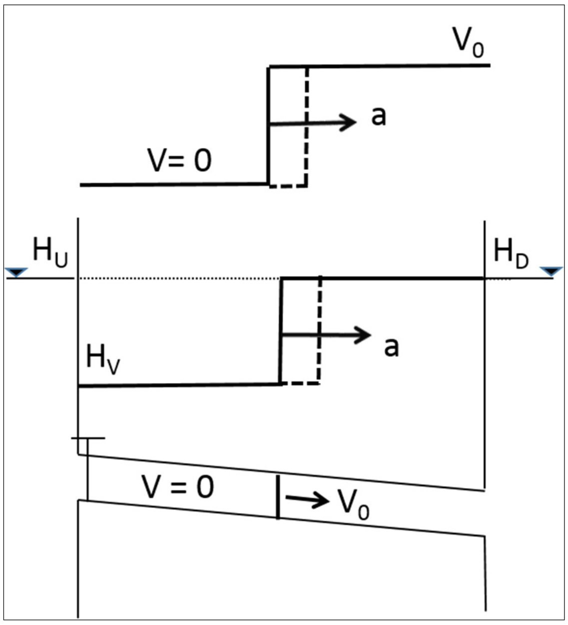

Figure 1. Velocity and head profiles at t (solid) and $t + dt$ (dashed) in a frictionless pipe.

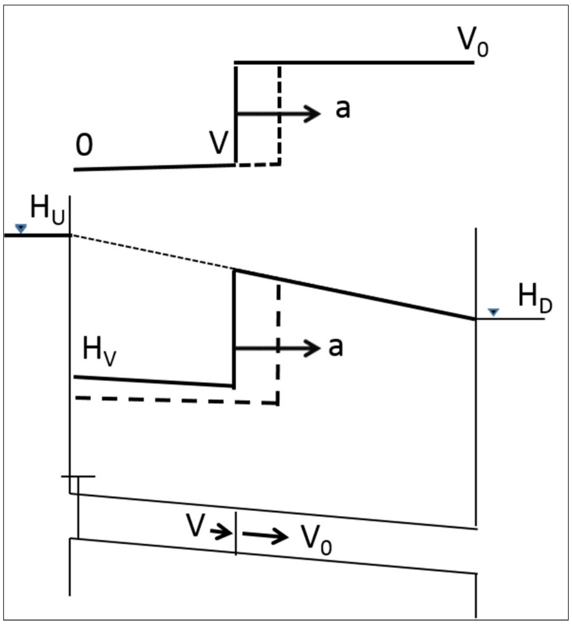

Figure 2. Velocity and head profiles at t (solid) and $t + dt$ (dashed) in a pipe with friction.

2 THE SUSTAINED HEAD DROP AT PIPE INLET

Parallel to the develop in Liou (2016) where an analytical approximation for line packing subsequent to a sudden flow stoppage at a pipeline outlet, the sustained head drop at the pipe inlet subsequent to a sudden flow stoppage at the inlet is approximated as (Liou et al., 2017):

$$\frac{H_v(2T)}{\Delta H_0} = \frac{H_D}{\Delta H_0} + R - 1 - RT\left[1 - \frac{1}{3}\tanh^2\left(\frac{RT}{2}\right)\right] \quad for \quad 0 \le T \le 1 \qquad [1]$$

with:

$$T = \frac{a}{L}t \qquad [2]$$

$$\Delta H_0 = \frac{a}{g}V_0 \qquad [3]$$

$$R = \frac{f L V_0}{2aD} \qquad [4]$$

In the above equations, T is time scaled by the travel time of a water hammer wave over the pipe length L. ΔH_0 is the Allievi-Joukowsky head change, and R is a dimensionless friction number. For cross-country oil pipelines, R is around 2 to 3, with 10 being a reasonable upper bound (Liou, 1993). The minimum head at the pipeline inlet occurs at $T = 1$ in Eq. [1]. Let F denote this minimum head relative to the reservoir head H_D, scaled by ΔH_0:

$$F = \frac{H_v(2) - H_D}{\Delta H_0} = \frac{R}{3}\tanh^2\left(\frac{R}{2}\right) - 1 \qquad [5]$$

Let G denote the maximum head drop (minimum head – pre-transient head) scaled by ΔH_0. It can be readily shown that:

$$G = F - R \qquad [6]$$

The variations of F and G with R are shown in Figure 3.

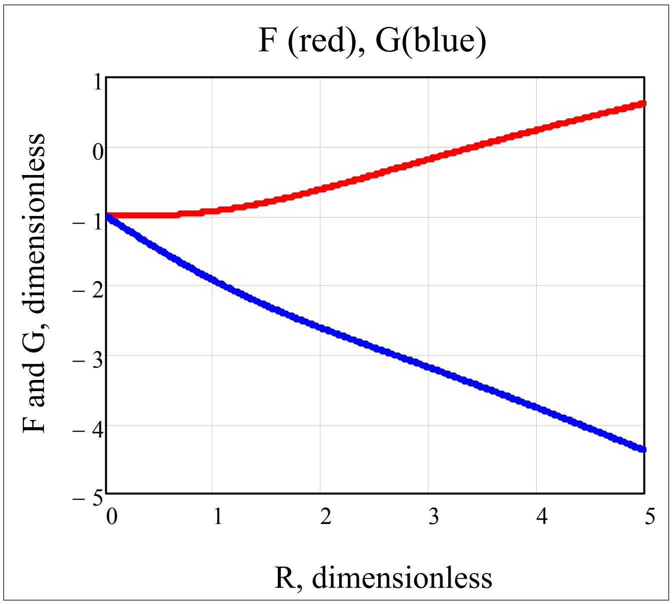

Figure 3. Scaled minimum head (red) and maximum head drop (blue) at the inlet asfunctions of friction number.

The fact that F increases with R while G decreases with R indicates that the initial steady state head at the valve cannot be completely used up by line drafting. The reserve, so to speak, increases with *R*.

3 FIELD DATA

In Recananti, Italy, water from Vallememoria well-field was pumped to an elevated reservoir 4170 m away through a rising steel water main, managed by ASTEA SpA (Osimo, Italy). The small capacity of the reservoir necessitated frequent pump starts and stops at the well-field. Hydraulic transients so created have been measured and studied by Brunone et al. (2001; 2002) and Meniconi et al. (2014). Because of friction and the considerable pipeline length, line drafting was evident. This system provides field data valuable in evaluating the reasonableness of Eq. [1], [5], and [6] at high Reynolds numbers which are not attainable in laboratory tests.

3.1 The rising main of Recanati, Italy

The elevation profile of the pipeline is shown in Figure 4. The pipeline's diameter was 260 mm, a wall thickness of 6.5 mm, and a length of 4170 m.

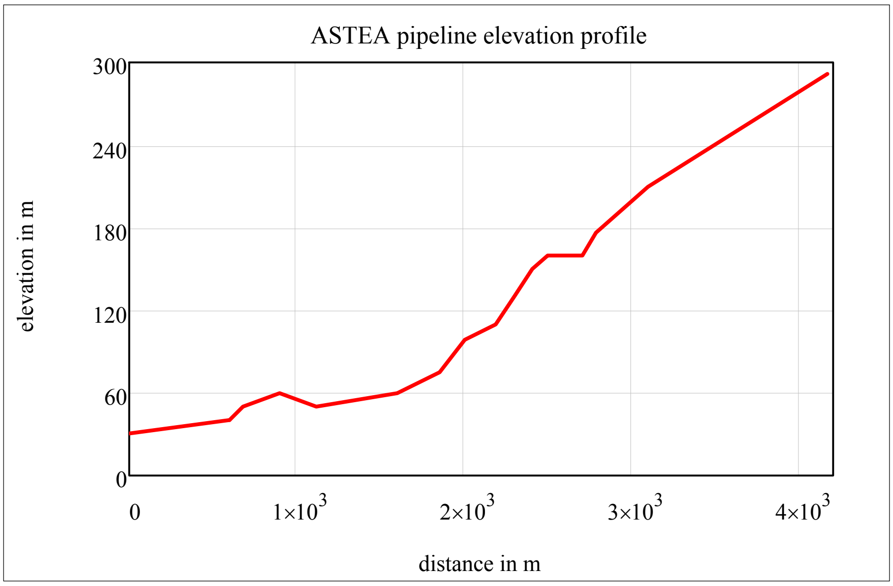

Figure 4. The elevation profile of the pipeline.

At the pump station, the pre-transient discharge was measured by a magnetic flow meter upstream of a quick-acting check valve (CK). The pressure immediately at the downstream of the check valve was measured by a strain-gauge type pressure transducer with a full scale (f.s.) of 400 m scanned every 50 ms. For each transient episode, the data set are the steady state flow rate, the (constant) level of the elevated reservoir, and the pressure time trace just prior to and after the pump shutdown. Assuming a kinematic viscosity of water at 20 °C, and using the measured pressure head just prior to the pump shutdown, and the constant reservoir level, the estimated absolute roughness of the pipe was 2.2 mm (Brunone, 2001) was used here. The water hammer wave speeds, tabulated in Table 1, were estimated from the pressure traces. More details of the system can be found in Brunone et al. (2001). There were no surge control devices on this pipeline which made the data clear cut for this study.

3.2 Data sets

Six sets of data were used. In general, pump shutdowns of a rising water main with an undulating elevation profile is prone to water column separation. But the pressure traces indicated that column separation was minor or non-existent. The conditions are summarized in Table 1 according to the magnitude of the friction number *R* - calculated using Eq. [4] - in ascending order. The initial upstream head is the head just before the check valve first dropped. The fixed downstream head is computed from the initial upstream head, the flow, and the friction factor according to the Darcy-Weisbach equation.

The important uncertainties data that impact this study were:

1. Pressure head: 0.5% of range of 0 to 400 m of water column or 2 m (Brunone et al., 2001);
2. Pre-transient flow: 0.5% of reading (an assumed value which is typical for magnetic flow meters);
3. Time period for wave to travel a distance of 2 *L/a*: twice the 50 ms (Brunone et al. 2001) separation between two consecutive pressure head data.

These uncertainties propagated to the calculated results. The 2m uncertainty in the head data directly impacted the experimental values of F and G. The flow and the timing uncertainties impacted a and ΔH_0 . The latter was used computing F and G. The uncertainty in the friction number R was not noticeably influenced by the data uncertainties.

3.3 Estimating the transient flow rates at the pipeline inlet

The theory that leads to Eq. [1] assumes that the flow at the inlet of the pipeline is stopped instantaneously. In the field tests, the flow reduces over time as the pumps spun down. To get some idea of how close the field inlet flow reduction approaches sudden flow stoppage, we estimated the inlet flow in the following way. For each test, the measured transient head at the check valve discharge and the fixed head at the downstream elevated reservoir were used as the boundary conditions in a method of characteristic model (Wylie and Streeter, 1993) of the pipeline. The Darcy-Weisbach friction factor established from the pre-transient flow was used. The needed inlet flow was computed from this model

Table 1. Parameters of the field tests.

Test no.	Pre-transient flow (m^3/s)	friction factor	Wave speed (m/s)	Initial upstream head (m)	Fixed downstream head, (m)	Friction number ***R***
10	0.00566	0.0387	1,224	293.63	293.27	0.027
7	0.01259	0.0373	1,210	295.21	293.50	0.059
6	0.01993	0.0368	1,231	297.60	293.37	0.090
9	0.02780	0.0366	1,231	301.74	293.56	0.125
1	0.04900	0.0363	1,231	319.86	294.65	0.218
2	0.07890	0.0361	1,285	361.29	296.20	0.335

4 THEORY AND FIELD DATA COMPARISON

For each test, the timing of the beginning of the transients and the timing when the wave reflected from the downstream elevated reservoir to the pressure transducer at the check valve can be identified from the recorded time trace without any ambiguity. The head at the arrival of the reflected wave at the pipeline inlet is the minimum head $H_{\min}$ (same as $H_v(2)$ in Eq. [1]) for that test. Based on the definition of F and G, we compute their values from:

$$F = \frac{H_{\min} - H_D}{\Delta H_0} \quad [7]$$

$$G = \frac{H_{\min} - H_U}{\Delta H_0} \quad [8]$$

Table 2. Computed F and G according to the field data at 2 L/a seconds.

Test no.	ΔH_0 (m)	$H_{\min}$ (m)	F	G
10	43.57	280.19	-0.985	-1.012
7	95.82	264.30	-1.000	-1.058
6	154.31	246.73	-0.991	-1.081
9	215.25	229.91	-0.970	-1.095
1	379.39	183.52	-0.961	-1.179
2	637.70	124.37	-0.884	-1.219

In Figure 5, the field extreme values of the head are compared with the theoretical ones.

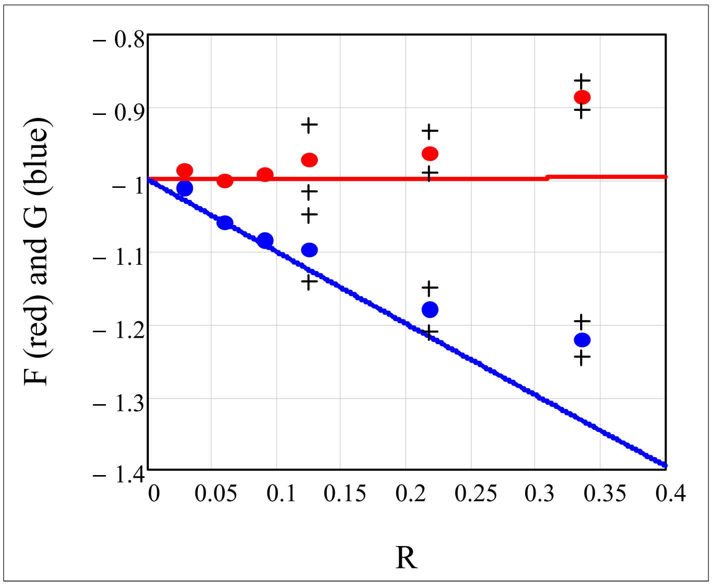

Figure 5. Comparison of the minimum F, and maximum G, heads between the theory and the field data.

The comparisons of head over time are presented in Figure 6-11. For each test, the top panel shows the measured head and the computed discharge at the pipeline inlet. The bottom panel compares the measured head and the head computed from Eq. [1] for the first 2 L/a seconds.

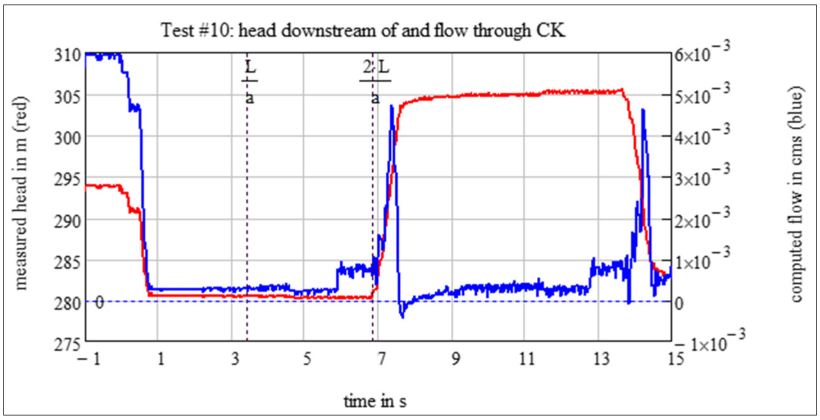

Figure 6. Theoretical and measured inlet heads for R = 0.027.

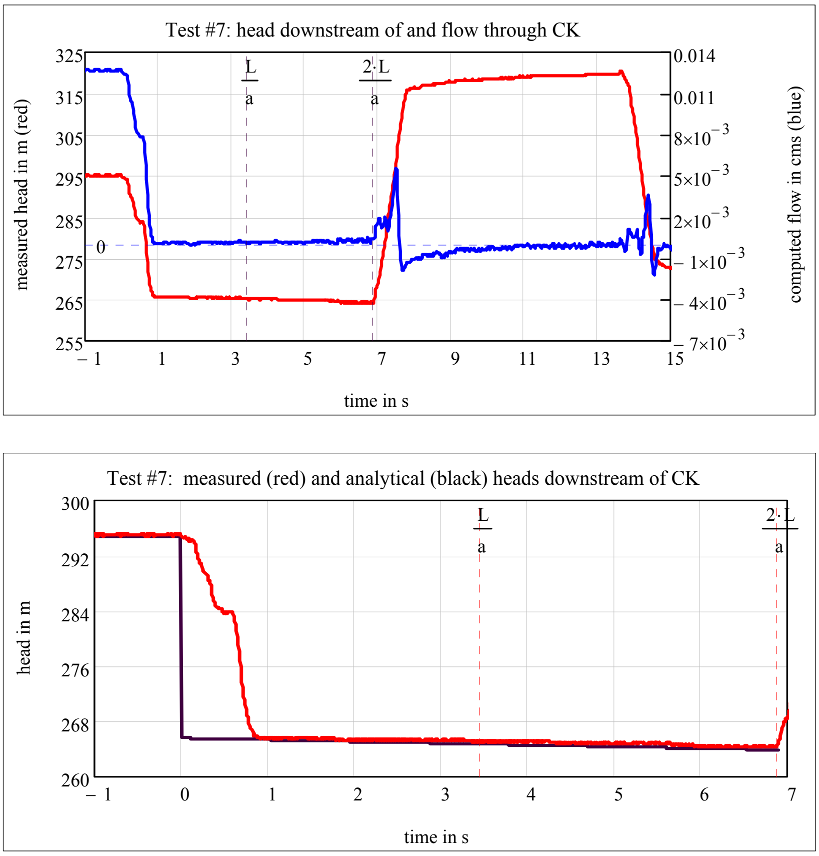

Figure 7. Theoretical and measured inlet heads for R = 0.059.

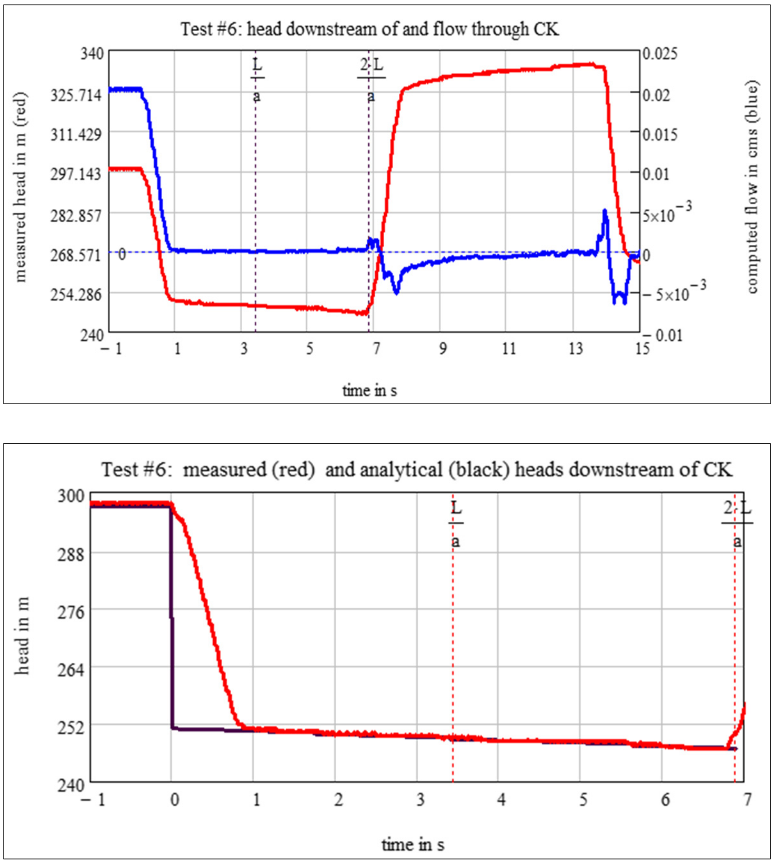

Figure 8. Theoretical and measured inlet heads for R = 0.090.

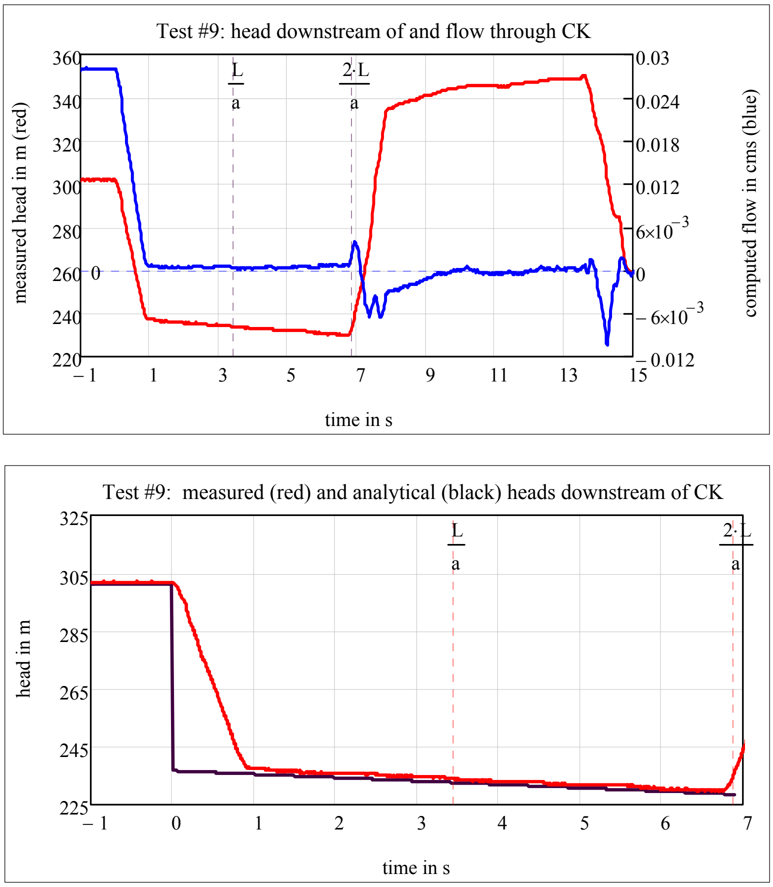

Figure 9. Theoretical and measured inlet heads for R = 0.125.

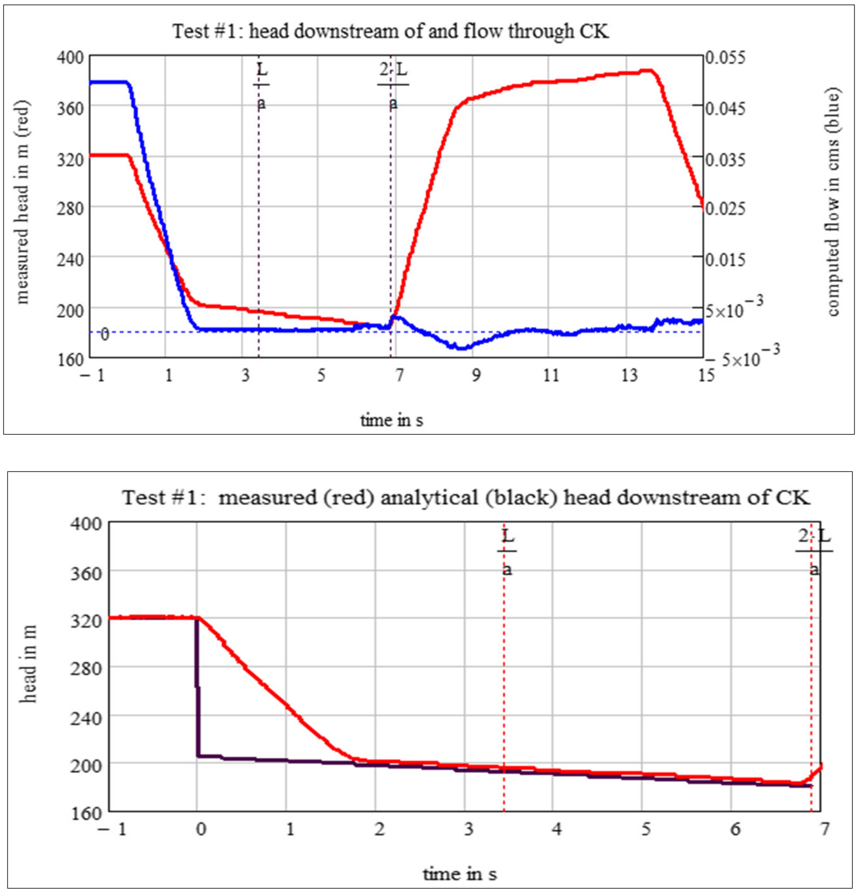

Figure 10. Theoretical and measured inlet heads for R = 0.218.

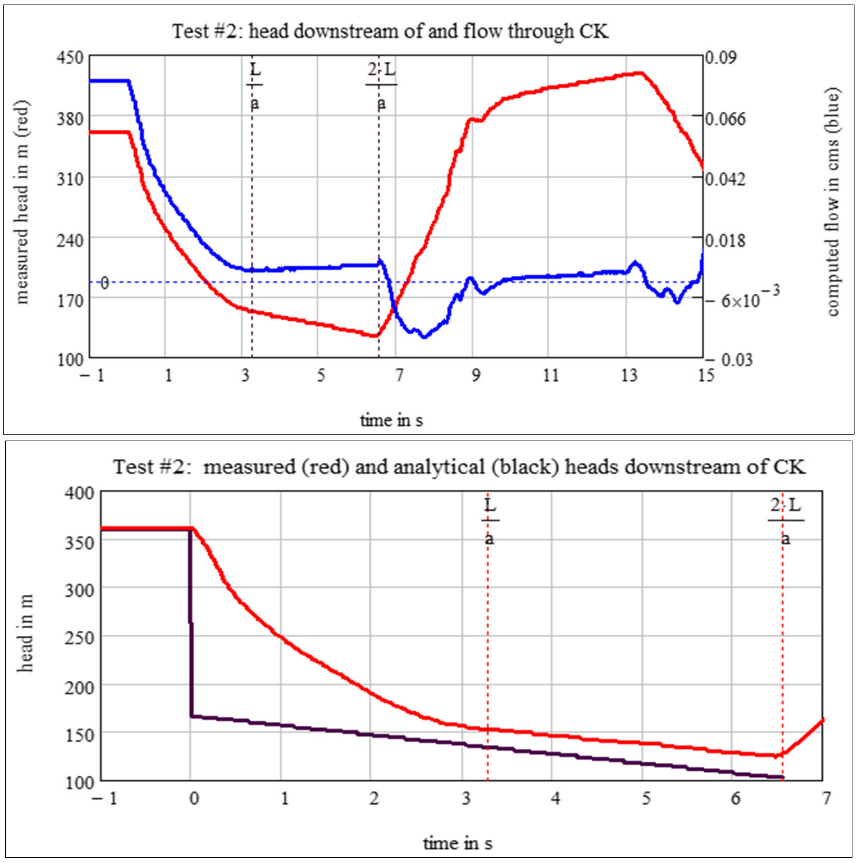

Figure 11. Theoretical and measured inlet heads for R = 0.335.

5 DISCUSSIONS AND CONCLUSIONS

Figure 5 shows that the theory matches the minimum inlet head for tests 10, 7, and 6. The degree of match was not as clear for tests 9, 1 and 2. Estimated uncertainty bounds were indicated for these three tests. It is seen that the theory still matches the data reasonably well for tests 9 and 1 but not 2. The reason for the test 2 mismatch is that, as indicated in the top panel of Figure 11, the flow through the check valve did not stop during the first 2 L/a seconds. Thus, we do not expect the theory to match the test 2 result.

The trend that theory lies below the field data as R (or pre-transient flow) increases is because it takes longer to stop a greater initial flow at the pipeline inlet. This deviates further away from the instantaneous inflow stoppage assumption of the theory. Despite this observation, we note that the theory yields reasonable results for practical applications. This attests the usefulness of the "instantaneous flow stoppage" as a boundary condition for transients modeling.

The simulated discharges at the pipe inlet in Figure 6 to 11 suggest that the check valve closed sooner for smaller initial discharges. This is expected since the initial opening of the check valve would be smaller for smaller pre-transient flow. Again, the theoretical sudden inflow stoppage can be a good model for the pump shutdown. Unfortunately, smaller initial discharge has less frictional head loss resulting in less drafting. This makes the comparison less meaningful. Test 10 is such a case. For the same reason, the initial opening of the check valve would be greater for greater pre-transient flows. Therefore, it would take a longer time for the check valve to close, or it might not even close fully during the first 2 L/a seconds. Test 2 appears to be such a case and the sudden inlet flow stoppage would not be appropriate.

Based on the simulated inlet discharges, the timing of check valve closure for tests 7, 6, 9, and 1, are approximately 0.24, 0.25, 0.26, and 0.53 L/a seconds. Since the inflows were all stopped in less than L/a seconds, the sudden inflow stoppage appears to be a reasonable model for these pump shutdowns where line drafting are still easily noticeable. These comparisons show that the theory can accurately predict line drafting and the minimum head for water mains where the inlet flow was stopped in 2 L/a seconds.

The field data provides an opportunity to verify the theory only at low R values. Nonetheless, the data are valuable and rare. The flow for all the field tests were in the fully turbulent rough pipe zone of the Moody diagram. Such flows are not attainable in laboratories.

ACKNOWLEDGEMENTS

This research was jointly funded by the University of Perugia and the University of Idaho. The support of ASTEA SpA (Osimo, Italy) in the field tests is highly appreciated.

REFERENCES

Brunone, B., Ferrante, M. & Calabresi, F. (2001). High Reynolds Number Transients in a Pump Rising Main. Field Tests and Numerical Modeling. *Proceeding of 4th Conference Water Pipeline Systems,* 339-348.

Brunone, B., Ferrante, M. & Calabresi, F. (2002). Discussion of Evaluation of Unsteady Flow Resistances by Quasi-2D or 1D Models. *Journal of Hydraulic Engineering, ASCE,* 128(6), 646-647.

Liou, Jim, C.P., Brunone, B. & Meniconi, S. (2017). *Understanding Line Drafting in Frictional Water Hammer,* Manuscript under Preparation.

Liou, Jim, C.P. (2016). Understanding Line Packing in Frictional Water Hammer. *ASME Journal of Fluids Engineering,* 138(8), 1-6.

Liou, Jim, C.P. & Wylie, E.B. (2016). *Water Hammer, Handbook of Fluid Dynamics.* CRC Press – Taylor & Francis Group, Roca Raton, FL, Chapter 25.

Liou, Jim, C.P. (1993). *Pipeline Variable Uncertainties and Their Effects on Leak Detectability,* API Report 1149, American Petroleum Institute, Washington DC.

Meniconi, S., Duan, H.F., Brunone, B., Ghidaoui M.S., Lee, P.J. & Ferrante, M. (2014). Further Developments in Rapidly Decelerating Turbulent Pipe Flow Modeling. Journal of Hydraulic Engineering, ASCE, 140(7), 1-8.

Wylie E.B. & Streeter, V.L. (1993). Fluid Transients in Systems, Prentice-Hall, Englewood Cliffs, NJ.

OPTIMIZATION OF AFFECTING PARAMETERS OF PRESSURE RELIEF VALVE USING GENETIC ALGORITHM

HYUNJUN KIM(1), DAWON BAEK(2), GEONJI KIM(3), EUNHYUNG LEE(4), MINJI CHO(5), XIAOYI DONG (6) & SANGHYUN KIM(7)

(1,2,3,4,5,6,7) Department of Environmental Engineering, Pusan National University, Busan, Korea Rep.,
khj.pnu@gmail.com; da095@naver.com; anmhon1212@naver.com; dmstmd14@naver.com; phicnic@naver.com; blueking1992@gmail.com; kimsangh@pusan.ac.kr

ABSTRACT

The purpose of this research is to optimize the performance of the pressure relief valve (PRV) in pipeline systems. The design and operation parameters, such as set pressure, open and closing times and valve coefficient can influence the performance of the PRV. Determination of optimum parameters had been a traditional engineering problem to surge control. This study expands the parameters for system design and operation control. Therefore, this study proposed the methodology for determining design and operation parameters both. Standard reservoir-pipe-valve-reservoir system and a reservoir-pump-pipe-valve-reservoir system are employed to illustrate the analysis for the surge pressure introduced by a sudden valve closure. As an optimization scheme genetic algorithm (GA) is used to find the optimum solution, application of proposed methodology resulted in improving the performance of PRV for surge control.

Keywords: Pressure relief valve; PRV; surge pressure; genetic algorithm; optimization.

1 INTRODUCTION

A change of flow velocity in pipeline system induces change in pressure. The rapid change of the flow condition due to sudden valve closure or pump shutdown causes large pressure variation. The high pressure can cause physical damage to hydraulic components of the pipeline system, such as pipeline element, pump or fittings. The damage can extend to water quality problem or safety issues, which are associated with the pipeline system leakage.

To prevent these problems, proper installation of surge control devices, pressure relief valve, pressure reducing valve, air chamber and air valve is commonly suggested (Jung and Karney, 2006). Pressure relief valve (PRV) is one of the most widely used devices to control water hammer in the pipeline system due to its feasibility in application, efficiency and cost-effectiveness (Boulos et al., 2004; Karney and Simpson, 2007; Wylie and Streeter, 1993). Zhang et al. (2007) conducted an investigation that looked at the affecting parameters of performance of PRV, namely set pressure, opening-closing time and valve size.

The performance of PRV strongly depends on operation parameters and determination of these parameters can be a challenging issue for decision makers. The previous study of Jung and Karney (2006) suggested the methodology for determine proper strategy for the surge control. The proposed methodology focused only on the design and installation parameters where decision has to be made before installation.

In this study, a methodology to determine optimum parameters of PRV is proposed. One-dimensional water hammer simulation model was used to analyze a standard reservoir-pipe-valve-reservoir system and a reservoir-pump-pipe-valve-reservoir system. To obtain an optimum parameter set, genetic algorithm (GA) is integrated into the transient flow analysis model.

2 METHODOLOGY

Zhang et al. (2007) investigated the study about the factors affecting performance of PRV and summarized the decision variable of PRV optimization. The determined decision variable is valve coefficient, setting pressure and opening/closing time. As the objective of this study is to determine optimum design variables, objective function of this study can be written as follow:

$$Minimize\ \Delta h = Max\left[H\left(K_v, SP, OT, CT\right)\right] - \min\left[H\left(K_v, SP, OT, CT\right)\right]$$

where K_v is valve coefficient, SP is setting pressure, OT is opening time, and CT is closing time.

Figure 1 shows the schematic of flowchart of proposed methodology for PRV optimization. GA is integrated into surge analysis model (Wylie and Streeter, 1993). Genetic algorithm is optimization algorithm, which belongs to the class of evolution algorithm that aimed to find global optimization of given problem. Specifically, the GA includes binary coding for the individuals, the probability of the mutation is 0.02, the probability of crossover is 0.5, the population size is 20, the length of each chromosome is 60, and simulations are run for 100 iterations.

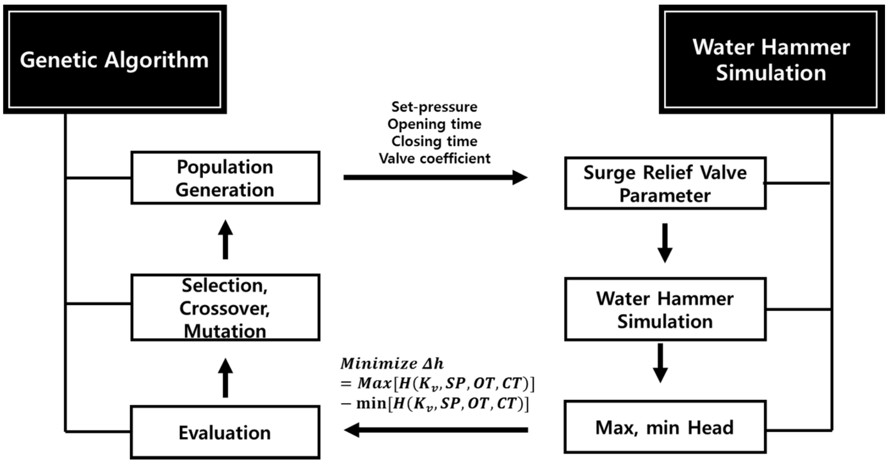

Figure 1. Flowchart for optimization of factors affecting performance of the SRV.

3 RESULTS

Figure 2a shows the schematic of standard reservoir-pipe-valve-reservoir system with two reservoir of 80 m and 60 m of constant head. Two reservoirs are connected by pipeline with a total length of 250 m, diameter of 1.0 m and flow in the pipe line is 3.49 m^3/s. The control valve, which installed at the end of the pipe line, is fully closed within 1.0 s. The methodology proposed in previous chapter was used to select optimum pressure relief valve and after ten iterations and converged, solution for objective variables were obtained. Figure 2b shows the temporal variation of pressure head without PRV and with PRV before optimization and after optimization. Table 1 summarizes the maximum head, minimum head and difference between the maximum and minimum head.

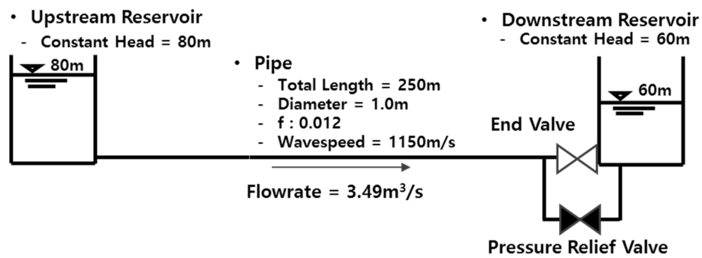

(a) Schematic of standard reservoir-pipe-valve-reservoir system

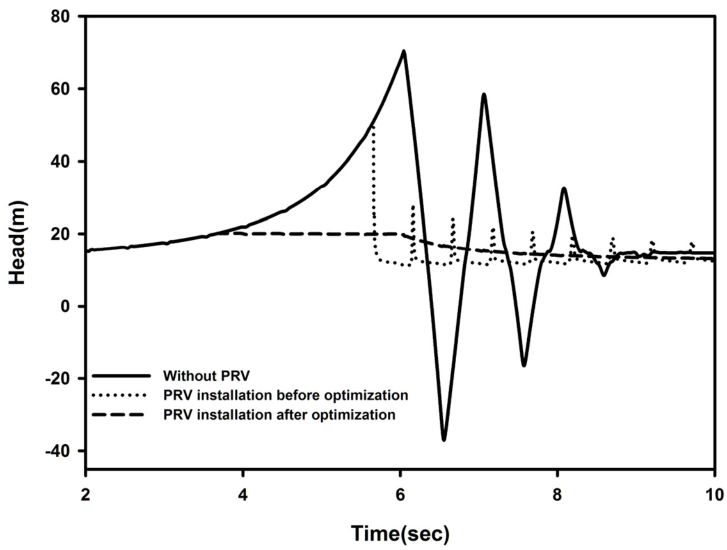

(b) Comparison between without PRV, PRV installation before optimization and after optimization

Figure 2. Schematic and optimization result of standard reservoir-pipe-valve-reservoir system.

The head difference between the maximum and minimum head of the system is 63.0% and 93.1% decrease after installation of unappropriated PRV and optimized PRV, respectively.

Table 1. The maximum head, minimum head and difference between the maximum and minimum head.

	Without PRV	**Before optimization**	**After optimization**
Maximum head(m) $(\mathrm{Max}[H])$	70.5136	51.0437	20.2613
Minimum head(m) $(\min[H])$	-37.0925	11.2509	12.7958
Head difference(m) $(\Delta[H] = \mathrm{Max}[H] - \min[H])$	107.6061	39.7928	7.4655

Figure 3a shows reservoir-pump-pipe-valve-reservoir system. The pressure head of upstream and downstream reservoir is 15 m and 12 m, respectively. The constant speed centrifugal pump is installed at the upstream reservoir and valve at the downstream reservoir is fully closing with in 1.0 s. Optimization was conducted to select optimum feature of PRV and objective variable of the PRV is opening, closing time, set pressure and valve constant. Figure 3b shows the temporal variation of pressure head without PRV, with PRV before optimization and after optimization. Table 2 summarizes the maximum head, minimum head and difference between the maximum and minimum head.

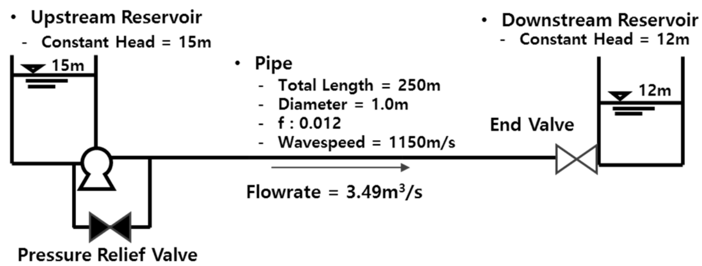

(a) Schematic of reservoir-pump-pipe-vale-reservoir system

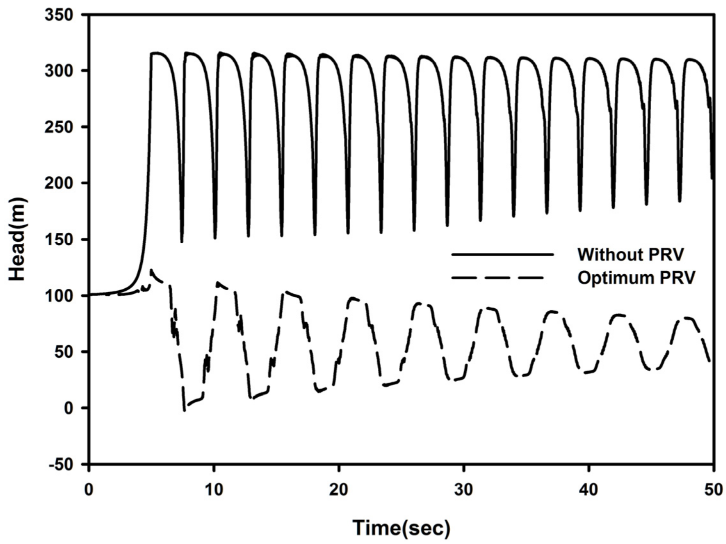

(b) Comparison between without PRV and with PRV

Figure 3. Schematic and optimization result of standard reservoir-pump-pipe-valve-reservoir system.

Table 2. The maximum head, minimum head and difference between the maximum and minimum head.

	Without PRV	After optimization
Maximum head(m) ($\mathrm{Max}[H]$)	316.1552	122.4113
Minimum head(m) ($\min[H]$)	100.9652	-2.2725
Head difference(m) ($\Delta[H] = \mathrm{Max}[H] - \min[H]$)	215.19	124.6838

The head difference between the maximum and minimum head of the system is 42.1% decrease after optimization as compared to without PRV.

The result of proposed methodology shows significant performance on the surge pressure relief. Not surprisingly, the case study shows the performance of the optimized PRV is sensitive to the properties of pipeline system, such as geometrical structures and hydraulic devices of the pipeline system.

4 CONCLUSIONS

This research proposed the methodology for optimization of system and operational parameters for the pressure relief valve. The decision variables affecting performance of the PRV were selected and evolutionary algorithm was integrated into the conventional 1D transient flow analysis scheme. A standard reservoir-pipe-valve-reservoir system and a reservoir-pump-pipe-valve-reservoir system were simulated and the proposed methodology shows excellent performances for optimization of PRV operation parameters.

Even though the methodology shows notable results to surge control, the more research is required to optimize the design factors, such as mass and diameter of the valve disk, spring constant, maximum lift, etc.

ACKNOWLEDGEMENTS

This subject is supported by Korea Ministry of Environment as “Projects for Developing Eco-Innovation Technologies (RE201606133)”.

REFERENCES

Boulos, P.F., Lansey, K.E. & Karney, B.W. (2004). *Comprehensive Water Distribution Systems Analysis Handbook for Engineers and Planners*, MWH SOFT, Inc., Pasadena, Calif.

Jung, B.S. & Karney, B.W. (2006). Hydraulic Optimization of Transient Protection Devices Using GA and PSO Approaches. *Journal of Water Research PL. ASCE Journal*, 142 (1), 44-52.

Karney, B.W. & Simpson, A.R. (2007). In-line Check Valves for Water Hammer Control. *Journal of Hydrology. Research, IAHR*, 45(4), 547-554.

Wylie, E.B., Streeter V.L. & Suo, L. (1993). *Fluid Transients in Systems*. Prentice-Hall Inc., Englewood Cliffs, N.J.

Zhang, K.Q., Karney, B.W. & McPherson, D.L. (2008). Pressure-relief Valve Selection and Transient Pressure Control. *Journal of American Water Works Association*, 100(8), 62-69.

INVERSE TRANSIENT ANALYSIS PARAMETER ESTIMATION ACCURACY FOR SYSTEMS SUBJECT TO HYDRAULIC NOISE AND SHORT DAMAGED SECTIONS

CHI ZHANG(1), AARON ZECCHIN(2), JINZHE GONG(3), MARTIN LAMBERT(4) & ANGUS SIMPSON(5)

(1, 2, 3, 4, 5) School of Civil, Environmental and Mining Engineering, the University of Adelaide, Adelaide, Australia,
chi.zhang05@adelaide.edu.au; aaron.zecchin@adelaide.edu.au; jinzhe.gong@adelaide.edu.au;
martin.lambert@adelaide.edu.au; angus.simpson@adelaide.edu.au

ABSTRACT

Hydraulic transient based methods have been widely studied for anomaly detection and pipeline condition assessment in water distribution systems. Among existing hydraulic transient based methods, Inverse Transient Analysis (ITA) has the potential to achieve cost-effectiveness and spatially continuous assessment of transmission pipelines. In ITA, system parameters are estimated by minimizing the difference between a measured and simulated pressure trace. Measured pressure traces in the field are inevitably contaminated by hydraulic noise. A coarse grid is typically used in ITA to limit the number of decision variables and the model complexity. Research into ITA parameter estimation accuracy, subject to hydraulic noise and damaged section whose length is shorter than the resolution used in ITA, is undertaken in this paper. The investigations are based on a simulated reservoir-pipe-valve model, where a randomly fluctuating head at the reservoir is used to simulate different levels of hydraulic noise. The wavespeeds of the pipes are estimated using the noisy measured pressure traces by the ITA approach. The wavespeeds estimated by ITA approach were compared to the true wavespeeds of the model. ITA was shown to be robust for the numerical case study in this paper.

Keywords: Inverse Transient Analysis (ITA); parameter estimation; noise; pipeline condition; wavespeed.

1 INTRODUCTION

Rehabilitation, repair, or replacement of pipeline infrastructure is a significant challenge for water utilities. Recently, transient based methods for the purposed of leak detection (Gong et al., 2012), blockage detection (Duan et al., 2013), wall condition assessment (Gong et al., 2016) and general parameter estimation (Zecchin et al., 2013), have been widely studied. Inverse Transient Analysis (ITA), a method to match the hydraulic response of pipeline system by adjusting pipeline parameters, has been applied in both the laboratory (Covas and Ramos, 2010) and the field (Stephens et al., 2013).

The work presented within this paper focuses on the investigation of the impact that hydraulic noise has on parameter estimation accuracy. Firstly, noisy pressure traces were numerically generated by a reservoir pipe valve system whose reservoir head has uniform random fluctuations. A novel ITA was applied to those noisy pressure traces to estimate wavespeeds along the pipe section of interest. A comparison of results showed that damaged sections were identified successfully, although the pressure traces were contaminated by hydraulic noise.

2 PROBLEM OUTLINES

The scenario considered by this research is given in Figure 1. The reservoir pipe valve system was used to simulate a transmission main. The pressure wave generator (a fast closing side discharge valve) and pressure measurement sites are installed within the range of pipe section of interest. ITA is to be applied to the pressure traces with the pressure wave reflections created by impedance changes in the damaged sections of pipe. Measured pressure traces in the field are inevitably contaminated by hydraulic noise. The resolution of ITA is limited by the number of decision variables and computational resources. The choice of finer resolution will increase the number of decision variables and complexity of the model, making the problem unmanageable. The question of interest within this paper is twofold. Firstly, accuracy of parameter estimation when ITA was applied to those noisy pressure traces. Secondly, the detectability of the damaged section whose length is short when a coarse numerical grid used in ITA.

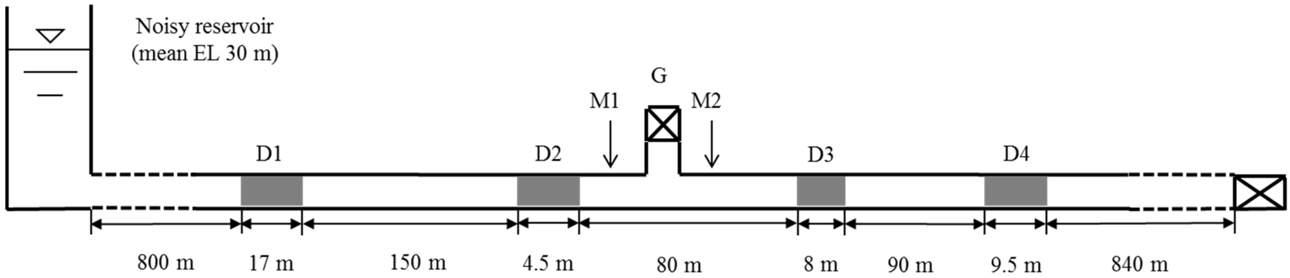

Figure 1. System configration considered by this paper.

3 METHODOLOGY

The methodology within this paper involves calibrating an inverse model to simulated noisy hydraulic data. The simulated noisy data was generated using a method of characteristics approach, solving the standard nonlinear water hammer equations (*i.e.,* using a steady-friction term), where the boundary conditions (*i.e.,* the upstream reservoir head) varied stochastically. A Head Based Method of Characteristics (HBMOC) with a flexible grid was used as the inverse model. A diamond grid for the computation of head using the HBMOC is given in Figure 2. The equation representing the generation of transient waves is derived from the frictionless water hammer equations as:

$$H(x,t) = \frac{2B_2}{B_1+B_2}H(x-\Delta x_1, t-\Delta t) + \frac{2B_1}{B_1+B_2}H(x+\Delta x_2, t-\Delta t) - H(x, t-2\Delta t) + \frac{B_1 B_2}{B_1+B_2}[Q_l(x,t-2\Delta t) - Q_l(x,t)] \quad [1]$$

in which H is the piezometric head, the impedance B is defined as $B_i = a_i/gA_i$, where a = wavespeed of the transient, g = gravitational acceleration, and A = cross-sectional area (note that subscript i = 1 refers to the section just upstream of x and i = 2 refers to the section just downstream from x).

The computation of head and flow can be decoupled to enhance computational efficiency. The derivation of this equation can be found in Zhang et al. (2017). If the node has a zero discharge to the exterior of the pipe, Eq. [1] can be simplified to the following representation of propagation of transient waves:

$$H(x,t) = \frac{2B_2}{B_1+B_2}H(x-\Delta x_1, t-\Delta t) + \frac{2B_1}{B_1+B_2}H(x+\Delta x_2, t-\Delta t) - H(x, t-2\Delta t) \quad [2]$$

This equation was used in a time marching process to form the HBMOC.

A flexible grid is used in the iterative process of inverse modelling. The length of each reach was adjusted by holding $\Delta x_i = a_i \Delta t$ to eliminate the need of interpolation while working within a fixed temporal grid.

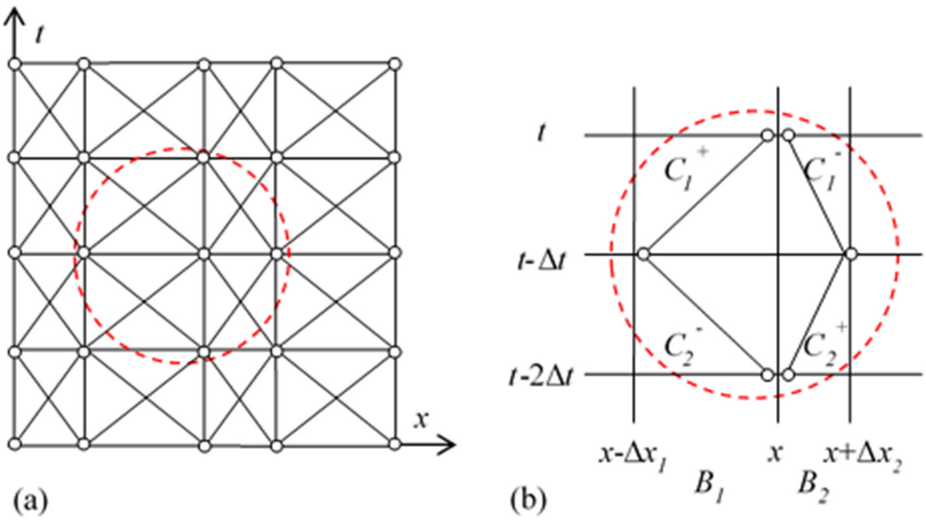

Figure 2. (a) A typical flexible characteristic grid and (b) its diamond sub-grid for HBMOC simulation.

4 NUMERICAL CASE STUDIES

4.1 Preliminaries

The configuration of the numerical case study is depicted in Figure 1. The 2 km reservoir-pipe-system was used to simulate a transmission main with deteriorated sections of pipe. The upstream reservoir has a mean of 30 m of head with uniform random fluctuations of varying magnitude (to be discussed below). The downstream valve has a constant 0.45 m^3/s discharge into air. The pipe has a constant diameter of 600 mm. The wavespeed of the intact pipe sections is 1000 m/s. The four damaged sections were assumed to simulate sections with deteriorated pipe condition and their wavespeeds and length can be found in Table 1.

Table 1. Wavespeed and length of four damaged sections.

	D1	D2	D3	D4
Wavespeed (m/s)	850	900	800	950
Length (m)	17	4.5	8	9.5

The pipe length of interest was a section of 500 m in the middle of the 2 km line transmission main. One transient wave generator (*i.e.,* a fast closing side discharge valve) and two pressure measurement sites were placed in the middle of the section of interest (see Figure 1). The distance from each measurement site to the generator is 10 m. The generator has a discharge of 0.05 m^3/s, and is instantaneously closed (at the time t = 1.5 s).

The raw data to be analysed by the ITA was numerically generated by the method of characteristics with Δt = 0.001 s. Three scenarios to represent different levels of noise were considered in this paper. A stochastic reservoir head of 30 ± 0.1 m, 30 ± 0.3 m and 30 ± 0.5 m were used simulate low, medium and high levels of hydraulic noise (uniformly distributed noise within each range was imposed on the system), respectively. For each level of noise, five sets of pressure traces were generated, each using different reservoir noise sequences. The SNR (signal-to-noise ratio) of each set of pressure trace is calculated by:

$$SNR = \log_{10}\left[\frac{rms(signal)}{rms(noise)}\right] \quad [3]$$

The averaged SNR (signal-to-noise ratio) of three levels of noise are 8.70, 7.57 and 4.91, respectively.

Example pressure traces recorded at the generator with the different levels of noise are given in Figure 3. It can be seen that in the pressure trace without noise, initial reflections and multiple reflections from the damage sections were clearly observed to deviate from the plateau of the step pressure rise. After adding noise to the system from the upstream reservoir, the initial reflections were contaminated, where it is clearly difficult to distinguish the multiple reflections from the pressure traces.

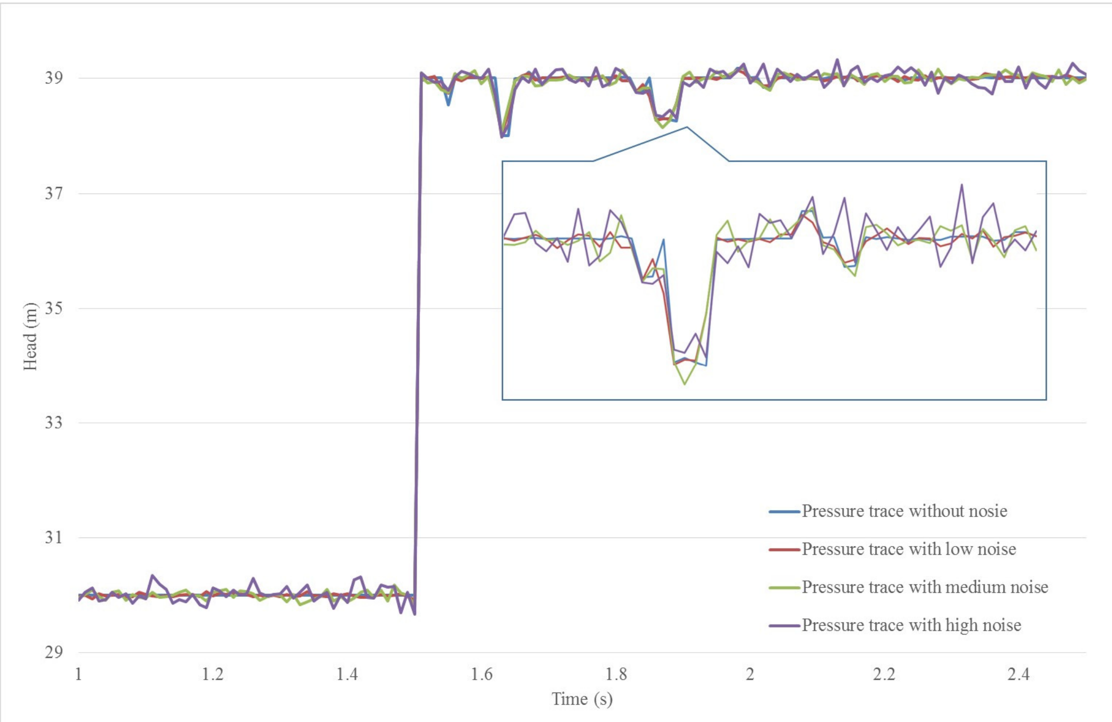

Figure 3. Pressure traces at the generator with different levels of noise used in ITA.

Considering the 500m pipe section of interest, a duration of 2.08 s from the pressure traces were used in ITA. After uniformly distributed noise was imposed at the reservoir, it spreads along the pipeline. Noisy initial steady state conditions recorded at measurement sites are also very close to being uniformly distributed. A higher time resolution used in ITA results in a larger number of reaches, and thus a larger number of decision variables to calibrate. In the field application, considering the model complexity and computational time, a time resolution lower than the sampling rate is typically used. In this paper, the time resolution was set to be 0.01 s (10 times the time step used in generation of synthesized measured data) in the inverse model, resulting in a total of 60 reaches for the inverse model. Due to the adaption of the flexible grid, the space resolution is not fixed. The space resolution for reaches of different wavespeeds can be calculated by $\Delta x_i = a_i \Delta t$. It is worth to be pointed out that the length of damaged section D2 was less than its resolution in the ITA.

The inverse model was calibrated to each data set using the optimization heuristic particle swarm optimisation (PSO). As the number of decision variables was 60, the number of particles was set to be a greater value at 100. The number of iterations was set to be 5000, resulting in 500,000 evaluations overall for the inverse model. The search space interval for the unknown wave speeds was set to be [750, 1050] m/s. Considering the random nature of the optimization algorithm, for each pressure trace, the ITA was run for 50 independent runs, and the results were averaged across the runs compare. The objective function was defined as the squared difference between the “measured” pressure traces and the predicted pressure traces by the calibrated ITA model. A low pass filter was applied to the higher frequency synthetically generated noisy pressure traces before the ITA was employed, so the synthetic data matched the time-grid of the inverse model

4.2 Results and discussions

All the objective function values of each independent ITA run with different scenarios are given in Figure 4. The objective function is the indicator of “goodness of fit” between measured responses and predicted responses by the calibrated model. On average, the objective function values increase with the increasing level of noise introduced into the simulated pipe system. It is worth noting that even for the case without noise, the objective function values are relatively large, this is to be expected due to the coarse grid used in the inverse model, and existence of the damaged section D2 (which is finer than the temporal discretization that the inverse model allows), meaning that the exact solution (which would provide a perfect fit) does not exist in the search space.

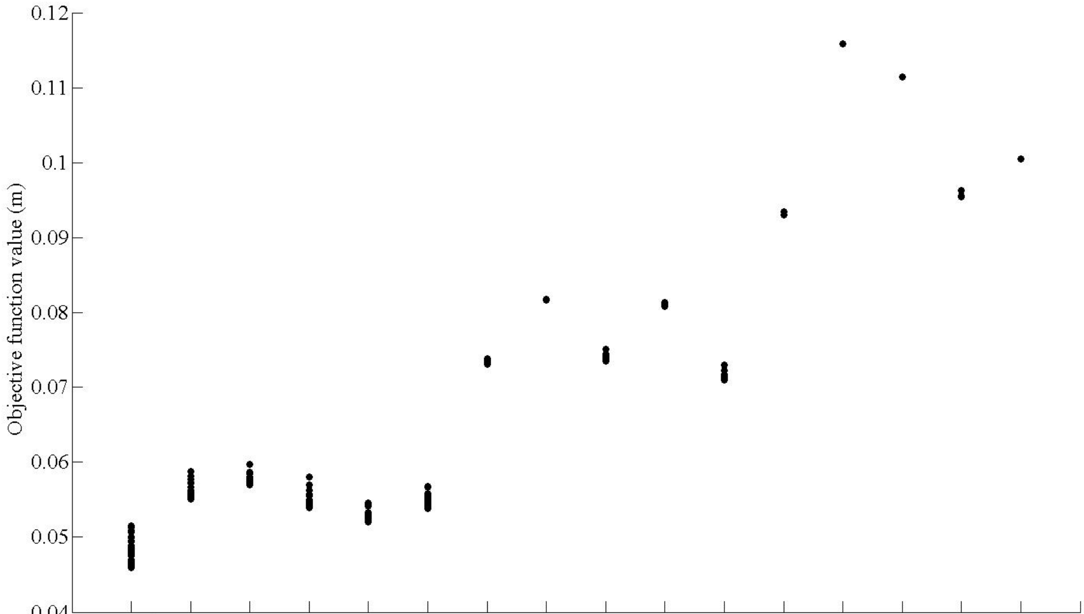

Figure 4. Objective function values of each independent run when different level of noisy pressure traces were used.

Figure 5 represent the wavespeeds estimated by ITA using the five sets of pressure traces without noise. It can be seen that four damaged sections were successfully identified. The average of absolute error was as small as 8.0 m/s. (Absolute error = |estimated value – true value| / true value)

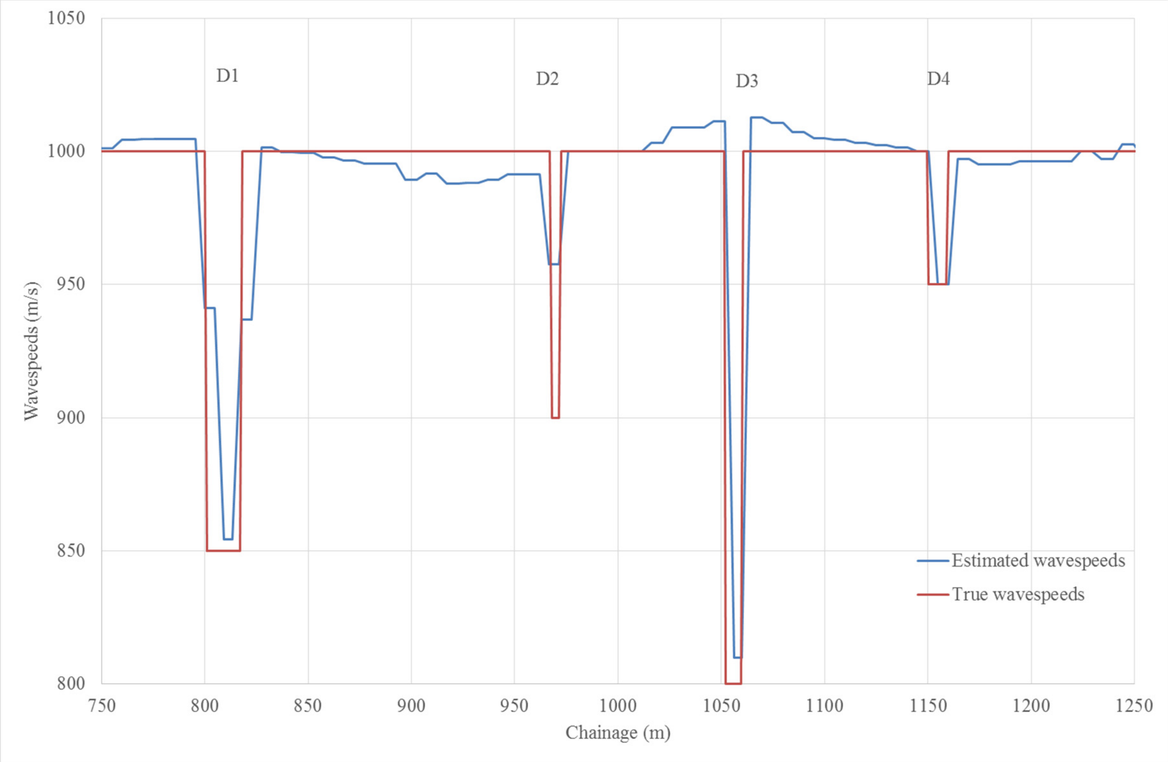

Figure 5. Wavespeeds estimated by ITA pressure traces without noise.

Despite the fact that the length of D2 is short and as the result, its wave propagation time is less than the temporal resolution used by the ITA, it was still identified by ITA. An interesting point to note is that the wavespeed of D2 was identified as 957.7 m/s, which is significantly overestimated. However, the estimated length was calculated to be 9.577 m, which is quite close to its true value of 9.5 m.

Figure 6 represents the wavespeeds estimated by ITA using five sets of pressure traces when the levels of noise are at the low scenario. It can be seen that four damaged sections were successfully identified, and the estimated wavespeed of D2 was overestimated due to its short length. The average of absolute error was 10.0 m/s, which is slightly greater than that of no noise scenario. (Note: This average of absolute error is the average of five absolute relative errors).

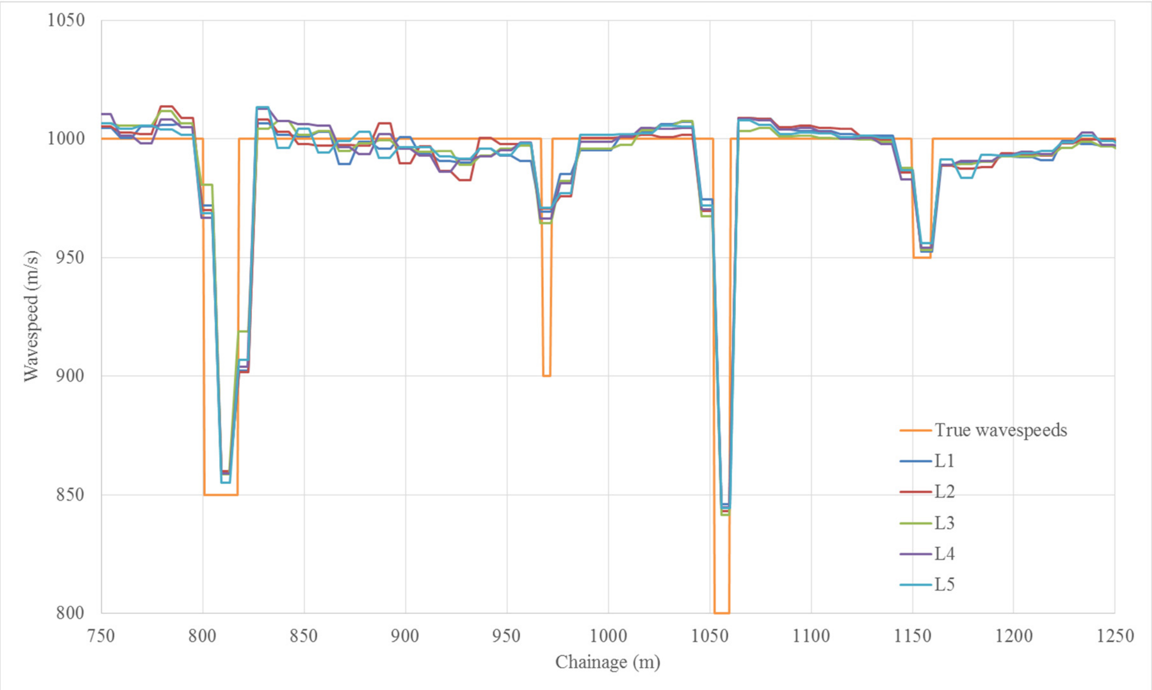

Figure 6. Wavespeeds estimated by ITA using different sets of pressure traces with low noise.

Figure 7 represents the wavespeeds estimated by ITA using five sets of pressure traces when the levels of noise is at the medium scenario. It can be seen that four damaged sections were still successfully identified. However, several high magnitude absolute errors (the maximum absolute error was as high as 108.4 m/s) in the wavespeed estimation have occurred. That are of the same size as D2. As discussed later, these errors in the wavespeed estimation could lead to a false-positive detection of a deteriorated section. The average of absolute error increases to 12.5 m/s.

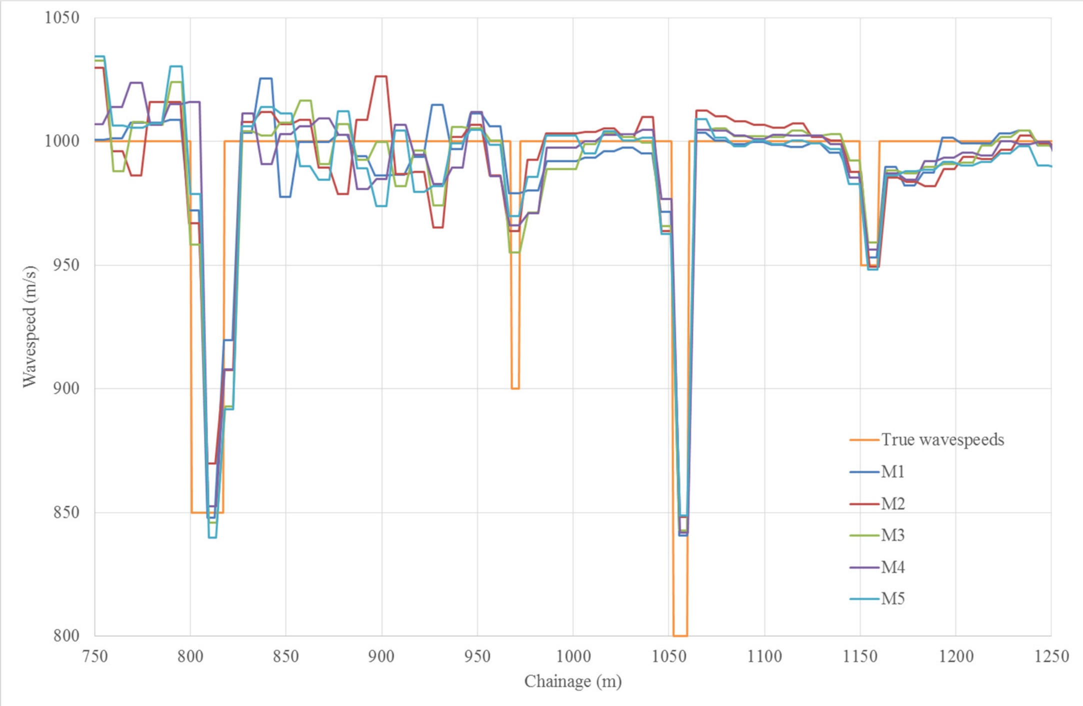

Figure 7. Wavespeeds estimated by ITA using different sets of pressure traces with medium noise.

Figure 8 represents the wavespeeds estimated by ITA using five sets of pressure traces when the levels of noise are at the high scenario. It can be seen that four damaged sections were still successfully identified. However, an increasing number of high localized errors exist in the wave speed estimation. The average of absolute error reaches 16.0 m/s.

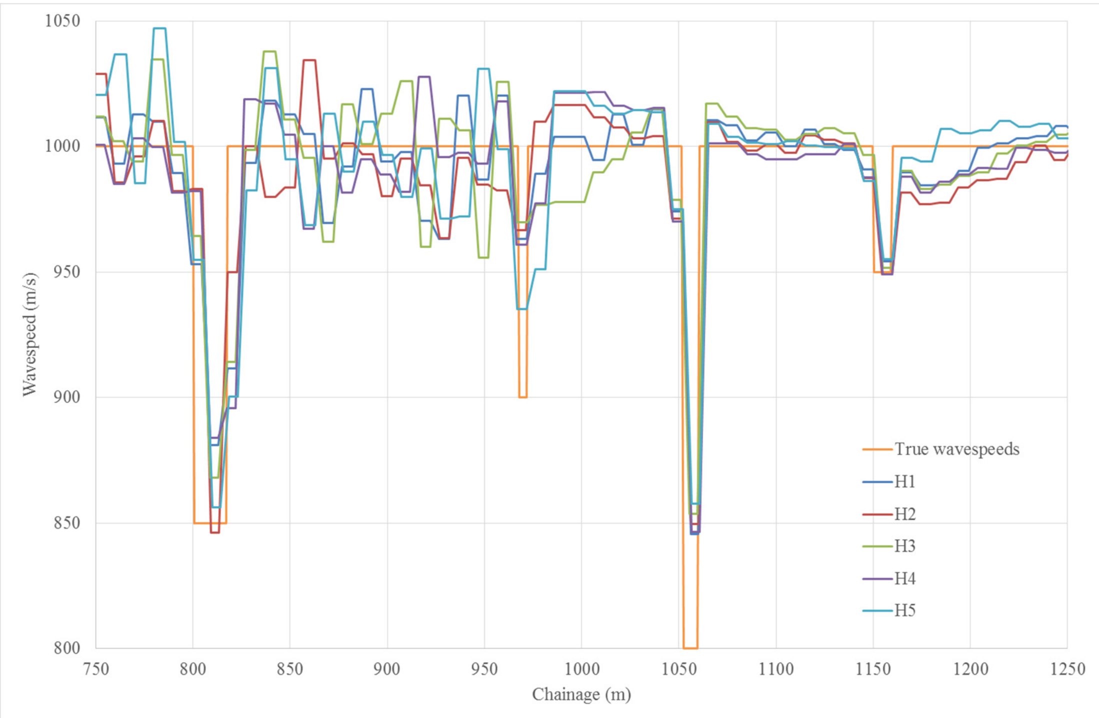

Figure 8. Wavespeeds estimated by ITA using different sets of pressure traces with high noise.

As the wavespeed of an intact pipe section is assumed known to be 1000 m/s, for the purposes of identifying anomalies, any section which has a wavespeed greater than 1025 m/s or less than 975 m/s was identified as an abnormal section with a deteriorated condition. The average absolute error of damaged sections and the number of false-positive detections for the different levels of noise is summarized in Table 2.

Table 2. The average absolute error of damaged sections and the number of false-positive in different levels. of noise.

		D1	D2	D3	D4	Number of false-positive detections
Low Noise	1	3.64%	7.72%	5.75%	0.26%	0
	2	3.64%	7.87%	5.39%	0.34%	0
	3	4.55%	7.18%	5.21%	0.35%	0
	4	3.70%	7.37%	5.58%	0.43%	0
	5	3.64%	7.88%	5.56%	0.66%	0
Medium Noise	1	3.97%	8.79%	5.07%	0.31%	1
	2	4.55%	7.09%	6.03%	0.08%	3
	3	2.27%	6.14%	5.35%	0.96%	2
	4	3.55%	7.35%	5.22%	0.66%	1
	5	1.85%	7.74%	6.08%	0.18%	2
High Noise	1	5.45%	7.02%	5.71%	0.45%	4
	2	5.65%	7.41%	6.21%	0.09%	6
	3	4.85%	7.74%	6.70%	0.17%	6
	4	4.69%	6.76%	5.79%	0.09%	4
	5	3.34%	3.92%	7.20%	0.54%	6

(Note: Relative error = |estimated value – true value| / true value)

The four damaged sections, including the section whose length is shorter than the time resolution used in ITA, were successfully detected by all case studies. The relative error is at its highest for estimation of D2 due to its short length (the 5th data set of high noise was the only exception). It is also worth to be pointed out that when the level of noise increases, the number of false-positives increase, which are due to over adjusting the wavespeeds to match the noisy pressure traces.

5 CONCLUSIONS

This paper investigates the impact that hydraulic noise has on the accuracy of wavespeed estimation by ITA and the detectability of a reach whose wave propagation time is less than the temporal resolution used by the ITA. A novel flexible grid ITA was applied to the pressure traces with hydraulic noise simulated by a reservoir with a stochastically fluctuating head. The results show that all damaged sections, including the section whose length is shorter than the temporal resolution used by the ITA can be successfully identified, despite the fact that the pressure traces were contaminated by noise. ITA was shown to be robust for the numerical cases considered in this paper.

REFERENCES

Covas, D. & Ramos, H. (2010). Case Studies of Leak Detection and Location in Water Pipe Systems by Inverse Transient Analysis. *Journal of Water Resources Planning and Management*, 136(2), 248-257.

Duan, H.-F., Lee, P.J., Kashima, A., Lu, J., Ghidaoui, M. & Tung, Y.-K. (2013). Extended Blockage Detection in Pipes Using The System Frequency Response: Analytical Analysis and Experimental Verification. *Journal of Hydraulic Engineering*, 139(7), 763-771.

Gong, J., Lambert, M., Zecchin, A., Simpson, A., Arbon, N. & Kim, Y.-i. (2016). Field Study on Non-Invasive and Non-Destructive Condition Assessment for Asbestos Cement Pipelines by Time-Domain Fluid Transient Analysis. *Structural Health Monitoring*, 15(1), 113-124.

Gong, J., Lambert, M.F., Simpson, A.R. & Zecchin, A.C. (2012). Single-Event Leak Detection in Pipeline Using First Three Resonant Responses. *Journal of Hydraulic Engineering*, 139(6), 645-655.

Stephens, M.L., Lambert, M.F. & Simpson, A.R. (2013). Determining The Internal Wall Condition of a Water Pipeline in The Field Using an Inverse Transient. *Journal of Hydraulic Engineering*, 139(3), 310-324.

Zecchin, A., Lambert, M., Simpson, A. & White, L. (2013). Parameter Identification In Pipeline Networks: Transient-Based Expectation-Maximization Approach for Systems Containing Unknown Boundary Conditions. *Journal of Hydraulic Engineering*, 140(6), 04014020.

Zecchin, A.C., White, L.B., Lambert, M.F. & Simpson, A.R. (2014). Parameter Identification of Fluid Line Networks by Frequency-Domain Maximum Likelihood Estimation. *Mechanical Systems and Signal Processing*, 37(1), 370-387.

Zhang, C., Gong, J., Zecchin, A.C., Lambert, M.F. & Simpson, A.R. (2017). Faster Inverse Transient Analysis with a Head Based Method of Characteristics and a Flexible Computational Grid for Pipeline Condition Assessment. *Journal of Hydraulic Engineering.* (under review)

Proceedings of the 37th IAHR World Congress
August 13 – 18, 2017, Kuala Lumpur, Malaysia

FAULT DETECTION IN A REAL TRANSMISSION MAIN BY THE PORTABLE PRESSURE WAVE MAKER (PPWM)

SILVIA MENICONI[(1)], BRUNO BRUNONE[(2)], M. FRISINGHELLI[(3)], CATERINA CAPPONI[(4)] & ELISA MAZZETTI[(5)]

[(1,2,4,5)] Department of Civil and Environmental Engineering, University of Perugia, Italy,
silvia.meniconi@unipg.it; bruno.brunone@unipg.it; caterina.capponi@studenti.unipg.it; elisa.mazzetti@unipg.it
[(3)] Novareti SpA, Trento, Italy,
m.frisinghelli@novareti.eu

ABSTRACT

In the last decades, several reliable technologies have been proposed for leak detection and location in water distribution networks (WDNs), whereas there are some limitations for transmission mains (TM). For TM inspection, the most common leak detection technologies are of inline types – with sensors inserted into the pipelines – and are more expensive with respect to those used in WDNs. An alternative to in-line sensors is given by transient test-based techniques (TTBTs), where pressure waves are injected in pipes "to explore" them. In this paper, the performance of TTBTs was checked in a real TM, in which a small pressure wave was generated by means of the Portable Pressure Wave Maker (PPWM), refined at the University of Perugia, Italy, that can be easily connected to the pipe. It is shown that this technique allows the detection of the most important singularities of the TM.

Keywords: Diagnosis; inspection; transmission mains; pressurized pipe; pressure wave generation.

1 INTRODUCTION

Until a few years ago, when systematic actions to reduce Non-Revenue-Water (NRW) were executed because of the negative effects of leaks on the management of modern cities and budget of water utilities, attention was focused mainly on water distribution networks (WDNs). The "official" reasons of such an approach were many: the need of avoiding damages to the foundations of roads and buildings as well as flooding of strategic areas (e.g., the stock market neighbourhood), the large number of joints – each of them being a possible origin of leakage – due to the large number of users and connections, on one side, and the idea that losses in transmission mains (TM) could be countered simply by measuring the inflow and outflow discharge, on the other side. Thus, even if TMs carry the whole discharge – and then also a small percentage of losses implies a large volume of wasted water – very often they have been excluded from leak detection programs. As a consequence, in the last decades several reliable technologies have been proposed for leak detection and location in WDNs, whereas we cannot say the same thing for TMs, apart from the very last few years. The very reasons of such an apparent inexplicable behaviour of water supply managers are of economic origin as lucidly identified by Laven and Lambert (2012) in their paper with the emblematic title "What do we know about real losses on transmission mains?". In fact, since TMs (Figure 1) – which have less appurtenances of WDNs – are buried more deeply and in less accessible locations than WDNs (Laven and Lambert, 2012), inspection technologies are of an inline type – with sensors inserted into the pipelines (Figure 2) – and more expensive with respect to those used in WDNs. An alternative to the use of tethered and free-swimming sensors or acoustic correlators placed inside the pipelines is given by the transient test-based techniques (TTBT) where pressure waves are injected in pipes "to explore" them (e.g. Colombo et al., 2009). It is worth noting that TTBTs can be used to detect not only leaks (e.g. Brunone, 1999; Lee et al. 2007; Covas and Ramos, 2010; Duan et al., 2011; Meniconi et al., 2015), but also other types of faults, such as partial blockages (e.g. Mohapatra et al., 2006; Lee et al., 2008; Meniconi et al. 2013; 2016; Louati et al., in press), partially closed in-line valves (e.g. Meniconi et al., 2011a; 2011b), pipe wall conditions (e.g. Stephens et al., 2013), and illegal branches (e.g. Meniconi et al., 2011d).

To discuss about merits and drawbacks of TTBTs is beyond the scope of this paper where attention is focused on the performance of a device – the Portable Pressure Wave Maker (PPWM) – refined at the Water Engineering Laboratory (WEL) of the University of Perugia, Italy (Brunone et al., 2008; Meniconi et al., 2011c). Such a device allows the generation of a small amplitude pressure wave, which resolves one of the most crucial – maybe the most critical – problem when TTBTs are used. In this paper, the use of the PPWM in a real TM is discussed with particular attention on the achieved precision of fault location.

  / ISSN 1562-6865 (Online) - ISSN 1063-7710 (Print)

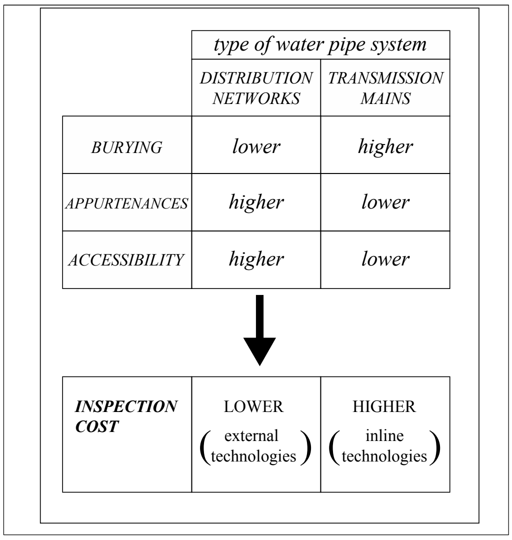

Figure 1 Inspection cost analysis for WDNs and TMs.

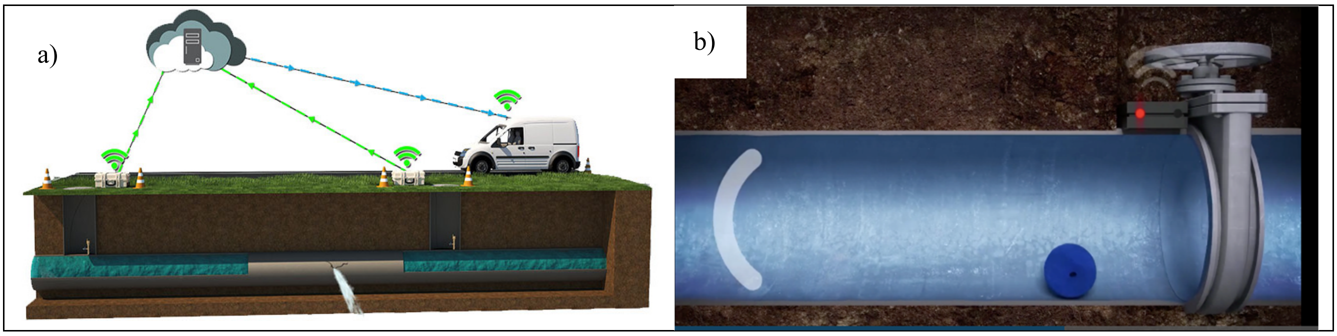

Figure 2 Inline inspection technologies for TMs: a) acoustic sensors with proven wireless communication networks (from www.echologics.com); b) SmartBall® free-swimming sensor (from www.puretechltd.com).

2 MATERIALS AND METHODS

2.1 Field setup

Transient tests have been executed on the iron TM that supplies the city of Trento in the northeast of Italy. Such a pipe, managed by Novareti S.p.A., connects the "Spini" well-field (Figure 3a) to the "10000" reservoir (Figure 3b).

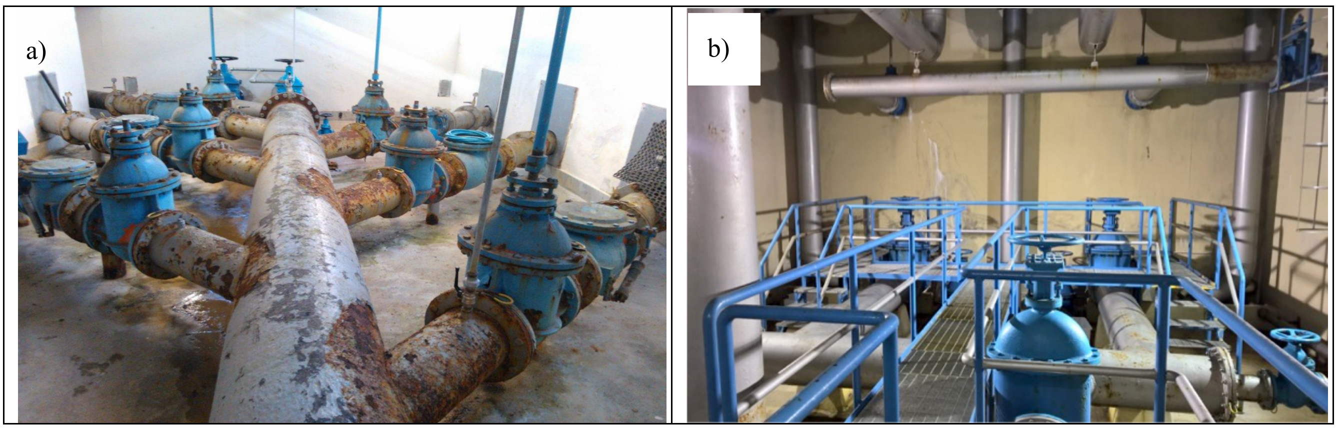

Figure 3 Trento supply system: a) the collecting pipe at the "Spini" well-field, and b) the manoeuvre chamber at the "10000" reservoir.

After the transient tests (Meniconi et al., in press), the water utility technicians executed a strong survey of the TM, and the resulting schematic of the system is reported in Figure 4. The main pipe (bold line in Figure 4) – with a nominal diameter of DN500, internal diameter D = 506.6 mm and wall thickness e = 4.19 mm – has a total length of 1321.97 m. Moreover, the in-line valves 3, 12, 21 24, and 32 are fully open and the short branches, indicated in Table 1, connect the main pipe to dead ends. Particular attention has to be devoted to branches 15-16 and 16-34. In fact, in the preliminary analysis (Meniconi et al., in press), valve 16, at a distance of 2.96 m from the main pipe, was considered closed by the technicians, since node 34 is a well (the "San Lazzaro2" well) that is disused.

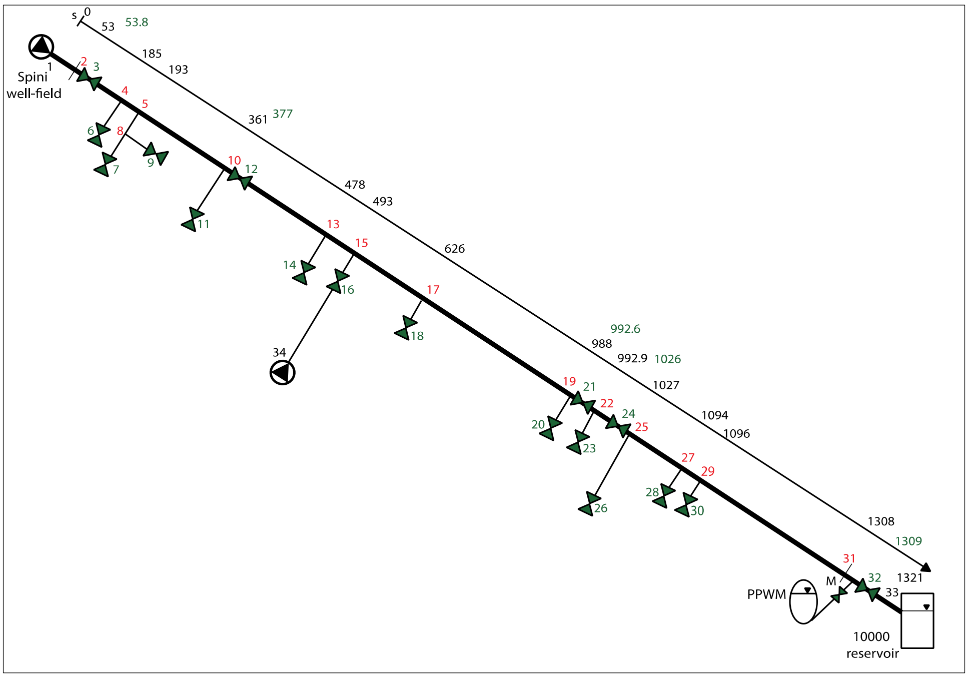

Figure 4 Schematic of the Trento supply system: the main pipe is highlighted by a bold line, whereas valves and connections are indicated in green and red, respectively (*s* = spatial coordinate, starting at the "Spini" well-field).

Table 1. Trento supply system: characteristics of the branches.

Node i	Node j	D (mm)	L (m)	Pipe material
4	6	150	1.723	IRON
5	8	506.62	3.105	IRON
8	7	506.62	1.803	IRON
8	9	200	2.741	IRON
10	11	506.62	3.552	IRON
13	14	80	0.72	IRON
15	16	246.8	2.96	HDPE
16	34	246.8	15.54	HDPE
17	18	100	1.118	IRON
19	20	506.62	3.023	IRON
22	23	200	2.979	IRON
25	26	506.62	6.8	IRON
27	28	150	1	IRON
29	30	200	0.765	IRON

2.2 Field tests

As indicated in Figure 4, the PPWM has been installed at a distance of 13.8 m from the "10000" reservoir, and has been connected to the main pipe by a short connection pipe (about 1 m long) and 1/2'' valve (CV in Figure 5); the pressure inside the PPWM is set by means of a compressor (C in Figure 5). The manual and fast opening of such a valve allows injecting a quite sharp pressure wave into the system. Two piezoresistive transducers have been installed at the PPWM and immediately upstream of the CV (section M of Figure 4), respectively: the first one is to check the pressure at the device, and the second is to measure the injected pressure wave. Just before the transient test, the TM has been isolated by closing the valve just upstream of the "10000" reservoir – not indicated in Figure 4 – and stopping the pumping group at the well-field.

As an example of the executed tests, in Figure 6, the acquired pressure signal at section M is reported. Before the test starts, the pressure at the PPWM (= 316.33 m s.l.m.) was set at a value larger than that in the pipe (= 268.19 m s.l.m.). Then, since the CV can be opened quickly (the maneuvering time is about 0.09 s), a sharp and small pressure wave, F_1 (= 0.87 m), was injected into the pipe travelling with a velocity equal to the water hammer wave speed, *a*. The repeatability of tests has already been proven and discussed in Meniconi et al. (in press).

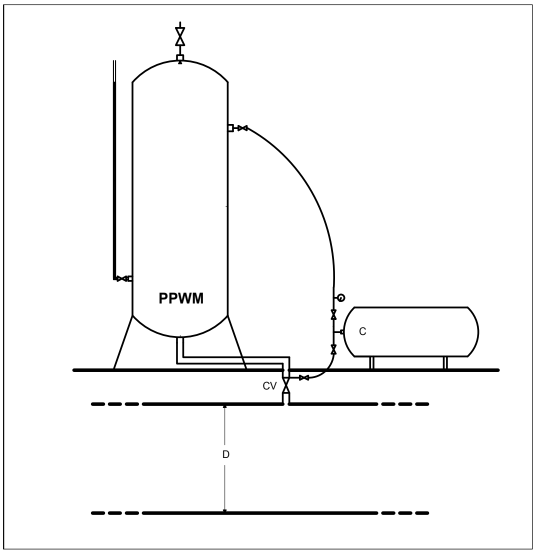

Figure 5 Schematic of the PPWM with the connection to the main pipe.

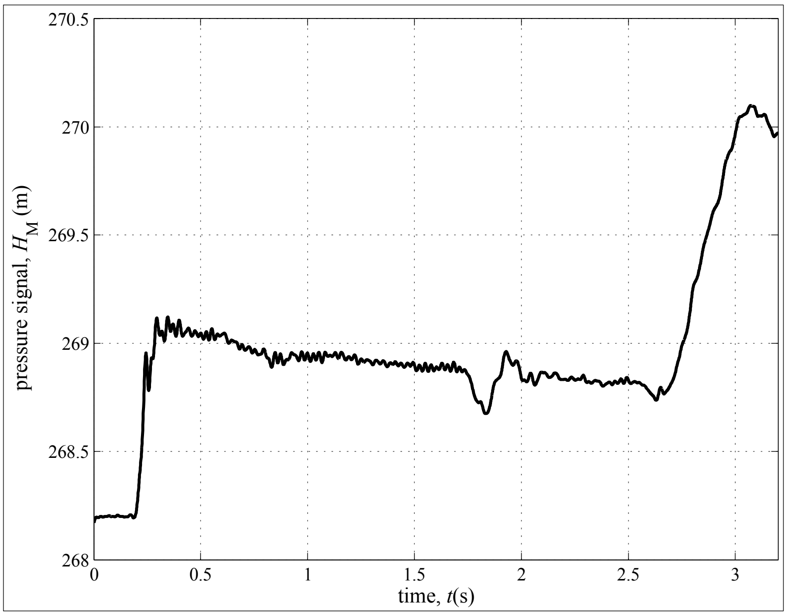

Figure 6 Transient test executed in the Trento supply system: experimental pressure signal acquired at section M (node 31) of Figure 4.

At any singularity (e.g., junctions, valves, dead ends, reservoirs) or anomaly (e.g., leaks, partial blockages, illegal branches, valves certified closed but open or vice versa) the injected pressure wave gives rise to a reflected, f_1, and one or more transmitted waves, F_i (with i = 2…*n* and *n* = number of branches connected to the singularity). The presence of a discontinuity in the pressure signal due to the reflected ore transmitted pressure waves allows in detecting the anomaly. To define the behavior of the anomaly and to detect it, it is useful to introduce the dimensionless reflection and transmission coefficients, C_R and C_T, defined as:

$$C_R = \frac{f_1}{F_1},\ C_T = \frac{F_i}{F_1} \qquad [1]$$

Just to give some examples, under the hypotheses of a frictionless fluid and instantaneous maneuver, at a dead end:

$$C_R = +1,\ C_T = 0 \qquad [2]$$

In other words, the reflected pressure wave is equal to the incident one; and at a junction with n = 3:

$$C_R = \frac{A_1/a_1 - A_2/a_2 - A_3/a_3}{A_1/a_1 + A_2/a_2 + A_3/a_3},\ C_T = \frac{2A_1/a_1}{A_1/a_1 + A_2/a_2 + A_3/a_3} \qquad [3]$$

where A is the pipe area, whereas the subscripts indicate the branches. In Table 2, the theoretical values of f_1 are indicated for all the junctions of the main pipe.

Table 2 Theoretical values of f_1, F^*, and Δt for junctions of the main pipe (in bold the junctions whose behavior is discussed in detail).

Junction (#)	f_1 (m)	F^* (m)	Δt (s)
4	-0.04*F_1	+0.16*F_1	0.003
5	-0.33*F_1	+0.89*F_1	5->8->7 and return: 0.009 **5->8->9 and return: 0.011**
10	-0.33*F_1	+0.89*F_1	0.007
13	-0.01*F_1	+0.05*F_1	0.001
15	-0.24*F_1	+0.73*F_1	**15->16 and return: 0.014** **15->16->34 and return: 0.092**
17	-0.02*F_1	+0.07*F_1	0.006
19	-0.33*F_1	+0.89*F_1	0.006
22	-0.07*F_1	+0.27*F_1	0.006
25	-0.33*F_1	+0.89*F_1	**0.013**
27	-0.04*F_1	+0.16*F_1	0.002
29	-0.07*F_1	+0.27*F_1	0.001

3 RESULTS AND DISCUSSION

It has to be pointed out that in Figure 6, the signal to noise ratio is really high due to both the not so smooth manoeuvre – which is manual – and the very small value of the pressure rise. Consequently, the error in the discontinuity detection can be really significant. In order to improve the accuracy with respect to the time-domain analysis given in Meniconi et al. (2017), the signal of Figure 6 is examined by means of the wavelet transform (Meniconi et al., 2015). The singularities of the signal correspond to chains of maximum local moduli of the wavelet transform, indicated in Figure 7b by dash-dotted lines.

The wavelet transform allows pointing out several discontinuities: among the others, the first one is definitely due to the manoeuvre and happens at t = 0.237 s. The wave caused by the arrival at section M of the pressure wave reflected by the “Spini” well field has to be summed to the one reflected back by the closed valve at the “10000” reservoir, since the distance between section M and such a reservoir is very small. A clear increase in pressure, started at t = 2.741 s, is evidenced by wavelet transform. By associating such a singularity to the overlapping of these two waves, the resulting pressure wave speed of the main pipe can be estimated; the resulting value of a (= 1055.88 m/s) is compatible with the mechanical and geometrical characteristics of the pipe. During the test, the pumps at “Spini” well-field are stopped, and the activation of the check valves is not assured since the wave generated by the PPWM causes a negligible inverse flow (of the order of 10^{-3} m^3/s). Consequently, in terms of boundary conditions, the well-field does not behave exactly as a dead end, and then causes a pressure rise smaller than the theoretical value.

By considering the obtained value of a for all the iron pipes of the system, and a representative value of 400 m/s for the 15-16 and 16-34 HDPE branches, it is possible to evaluate the theoretical values of the first reflected pressure waves, f_1, at the junctions that connect the main pipe to the dead ends. For a given junction, the wave F^* arrives at section M after a time lag, Δt, with respect to the arrival of f_1 (Table 2). Such a wave is the result of the first transmission of F_1 towards the dead end, the successive reflection from the dead end, and the final transmission towards section M.

If the value of Δt is significantly smaller than the maneuver duration (about 0.09 s), the arrivals of f_1 and F^* (that are opposite in sign) at section M cannot be distinguished. In addition, the successive reflections and transmissions of waves at junctions and dead ends can cancel each other. For this reason, only the junctions that cause very large values of f_1 and F^* but only with a very large value of Δt, can cause discontinuities in the pressure signal. By analyzing Table 2, the junctions with these characteristics are #25, and #15. On the contrary, due to the complexity of connected branches, for junction #5 a withdrawal of effects can be expected.

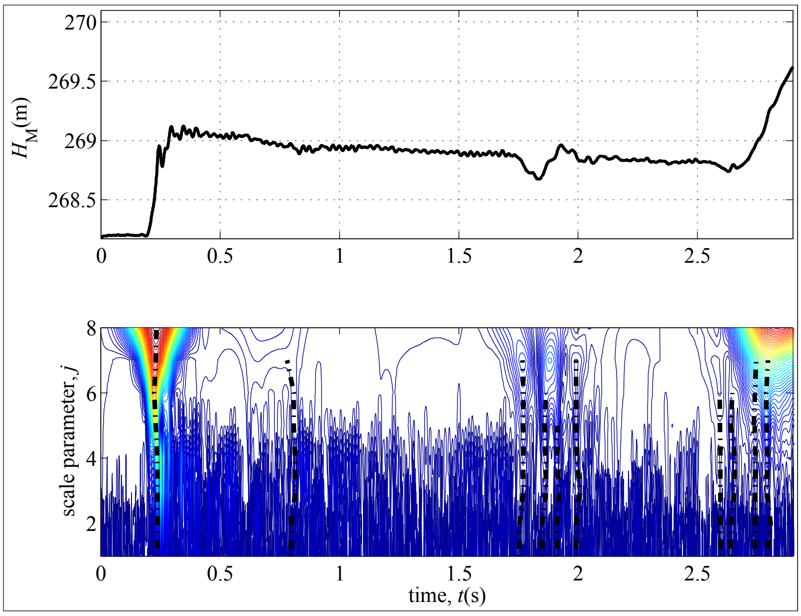

Figure 7 Transient test executed in the Trento supply system: a) experimental pressure signal of Figure 6; b) wavelet transform in the scale-time domain.

At t = 0.798 s, the wavelet analysis points out the second chain of extreme values, even if the corresponding discontinuity is not clearly visible by eye in the pressure signal. This chain can be associated to the wave reflected by junction #25. By assuming such an instant of time as a reference, the estimated distance of junction #25 from section M is 296 m (instead of 280 m), with an error of 5.68% that can be ascribed to the small value of Δt.

A further clear discontinuity is pointed out at 1.755 s and it is due to the wave reflected by junction #15. The estimated distance of junction #15 from section M is 801 m (instead of 814 m), with an error of 1.63%. Such an error is smaller than the one (= 2.44 %) evaluated in the time domain in Meniconi et al. (2017).

The successive discontinuity at t = 1.85 s corresponds to a singularity at a distance of 19 m from junction #15. A further check of the water utility technicians reveals that the valve #16 is not closed and such a discontinuity is caused by the reflection at node #34, at a distance of 18.5 m from junction #15 (the error in the localization of this node is 2.70%).

ACKNOWLEDGEMENTS

This research has been funded by the University of Perugia, Italian Ministry of Education, University and Research (MIUR) under the following projects of relevant national interest: “Advanced Analysis Tools for the Management of Water Losses in Urban Aqueducts” and “Tools and Procedures for an Advanced and Sustainable Management of Water Distribution Systems”; and Fondazione Cassa Risparmio Perugia, under the project “Hydraulic and Microbiological Combined Approach Towards Water Quality Control (No. 2015.0383.021).” The support of Claudio Del Principe in refining the experimental equipment is highly appreciated.

REFERENCES

Brunone, B. (1999). A Transient Test-Based Technique for Leak Detection in Outfall Pipes. *Journal of Water Resources Plannning and Management*, 125(5), 302-306.

Brunone, B., Ferrante, M. & Meniconi, S. (2008). Portable Pressure Wave-Maker for Leak Detection and Pipe System Characterization. *Journal (American Water Works Association),* 100(4), 108–116.

Colombo, A., Lee, P.J. & Karney, B.W. (2009). A Selective Literature Review of Transient-Based Leak Detection Methods. *Journal of Hydro-environment Research*, 2(4), 212-227.

Covas, D. & Ramos, H. (2010). Case Studies of Leak Detection and Location in Water Pipe Systems by Inverse Transient Analysis. *Journal of Water Resources Planning and Management*, 136(2), 248–257.

Duan, H.-F., Lee, P.J., Ghidaoui, M. & Tung, Y. (2011). Leak Detection in Complex Series Pipelines by Using System Frequency Response Method. *Journal of Hydraulic Research*, 49(2), 213–221.

Laven, L. & Lambert, A.O. (2012). What do we Know About Real Losses on Transmission Mains?. *Proceeding, IWA Specialised Conference Water Loss*, Manila (RP), 1-10.

Lee, P.J., Vitkovsky, J.P., Lambert, M.F., Simpson, A.S. & Liggett, J.A. (2007). Leak Location in Pipelines using the Impulse Response Function. *Journal of Hydraulic Research*, 45(5), 643–652.

Lee, P.J., Vitkovsky, J.P., Lambert, M.F., Simpson, A.S. & Liggett, J.A. (2008). Discrete Blockage Detection in Pipelines using the Frequency Response Diagram: Numerical Study. *Journal of Hydraulic Engineering*, 134(4), 658–663.

Louati, M., Meniconi, S., Ghidauoi, M.S. & Brunone, B. (in press). Experimental Study of the Eigenfrequency Shift Mechanism in Blocked Pipe System. *Journal of Hydraulic Engineering*.

Meniconi, S., Brunone, B. & Ferrante, M. (2011a). In-Line Pipe Device Checking by Short Period Analysis of Transient Tests. *Journal of Hydraulic Engineering*, 137(7), 713-722.

Meniconi, S., Brunone, B., Ferrante, M. & Massari, C. (2011b). Potential of Transient Tests to Diagnose Real Supply Pipe Systems: What Can be Done with a Single Extemporary Test. *Journal of Water Resources Planning and Management*, 137(2), 238–241.

Meniconi, S., Brunone, B., Ferrante, M. & Massari, C. (2011c). Small Amplitude Sharp Pressure Waves to Diagnose Pipe Systems. *Water Resource Management*, 25(1), 79–96.

Meniconi, S., Brunone, B., Ferrante, M. & Massari, C. (2011d). Transient Tests for Locating and Sizing Illegal Branches in Pipe Systems. *Journal of Hydroinformatics*, 13(3), 334-345.

Meniconi, S., Duan, H.-F., Lee, P.J., Brunone, B., Ghidaoui, M. & Ferrante, M. (2013). Experimental Investigation of Coupled Frequency- and Time-Domain Transient Test-Based Techniques for Partial Blockage Detection in Pipelines. *Journal of Hydraulic Engineering*, 139(10), 1033-1040.

Meniconi, S., Brunone, B., Ferrante, M., Capponi, C., Carrettini, C.A., Chiesa, C., Segalini, D. & Lanfranchi, E.A. (2015). Anomaly Pre-Localization in Distribution-Transmission Mains. Preliminary Field Tests in the Milan Pipe System. *Journal of Hydroinformatics*, 17(3), 377–389.

Meniconi, S., Brunone, B., Ferrante, M. & Capponi, C. (2016). Mechanism of Interaction of Pressure Waves at a Discrete Partial Blockage. *Journal of Fluids and Structures*, 62, 33–45.

Meniconi, S., Brunone, B., Frisinghelli, M., Mazzetti, E., Larentis, M. & Costisella, C. (2017). Safe Transients for Pipe Survey in a Real Transmission Main by Means of a Portable Device: the Case Study of the Trento (I) Supply System. *Procedia Engineering*.

Mohapatra, P. K., Chaudhry, M. H., Kassem, A. A. & Moloo, J. (2006). Detection of Partial Blockage in Single Pipelines. *Journal of Hydraulic Engineering*, 132(2), 200–206.

Stephens, M., Lambert, M.F. & Simpson, A.S. (2013). Determining The Internal Wall Condition Of A Water Pipeline In The Field Using An Inverse Transient. *Journal of Hydraulic Engineering*, 139(3), 310–324.

EFFECT OF LEAK SIZE ON THE TRANSIENT BEHAVIOR OF A VISCOELASTIC PIPE

SILVIA MENICONI(1), BRUNO BRUNONE(2) & CATERINA CAPPONI(3)

(1,2,3) Department of Civil and Environmental Engineering, University of Perugia, Italy,
silvia.meniconi@unipg.it; bruno.brunone@unipg.it; caterina.capponi@studenti.unipg.it

ABSTRACT

Most of the literature on the transient response of polymeric pipes concerns the case of a single pipe; on the contrary, in very few cases, more complex pipe systems are considered. In this paper, the effect of the leak size on the value of the parameters of a Kelvin-Voigt (KV) single element model was examined. Specifically, the values of the KV parameters – i.e., the Young and dynamic modulus of elasticity, and the retardation time of the viscous damper of the KV element – obtained for the case of an integer pipe, were used to simulate transients in a pipe with a leak. The results of such a preliminary analysis indicate that the performance of the numerical model deteriorates with increasing the leak size.

Keywords: Leak pressurized pipe; transient; polymeric pipes; viscoelasticity.

1 INTRODUCTION

Most of the literature about the simulation of transients in polymeric pipes by means of 1-D models focuses on the optimal number of the conceptual elements (i.e., springs and dashpots) and numerical procedures to use for evaluating their parameters – retardation time and elastic modulus – within the Kelvin-Voigt (KV) approach (e.g., Weinerowska-Bords, 2006). Moreover, attention has been mostly paid to the transient behavior of single pipes for which it has been recently pointed out the dependence of the retardation time on the pipe length (Pezzinga et al., 2016). Only in few cases, the effect of the configuration – as in Ferrante et al. (2009) and Evangelista et al. (2015) for Y systems – and a singularity – e.g., a partially closed in-line valve (e.g., Contractor, 1965; Meniconi et al., 2011) and a partial blockage (e.g., Meniconi et al., 2013a; Mohapatra et al., 2006) – has been explored.

As a concise state-of-the-art, it can be affirmed that the use of KV models in the design phase is still not straightforward because of the unknown role played by the pipe geometrical characteristics. Even less awareness exists in the check procedures in which the effect of a possible fault – e.g., a leak or a partial blockage – on the transient response is known mainly from the phenomenological point of view (i.e., it causes a larger damping of the pressure peaks with respect to the intact pipe).

The aim of this paper – an extension of the preliminary analysis reported in Meniconi et al. (2013b) – is to test whether leak size affects the value of the KV parameters obtained for the same but leak-free pipe. The analysis is based on the results of experimental runs executed at the Water Engineering Laboratory (WEL) of the University of Perugia (Italy) and the numerical simulations given by a previously refined 1-D model (Meniconi et al., 2014).

2 MATERIALS AND METHODS

2.1 Laboratory tests

Experiments were carried out at WEL. The laboratory set-up consists of a high-density polyethylene (HDPE) pipe (length L = 166.28 m, internal diameter D = 93.3 mm, and wall thickness, e = 8.1 mm), which was connected to a pressurized tank (Figure 1), in which the pressure is generated by a pump. A pneumatic valve placed at the downstream end section was used to generate fast closure transients (MV in Figure 1). A device (Figure 2a) placed at a distance equal to 138.58 m from the maneuver valve simulated a rectangular leak. Both MV and the leak discharge into the atmosphere. During tests, for a given value of the pre-transient flow discharge, Q_0, four leaks of different area, Σ_{leak}, (Table 1) were installed by changing the steel plate with orifices of rectangular shape (Figure 2b). The values of the leak effective area, $\mu\Sigma_{leak}$, reported in Table 1 were obtained by means of preliminary steady-state tests.

During transient tests, the pressure time-histories (pressure signals, H) were acquired at 1024 Hz by means of piezoresistive transducers placed at the supply tank, sections UL and DL and just upstream of the maneuver valve (section MS in Figure 1). The pre-transient discharge and water temperature were measured by means of a magnetic flow meter and digital resistance thermometer, respectively.

As an example of the four executed tests, in Figure 3, the pressure signals measured during test no. 2 are reported. According to literature (e.g., Brunone and Ferrante, 2001; Covas et al., 2004), pressure wave reflected by the leak gives rise to a pressure drop in the pressure signals measured at sections DL and MS, H_{DL} and H_{MS}. Moreover, due to the total flow stoppage caused by the complete closure of the maneuver valve, the pressure at the tank, H_T, increased during the tests, according to the pump characteristic curve.

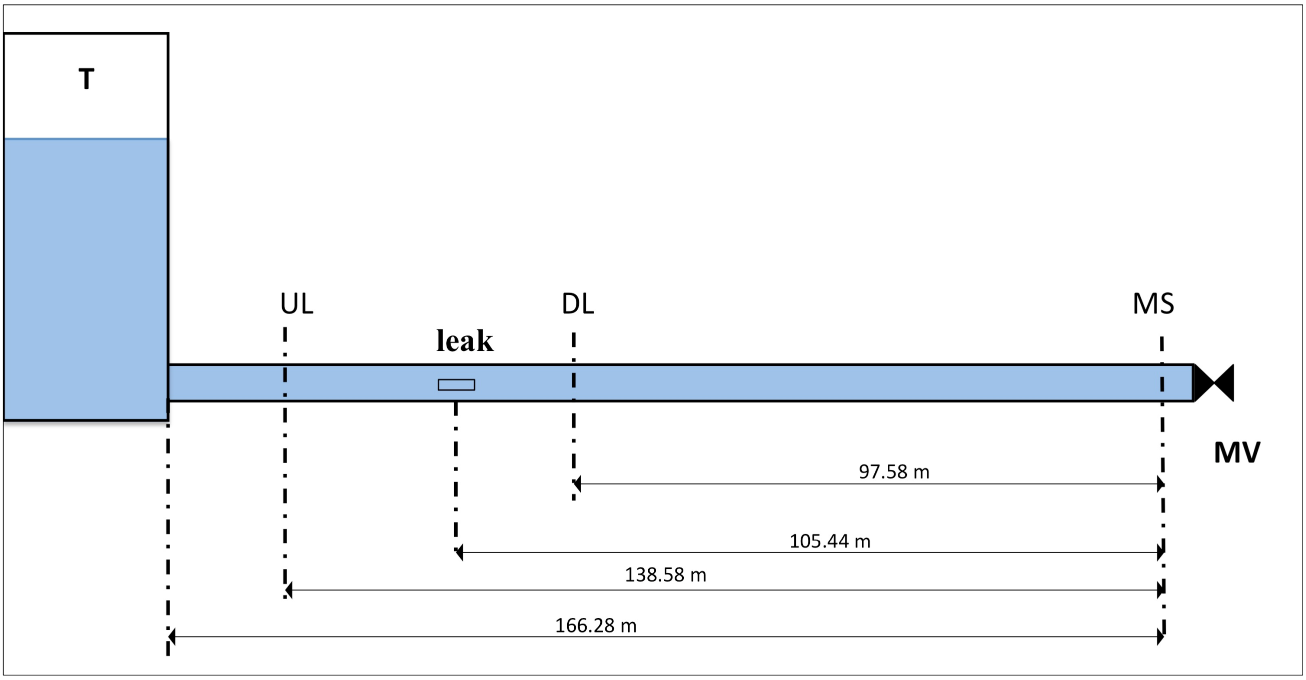

Figure 1 Sketch of the experimental set-up at the Water Engineering Laboratory (WEL) of the University of Perugia, Italy (T = tank, UL, DL, MS = pressure measurement sections upstream of the leak, downstream of the leak, and immediately upstream of the maneuver valve, L = leak device, and MV = maneuver valve).

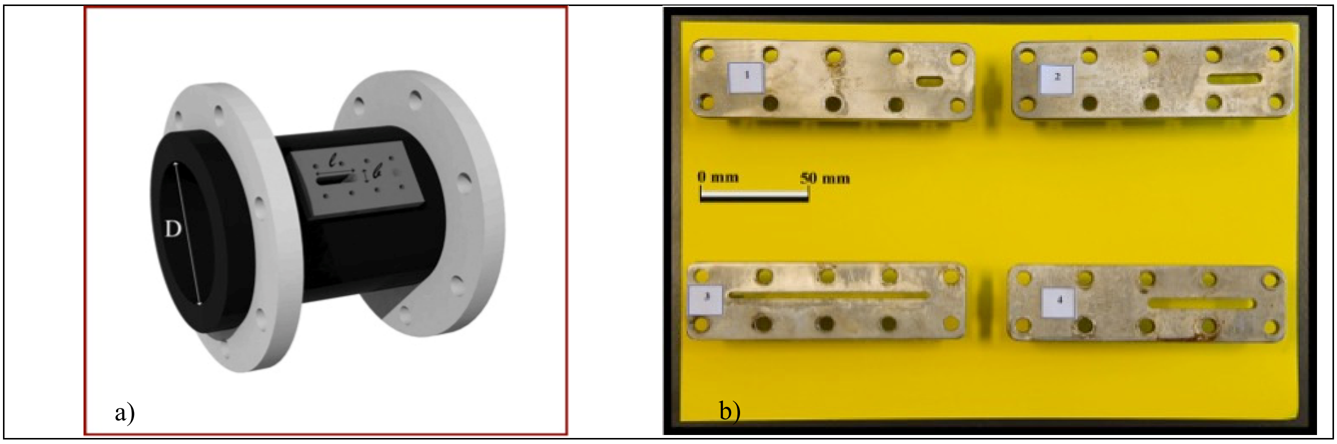

Figure 2 Device simulating the leak: a) branch of pipe with the leak; b) steel plates with the orifice of rectangular shape.

Table 1 Parameters of the laboratory tests.

Test (no.)	Pre-transient discharge, Q_0 (L/s)	Orifice area, Σ_{leak} (mm²)	Leak effective area, $\mu\Sigma_{leak}$ (m²)
1	4.75	52.52	$3.36\ 10^{-5}$
2	4.75	116.64	$6.80\ 10^{-5}$
3	4.75	187.64	$8.26\ 10^{-5}$
4	4.75	232.46	$1.85\ 10^{-4}$

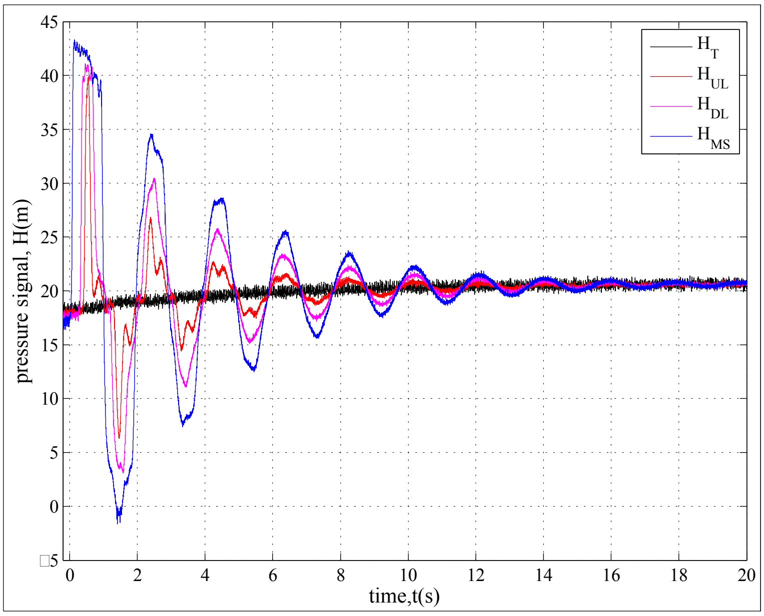

Figure 3 Pressure signals, *H*, acquired during test no. 2 of Table 1.

2.2 Numerical model

The 1-D model used to simulate transients in polymeric pipes includes the momentum equation:

$$\frac{\partial H}{\partial s} + \frac{Q}{gA^2}\frac{\partial Q}{\partial s} + \frac{1}{gA}\frac{\partial Q}{\partial t} + \frac{4\tau_w}{\rho g D} = 0 \qquad [1]$$

where A = pipe cross-section area, g = gravitational acceleration, ρ = fluid density, τ_w = wall shear stress = $\tau_{ws} + \tau_{wu}$ (with the subscript s and u indicating the steady- and unsteady-state component, respectively), s = axial co-ordinate; and the continuity equation:

$$\frac{\partial H}{\partial t} + \frac{a^2}{gA}\frac{\partial Q}{\partial s} + \frac{2a^2}{g}\frac{d\varepsilon_r}{dt} = 0 \qquad [2]$$

where ε_r = retarded strain, and a = pressure wave speed. The unsteady-state wall shear stress component, τ_{uw}, is evaluated within the Instantaneous Acceleration Based (IAB) approach (Brunone et al., 1995; Brunone and Golia, 2008):

$$\tau_{uw} = \frac{\rho k_{uf} D}{4}\left(\frac{\partial V}{\partial t} + sign\left(V\frac{\partial V}{\partial s}\right) a \frac{\partial V}{\partial s}\right) \qquad [3]$$

where k_{uf} = unsteady friction coefficient, V = mean flow velocity, and sign($V\partial V/\partial s$) = (+1 if $V\partial V/\partial s \geq 0$ and -1 if $V\partial V/\partial s < 0$).

In this paper, a single element KV model was used with the viscoelastic behavior simulated by means of a viscous damper and an elastic spring connected in parallel and jointed to a simple elastic spring in series. As a consequence, the third term of Eq. [1] is described by the following relationship:

$$\sigma = E_r \varepsilon_r + \frac{E_r}{T_r}\frac{d\varepsilon_r}{dt} \qquad [4]$$

where σ = circumferential stress (= $\psi pD/2e$, with ψ = dimensionless parameter that takes pipe size and constraints into account, and p = internal pressure), E_r = dynamic modulus of elasticity, and T_r = retardation time of the viscous damper of the KV element. The elastic strain, ε_{el}, of the spring is given by:

$$\varepsilon_{el} = \frac{\sigma}{E_{el}} \qquad [5]$$

where the Young modulus of elasticity, E_{el}, is linked to the pressure wave speed, a, by

$$a = \frac{\sqrt{\frac{k}{\rho}}}{\sqrt{1+\psi\frac{kD}{eE_{el}}}} \qquad [6]$$

with k = bulk modulus of elasticity.

By means of the calibration procedure executed for an intact pipe and described in Meniconi et al. (2012), the following values of the parameters were obtained: ψ = 1.2535, E_r = 8.10 10^9 N/m^2, T_r = 0.15 s, and E_{el} = 2.20 10^9 N/m^2. The unsteady friction coefficient, k_{uf} (= 0.0015), was evaluated on the basis of the plots proposed by Pezzinga (2000) whereas the pressure wave speed (a = 377.15 m/s) was obtained by measuring the pipe characteristic time given by the pressure signals.

As a boundary condition at the leak, the following relationship was considered:

$$Q_{leak} = \mu\Sigma_{leak}\sqrt{2g(H_{leak} - z_{leak})} \quad [7]$$

with z = elevation. To take into account of the mentioned pressure rise at the supply tank, the pressure signal acquired at the tank during the test was assumed as a known boundary condition.

3 NUMERICAL SIMULATIONS AND DISCUSSION

Transients of Table 1 were simulated by assuming the same values of the parameters obtained for the integer pipe. The aim of such a preliminary test is to check the influence of the leak size on the transient behavior of the HDPE laboratory pipe or rather to verify whether the values of the KV model, which allow simulating properly the transient response of a leak-free pipe, still perform properly when transients happen in a leaky pipe. In Figure 4, the numerical, H_n, and experimental, H_e, pressure signals are compared for tests of Table 1. Such plots show that the quality of the numerical simulation is reasonably good for the case of the smallest leak (test no. 1 in Figure 4a) whereas it gets worse and worse with increasing leak size. It is worth noting (Table 1) that in the executed tests, leak effective area, $\mu\Sigma_{leak}$, varied between 3.36*10^{-5} m^2 and 1.85 10^{-4} m^2, with an increase of an order of magnitude.

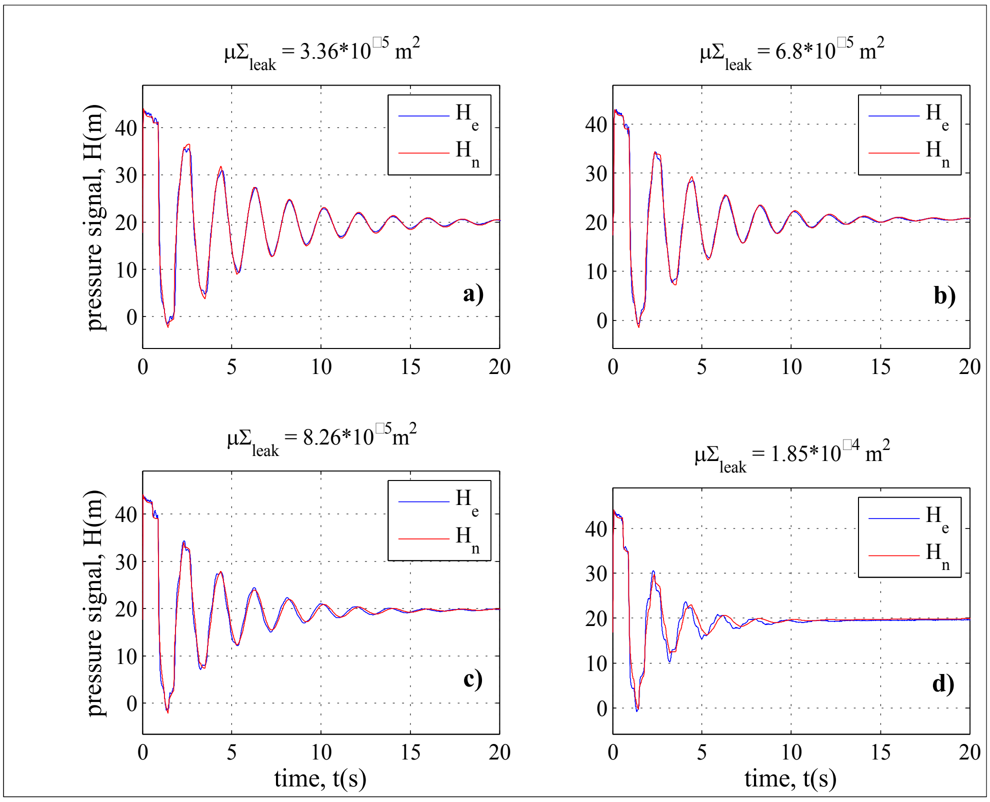

Figure 4 Numerical, H_n, vs. experimental, H_e, pressure signals.

According to Figure 4 plots, it can be stated that, as for tests in which different pipe lengths were considered (Pezzinga et al., 2016), the values of the KV model parameters depend on the geometrical characteristics of the examined pipe system. For the tests of Table 1, the "geometrical" difference is given by the presence of the leak that may (for the larger values) or may not (for the smaller values) divide the pipe into two branches (i.e., the one upstream of the leak and the one downstream of it) from the viscoelasticity modeling point of view. Such two branches behave differently with respect to the leak-free pipe with a larger length.

In the successive phases of the analysis, further tests are needed to determine the critical size of the leak, which influences significantly the transient behavior of the pipe as well as the possible influence of the functioning conditions.

ACKNOWLEDGEMENTS

This research has been funded by the University of Perugia, the Hong Kong Research Grant Council (RGC) under the project: "Smart Urban Water Supply System", the Italian Ministry of Education, University and Research (MIUR) under the following projects of relevant national interest: "Advanced Analysis Tools for the Management of Water Losses in Urban Aqueducts" and "Tools and Procedures for an Advanced and Sustainable Management of Water Distribution Systems", and Fondazione Cassa Risparmio Perugia, under the project "Hydraulic and Microbiological Combined Approach Towards Water Quality Control (No. 2015.0383.021)." The support of Elisa Mazzetti and Claudio Del Principe in the laboratory tests is highly appreciated.

REFERENCES

Brunone, B., Golia, U. M. & Greco, M. (1995). Effects of Two Dimensionality on Pipe Transients Modelling. *Journal of Hydraulic Engineering*, 121(12), 906–912.

Brunone, B. & Golia, U. M. (2008). Discussion of Systematic Evaluation of one-Dimensional Unsteady Friction Models in Simple Pipelines by J. P. Vitkovsky, A. Bergant, A. R. Simpson, and M. F. Lambert. *Journal of Hydraulic Engineering*, 134(2), 282–284.

Contractor, D. N. (1965). The Reflection of Waterhammer Pressure Waves from Minor Losses. *Journal of Basic Engineering*, 87(2), 445–451.

Covas, D., Stoianov, I., Mano, J., Ramos, H., Graham, N. & Maksimovic, C. (2004). The Dynamic Effect of Pipe-Wall Viscoelasticity in Hydraulic Transients. Part I – Experimental Analysis and Creep Characterization. *Journal of Hydraulic Research*, 42(5), 516–530.

Evangelista, S., Leopardi, A., Pignatelli, R. & de Marinis, G. (2015). Hydraulic transients in viscoelastic branched pipelines. *Journal of Hydraulic Engineering*, 141(8).

Ferrante, M., Brunone, B. & Meniconi, S. (2009). Leak Detection in Branched Pipe Systems Coupling Wavelet Analysis and a Lagrangian Model. *Journal of Water Supply: Research and. Technology* - AQUA, 58(2), 95–106.

Meniconi, S., Brunone, B. & Ferrante, M. (2011). In-Line Pipe Device Checking by Short Period Analysis of Transient Tests. *Journal of Hydraulic Engineering*, 137(7), 713-722.

Meniconi, S., Brunone, B., Ferrante, M., & Massari, C. (2012). Transient Hydrodynamics of in-Line Valves in Viscoelastic Pressurised Pipes. Long Period Analysis. *Experiments in. Fluids*, 53(1), 265-275.

Meniconi, S., Duan, H.-F., Lee, P.J., Brunone, B., Ghidaoui, M. & Ferrante, M. (2013). Experimental Investigation of Coupled Frequency- and Time-Domain Transient Test-Based Techniques for Partial Blockage Detection in Pipelines. *Journal of Hydraulic Engineering*, 139(10), 1033-1040.

Meniconi, S., Brunone, B., Ferrante, M. & Massari, C. (2013). Numerical and Experimental Investigation of Leaks in Viscoelastic Pressurized Pipe Flow. *Drinking Water Engineering and Sciences*, 6(1), 11-16.

Meniconi, S., Brunone, B., Ferrante, M. & Massari, C. (2014). Energy Dissipation and Pressure Decay During Transients in Viscoelastic Pipes with an in-Line Valve. *Journal of Fluids and Structures*, 45, 235-249.

Mohapatra, P. K., Chaudhry, M. H., Kassem, A. A. & Moloo, J. (2006). Detection of Partial Blockage in Single Pipelines. *Journal of Hydraulic Engineering*, 132(2), 200–206.

Pezzinga, G. (2000). Evaluation of Unsteady Flow Resistances by Quasi-2D or 1D Models." Journal of Hydraulic Engineering, 126(10), 778–785.

Pezzinga, G., Brunone, B. & Meniconi, S. (2016). On the Relevance of Pipe Period on Kelvin-Voigt Viscoelastic Parameters: 1-D and 2-D Inverse Transient Analysis. *Journal of Hydraulic Engineering*, 142(12).

Weinerowska-Bords, K. (2006). Viscoelastic Model of Waterhammer in Single Pipeline – Problems and Questions. *Archives of. Hydro Engineering Environmental Mechanics*, 53(4), 331–351.

DESIGN OF AIR CHAMBER FOR MITIGATING TRANSIENT PRESSURES IN A PUMPING MAIN

NANGIGADDA MOWLALI [(1)], RUBEN NERELLA [(2)] & VENKATA RATHNAM ERVA [(3)]

[(1,3)]Department of Civil Engineering, National Institute of Technology, Warangal, India,
[(1)]nmowlali@gmail.com; [(3)]evr@nitw.ac.in
[(2)] PACE Institute of Technology and Sciences, Ongole, India
[(2)]ruben_n@pace.ac.in

ABSTRACT

Transient mitigation in pumping mains may require the use of devices such as air chambers/ vessels, open surge tanks, air/vacuum valves, pressure relief valves, etc. Selection and design of suitable transient mitigation devices are dictated by the severity of transient causing events. The design of these systems is a challenging problem and selection, installation, and operation of these hydraulic devices depend on the layout, alignment, pipe and pump characteristics and flow rates. The paper presents a regression based artificial neural network (ANN) model for investigating optimized design variable of air chamber (air volume and chamber volumes) from the system parameters viz., pipeline length, pipe diameter, flow velocity, friction factor, wave celerity, maximum and minimum pressure heads. The system parameters were used as input variables and the corresponding air chamber volume as output variable to train the neural network model. The training has been done by feed forward, back propagation algorithm. The developed model has one input layer (8 system parameters), ten hidden layers (log sigmoid function) and one output layer (air chamber volume). A case study of pumping main of J.C.R. Devadula Lift Irrigation Project, India is presented. The neural network model simulations were compared with the sizes obtained from the results of commercial water hammer software and observed that ANN models provide economical sizes.

Keywords: Air chamber; transient pressures; mitigation; pumping main; ANN.

1 INTRODUCTION

Air chambers or air vessels are also known as closed surge tanks and are effective in protecting pipe system against negative as well as positive transient pressures. The typical shape of an air vessel can be found in Wylie et al. (1993); Stephenson (2002); Zaki and Elansary, (2011), which consists of three components (i) the vessel (ii) the connector pipe and (iii) inlet and outlet orifices controlling flow to and from air vessel. The design variables for optimal sizing of air vessels include: total volume of air vessel, initial gas volume, inflow resistance, outflow resistance (R), and a polytrophic exponent. The outflow resistance (R) can be defined as by Eq.[1].

$$R = \Delta H / Q^2 \qquad [1]$$

Where, ΔH = head drop in m; Q = flow rate in m^3/s. The resistance (R) is correspond to the orifice sizes (and pipe diameters) that are provided for inflow and outflow from pipe system to air vessel. Inflow resistance governs the rate of flow into the pipe system where as outflow resistance governs the rate of flow into the air vessel. Value of polytrophic exponent or the gas expansion constant has significant influence on the required air vessel size. The air vessel design problem can be stated as a constrained optimization problem in which objective is to find total volume of air vessel and initial air volume and the constraints to be considered as range of negative and positive water hammer pressures. For a typical cylindrical and vertically mounted vessel, the design variables are vessel volume C = hS, and initial air volume, which can be given by the initial height of air into the vessel(Z_R). The following physical, functional and fluid parameters dictate the size (volume) of air vessel for given problem. (i) Physical parameters of the pipe: static or geometric elevation to overcome-H, Length-L, diameter-D, friction factor-f; (ii) Fluid-pipe mixed parameters: celerity of the pressure wave-a, (iii) Parameters related to the steady-state velocity- V_R, (iv) Functional parameters that represent the extreme piezometric heads or pressures desirable at the upstream (without loss of generality) end- H_{max} and H_{min}.

There is no explicit and direct relationship between these parameters and the size of air vessel required. Several approaches based on different tests and heuristic criteria can be found in the literature. However, professionals find that air vessel optimization is usually a trial and error process, generally performed by using a transient simulation software package. This eventually, provides the minimum air vessel volume required so that the maximum and minimum developed pressures at the pumping station do not exceed H_{max} and H_{min}, respectively. A neural network that encapsulates this unknown trial and error process from a relevant number of cases, already solved, that allows to directly obtain the minimum air vessel volume required. As a tool to determine such a volume, it represents an important time saving aid for users. Eq. [2-3] represents basic water hammer equations (Wood et al., 2005; Almeida and Koelle, 1992; Wylie and Streeter, 1993).

$$\frac{\partial H}{\partial t}+\frac{a^2}{gA}\frac{\partial Q}{\partial x}=0 \qquad [2]$$

$$\frac{\partial H}{\partial x}=-\frac{1}{gA}\frac{\partial Q}{\partial t}+f(Q) \qquad [3]$$

Where Q = flow rate, H = pressure head, f(Q) = friction slope expressed as a function of flow rate, A = pipe flow area, a = pipe celerity or wave speed, g = gravitational acceleration, x and t the space-time coordinates. Advective terms are neglected in the above equations as they are negligibly small for most water distribution problems of practical importance. Solution of Equations [1] and [2] with appropriate boundary conditions will yield head (H) and flow (Q) values in both spatial and temporal coordinates for any transient analysis problem. The above equations are first order hyperbolic partial differential equations in two independent variables (space and time) and two dependent variables (head and flow). Many studies on surge mitigation devices can be found in the literature which include: Izquierdo et al. (2006), Lee (1998), Stephenson (2002), Kim (2008), De Martino and Fontana (2012), Zaki and Elansary (2011), Yu et al. (2011), Di Santo et al. (2002), Ramalingam and Lingireddy, S. (2014), Ze-xuan and Keat (2003) and Ramos et al. (2004).

2 NEURAL NETWORK MODEL

The multilayer perceptron(MLP) is one of the most widely used feed forward artificial neural networks. This network consists of a layer (input layer) of inputs, xi, another layer (output layer) of outputs, zK, and one or more intermediate layers (hidden layers) which takes into consideration only one hidden layer with outputs noted by yJ, and only one unit (neuron) in the output layer. Each unit of the hidden and output layers has a function assigned, f, (which may be non-linear), called transfer or activation function, such as a sigmoid or a hyperbolic tangent, etc.

The most frequent learning method for the multilayer perceptron is called “generalized delta rule” or “back propagation” of error. This type of learning is called supervised since to be performed, it is necessary to provide the network with the correct answer that the output layer has to produce for a number of cases that are already solved. For the network to learn correctly, the output ZK produced by the network should be close to the correct response, tK, called target, which will be provided to the network during the learning phase. This is achieved by adjusting the weights associated to the links (synapses) between units (neurons) and the links between certain inputs in the units called biases. We will call w_{JI} the weights of the hidden layer and w, those of the output layer. The biases will be, $\theta j and \theta' k$. The performance of the network can thus be expressed by Eq.[4].

Being the activation function of a sigmoid, such as the following:

$$f(x)=\frac{1}{1+e^{-x}} or f(x)=\tanh(\mathrm{x}) \qquad [4]$$

The generalized delta rule performs the adjustment of the weights by calculating the value of the error for a specific input and then transfers it, by back propagation(BP), to previous layers, so that each unit adjusts its associated weights to minimize an error function These steps are repeated for each input pattern of the so-called training set, what is known as online learning. Alternatively, if the updating of the weights is performed upon presenting all the training patterns to the network, the process is known as batch learning. In any case, the error function decreases gradually and the network learns. Given an input pattern x^V (v =1,..., p), the components of the network output, z^v are given by If t_v is the target, the correct output, corresponding to x^v, the function to be minimized.

The mean square error can be expressed by Eq.[5];

$$E(W_{ij},\theta_j,W_{KJ},\theta_K)=\frac{1}{2}\sum_v\sum_K(t_v-Z_r)^2 \qquad [5]$$

The minimization can be performed by means of different algorithms, which range from simple gradient descent algorithms, to conjugate gradient methods, second order Newton, which do not require the Hessian matrix, and the Newton method itself . The next section describes the methods used and their capabilities to solve the problem under study. There are several error minimization algorithms (2) that allow the progressive adjustment of the weights in the learning process. For this work, we have used some of the functions of Matlab®

Toolbox, nnet. The convergence rate of the deferent algorithms depends on the technique used and it is closely related to the mathematical foundations based on network design.

```
net=newff(minmax(Pn[nn1,nn2,1], {tansig, tasig, purelin}, trainlm);
net. trainparam. show      =50;
net. trainparam. epoches  =2000;
net. trainparam. goal       =1e-5;
for i=1:2;
net. layers{i}.initFcn =initwb;
net. biases{i}.nitFcn =rands;
end;
```

Once the training data have been correctly loaded in the working space, any of the functions implemented by Matlab must be fed with a number of parameters defining; (a) The design of the network structure and (b) The training algorithm. A typical set of commands to perform these tasks is shown above.

The first command creates the neural network ready to be trained within the object net. In the example corresponding to the figure, the network is created with three layers; the first one has nn1 neurons, the second nn2 and the third 1. Vector minmax(Pn) contains the maximum and minimum values of each one of the input data. The transfer functions are tansig in the first two layers and linear (the identity functions) in the output layer. The training function used in the example, trainlm, implements the Levenberg–Marquardt algorithm.

Once the network structure has been created, some parameters associated to the training function are initialized., in particular, defines the number, show, of iterations between two consecutive displays of the training status; the total number of iterations, epochs, which will be performed in the process; and a level, goal, of the error function value (2) to drop below. The two latter are mechanisms to stop the learning process. Next, it is performed the initialization of the network weights to random values ranging from -1 to 1. Different initializations were performed and very close behaviours of the network were obtained. Finally, the training function, train, is called by passing to it the object net, which defines the network, and the matrices that contain the inputs, Pn, and the targets, Kn, which will be used to carry out the learning. According to this basic procedure, several trials have been performed with different networks, changing the number of layers, the number of neurons per layer and the training function. With regard to the training function, the best results have been obtained, as would be reasonably expected, with some functions that implement the most powerful optimization techniques. As far as first order methods concern, the conjugate gradient in its Polak–Ribiere version (traincgp) has shown excellent performance. As for second order methods, the Levenberg–Marquardt (trainlm), which allows quadratic approach, and therefore is a Quasi Newton method, although it does not require the calculation of the Hessian matrix, presents also an excellent behaviour (Mowlali, 2014).

3 DATA ANALYSIS

As mentioned above, to train the network, we used a set of data from almost 150 real cases previously studied that had been recorded, and other 150 simulations specifically performed to cover cases not taken into consideration in those cases. On the other hand, a set of data was completed with another 150 patterns obtained from the Graze and Horlacher’s charts. These data were shuffled and distributed into three parts: training, validation and test data. The networks response can be assessed to a certain extent by the errors provided by the test data. The response for the test data has been perfect, as stated above. Nevertheless, it is interesting to study with more detail the networks response. One possibility is to carry out a regression analysis to assess such response. All the training, validation and test data were used and a regression analysis between the values used and the networks output performed. The Matlab toolbox nnet also provides an Appropriate tool: the postreg function.

a) Before doing the ANN the entire input and target data were normalised in between 0 and 1 using Eq.[6].

$$P_a = \left\{ \frac{(R_a - R_b) * (P - A)}{(B - A)} \right\} + R_b \qquad [6]$$

Where; Pa is a matrix of normalized data; Ra is 0.9 and Rb is 0.1; P is a matrix of raw data; A is minimum value of matrix P; B is maximum value of matrix P.

b) ANN is performed by using MATLAB. In this study, 75% of the data were used as training and 30% data used as testing and validation data.

c) In the present study, feed forward back propagation network is used.

d) MATLAB provides built-in transfer functions which were used in this study; linar (purelin), Hyperbolic Tangent Sigmoid (logig) and Logistic Sigmoid (tansig).

4 MODEL APPLICATION TO STUDY AREA

J. Chokka Rao Godavari Lift Irrigation project has been envisaged to lift 14m3/s of River Godavari water to EL. 308 m & partly up to EL. 540 m to irrigate approximately 0.285 Lacks Acres (114 Hecatres) of Command area. Project Envisages Lifting of water from Godavari River at Gangaram village, Eturnagaram, Warangal District in Telangana state in 7 stages with water conductor system 200.340 Kms approximately, long steel pipelines connecting 8 Nos. of existing tanks (i) intake to Dharmasagar via, Bhimghanpur, Salivagu (ii) from R.S. Ghanpur to Chittakodur via, Aswaraopalli, (iii) from Dharmasagar to Tapashpally via, Gandiramaram, Bommakur. The longitudinal alignment of pipeline and steady state HGL for the lift project is shown in Figure1. A model was developed (Mowlali 2014) based on the input data used for the training of neural network model. In this model grid (80x 2030), based key parameters were used as input. It was normalized by using the following normalizing factor. The neural network toolbox in Matlab 7.0 is used for training. The Neural Network model is three layered network with eight inputs, one hidden layer, the hidden layer consist of ten neurons to that of one in the output layer as shown in Figure2. The training was done by feeding forward back propagation algorithm. Back propagation algorithm updated the network weights and biases in the direction in which the performance function decreased most rapidly. One iteration of this algorithm can be written as Eq.[7].

$$X_{k+1} = X_k - \alpha_k g_k \qquad [7]$$

Where X_K is a vector of current weights and biases, gk is the current gradient, and ais the learning rate. There are two different ways in which this gradient descent algorithm can be implemented incremental mode and batch mode. In the incremental mode, the gradient is computed and the weights are updated after each input is applied to the network. In the batch, mode all of the inputs are applied to the network before the eight are updated. TRAINLM was used as training function for the network; TRAINLM is a training function that updates weights and bias values according to back propagation. Trainlm can train any network as long as its weight, net input, and transfer functions have derivative functions. Back propagation is used to calculate derivatives of performance with respect to the weight and bias variables X. Each variable is adjusted according to Eq.[8].

$$dX = deltaX * sign(\mathrm{gX}) \qquad [8]$$

Where the elements of deltaX are, all initialized to delta0 and gX is the gradient. At each iteration, the elements of deltaX are modified. If an element of gX changes signs from one iteration to the next, then the corresponding element of deltaX is decreased by delta dec. If element of gX maintains the same sign frm one iteration to the next, then the corresponding element of deltaX is increased by delta Inc. Log-Sigmoid transfer is used by the neurons to generate the output. The function log sigmoid generates output between 0 and as the neuron net input goes from negative to positive infinity as shown in Figure2. The performance of training data was compared by using sum squared error. The targeted error was set to zero. The network was simulated by using testing data and the generated data were compared to observed data at each location by calculating Regression coefficient. Now the network is ready to be trained. The samples were automatically divided into training, validation and test sets. The training set was used to teach the network. Training continues as long as the network continues improving on the validation set. The test set provides a completely independent measure of network accuracy. The NN Training Tool shows the network being trained and the algorithms used to train it. It also displays the training state during training and the criteria which stopped training will be highlighted in green. The buttons at the bottom open useful plots which can be opened during and after training. Links next to the algorithm names and plot buttons open documentation on those subjects.

To see how the network's performance improved during training, either click the “Performance" button in the training tool, or call PLOT PERFORM. Performance is measured in terms of mean squared error, and shown in log scale Figure 3. It rapidly decreased as the network was trained. Performance was shown for each of the training, validation and test sets. The regression plot is shown in Figure 5. The version of the network that did best on the validation set was after training. Another measure of how well the neural network has fit the data is the regression plot. Here the regression was plotted across all samples. The regression plot shows the actual network outputs plotted in terms of the associated target values. If the network has learned to fit the data well, the linear fit to this output-target relationship should closely intersect the bottom left and top-right corners of the plot. If this is not the case then further training, or training a network with more hidden neurons, would be advisable (Mowlali, 2014).

Table 1. Data for Pumping Main

Design discharge	14 m^3/s
Pumping main length	38252m
Diameter and thickness of pumping main	Diameter=3m, Thickness=16mm
Pipe material	Steel
Internal lining material	Epoxy
External coating/guniting thickness	25mm
Low water level and minimum water level at intake reservoir	+71.0m and +93.5m
Discharge level at upper reservoir	+166.94m
Number of parallel pumps	2
Pump rated head and rated discharge	Head=131m, discharge=7m^3/s

Table 2. Data and results from ANN Model

Chain distance of pumping main (m)	**Input 1** **Elevation (m)**	**Input 2** **Transimission length (m)**	**Input 3** **Diameter (m)**	**Input 4** **friction factor (f)**	**Input 5** **Wave celerity, C, (m/s)**	**Input 6** **Velocity, V (m/s)**	**Input7** **H_{max} (m)**	**Input 8** **H_{min} (m)**	**Output** **Optimal airvessel volume (m^3)**
0	134.5	38252	3	0.01	837.64	1.98	210.06	97.33	377.9
0	132	38252	3	0.01	837.64	1.98	210.06	97.33	375.7
35.8	132	38252	3	0.01	837.64	1.98	210.02	94.89	375.7
4972.8	118.7	38252	3	0.01	837.64	1.98	204.45	136.36	371.9
9945.5	116.1	38252	3	0.01	837.64	1.98	198.53	139.87	359.4
15109.5	117.6	38252	3	0.01	837.64	1.98	191.99	140.82	341.9
20273.6	123.3	38252	3	0.01	837.64	1.98	184.24	137.25	323.0
25246.3	118.5	38252	3	0.01	837.64	1.98	178.18	159.09	307.9
30984.1	115.0	38252	3	0.01	837.64	1.98	173.22	168.91	294.0
35765.6	114.7	38252	3	0.01	837.64	1.98	169.09	165.01	281.6
38252	118.2	38252	3	0.01	837.64	1.98	166.94	166.94	270.7

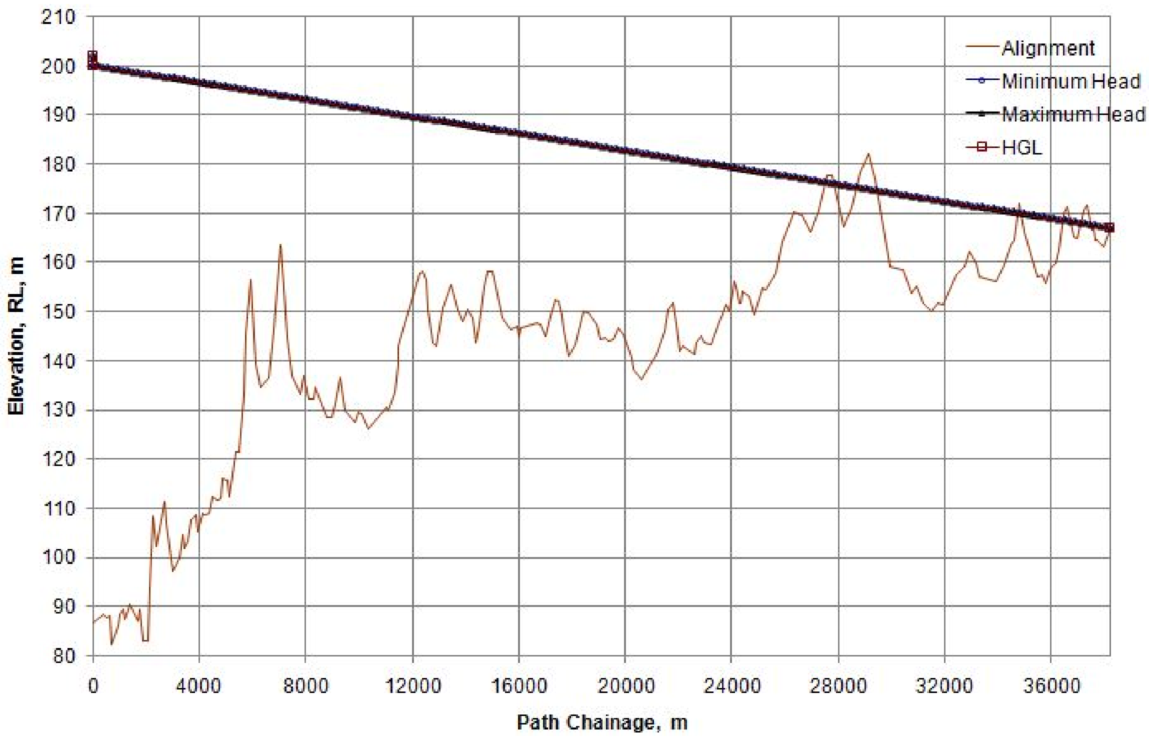

Figure 1. Longitudinal alignment of pipeline and HGL- Intake to Bhimganapuram.

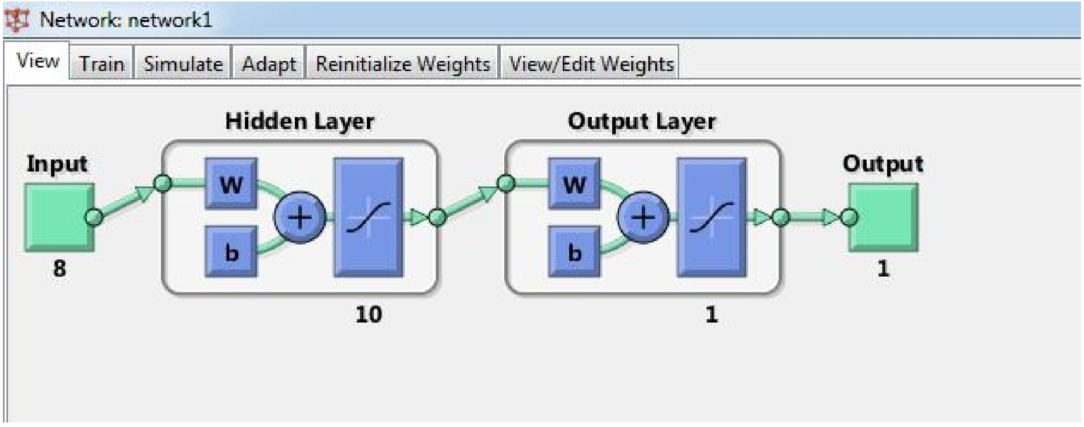

Figure 2. Three layered Neural Network model.

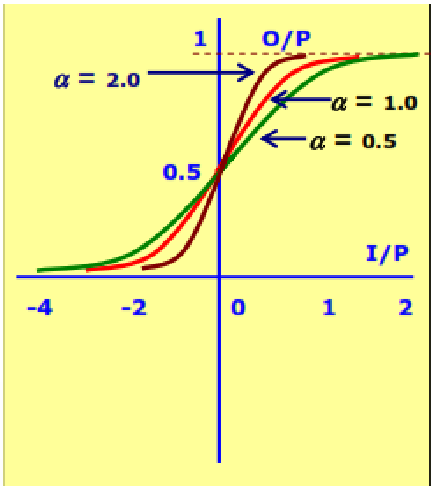

Figure 3. Log- Sigmoid transfer function.

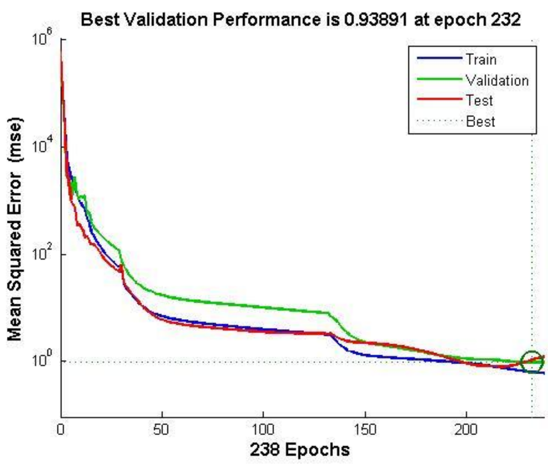

Figure 4. Performance plot.

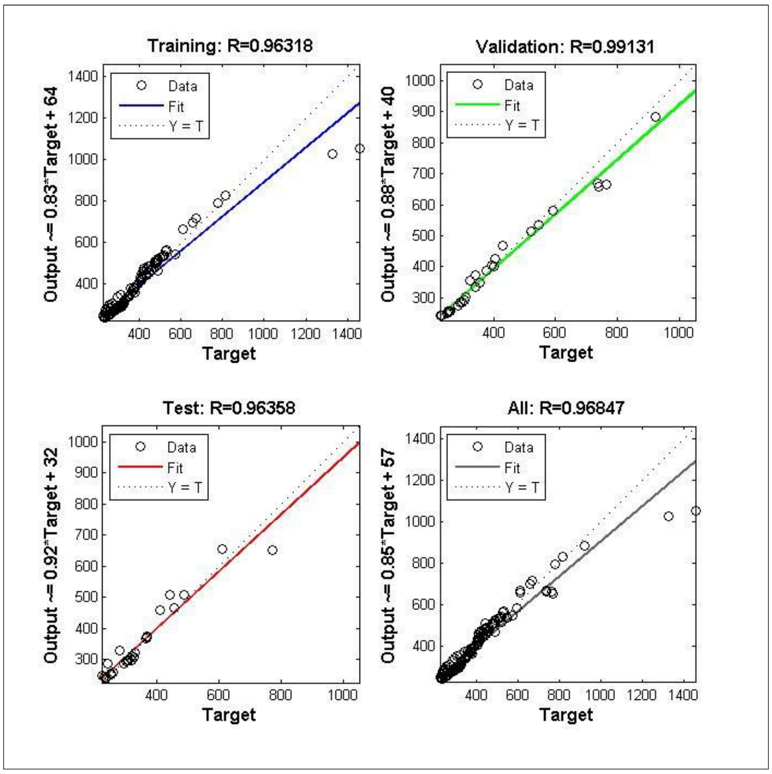

Figure 5. Regression plot.

5 CONCLUSIONS

A regression based ANN model was developed for sizing the air chamber for mitigating the transient pressures in a raising main of water pumping system. The ANN model investigated the optimized values of air volume and vessel volumes from the system parameters viz., pipe line length, pipe diameter, flow velocity, friction factor, wave celerity, maximum and minimum pressure heads. The system parameters were used as input variables and the corresponding air vessel parameters as output variables to train the neural network model. The trained neural network model was applied to large conveyance system in India (JCR Devadula Lift irrigation project). The neural network model predictions were compared with the sizes obtained from application of commercial software SAP2 (Surge Analysis Package version2.0) and observed that ANN models provide economical sizes.

REFERENCES

Afshar, M. H. & Rohani, M. (2008). Water Hammer Simulation by Implicit Method of Characteristic. *International Journal of Pressure Vessels and Piping*, 85(12), 851-859.

Chandramouli, V., Lingireddy, S. & Brion, G. M. (2007). A Robust Training Terminating Criterion for Neural Network Modeling of Small Datasets. *ASCE JI Computing Civil Engineering*, 21(1), 39.

Chang, J. S. (2005). Transients of Hydraulic Machine Installations, *Higher Education Press, Beijing, China.*

Combes, G. & Borot, B. (1952). New Graph for the Calculation of Air Reservoirs, Account Being Taken of the Losses of Head. *La Houille Blanche*, 5, 723-729.

De Martino, G. & Fontana, N. (2012). Simplified Approach for the Optimal Sizing of Throttled Air Chambers. *Journal of Hydraulic Engineering*, 138(12), 1101-1109.

Di Santo, A. R., Fratino, U., Iacobellis, V. & Piccinni, A. F. (2002). Effects of Free Outflow in Rising Mains with Air Chamber. *Journal of Hydraulic Engineering*, 128(11), 992-1001.

Graze, H. R. & Forrest, J. A. (1974). New Design Charts for Air Chambers. In *Fifth Australasian Conference on Hydraulics and Fluid Mechanics, Christ Church, New Zealand*, 34-41.

Izquierdo, J., Lopez, P. A., Lopez, G., Martinez, F. J. & Perez, R. (2006). Encapsulation of Air Vessel Design in a Neural Network. *Applied mathematical modelling*, 30(5), 395-405.

Jung, B. S. & Karney, B. W. (2006). Hydraulic Optimization of Transient Protection Devices Using GA and PSO Approaches. *Journal of water resources planning and management*, 132(1), 44-52.

Kim, C. Y., Bae, G. J., Hong, S. W., Park, C. H., Moon, H. K. & Shin, H. S. (2001). Neural Network Based Prediction of Ground Surface Settlements Due to Tunnelling. *Computers and Geotechnics*, 28(6), 517-547.

Kim, S. H. (2008). Impulse Response Method for Pipeline Systems Equipped with Water Hammer Protection Devices. *Journal of Hydraulic Engineering*, 134(7), 961-969.

Kwon, H. J. & Lee, J. J. (2008). Computer and Experimental Models of Transient Flow in a Pipe Involving Backflow Preventers. *Journal of Hydraulic Engineering*, 134(4), 426-434.

Lee, T. S. (1998). A Numerical Method for The Computation of The Effects of an Air Vessel on The Pressure Surges in Pumping Systems with Air Entrainment. *International journal for numerical methods in fluids*, 28(4), 703-718.

Mowlali. N. (2014). Artificial Neural Network Model for Optimization of Air Vessel to Control Hydraulic Transients, *MSc Thesis*, National Institute of Technology Warangal, India.

Nerella Ruben. (2017) Analysis of Hydraulic Transients in Water Conveyance Pumping Systems Using Discrete Vapour Cavitation Model, *PhD Thesis*, National Institute of Technology Warangal, India.

Yu, X., Zhang, J. & Hazrati, A. (2011). Critical Superposition Instant of Surge Waves in Surge Tank with Long Headrace Tunnel. *Canadian Journal of Civil Engineering*, 38(3), 331-337.

Di Santo, A. R., Fratino, U., Iacobellis, V. & Piccinni, A. F. (2002). Effects of Free Outflow in Rising Mains with Air Chamber. *Journal of Hydraulic Engineering*, 128(11), 992-1001.

Ramalingam, D. & Lingireddy, S. (2013). Neural Network–Derived Heuristic Framework for Sizing Surge Vessels. *Journal of Water Resources Planning and Management*, 140(5), 678-692.

Ramos, H., Covas, D., Borga, A. & Loureiro, D. (2004). Surge Damping Analysis in Pipe Systems: Modelling and Experiments. *Journal of Hydraulic Research*, 42(4), 413-425.

Stephenson, D (2002). Simple Guide for Design of Air Vessels for Water Hammer Protection on Pumping Lines. *Journal of Hydraulic Engineering*, 128(8), 792–797.

Wylie, E. B., Streeter, V. L. & Suo, L. (1993). *Fluid Transients in Systems*. Englewood Cliffs, NJ: Prentice Hall, Volume 1, 464.

Zaki, K. O. & Elansary, A. S. (2011), Optimal Design of Air Vessel for Water Hammer Protection in Water Distribution Network. Journal Engineering Applied. Science, 58(3), 219–236.

Ze-xuan, Z. H. O. U. & Keat, T. S. (2003). Theoretical, Numerical and Experimental Study of Water Hammer in Pipe System with Column Surge Chamber. *Journal of Hydrodynamics Series B-English Edition*, 15(5), 20-28.

Proceedings of the 37th IAHR World Congress
August 13 – 18, 2017, Kuala Lumpur, Malaysia

CFD ANALYSIS OF MULTI-SCALE TRANSIENT FLOWS ON THE FRANCIS TURBINE UNDER THE LOAD REDUCTION CONDITION

DAQING ZHOU[1] & JIE ZHANG[2]

[1,2] College of Energy and Electrical Engineering, Hohai University, Nanjing, P.R. China,
zhoudaqing@hhu.edu.cn; hhurdzj@163.com

ABSTRACT

For the sake of simplified geometric model and reducing the amount of calculation, labyrinth seals are usually not included in the numerical model of a hydraulic machinery, which consequently affects the results due to the regardless of disc friction losses and volume losses, as well as the pressure fluctuation in the labyrinth clearances. In this paper, we took all the geometrical details of labyrinth seals into consideration and performed multi-flow simulation under the load reduction condition upon a kind of high head Francis turbine using commercial software Ansys Fluent 17.0. Dynamic mesh and UDF programs were used to realize the motion of guide-vane from 9.84° to 0.8°. Firstly, main parameters of the turbine at reduction-load condition were investigated. By comparing numerical results and testing data, we found that calculation values of both torque and discharge were slightly less than the model test with the average value 20 N.m and 10 kg/s, so gap flow through the labyrinth seals needed to be conducted. Secondly, by comparing consequences of Francis turbine with and without labyrinth, the consideration of gap flows in labyrinth seals was proven to have great significance. The prediction of pressure fluctuation of Francis turbine with labyrinth in the vane-less zone and draft tube appears more close to the test data. Moreover, the research found that the maximum force on the top cap and sudden change of pressure in the gap may increase the risk of turbine-lifting and vibration accidents in a hydro plant.

Keywords: Francis turbine; labyrinth seals; multi-scale; leakage flow; transition process.

1 INTRODUCTION

With the development of hydro power station and the maturity of design technology, the research on physical fluctuations in the labyrinth seals of Francis turbine have become another hot spot (Schiffer et al., 2017). The current research mostly focus on the calculation of steady-state conditions aimed to get more accurate parameters (Thapa et al., 2017; Čelič et al., 2015) or detailed parameters (Jakobsen et al., 2017) and research the inner flow characteristics (Wang et al., 2014). In fact, leakage flow has been taken into consideration since early 20th century (Casartelli et al., 2005; Xiao et al., 2005). In the engineering projects, plant-vibration and turbine-lift accidents often prove to be caused by parameter variety in the clearance. For example: dangerous vibration accident took place in Tianhuangping Pumped Storage Power Station in China in 2003 which was caused by the pressure pulsation in the top cap clearance and was proven that upper labyrinth rings was clogged with calcium and the amplitude of pressure pulsation in the top cap clearance even reached 1.5Mpa (You et al., 2015). Transition process such as unit-start process and load-reduction process is another important factor to be considered in the hydraulic design and optimization of the turbine. The numerical study on the transition process of the Francis turbine is effective to monitor the flow characteristics inside the multi-scale passages of hydraulic turbine (Zhou et al., 2015; Zhang et al., 2014), which is just the main research content of the paper with the purpose to take advantages of multi-scale flow research method to find the changes of flow quantities during the transition process, and at the same time benefit the accident diagnosis.

2 NUMERICAL SIMULATION METHODS

2.1 Computation domain and meshing schemes

The numerical calculation domain consists of three parts: the large-scale main passage, the micro-scale gap region, and the transition region which connects them smoothly (Figure 1). The main flow passage includes a volute region with 14 stay vanes, a guide vane region with 28 guide vanes, a runner region with 15 long blades and 15 short blades, and a draft tube region. The micro-scale gap region combines of two parts (Figure 2(a)): one is the upper clearance (UC) between the upper surface of the crown and the lower surface of the top cap, and the other is the lower clearance (LC) between the lower surface of the band and the upper surface of the bottom ring. The transition zone refers to a cylindrical flow passage located between the guide vane outlet and the runner inlet with a wall thickness of 0.5 mm, which connects the upper and lower clearance with the main passage effectively. In addition, the exact locations of the measurement points VL02, DT05 and P1-P12 are shown in Figure 2.

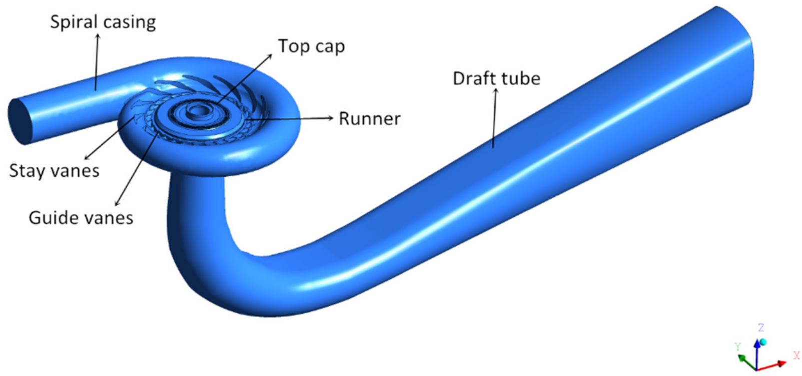

Figure 1. Numerical calculation zone.

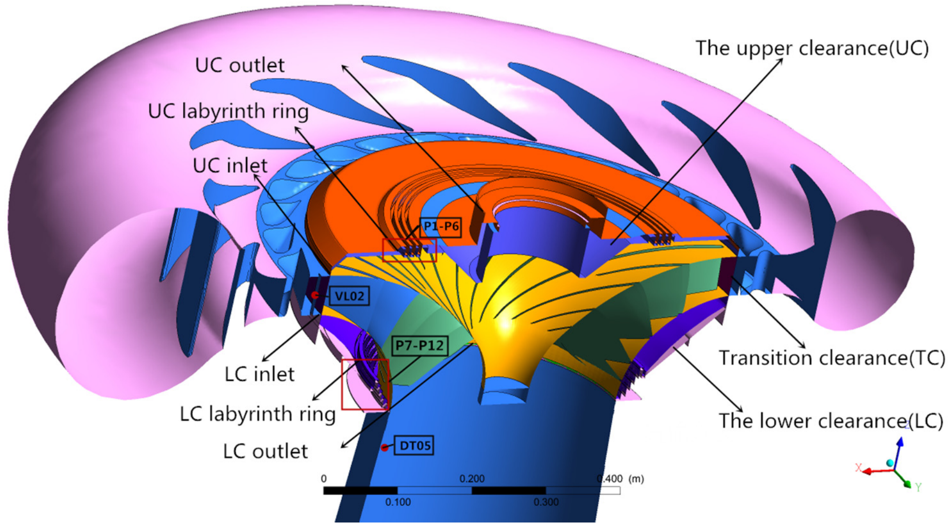

(a) A partial enlarged longitudinal sectional view of computational domain

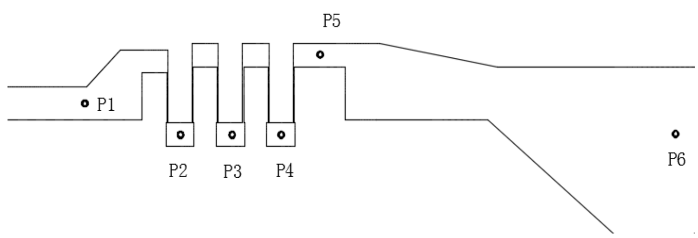

(b) P1-P6 in the upper clearance

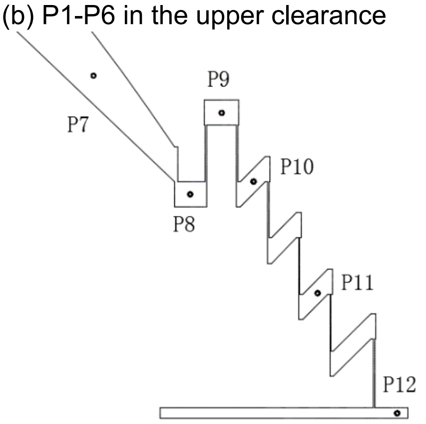

(c) P7-P12 in the lower clearance

Figure 2. Enlarged clearances and locations of pressure measuring points.

Test data is available at http://www.ltu.se/research/subjects/Stromningslara/Konferenser/Francis-99. The model (the diameter of the water inlet of model runner: $D_1 = 0.349m$, designed net head of model turbine: $H_r = 12m$, designed volume flow rate of model turbine: $Q_r = 0.2m^3/s$) was obtained by scaling the prototype turbine ($D_{P1} = 1.78m$, $H_{pr} = 377m$, $Q_{pr} = 31m^3/s$) at a ratio of 1: 5.1. The total sampling time of the model test is 10s, the sampling frequency is 5000Hz, and the guide vane is closed linearly from 9.84 ° to 0.8 ° in 8 seconds. The change of mass flow rate, net head, torque and rotation speed of the runner, the pressure pulsation of the measuring point VL02 in vane-less zone and DT05 in the draft tube were monitored. Table 1 shows the parameters of model test under the designed load (DL) condition and minimal load (ML) condition.

Table.1. Model test parameters during steady state measurements.

Parameter	DL	ML
Guide vane angle (°)	9.84	0.8
Net head (m)	11.94	12.14
Discharge (kg/s)	200	22
Torque to the generator (N.m)	616.13	11.16
Runner angular speed (rpm)	332.59	332.8
Hydraulic efficiency (%)	92.39	20.94

The computation domain was divided into grids by ANSYS ICEM 17.0 and Figure 3(a) shows the schematic diagram of grids at the designed point. The structural grid division technique was used in the runner, draft tube, transition zone, upper and lower clearance area in order to improve the accuracy and efficiency of the calculation. The tetrahedron unstructured grid division technique was used in the spiral casing. The dynamic grid technique based on the unstructured grid division can help the guide vane to successfully close from 9.84° to 0.8° under the load-reduction condition (Figure 3(b)).

Independence verification of grid quantity shown in Table 2(a) was based on the evaluation criteria of efficiency, and scheme 3 was chosen as the final computational grid. In this scheme, the value of dimensionless parameter y+ in the boundary layers of each component was determined: the spiral casing and guide vanes with the value of 6.5~89, the runner with the value of 7.5~48, the draft tube with the value of 6~77 and the clearance with the value of y+≈1, which satisfied the requirements of wall functions used in the turbulence model. Independence analysis of time steps shown in Table 2(b) was based on pressure and torque under the design load condition and the Δt=0.002s was applied as the final time step from the trade-off between the calculation time and accuracy.

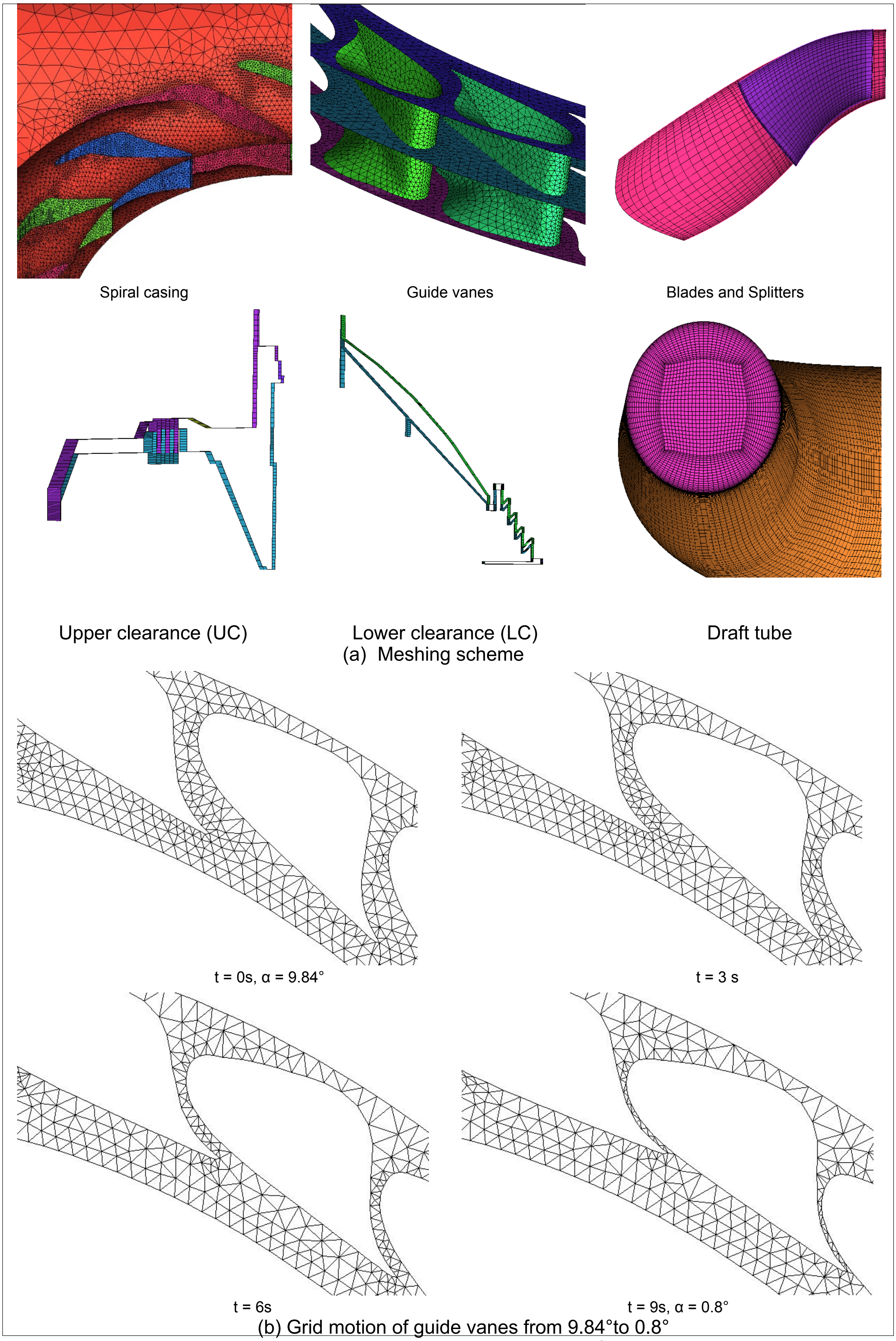

Figure 3. Meshing scheme and grid motion of guide vanes.

Table 2. Independence analysis.

(a) Independence analysis of grid number

Scheme number	1	2	3	4	Test*
Number of grid cells / $N(10^4)$	353	487	660	887	-
Hydraulic efficiency / η_M (%)	94.3	92.6	91.8	91.9	92.39

(b) Independence analysis of time step

Time steps / Δt (s)	0.01	0.005	0.002	0.001	Test*
Mass flow rate / Q(kg/s)	188.3	190.1	192.7	193.2	200
Torque of runner / T(N.m)	488.1	523.2	585.8	590.1	616.1

2.2 Turbulence model

In this article, transient calculation is the main study method, so the N-S equations based on ALE (Arbitrary Lagrange-Euler) method was used as the governing equations for dynamic mesh:

Continuous equation:
$$\frac{\partial \rho}{\partial t} + \nabla \cdot \rho\left(\boldsymbol{v} - \boldsymbol{u}\right) = 0 \quad [1]$$

Momentum equation:
$$\frac{\partial \rho \boldsymbol{v}}{\partial t} + \left(\rho \boldsymbol{v} \cdot \nabla\right)\left(\boldsymbol{v} - \boldsymbol{u}\right) = -\nabla p + \mu \nabla^2 \boldsymbol{v} + \rho \boldsymbol{g} \quad [2]$$

where, $\boldsymbol{v}$ refers to the fluid velocity vector, $\boldsymbol{u}$ is the grid movement velocity vector, p is static pressure, μ is viscosity, ∇ is Hamiltonian operator.

The SST *k-ω* turbulence model (Menter, 1994) was used to enclose the governing equations:

$$\frac{\partial(\rho_m k)}{\partial t} + \frac{\partial(\rho_m k u_i)}{\partial t} = P_k - \frac{\rho_m k^{3/2}}{l_{k-\omega}} \frac{\partial p}{\partial x_i}\left[\left(\mu + \frac{\mu_t}{\sigma_t}\right)\frac{\partial k}{\partial x_i}\right] \quad [3]$$

$$\frac{\partial(\rho_m \varepsilon)}{\partial t} + \frac{\partial(\rho_m \varepsilon u_i)}{\partial t} = \alpha_2 \frac{\omega}{k} P_\omega - \beta_2 \rho_m \omega^2 + \frac{\partial p}{\partial x_i}\left(\mu + \frac{\mu_t}{\sigma_{\omega 2}}\right)\frac{\partial k}{\partial x_i} + 2\rho_m\left(1 - F_1\right)\sigma_{\omega 2} \frac{1}{\omega} \frac{\partial k}{\partial x_i} \frac{\partial \omega}{\partial x_i} \quad [4]$$

where, k is turbulent kinetic energy, ε is the rate of dissipation of turbulent kinetic energy, ω is turbulence frequency, P_k、P_ω are generated terms for turbulence, F_1 is mixed function, σ_k、α_2、β_2、$\sigma_{\omega 2}$ are the empirical coefficients.

2.3 Boundary conditions and solution method

Ansys Fluent 17.0 was used as the solver. The finite volume method was used for the discretization of governing equations. The second-order central difference scheme was adopted for the diffusion term and the second order upwind scheme for the convection term. The SIMPLEC pressure-velocity coupling algorithm was used for iteration. The boundary conditions were set as: (1) in the steady calculation, the runner was defined in the reference rotating frame. In the transient calculation, the rotor part was defined as the rotation mesh. The other flow parts were defined in the stationary coordinate; (2) the spiral casing inlet was defined as the pressure inlet; the draft tube outlet and the upper clearance outlet were defined as the pressure outlet; (3) the upper surface of the crown and the lower surface of the band were defined as the rotation surfaces, and the rotation direction and rotation speed were consistent with the rotating wheel; and (4) the guide vanes closed according to the defined linear closure law. Surfaces of the guide vanes were defined as the rigid body motion areas, and the upper and lower surfaces of the guide vane area were defined as deforming surfaces.

3 NUMERICAL RESULTS OF LOAD-REDUCTION TRANSIENT PROCESS AT SYNCHRONOUS SPEED

Numerical simulation of the only main passage and the multi-scale passage with seal gaps were both conducted at the synchronous speed of 34.85 rad/s. During 0~1s and 8~10s, the guide vanes remained stationary; During 1s~ 8s, the guide vanes closed from 9.84 ° to 0.8 ° linearly.

The calculation time of the main passage was about 500 hours, we monitored the following parameters: the mass flow rate of inlet and outlet Q, the torque of runner T, radial force of blades F_r, axial force of blades F_z, the pressure of point VL02, and point DT05. The calculation of multi-scale passage cost about 650 hours. More parameters were monitored, which incude the axial forces, of upper and lower surfaces of crown and band $F_1/F_2/F_3/F_4$,the axial forces of top cap and bottom ring F_{tc}/F_{br}, mass flow rate of upper and lower clearances, pressure of points P1~P6 in upper clearance, and pressure of points P7-P12 in lower clearance.

3.1 Analysis of flow characteristics and forces in the main passage

From Figure 4, we can obtain the following information: (1) the initial value (0-1s, 190kg/s) and the termination value (t＞8s, 20kg/s) of flow calculation are consistent with the initial value (0-1s, 200kg/s) and the termination value (t＞8s, 22kg/s) of the model test; (2) the initial value of torque (0-1s, 585Nm) calculation agrees well with the initial value of the model test (0-1s, 616Nm). However, the termination value of torque calculation (t＞8s, -20Nm) has obvious difference with the test result (t＞8s,11.16Nm). The results of different time steps (Table 2) show that the time step has less influence on the prediction accuracy of the flow rate, but the sensitivity of the torque to the time step is higher, and we can shorten the time step to improve the torque prediction accuracy; and (3) the calculated values of flow and torque are slightly lower than the model test values during the whole load-reduction transition process, but the trends of numerical results are consistent with the model tests, indicating that the numerical simulation of the multi-scale passage is feasible for predicting the variation law of the flow and torque under the load-reduction condition.

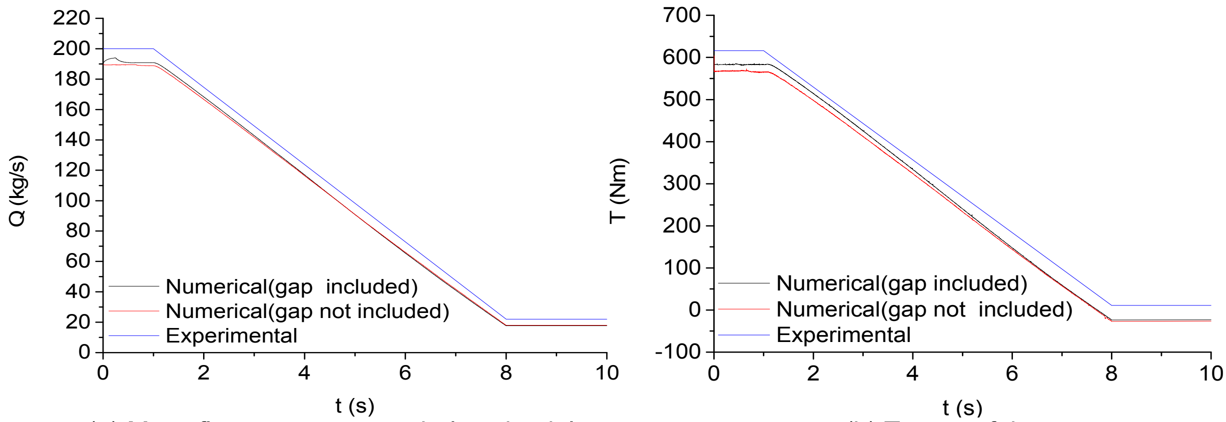

(a) Mass flow rate across spiral casing inlet. (b) Torque of the runner.

Figure 4. Numerical simulation and model test results of mass flow rate and torque.

In the Figure 5, the pressure pulsation curves of the two points (VL02 and DT05) may prove the consequences below: (1) the calculated static pressure of VL02 is slightly lower than the experimental value, and the trend is basically the same. Absolute error between the calculated value and the experimental value is about 20kPa and the relative error is about 10%. In addition, the numerical simulation precision of the multi-scale passage is better than that of only the main passage; and (2) during 0-4 s, the calculated static pressure of DT05 is less than the experimental value but there also are some similarities, for example: when t=1s, the pressure drop phenomenon is reflected in both of the simulation and test due to the water hammer when the guide vanes began to close; During 4-8s, the calculated static pressure of DT05 continues to increase while the static pressure in the test shows a trend of decline after 7s.

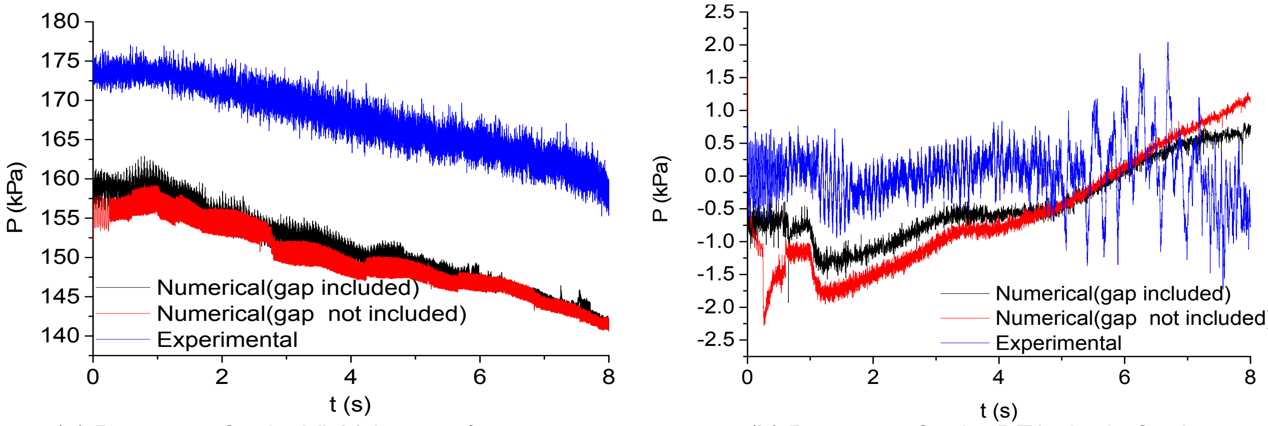

(a) Pressure of point VL02 in vane-less zone. (b) Pressure of point DT05 in draft tube.

Figure 5. Numerical simulation and model test results of pressure pulsation.

3.2 Analysis of flow characteristics and forces in the clearances

The analysis of gap flow curve shows: (1) when the size of both upper and lower clearance inlet is as long as 0.05mm, the mass flow rate of upper clearance is slightly larger than that of lower clearance; and (2) the fluctuation of discharge across the upper clearance is relatively larger during the load-reduction transition, which is due to the larger pressure pulsation in the front of the upper labyrinth ring than that of the lower labyrinth ring.

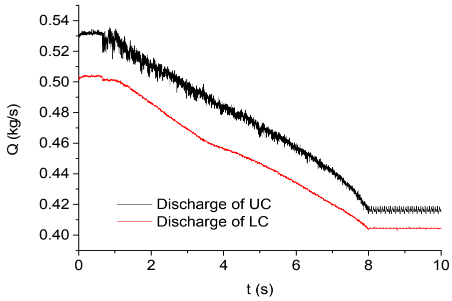

Figure 6. Mass flow rate across upper and lower clearance.

The pressure pulsation characteristics of the measuring points in the clearance passage are presented in Figure.7 as follows: (1) during t=0~1s in the steady-state of design conditions, and the pressure before the labyrinth ring (150kPa) is 50% more than pressure at the beginning of the labyrinth ring (100kPa). The points P_1 and P_2 are neighboring and the pressure difference is about 8kPa. The points P_2 and P_3 are separated by a piece of labyrinth ring cavity and the pressure difference is about 16kpa, indicating that the value of the pressure drop linearly with the number of labyrinth ring cavity N. The amplitude of pressure fluctuation before the labyrinth rings is greatly more than the amplitude of pressure fluctuation after the labyrinth rings, the amplitude of the pressure pulsation decreases gradually after the decompression of each cavity in the labyrinth rings, which is due to the consumption of mechanical energy in the form of vortex produced by the gap cavities; (2) at the time t=1s, the guide vanes begin to close, pressure in the front chamber of upper clearance and in the upper the labyrinth rings suddenly drops down and pressure in the front chamber of lower clearance and in the lower labyrinth rings suddenly rises up, which is due to the influence of water hammer. At the same time, this is one of the possible factors that lead to the runner-lifting phenomenon; (3) during t=1~8s, the guide vanes are closed and the load is reduced during the load-reduction process. The whole load-reduction process can be divided into two parts according to the value of pressure: firstly, when t=1~5.5s, the pressure in the upper clearance is stable and the pressure in the lower clearance decreases only slightly, and secondly, when t=5.5~8s, the pressure both in the upper and lower clearances decreases significantly. The phenomenon is so interesting because the decreasing percentage per unit time of guide vane opening has increased; and (4) during t=8~10s, the opening angle of the guide vanes is 0.8° and the turbine runs at the minimum load point. The pressure pulsation amplitude in the upper and lower clearance is greater than the amplitude during 0-8s, which may be due to the flow uncertainty caused by the poor flow regime of the small flow conditions.

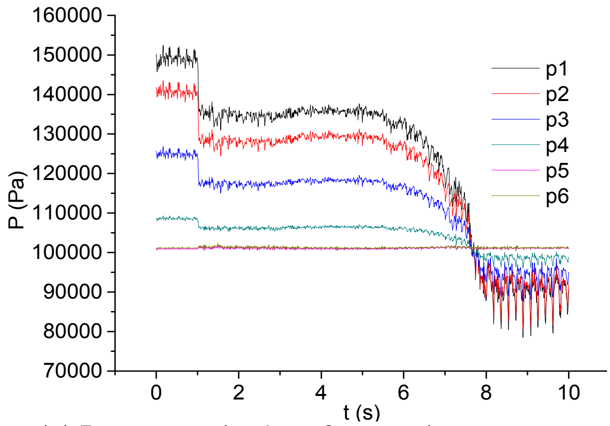

(a) Pressure pulsation of upper clearance.

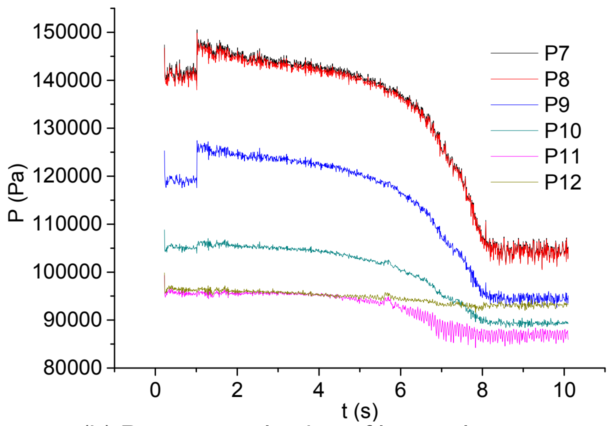

(b) Pressure pulsation of lower clearance.

Figure 7. Pressure pulsation of the pressure measuring point before and after labyrinth rings.

In Figure 8, we conclude the following variation laws of the radial force: (1) the total radial force of the blades is less than 20N, and the radial force decreases with the closing of guide vane. From the component stability to t = 6s, the force in X direction is greater than 0 and the force in Y direction is less than 0, so it can be inferred that the direction force of the radial force of the runner is directed to the second quadrant, which may be caused by the uneven distribution of flow when water flows through the guide mechanism of the turbine; and (2) the maximum amplitude (40N) of the radial force fluctuation of multi-scale passage is larger than that of the numerical simulation of the main passage (20N). So, if the radial force of the blades is too large, it will cause the eccentric movement of the runner or the bending of the main spindle.

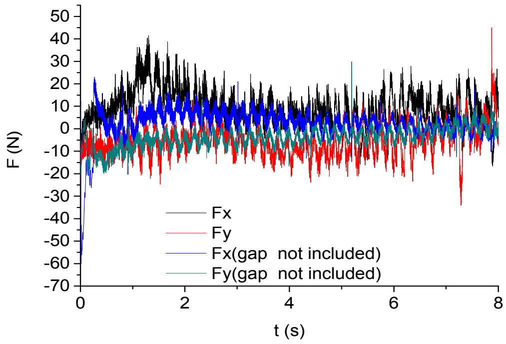

Figure 8. Numerical simulation of the radial force change of blade surfaces.

From Figure 9, it can be found that the total axial force, except the gravity of the runner, as follows: 750±50N in the design condition and 575±75N in the minimal load condition. The total axial force of runner remains relatively steady, which is cause by the change law that the axial force on the crown and band is linearly decreasing, while axial force the blades is linearly increasing, offsetting with each other. On one hand, the force of the blades appears to be a linear-growth trend and there are no obvious differences, whether the clearances are included or not. When t < 2.3s, the direction of axial force on the blade surface is vertical downward; when t > 2.3s, the direction of the axial force of the blade is vertical upward, which is caused by the different directions of torque. The axial force of the blades is more than 1200N, when t = 8s. On the other hand, the surfaces and the axial forces of the runner are as follows: the upper surface of crown (-40.4kN), the lower surface of crown (35kN), the upper surface of band (-25.6kN), the lower surface of band (32kN), and surfaces of blades (-0.22 kN). The total axial force of crown and band are 800N/upright in the design condition and 800N/vertical down in the minimal load condition. In addition, the axial force of lower surface of top cap is 38.4kN at the design conditions, and at the minimum opening conditions, the axial force of lower surface of top cap is 35.4kN/upright. During the whole process of load reduction, the axial forces of the top cap are linearly reduced.

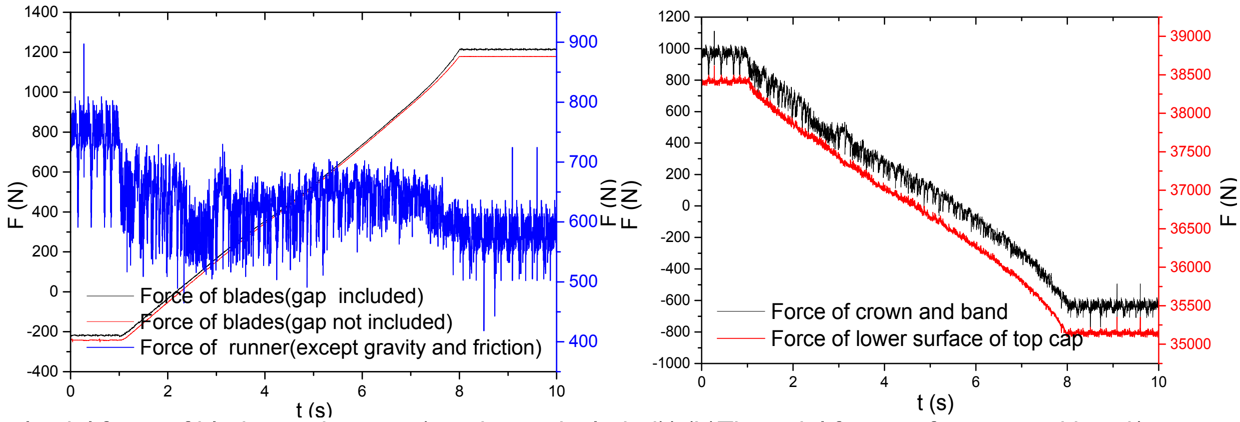

(a)Total axial force of blades and runner (gravity not included)* (b)The axial forces of crown and band/top cap.

Figure 9. Axial forces of runner and top cap.

*In the figure 9(a), Coordinate ruler for the total axial force of blades on the left while the runner on the right.

4 CONCLUSIONS

The numerical results of the multi-scale flow of the Francis turbine under the load-reduction condition were compared and verified with the test results, and some conclusions can be drawn as follows:

1. The gap flow rate in both the upper and lower clearance is very small, but the pressure fluctuation in the upper clearance is very strong;
2. When the guide vanes suddenly closed, the pressure in the crown gap suddenly dropped, while the pressure in the lower ring gap increased. In addition, when the guide vanes closed to a tiny opening, the internal pressure in both clearances sharply decreased;
3. During the load-reduction process, the axial force of the runner is relatively stable because the axial force of the blades increases while the sum of the axial force of the crown and band decreases, and the varying trend is the same as the lower surface of top cap.

ACKNOWLEDGEMENTS

The author(s) disclosed receipt of the following financial support for the research, authorship, and/or publication of this article: The study was supported by Open Research Fund Program of State Key Laboratory of Water Resource and Hydropower Engineering Science (2015SDG04). The support of Hohai University and Wuhan University, China is also gratefully acknowledged. We also appreciate Norwegian University of Science and Technology for providing the geometric model and test data.

REFRENCES

Casartelli, E., Cimmino, D., Staubli, T. & Gentner, C. (2005). Interaction of Leakage Flow with The Main Runner-Outflow in a Francis Turbine. *Proceedings of the HYDRO.*

Čelič, D. & Ondráčka, H. (2015). The Influence of Disc Friction Losses and Labyrinth Losses on Efficiency of High Head Francis Turbine. *Journal of Physics: Conference Series*. 579(1), 012007.

Jakobsen, K.R.G. & Holst, M.A. (2017). CFD Simulations of Transient Load Change on a High Head Francis Turbine. *Journal of Physics: Conference Series*. 782(1), 012002.

Menter, F.R. (1994). Two-Equation Eddy-Viscosity Turbulence Models for Engineering Applications. *AIAA journal*, 32(8), 1598-1605.

Schiffer, J., Benigni, H. & Jaberg, H. (2017). Analysis of the Leakage Behavior of Francis Turbines and Its Impact on the Hydraulic Efficiency—A Validation of an Analytical Model Based on Computational Fluid Dynamics Results. *Journal of Fluids Engineering*, 139(2), 021106.

Thapa, B.S., Dahlhaug, O.G. & Thapa, B. (2017). Sediment Erosion Induced Leakage Flow from Guide Vane Clearance Gap in a Low Specific Speed Francis Turbine. *Renewable Energy*, 107, 253-261.

Wang, W.Q., Yin, R. & Yan, Y. (2014). Analysis of Flow in Side Chamber and Path of Comb-Labyrinth Seal in Francis Turbine at Different Reynolds Numbers. *Journal of Drainage and Irrigation Machinery Engineering*, 32 (7), 611-616.

Xiao, R., Wei, C., Han, F. & Kubota, T. (2005). Numerical Analysis of Combined Leakage-Main Flows in Francis Turbine (Part 1: Leakage through Clearance around Runner-Band). *Turbomachinery*, 33 (4), 214-222.

You, G.H. (2015). Characteristics of Pump Turbine in Tianhuangping Pumped Storage Power Station. *Proceedings of Technology Construction and Management in Zhejiang Tianhuangping Pumped Storage Power Station*.

Zhou, D.Q. & Chen, Y. (2015). Numerical Simulation of Clearance Flow in Francis Turbine with Weep Holes. *Transactions of the Chinese Society for Agricultural Machinery*, 46(04), 53-58.

Zhang X.X., Cheng Y.G., Yang J.D., Xia L.S. & Xu L.A.I. (2014). Simulation of the Load Rejection Transient Process of a Francis Turbine by Using A 1-D-3-D Coupling Approach. *Journal of Hydrodynamics*, Ser. B, 26(5), 715-724.

SCATTERING BEHAVIOR OF HIGH FREQUENCY ACOUSTIC WAVES DUE TO BLOCKAGE IN PRESSURIZED WATER-FILLED PIPE

MOEZ LOUATI[(1)] & MOHAMED S. GHIDAOUI[(2)]

[(1,2)] Civil and Environmental Engineering, School of Engineering, Hong Kong University of Science and Technology, Hong Kong,
mzlouati@gmail.com; ghidaoui@ust.hk

ABSTRACT

Recently, high frequency acoustic waves (HFW) became of interest to increase the resolution for transient-based defect detection methods. For this purpose, one has to know how these HFW, which are dispersive waves, interact with defects. This paper considers the case of a blockage and studies numerically the scattering behaviour of HFW due to a single blockage in pipe system with non-reflective boundaries. For simplicity, axisymmetry is assumed and only signals that excite up to two radial modes are considred. Although the paper is mainly describing what was obtained from the numerical simulation, it is important to note that the objective is to understand the features of the scattering behaviour of HFW from a blockage that could be used for blockage detection. The results show that wave scattering increases the dispersion and distortion of HFW. This is because the energy of the incoming waves is distributed into multiple transmitted and reflected modes. Moreover, it is shown that the plane wave mode is highly affected by the severity of area reduction. The more severe the reduction is, the more the energy of a plane wave is reflected. However, radial modes have little interaction with the blockage and transmit most of their energy through both severe and shallow blockage cases.

Keywords: Transient waves; pipe system; wave-blockage interaction; wave dispersion; wave scattering.

1. INTRODUCTION

Although not well analyzed, there is an implicit recognition in the literature (Lee et al., 2014; Duan et al., 2011; Louati and Ghidaoui, 2015) that signals with wide frequency bandwidth (FBW) are most suitable for defect detection. Lee et al. (2014) recently demonstrated the importance of input signal FBW on pipe condition assessment through analytical, numerical and experimental means. The majority of transient wave generator technologies used in TBDDM are based on rapid valve closures (Meniconi et al., 2013; Lee et al., 2008; Stephens, 2008) or pump operation (Meniconi et al., 2015). The signals induced by valve-type generators induce significant loss of water, their signals are too crude, the reflections cannot be distinguished from normal system noise and their resolution is too low for localized defects. For example, the so-called rapid valve closure often takes about 0.05s to complete. As a result, the wave front is spread over a physical length of about 20 m along the pipe and cannot emphasize the effects of leaks and discrete blockages since their length scale is generally smaller than this wave front (Zhao et al., 2016).

Wave theory is widely used to probe and characterize various media and to convey information in various applications (e.g., non-destructive material testing, medical diagnostics, and underwater communications), where it is well known that the higher frequency of the waves the better is the resolution. Unsurprisingly, similar conclusions are found for TBDDM (Lee et al., 2014; Louati and Ghidaoui, 2015). In fact, transient waves used for TBDDM cannot resolve scales that are smaller than a/f, where a is the wave speed and f is the frequency. For example, Allen et al. (2011) simulated a sudden burst and reported that it could only be located to within ± 45m (*i.e.* 90m range) even though the sensor was only 20 m away from the fault. The wave resolution in this case was $a/f \sim 900/10 \sim 90$ m. Similarly, a simulated burst in Hong Kong could only be located to within ± 42 m (Hong Kong Water Supplies Department (WSD), private communication), and the wave resolution in this case was $a/f \sim 1200/10 \sim 90$m. In addition, Meniconi et al. (2015) conducted field investigation in the city of Milan (Italy) and reported that leaks could only be located to within 800m (Meniconi et al., 2015). Their wave resolution in this case was $a/f \sim 900/1 \sim 900$m.

Moreover, Duan et al. (2011) reported that the more measured eigenfrequencies included into the objective function the better is the accuracy given by the inverse optimization technique. This is natural given that higher frequencies (*i.e.*, shorter wavelengths) provide higher resolution in defect detection and are better at localizing multi-defects with multi-scales.

However, the use of high frequency waves (HFW) excites radial and azimuthal waves (dispersive waves) and they are highly affected by the multipath effect (Rienstra and Hirschberg, 2003). This work studies numerically the scattering behaviour of high frequency wave due to the presence of a blockage in an unbounded pipe, where the blockage is modeled as a pipe segment with smaller diameter. This work considers only axi-symetric pipe system, and therefore, blockages are assumed axi-symmetric. Although the paper is mainly describing what was obtained from the numerical simulation, it is important to note that the objective is to understand the features of the scattering behaviour of HFW from a blockage that could be used for blockage detection.

2. HIGH FREQUENCY WAVES IN BLOCKED PIPE SYSTEM

At a junction of two pipe segments (see Figure 1), an incident wave is scattered into reflected and transmitted modes such that the continuity of pressure and velocity is satisfied, and by consequences, the energy is conserved (Rienstra and Hirschberg, 2003). This section studies numerically the scattering behaviour of high frequency wave due to blockage in an unbounded pipe, where the blockage is modeled as a pipe segment (Figure 2).

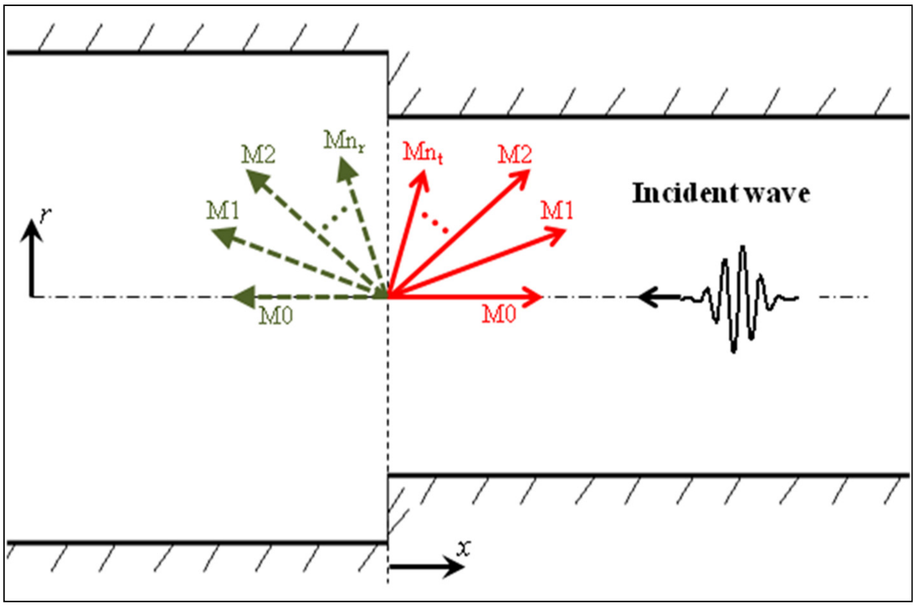

Figure 1. Mode matching at discontinuity.

The three pipe segments in Figure 2 are defined as pipe 1 with length extending from negative infinity to junction 2 and diameter $D_1 = D$; pipe 2 with length l_2 and diameter $D_2 < D$; and pipe 3 with length extending from junction 1 to positive infinity and diameter $D_3 = D$ where D is the intact pipe diameter. It was assumed that the wave speed (a) was not affected by the change in diameter. Two D_2 cases were considered in this section. The first case was D_2 / D=0.8 and it was referred to as shallow blockage case. The second case was D_2 / D=0.4 and was referred to as severe blockage case. The incident wave generated at a source located at x=L had a waveform as shown in Figure 3 with central frequency, f_c = 4000Hz and a narrow FBW [0.9f_c to 1.1f_c] ≡ [3600Hz to 4400Hz].

A long blockage length l_2=100m was considered so that the interaction of the incident wave with the blockage could be clearly analysed in two parts. The first part considered the wave scattering at junction 1. The second part considered the wave scattering at junction 2.

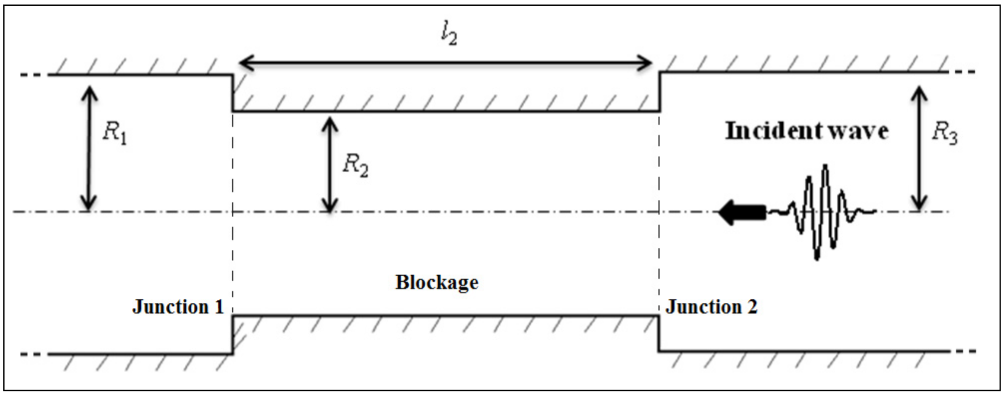

Figure 2. Sketch of blocked pipe system in unbounded pipe.

 / ISSN 1562-6865 (Online) - ISSN 1063-7710 (Print)

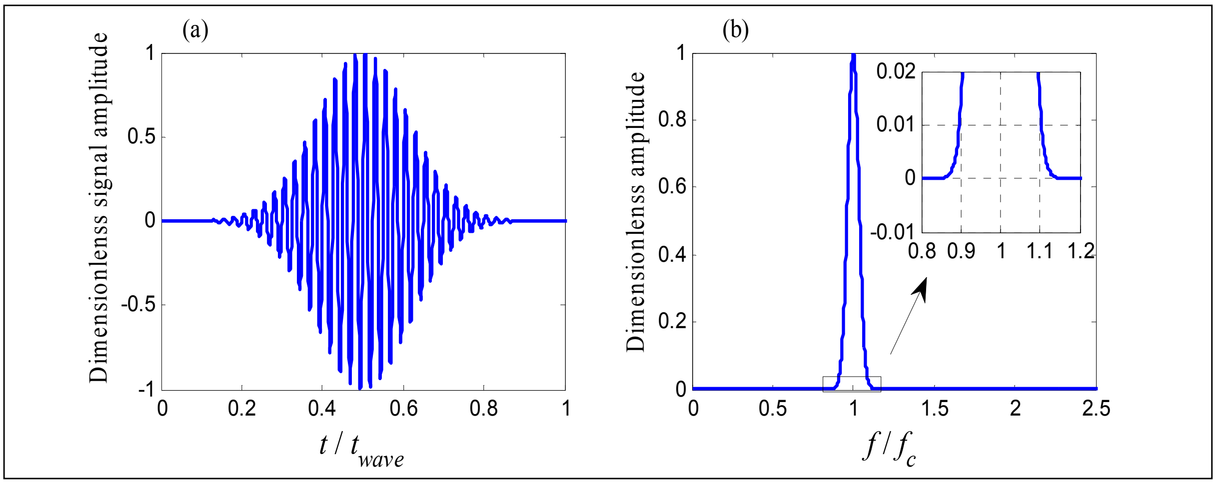

Figure 3**. Probing wavefrom ($\beta = 80\pi$) (Louati, 2016). (a) Time domain; (b) Frequency domain.**

For the shallow blockage case (D_2/D=0.8), Figure 4 gives the pressure distribution in the *r-x* plane where only a plane wave mode was generated at the source (D_s=D). Figure 4a is at time before the incident wave reached the blockage, whereas Figure 4b is at time after the incident wave reached junction 1 but before it reached junction 2. Figure 4b shows that the incident plane wave was scattered into reflected M0 ($\mathrm{M0}_0^R$) and M1 ($\mathrm{M1}_0^R$) and into transmitted M0 ($\mathrm{M0}_0^T$) and M1 ($\mathrm{M1}_0^T$). However, in Figure 5 which shows the severe blockage case (D_2/D=0.4), only M0 was transmitted through the blockage. The reason for this is that the M1 cut-off frequency in pipe 2 (*i.e.* blockage) for the shallow blockage case was (see Louati and Ghidaoui, 2017) $f_1 = \alpha_{r1}/\pi \times a/D_2$ ≈ 3800Hz which means that waves propagating at frequencies within [3800Hz to 4400Hz] excited M1. However, the M1 cut-off frequency in pipe 2 for the severe blockage case was $f_1 = \alpha_{r1}/\pi \times a/D_2$ ≈ 7600Hz which washigher than the upper bound frequency content (UBFC) 4400Hz of the incident signal. Therefore, M1 in the blockage did not get excited.

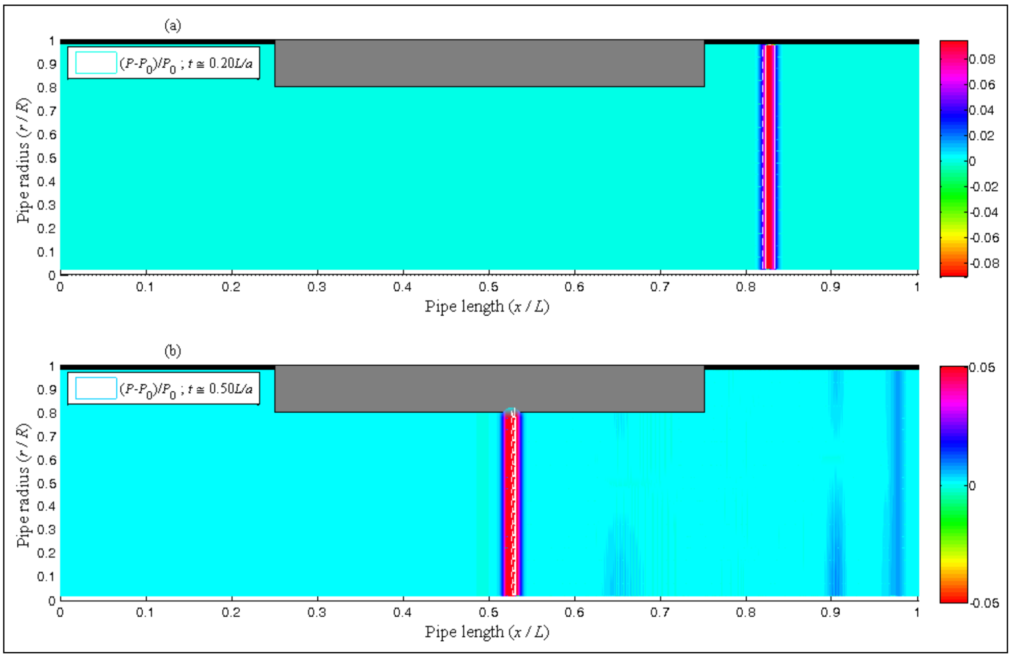

Figure 4. Dimensionless pressure distribution in the r-x space plane for shallow blockage case where only M0 is injected. (f_c=4000Hz and L=200m; l_2=100m and l_3=50m). (a) At time t ≈ 0.2L/a: before the incident waves reach the blockage; (b) At time t ≈ 0.5L/a: after the incident waves reach the blockage.

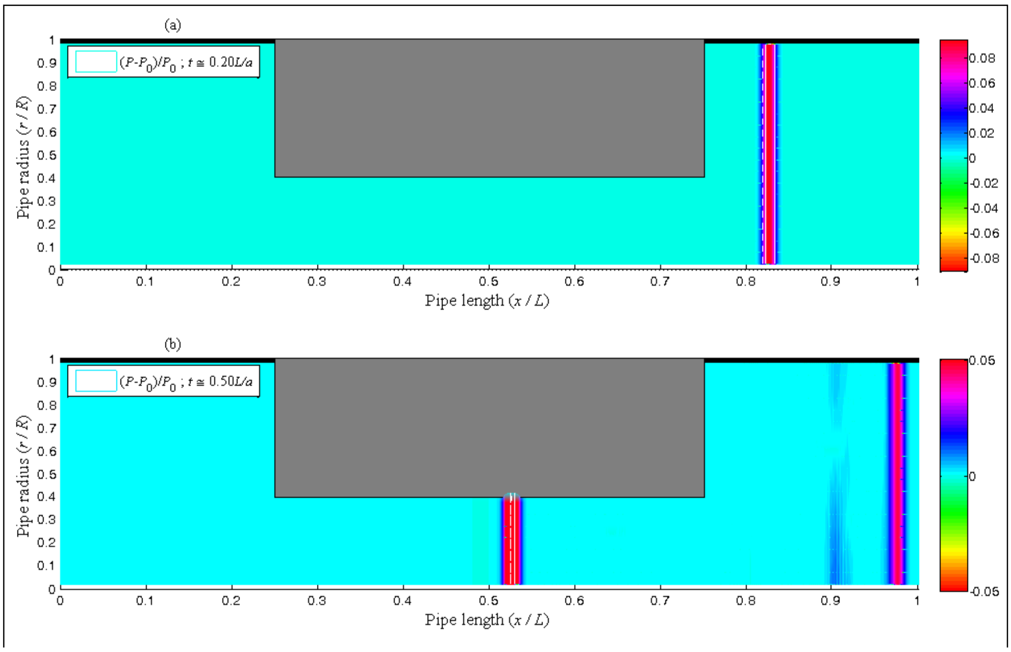

Figure 5. Dimensionless pressure distribution in the r-x space plane for severe blockage case where only M0 is injected. (f_c=4000Hz and L=200m; l_2=100m and l_3=50m). (a) At time t ≈ 0.2L/a: before the incident waves reach the blockage; (b) At time t ≈ 0.5L/a: after the incident waves reach the blockage.

Figure 6 gives an enlarged plot of the pressure distribution at the time right after the wave interacts with junction 1. Figure 6 shows the presence of M1 and a third high mode just to the left and to the right of junction 1, respectively. These two modes were evanescent; they got excited at junction 1 to conserve the continuity of pressure and velocity but they did not propagate along the pipe. They got attenuated over a short range near the junction (see Rienstra and Hirschberg, 2003). The scale of attenuation of these evanescent modes is of the order of pipe diameter.

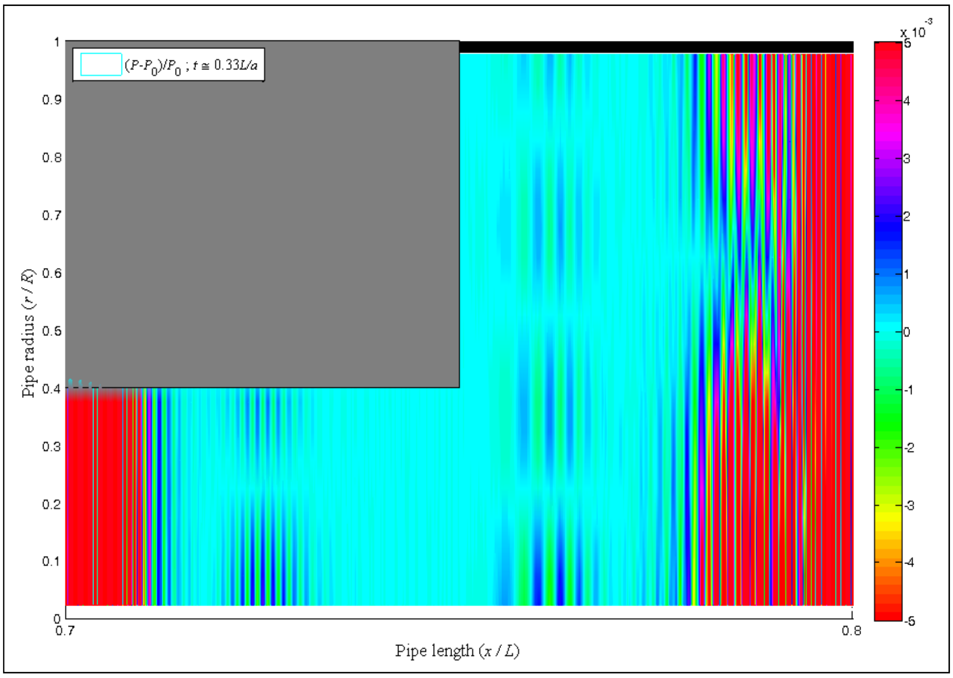

Figure 6. Enlarged plot of dimensionless pressure distribution in the r-x space plane for severe blockage case where only M0 is injected showing the presence of evanescent modes. (f_c=4000Hz and L=200m; l_2=100m and l_3=50m).

Similarly, Figure 7 and 8 give the pressure distribution in the *r-x* plane, respectively, for the case of D_2=0.8D and D_2=0.4D where M1 was excited (D_s=0.2D) and separated from M0 before reaching the blockage (see Figure 7a and 8a). The M0 waves in Figures 7 and 8 scatter as discussed above (see Figure 4 and 5). Figure 7b shows

  / ISSN 1562-6865 (Online) - ISSN 1063-7710 (Print)

that, for the shallow blockage case, M1 was scattered into reflected M0 ($M0_1^R$) and M1 ($M1_1^R$) and into transmitted M0 ($M0_1^T$) and M1 ($M1_1^T$). However, Figure 8b shows that, for the severe blockage case, only $M0_1^T$ waves were transmitted through the blockage. This is because, for the shallow blockage case, the transmitted M1 waves at frequencies within [3600 and 3800] were cut-off in pipe 2, whereas M1 waves at frequencies within [3800 and 4400] were cut-on for pipe 1. On the other hand, for the severe blockage case, all transmitted M1 waves were cut-off in pipe 2.

Figure 9 and 10 give the velocity vector field for shallow and severe cases and show the existence of M1 where radial velocity was present. Noticed that in Figures 7b and 9, the transmitted M1 from the incident M0 ($M1_0^T$) was not clear because it carried little energy (see Figure 4) and it was located where $M0_1^T$ was dominant.

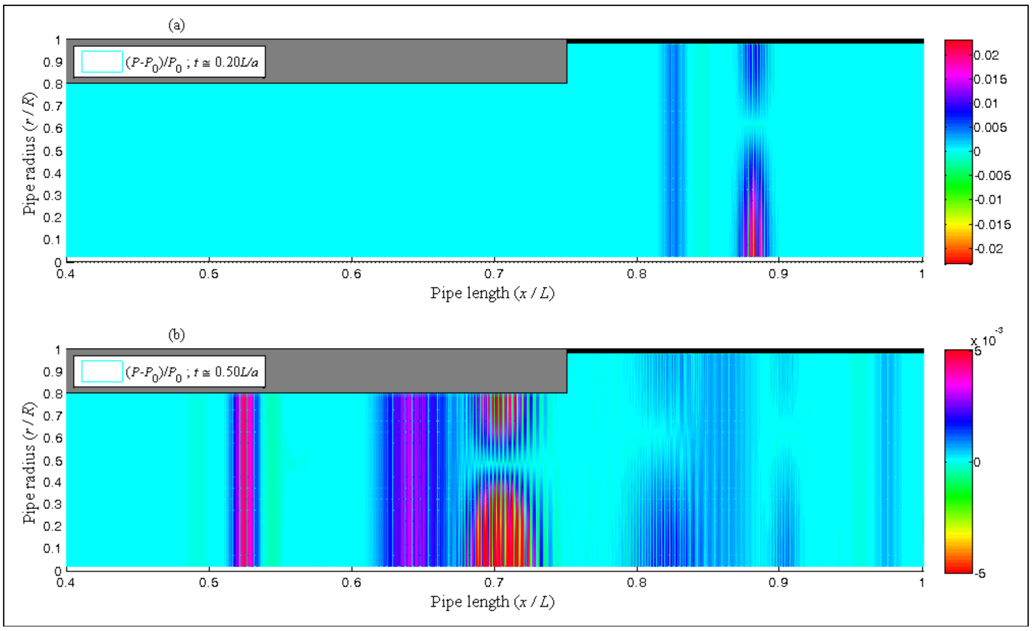

Figure 7. Dimensionless pressure distribution in the r-x space plane for shallow blockage case where M0 and M1 are injected. (f_c=4000Hz and L=200m; l_2=100m and l_3=50m). (a) At time t ≈ 0.2L/a: before the incident waves reach the blockage; (b) At time t ≈ 0.5L/a: after the incident waves reach the blockage.

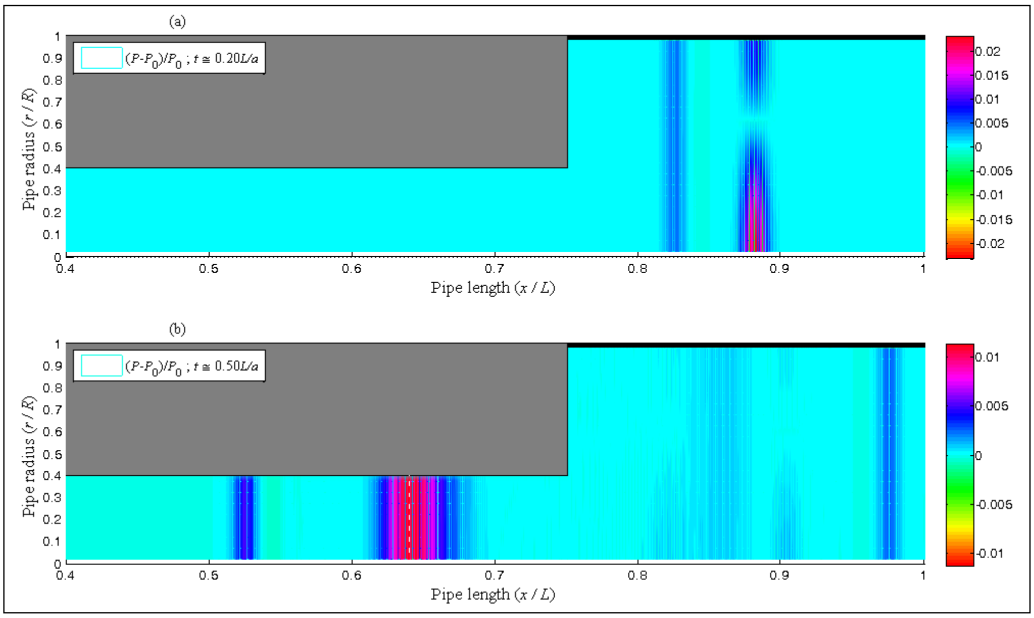

Figure 8. Dimensionless pressure distribution in the r-x space plane for severe blockage case where M0 and M1 are injected. (f_c=4000Hz and L=200m; l_2=100m and l_3=50m). (a) At time t ≈ 0.2L/a: before the incident waves reach the blockage; (b) At time t ≈ 0.5L/a: after the incident waves reach the blockage.

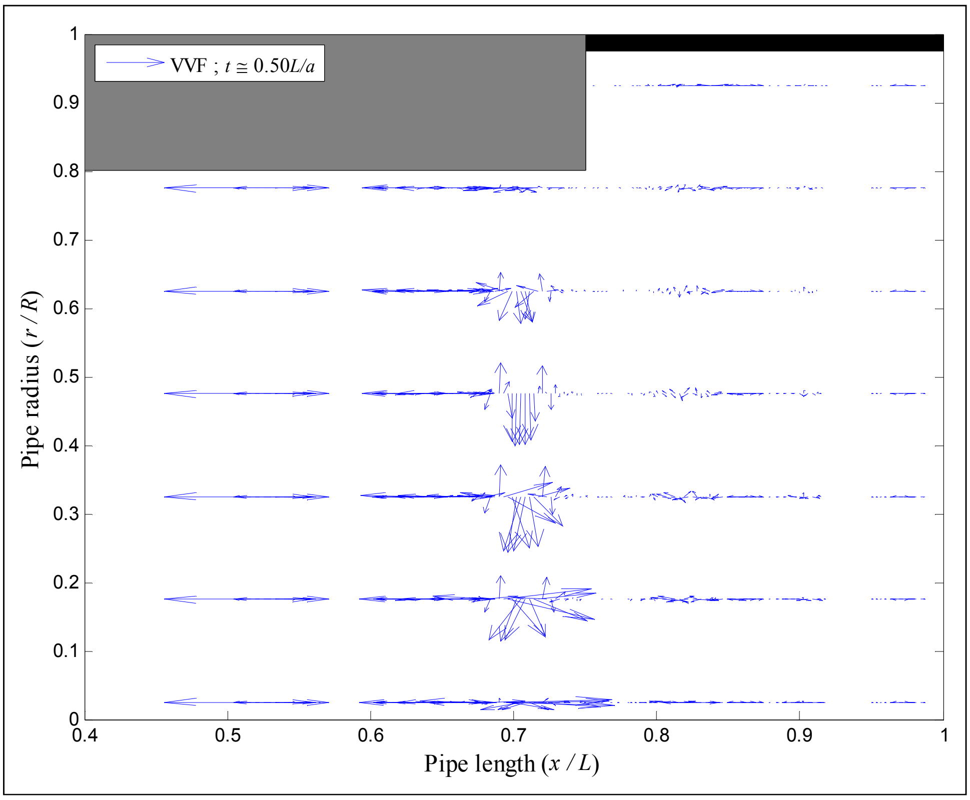

Figure 9. Vector velocity field (VVF) distribution in the r-x space plane at time t ≈ 0.5L/a for shallow blockage case where M0 and M1 are injected. (f_c=4000Hz and L=200m; l_2=100m and l_3=50m).

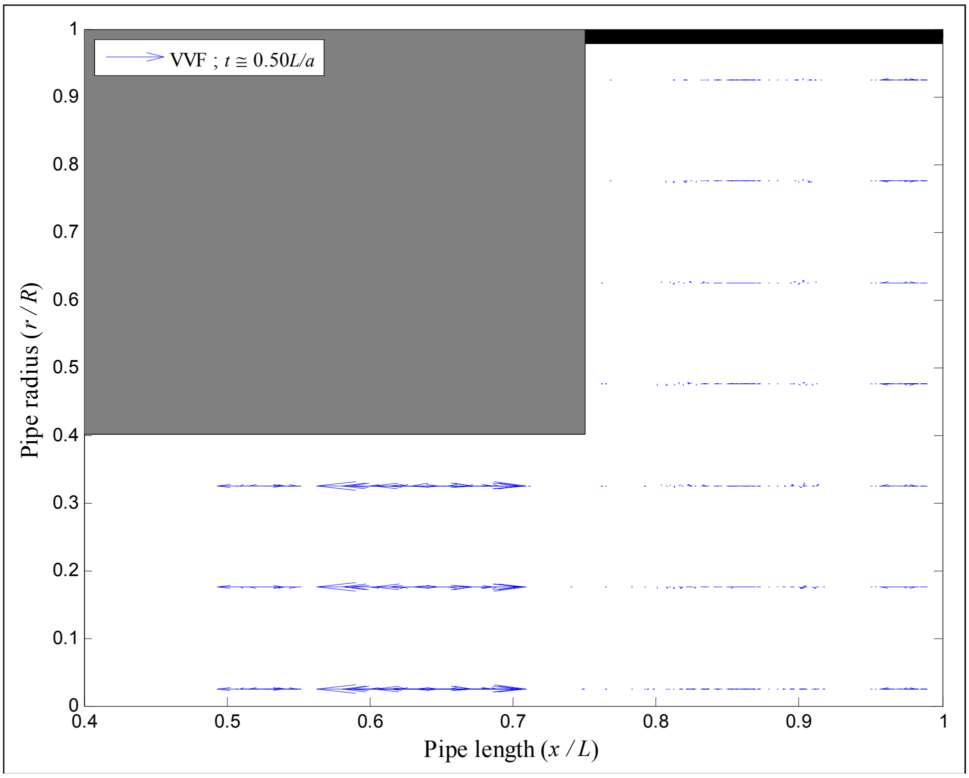

Figure 10. Vector velocity field (VVF) distribution in the r-x space plane at time t ≈ 0.5L/a for severe blockage case where M0 and M1 are injected. (f_c=4000Hz and L=200m; l_2=100m and l_3=50m).

The scattered incident wave distributes its energy into transmitted and reflected modes such that the continuity of pressure and velocity at the discontinuity is satisfied. Figure 11a and 11b give the energy distribution for shallow and severe blockage corresponding to the cases shown in Figure 7b and 8b, respectively. Figure 11a and 11b show that the reflected and transmitted energy from the incident M0 was very different for severe and shallow blockage cases where severe blockage reflects much more of M0 energy than shallow blockage. However, the amount of energy reflected from the incident M1 was similar for both severe and shallow blockage cases. One reason for this is that most of M1 energy is trapped near the pipe centreline and therefore it does not interfere much with the blockage in comparison with M0 (Louati and Ghidaoui, 2017b). It is such wave scattering features that one is looking to explore and make use of it (or take it into account) in inverse problem. The behaviour of wave scattering is only fully analysed is the scattering from the second junction is studied.

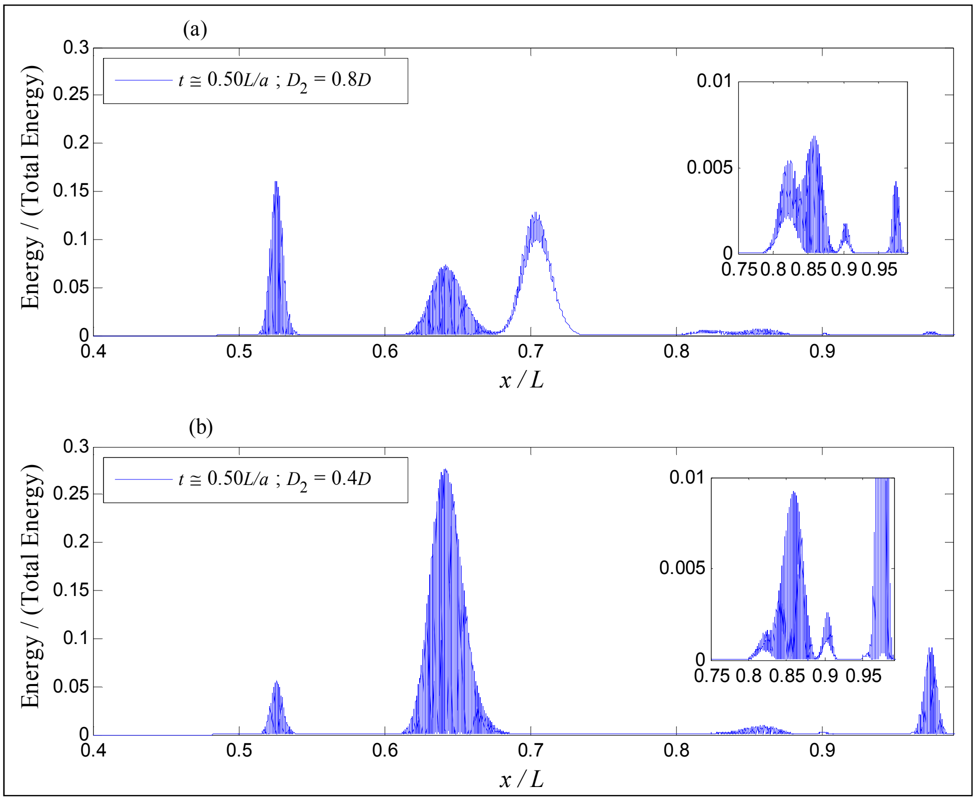

Figure 11. Dimensionless area-averaged energy variation along the pipe at time t ≈ 0.5L/a where M0 and M1 are injected. (f_c =4000Hz and L=200m; l_2=100m and l_3=50m). (a) Shallow blockage case; (b) Severe blockage case.

To discuss the wave scattering at junction 2, the pressure distribution in the *r-x* plane where only M0 was injected is given in Figure 12 and 13 respectively for the case of shallow and severe blockage cases. Figure 12a and13a are given at the time before the incident M0 exits the blockage, whereas Figure 12b and 13b are given at the time after the incident M0 exited the blockage. Figure 12b shows that the incident M0 wave was scattered into transmitted M0 and M1 and into reflected M0 and M1 for the case of shallow blockage. However, Figure 13b shows that, for the case of severe blockage, the incident M0 wave in the blockage and impinging on junction 2 got scattered into transmitted M0 and M1 and into only reflected M0 (without reflected M1). The absence of a reflected wave from junction 2 is due to the fact that M1 is cut-off in pipe 2 (*i.e.* blockage) for severe blockage as discussed above. Figure 12b and13b show two main features of plane wave scattering at junction 2. First, at junction 2, shallow blockage induced much more reflected waves than for the case of severe blockage. Second, most of the transmitted energy from a shallow blockage was carried by the transmitted M0 waves rather than by M1 waves. Conversely, most of the transmitted energy from a severe blockage was carried by the transmitted M1 waves rather than by M0 waves. This shows how different blockages induces different signature on the injected signal. It is these differences that could be exploited in using high frequency waves for blockage detection.

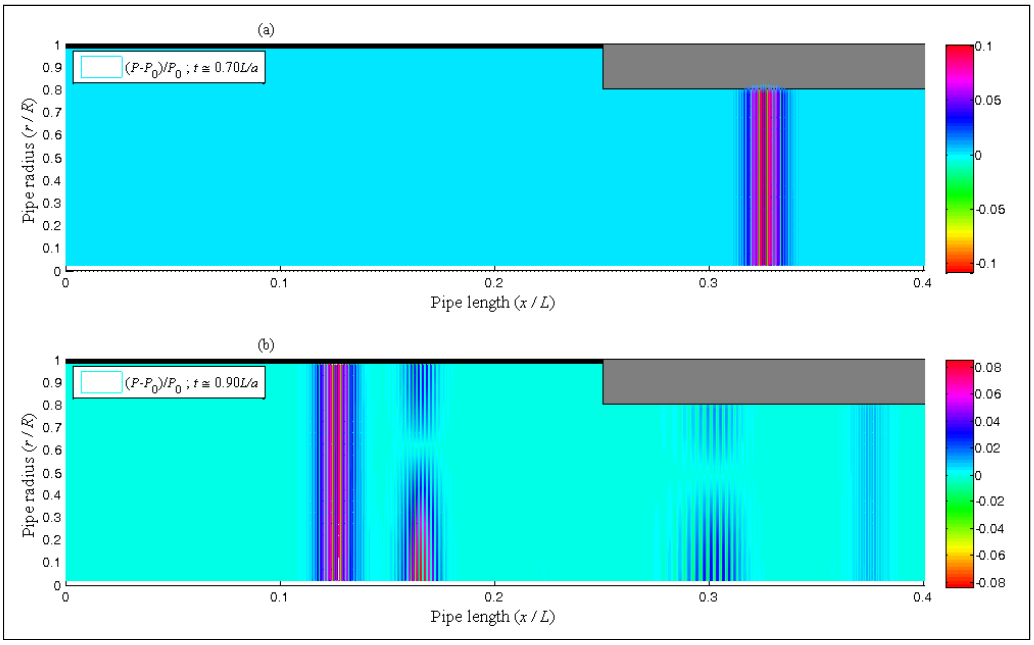

Figure 12. Dimensionless pressure distribution in the r-x space plane for shallow blockage case where only M0 is injected. (f_c=4000Hz and L=200m; l_2=100m and l_1=50m). (a) At time t ≈ 0.7L/a: before the incident waves exits the blockage; (b) At time t ≈ 0.9L/a: after the incident waves exited the blockage.

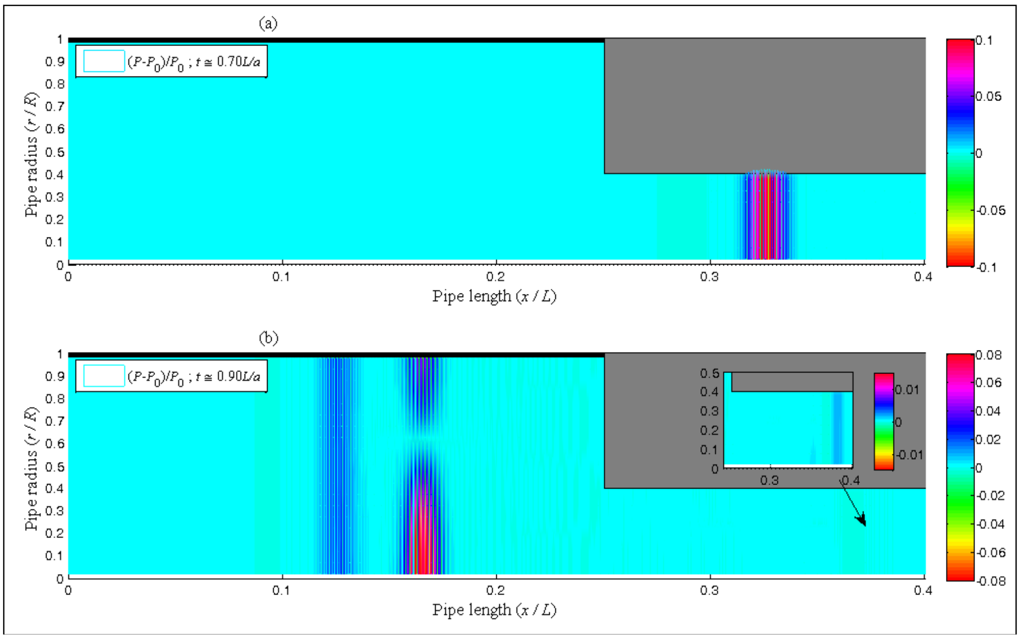

Figure 13. Dimensionless pressure distribution in the r-x space plane for severe blockage case where only M0 is injected. (f_c = 4000Hz and L=200m; l_2=100m and l_1=50m). (a) At time t ≈ 0.7L/a: before the incident waves exits the blockage; (b) At time t ≈ 0.9L/a: after the incident waves exited the blockage.

3. CONCLUSIONS

Scattering of high frequency acoustic waves due to the presence of a blockage was studied. It showed that each incident mode was scattered into multiple of reflected and transmitted modes. The plane wave mode was highly affected by the severity of area reduction. The more severe the reduction is, the more energy of a plane wave is reflected. However, high radial modes had little interaction with the blockage and transmitted most of their energy through both severe and shallow blockage. This was because most of the high radial modes energy was trapped near the pipe centreline. This work considered only axi-symetric pipe system, and therefore, blockages are assumed axi-symmetric.

ACKNOWLEDGEMENTS

This study is supported by the Hong Kong Research Grant Council (projects 612712 & 612713 & T21-602/15R) and by the Postgraduate Studentship.

REFERENCES

Allen, M., Preis, A., Iqbal, M., Srirangarajan, S., Lim, H.B., Girod, L. & Whittle, A.J. (2011). Real-Time in-Network Distribution System Monitoring to improve Operational Efficiency. *Journal American Water Works Association (AWWA),* 103(7), 63-75.

Duan, H., Lee, P.J., Ghidaoui, M.S. & Tung, Y. (2011). Extended Blockage Detection in Pipelines by using the System Frequency Response Analysis. *Journal of Water Resources Planning and Management,* 138(1), 55-62.

Hong Kong Water Supplies Department, (WSD). Private Communication.

Lee, P.J., Duan, H., Tuck, J. & Ghidaoui, M. (2014). Numerical and Experimental Study on the Effect of Signal Bandwidth on Pipe Assessment using Fluid Transients. *Journal of Hydraulic Engineering,* 141(2), 1-11.

Lee, P.J., Vítkovský, J.P., Lambert, M.F., Simpson, A.R. & Liggett, J.A. (2008). Discrete Blockage Detection in Pipelines using the Frequency Response Diagram: Numerical Study. *Journal of Hydraulic Engineering,* 134(5), 658-663.

Louati M. & Ghidaoui M.S. (2017). High Frequency Acoustic Waves in Pressurized Inviscid Fluid in a Conduit. Part 1: Dispersion and Multi-Path Behaviour. *Journal of Hydraulic Research,* (accepted).

Louati M. & Ghidaoui M.S. (2017b). High Frequency Acoustic Waves in Pressurized Viscous Fluid in a Conduit. Part 2: Range of Propagation. *Journal of Hydraulic Research,* (accepted).

Louati, M. & Ghidaoui, M.S. (2015). Wave Blockage Interaction in Pipes. *E-Proceedings of the 36th IAHR World Congress*, 28 June – 3 July, 2015, The Hague, the Netherlands.

Louati, M. (2016). In-Depth Study of Plane Wave-Blockage Interaction and Analysis of High Frequency Waves Behaviour in Water-Filled Pipe Systems, *Doctoral Dissertation.* HKUST. Available at: (http://lbezone.ust.hk/bib/b1618552).

Meniconi, S., Brunone, B., Ferrante, M., Capponi, C., Carrettini, C., Chiesa, C. & Lanfranchi, E. (2015). Anomaly Pre-Localization in Distribution–Transmission Mains by Pump Trip: Preliminary Field Tests in the Milan Pipe System. *Journal of Hydroinformatics,* 17(3), 377-389.

Meniconi, S., Duan, H., Lee, P., Brunone, B., Ghidaoui, M. & Ferrante, M. (2013). Experimental Investigation of Coupled Frequency and Time-Domain Transient Test–Based Techniques for Partial Blockage Detection in Pipelines. *Journal of Hydraulic Engineering,* 139(10), 1033-1040.

Rienstra, S.W. & Hirschberg, A. (2003). An Introduction to Acoustics. *Eindhoven University of Technology,* 18, 19.

Stephens, M. (2008). *Transient Response Analysis for Fault Detection and Pipeline Wall Condition Assessment in Field Water Transmission and Distribution Pipelines and Networks, PhD.* The University of Adelaide, Australia.

Zhao, M., Ghidaoui, M.S., Louati, M. & Duan, H.F. (2016). Transient Wave and Extended Blockage Interaction in Pipe Flows. *Journal of Hydraulic Research*, IAHR, (accepted).

Proceedings of the 37th IAHR World Congress
August 13 – 18, 2017, Kuala Lumpur, Malaysia

SOME INTRIGUING ASPECTS OF BOUNDARY CONDITIONS IN WATER HAMMER

ARRIS S. TIJSSELING[(1)] & ALAN E. VARDY[(2)]

[(1)]Department of Mathematics and Computer Science, Eindhoven University of Technology,
P.O. Box 513, 5600 Mb Eindhoven, The Netherlands
a.s.tijsseling@tue.nl
[(2)]University Of Dundee, Dundee Dd1 4hn, United Kingdom
a.e.vardy@dundee.ac.uk

ABSTRACT

The influence of boundary conditions on water hammer in a traditional reservoir-pipeline-valve system is studied. At first sight this seems a trivial matter. However, a second look reveals some surprising aspects not known to many and therefore presented herein. Water hammer consists of transient pressures P and transient velocities V, the histories of which are largely determined by sonic speed c, pipeline length L, liquid density ρ, initial flow velocity V_0, and effective valve closure time τ. The last parameter is zero herein, because, for clarity, we consider instantaneous valve closures in frictionless pipelines. The questions raised and discussed in this paper are: i) $4L/c$ versus $2L/c$ systems, and do $3L/c$ systems exist?; ii) is an orifice an open end or a closed end, or neither of these?; iii) can all the hydraulic system's resonance frequencies be found from a measured water-hammer history?; iv) can measured pressures reliably be used as boundary conditions?; v) why can we have two boundary conditions at one end in the frequency domain, and not so in the time domain?; vi) are wave speed and phase velocity the same thing?; vii) is my valve structurally fixed? Things are explained from basic principles and simple test cases.

Keywords: Water hammer; pressure surges; fluid transients.

1 INTRODUCTION

Water hammer is a well-known and well-studied phenomenon that deserves continuing attention simply because it will always be there with incidents and accidents. It is assumed herein that the reader is fully familiar with the phenomenon, the Joukowsky pressure, method of characteristics (MOC), transfer matrices (TMM), etc., as documented in classic texts like those of Wylie and Streeter (1993), Ghidaoui et al. (2005) and Chaudhry (2014). Seven simple questions are posed in an attempt to find definite answers. To keep things as basic as possible, a frictionless pipeline is considered with either valves or reservoirs at its extremities. The purpose of the paper is to show the remarkable influence of boundary conditions on hydraulic system behaviour.

2 4*L*/*C* VERSUS 2*L*/*C* SYSTEMS, AND DO 3*L*/*C* SYSTEMS EXIST?

A reservoir-pipe-valve (RPV) system is known as a $4L/c$ system because its period of water-hammer oscillation is $4L/c$ when the valve is fully closed (Fig. 1a). A system with either two open or two closed ends is a $2L/c$ system (Fig. 1c). There are different ways to see why this is the case. First, one can follow the wave fronts and the reflections at the ends to see that things repeat after a certain period T. In a RPV system the reflections are different at each end and this fact results in a two times smaller period than when the reflections are the same. Second, one can find the fundamental period of free oscillation from an elementary theoretical analysis. Third, one can excite the system (harmonically or by impact) and observe at which frequency $f = 1/T$ resonance occurs. But, do $3L/c$ systems exist?

3 IS AN ORIFICE AN OPEN END OR A CLOSED END, OR NEITHER OF THESE?

The transient behaviour with pipe ends that are fully open or fully closed is clear. But what happens when we have something in between, say a partially closed valve or an orifice? Do we still have our traditional $4L/c$ or $2L/c$ systems, or do we have something in between, say a $3L/c$ system? The answer to this question can be found in (Wylie and Streeter, 1993, Section 12-5), in terms of complex analysis, and by Peng and Moody (2003), who applied Laplace transforms and infinite series. The main message is that the orifice acoustically acts as a closed end as long as its constant impedance (resistance) is larger than the impedance ρc of the liquid, and that it acts as an open end when its impedance is smaller. This is a little strange, because it means that hydraulic systems suddenly change from $4L/c$ systems to $2L/c$ systems when valves are opened gradually. This unexpected discontinuity has been investigated by Tijsseling et al. (2012) who found out that the change of acoustic behaviour yet is gradual. The change of fundamental period depends on the orifice's acoustic impedance and at the critical point the orifice acts as a non-reflecting boundary condition thereby prohibiting standing oscillations. This might seem a little strange, but stranger things happen when a closed end houses a

  ISSN 1562-6865 (Online) - ISSN 1063-7710 (Print)

trapped air pocket behaving as a massless spring (Tijsseling et al., 1999). The stiffness of the entrapped gas pocket may range from very soft to very hard and that makes the system range from 2*L*/*c* to 4*L*/*c*. Now there is *not* a critical point where the gas pocket acts as a non-reflecting boundary, because its impedance depends on the period of oscillation. At last it is noted that orifice resistance and skin friction make the acoustic system nonlinear, so that there is not a *constant* period of oscillation.

It is commonly assumed that a system with an upstream reservoir will behave in a 4*L*/*c* manner if the downstream boundary is a prescribed-pressure variation (as with P = constant, for instance), but in a 2*L*/*c* manner if the downstream boundary is a prescribed-velocity variation (as with V = constant, for instance). But what happens if the prescribed-pressure variation is chosen to be identical to the familiar 4*L*/*c* signal shown in Fig. 1a (where the initial velocity $V_0 > 0$)? The velocity at the valve will necessarily become zero and remain zero (Fig. 1b), and so the system is 4*L*/*c*, not 2*L*/*c* as implied by the general statement at the beginning of this paragraph. At the other extreme, if a 2*L*/*c* pressure signal is imposed at the downstream end (Fig. 1c), resonance occurs at 2*L*/*c* as expected (Fig. 1d) because the system is equivalent to an open-open pipeline. Strangely enough, resonance (or a beat of very low frequency) also occurs for a 3*L*/*c* pressure excitation (Fig. 1e) as is evident from Fig. 1f, although the excitation period 3*L*/*c* is larger than the fundamental period 2*L*/*c*. The response "period" *L*/*c* is the result of a combined free and of forced oscillation.

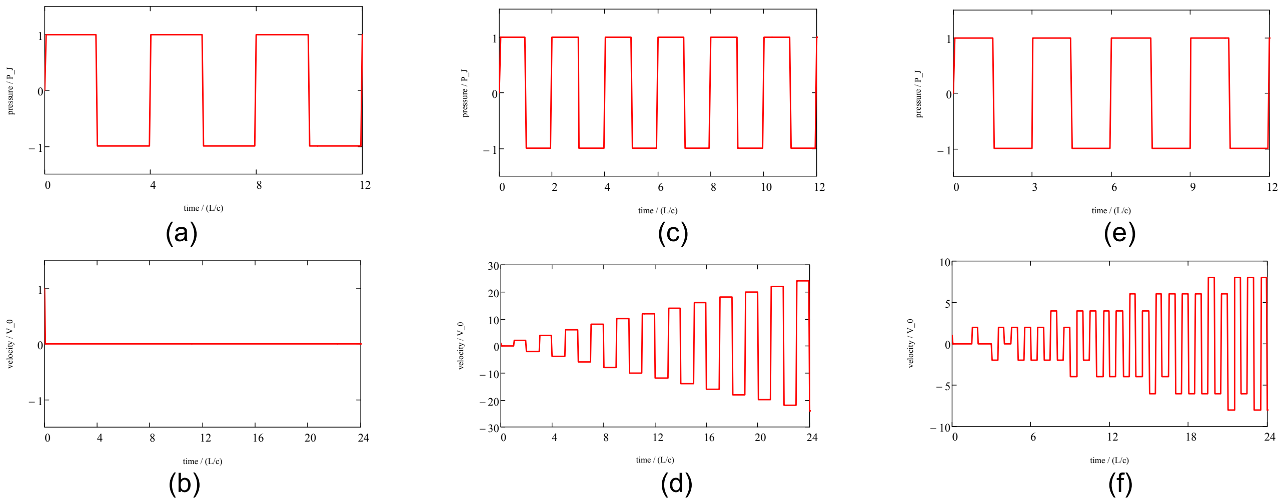

Figure 1. Imposed end pressures (divided by the Joukowsky pressure) and same-end velocity responses (divided by the initial velocity) versus time (divided by *L*/*c*): (a-b): 4*L*/*c* excitation, (c-d): 2*L*/*c* excitation, (e-f): 3*L*/*c* excitation. Exact calculations according to (Tijsseling and Bergant, 2007).

4 CAN ALL THE HYDRAULIC SYSTEM'S RESONANCE FREQUENCIES BE FOUND FROM A MEASURED WATER-HAMMER HISTORY?

The resonance frequencies of a system can be detected from the response to an impact load (Zhang et al., 1999). If the impact load misses "frequency content", not all potential resonances will be activated. Suppose that one uses water hammer to excite a RPV system. In this case, the response ideally contains all relevant system information. Suppose, however, that a short pulse is generated by closing and then re-opening a valve. In this case, the system will be 4*L*/*c* for part of the time and 2*L*/*c* for another part of the time. This may lead to erroneous conclusions. Not re-opening of the valve gives the frequency response of a 4*L*/*c* system and not that of the original 2*L*/*c* system.

5 CAN MEASURED PRESSURES RELIABLY BE USED AS BOUNDARY CONDITIONS?

This is a common procedure that possibly is not valid when the system is operating near resonance (Tijsseling et al., 2010). It is noted that (unsteady) friction, (structural) damping and fluid-structure interaction (FSI) become important in a resonating system.

6 WHY CAN WE HAVE TWO BOUNDARY CONDITIONS AT ONE END IN THE FREQUENCY DOMAIN, AND NOT SO IN THE TIME DOMAIN?

Water-hammer analyses can be carried out either in the time domain or in the frequency domain. The time domain is more suitable for impact excitations like instantaneous valve closures, whereas the frequency domain is the better choice for oscillatory excitation and resonance. Nevertheless, the analyses in both domains concern and contain exactly the same information. It is therefore strange that in the time domain one boundary condition is required at each pipe end, because (for sub-sonic systems) there is only one information-carrying characteristic line reaching the boundary (Fig. 2a), whereas in the frequency domain two boundary conditions is also a valid possibility. One way to explain this is as follows. The time-domain variables P and V are transformed to the frequency-domain variables $\tilde{P}$ and $\tilde{V}$, for example by a Laplace transform. The latter is a weighted average over time, where time goes from zero to infinity. But this means that the solution for P and V is *assumed* to be known for all times t in advance in order to determine $\tilde{P}$ and $\tilde{V}$, and therefore it is allowed to travel backwards in time as shown in Fig. 2b, where two information-carrying characteristic lines meet at the boundary. This boundary can do without extra condition, but then – to compensate – the other one needs two.

One important restriction for frequency-domain analysis is that the system must be linear or linearised, and therefore does not contain exactly the same information as the time-domain system. The frequency domain is inappropriate for strongly non-linear systems, i.e. equations *and* boundary conditions. Frequency-domain calculations are usually performed with complex numbers in order to take full advantage of the pleasant properties of exponential functions; they may lead to exact solutions, where the time-domain calculation does not.

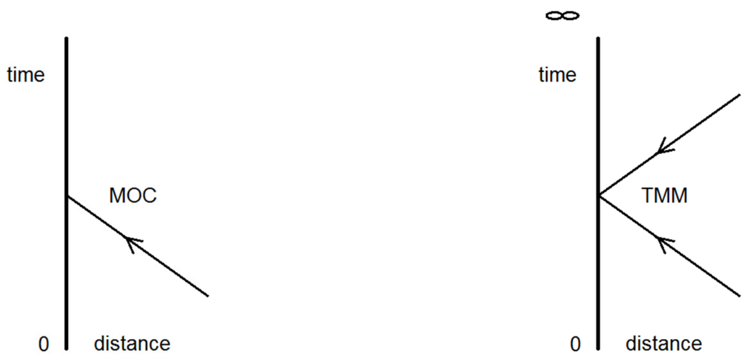

(a) (b)

Figure 2. Characteristic lines in the distance time plane: (a) MOC, (b) TMM.

7 ARE WAVE SPEED AND PHASE VELOCITY THE SAME THING?

The wave speed in real systems is usually found from the fundamental water-hammer period T under the assumption that the pipeline is a $4L/c$ or a $2L/c$ system. We have seen that a partially open (or leaking) valve does not affect this assumption, but that an entrapped air pocket at a dead end might do so. For short pipes, it is noticed that waves reflect from a point somewhat into the reservoir, so that L should be taken a little longer than the actual pipe length. Another issue discussed by Tijsseling and Vardy (2015) is that a travelling wave front in the time domain is something different from a sinusoidal wave train in the frequency domain. The wave front is a local jump, whereas the wave train is global in the sense that it covers the entire pipeline. The front travels with the wave speed and the train has a phase velocity. For non-dispersive systems, these are the same, but for dispersive systems the latter is frequency-dependent and may have magnitudes either smaller or larger than the physically possible maximum wave speed, say 1480 m/s in pure water. In a similar way, time delays at boundaries (e.g. the response of a pump to a sudden change in flow rate) cause diffusion of reflected signals and hence change the frequency-response character of the overall flow.

8 IS MY VALVE STRUCTURALLY FIXED?

The valve in a RPV system experiences heavy and sudden loads during a water-hammer event, in particular when repeated column-separations occur (Bergant et al., 2006). The valve will – depending on its anchorage – certainly move or vibrate to a certain extent. Does this motion or vibration have an influence on the system's $4L/c$ or $2L/c$ behaviour? The importance of this fluid-structure interaction mechanism depends on the relevant time scales (Wylie and Streeter, 1993, Section 11-2; Tijsseling and Vardy, 2008). Wylie and Streeter (1993, Section 6-8) considered a simple spring-mass model where the valve has mass m and stiffness k. If the valve has no explicit support, the spring stiffness comes from the adjacent pipe section so that $k = EA/L$, where E and A are Young's modulus and cross-sectional area of the pipe wall. This model addition will certainly affect system behaviour, just like the gas pocket modelled as a massless spring (but now with significant mass added to it). If the spring is relatively soft, the liquid will tend to behave similarly to a rigid column for which $L/c = 0$. If the spring is extremely stiff or the valve mass very large, we have a closed end.

9 CONCLUDING REMARKS

A mix of issues related to boundary conditions in water hammer has been addressed without presenting the mathematics behind it. The phenomena were explained as simply as reasonably possible and in this sense the paper has an educational character. Hopefully the reader is enthused to study some of the discussed aspects of hydraulic transients and in particular the questions that – in his/her opinion – have not been answered satisfactorily.

REFERENCES

Bergant, A., Simpson, A. R. & Tijsseling, A. S. (2006). Water Hammer with Column Separation: A Historical Review. *Journal of fluids and structures*, 22(2), 135-171.

Chaudhry M.H. (2014) *Applied Hydraulic Transients (third edition)*. Springer.

Ghidaoui M.S., Zhao M., McInnis D.A. & Axworthy D.H. (2005) A Review of Water Hammer Theory and Practice. *Applied Mechanics Reviews*, 58(1), 49-76.

Peng, M. M. & Moody, F. J. (2003). Natural Frequencies in Pipes with Orifice Terminations. In *ASME 2003 International Mechanical Engineering Congress and Exposition*. American Society of Mechanical Engineers, 165-169.

Tijsseling, A. S. & Bergant, A. (2007). *Meshless Computation of Water Hammer*. Department of mathematics and computer science, University of technology, vol. 52(66), No. 6, 65-76.

Tijsseling, A. S., Hou, Q., Svingen, B. & Bergant, A. (2010). Acoustic Resonance in a Reservoir-Pipeline-Orifice System. In *ASME 2010 Pressure Vessels and Piping Division/K-PVP Conference*. American Society of Mechanical Engineers, 303-314.

Tijsseling, A. S., Hou, Q., Svingen, B. & Bergant, A. (2012). Acoustic Resonance in a Reservoir-Double Pipe-Orifice System. In *ASME 2012 Pressure Vessels and Piping Conference*. American Society of Mechanical Engineers, 183-191.

Tijsseling, A. S., Kruisbrink, A. C. H. & Pereira da Silva, A. (1999). The Reduction of Pressure Wave Speeds by Internal Rectangular Tubes. In *Proceedings the of Third ASME & JSME Joint Fluids Engineering Conference, Symposium S-290 Water Hammer, San Francisco, USA*, 1-8.

Tijsseling, A. S. & Vardy, A. E. (2008, May). Time Scales and FSI Ii Oscillatory Liquid-Filled Pipe Flow. In *10th International Conference on Pressure Surges, S. Hunt, ed., Edinburgh, UK, BHR Group, Cranfield, UK*, 553-568.

Tijsseling A.S. & Vardy A.E. (2015) What is Wave Speed? In *Proceedings of the 12th International Conference on Pressure Surges, Dublin, Ireland, November 2015*, 343-360.

Wylie, E. B., Streeter, V. L. & Suo, L. (1993). *Fluid Transients in Systems*. Englewood Cliffs, NJ: Prentice Hall, Book, Volume 1, 464.

Zhang, L., Tijsseling, S. A. & Vardy, E. A. (1999). FSI Analysis of Liquid-filled Pipes. *Journal of sound and vibration*, 224(1), 69-99.

Proceedings of the 37th IAHR World Congress
August 13 – 18, 2017, Kuala Lumpur, Malaysia

THEORETICAL ANALYSIS OF THE INFLUENCE OF BLOCKAGE IRREGULARITY ON TRANSIENT WAVES IN WATER SUPPLY PIPELINES

TONG-CHUAN CHE[1], HUAN-FENG DUAN[2], PEDRO J. LEE[3] & MOHAMED S. GHIDAOUI[4]

[1,2] Department of Civil and Environmental Engineering, The Hong Kong Polytechnic University, Hung Hom, Kowloon, Hong Kong,
tong-chuan.che@conect.polyu.hk; hf.duan@polyu.edu.hk
[3] Department of Civil and Natural Resources Engineering, The University of Canterbury, Private Bag 4800, Christchurch, New Zealand,
pedro.lee@canterbury.ac.nz
[4] Department of Civil and Environmental Engineering, The Hong Kong University of Science and Technology, Kowloon, Hong Kong,
ghidaoui@ust.hk

ABSTRACT

Extended partial blockages are commonly formed in urban water supply systems (UWSS) and can result in many problems, such as reducing water carrying capacity, increasing energy loss, and deteriorating water quality. A variety of blockage detection methods have been developed, among which the transient-based blockage detection method (TBBDM) is thought to be a promising way for diagnosing pipeline blockages for its advantages of active, economic, efficient and non-destructive operations. Despite of the successful validation and application of the TBBDM in the literature, blockages considered in these studies were mainly idealized or simplified to regular shapes, which are equivalent to pipelines in series with different diameters. However, blockages with regular shapes are not common in practical UWSS. Therefore, a better understanding of the influences of blockages with more realistic shapes (termed as irregular blockages) on transient waves is necessary and critical to the development and application of the current TBBDM. This study aims to: (i) obtain the nontrivial solutions of one-dimensional (1D) wave equation for a conduit with varying pipe cross-sectional area in different irregular blockage patterns; (ii) derive the analytical transfer matrix for the pipeline with a linear irregular blockage based on these solutions; and (iii) investigate the influences of the linear irregular blockage on the system frequency responses by using the analytical transfer matrix method. The results indicate that the resonant frequency shift pattern caused by the linear irregular blockage is significantly different from that caused by the uniform blockage. These findings may help to gain useful insights and implications for further improvement of the current TBBDM.

Keywords: Water pipelines; transient wave; blockage irregularity; wave-blockage interaction; plane wave solution.

1 INTRODUCTION

Blockages commonly exist in fluid conveying pipelines due to various physical, chemical and biological processes including corrosion, biofilm growth and deposition of sediments. Blockages in urban water supply systems (UWSS) reduce pipe diameters and increase pipe wall roughness, resulting in low water carrying capacity, additional energy loss and deterioration of water quality. Unlike leaks, blockages are easily masked in pipeline network since they lack external evidence needed for direct detection. In addition, the lost pressure and flow can be supplied by other branch pipelines in the network (Stephens, 2008). From this perspective, identifying and detecting blockages in pipelines are crucial and necessary for creating sustainable and smart UWSS.

Recently, the transient-based blockage detection method (TBBDM) has been widely developed in the literature (Duan et al., 2012; 2013; Meniconi et al., 2013), which is thought to be a promising way of diagnosing pipeline blockages because of its efficiency, non-destructiveness and fast response time. The principle of the TBBDM is that the blockage can be detected by injecting a transient signal into the pipeline and then measuring and analyzing the transient responses.

Despite of the successful applications of the TBBDM in many numerical and laboratory tests, the blockages used for analysis in previous studies were mainly idealized or simplified to regular shapes (for example, axisymmetric and uniform) (Duan et al., 2012; 2013; Meniconi et al., 2013). Actually, these simplified situations are equivalent to pipelines with different diameters connected with each other, as shown in Figure 1a, which are not common in realistic UWSS, as illustrated in Figure 2. As a result, the current TBBDM may become invalid or inaccurate when it is applied to practical UWSS. Therefore, the understanding of the effects of blockages with more realistic shapes (referred to as blockage irregularities), as shown in Figures 1b and 1c, on transient waves is essential and important for accurate blockage detection in UWSS, which is the main scope of this research.

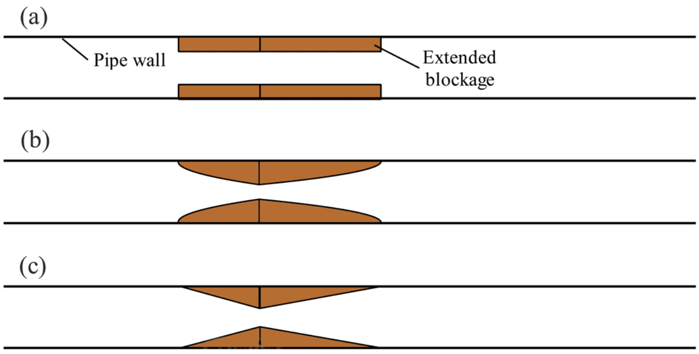

Figure 1. Extended blockage with pipe radius change in (a) uniform shape, (b) exponential shape, and (c) linear shape.

To investigate the influences of irregular blockages on transient waves, the one-dimensional (1D) wave equation for a conduit with varying pipe cross-sectional area is solved analytically for two different irregular blockages. Based on these analytical solutions, the overall transfer matrix for the pipeline system with a linear irregular blockage is derived, which is then validated by a numerical experiment. Finally, a more practical water supply pipeline system with same volume of linear irregular and uniform blockages is adopted to investigate the effect of the linear irregular blockage on the system frequency responses.

(a) (b)

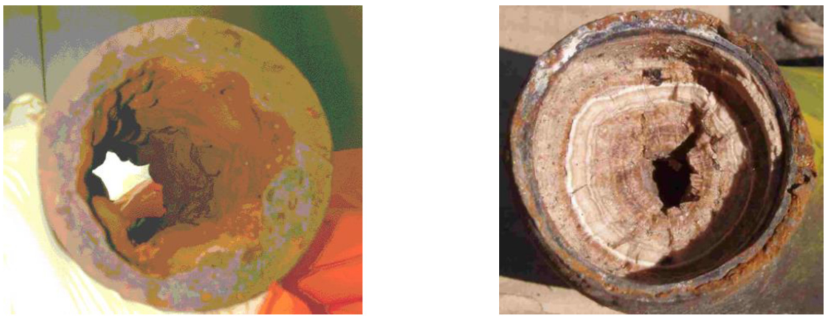

Figure 2. Blockages with irregular shapes in practical water supply pipelines, (a) encrustation and biofouling in a cast iron pipeline (James and Shahzad, 2003), and (b) clogged section in a seawater pipeline (*http://pureelementswater.net/*).

2 GOVERNING EQUATIONS

The classical 1D water hammer model (Wylie et al., 1993; Ghidaoui et al., 2005; Chaudhry, 2014; Duan et al., 2014) for a pipe with varying cross-sectional area, by ignoring frictional effect, is:

$$\frac{\partial(\rho A)}{\partial t}+\frac{\partial(\rho A V)}{\partial x}=0 \qquad [1]$$

$$\frac{\partial(\rho A V)}{\partial t}+A\frac{\partial P}{\partial x}=0 \qquad [2]$$

where t = time, x = axial coordinate along the pipeline, P = pressure in the time domain, V = velocity in axial direction, A = pipe cross-sectional area, and ρ = density of the fluid.

Based on Eq. [1] and [2], Duan et al. (2011; 2014) derived the following 1D wave equation for a conduit with varying cross-sectional area:

$$A\frac{\partial^2 P}{\partial t^2}=a^2\frac{\partial}{\partial x}\left(A\frac{\partial P}{\partial x}\right) \qquad [3]$$

where a = wave speed.

This wave equation can be rewritten in the following form:

$$\frac{\partial^2 P}{\partial t^2} - a^2 \frac{\partial^2 P}{\partial x^2} = a^2 \frac{A'}{A} \frac{\partial P}{\partial x} \tag{4}$$

The term on the right hand side (RHS) of Eq. [4] stands for the effect of varying pipe cross-sectional area on the original blockage-free wave equation (when RHS = 0).

For steady-oscillatory flow, the instantaneous pressure (P) may be separated into two parts (Chaudhry, 2014):

$$P = P_0 + p^* \tag{5}$$

where P_0 = mean pressure and p^* = pressure deviation from the mean.

Since friction is not considered in this study:

$$\frac{\partial P_0}{\partial t} = \frac{\partial P_0}{\partial x} = 0 \tag{6}$$

Substituting Eq. [5] and [6], Eq. [4] becomes:

$$\frac{\partial^2 p^*}{\partial t^2} - a^2 \frac{\partial^2 p^*}{\partial x^2} = a^2 \frac{A'}{A} \frac{\partial p^*}{\partial x} \tag{7}$$

If p* is assumed harmonic in time (Chaudhry, 2014):

$$p^*(x,t) = \mathrm{Re}\left(p(x)e^{i\omega t}\right) \tag{8}$$

where p = complex variable and is function of x only, ω = frequency, i = imaginary part, and "Re" = real part.

Then, Eq. [7] is simplified into the following form:

$$\frac{\mathrm{d}^2 p}{\mathrm{d}x^2} + \frac{A'}{A} \frac{\mathrm{d}p}{\mathrm{d}x} + k^2 p = 0 \tag{9}$$

where $k = \omega/a$ is the incident wave number.

The wave equation, Eq. [9] for each pipe section can be expressed as:

$$\frac{\mathrm{d}^2 p_j}{\mathrm{d}x^2} + \frac{A_j'}{A_j} \frac{\mathrm{d}p_j}{\mathrm{d}x} + k_j^2 p_j = 0 \tag{10}$$

where $j = 1$, 2 or 3 is the number of each pipe section (as shown in Figure 3).

3 ANALYTICAL INVESTIGATIONS

The analytical method used in this study is inspired by the earlier work done by Skudrzy (1971) who investigated the behavior of acoustic waves in wind instruments, whose radiuses changed exponentially along the axial direction. Similarly, the wave equation Eq. [10] in the present study can be solved analytically by assuming a plane wave solution, whose amplitude is modified by the changing pipe radiuses. The analytical method is applied into a 1D unbounded pipeline system, in order to highlight the effects of irregular blockages on transient wave propagation. Two types of blockages, including radiuses changing in exponential and linear shapes, as shown in Figure 3a and Figure 3b, are investigated in this study.

In this preliminary study, friction effects (steady and unsteady) are not considered and included in the following analysis, in order to highlight the effects of different types of irregular blockage on transient waves. The influences of other factors (such as viscoelasticity and air cavity) on the derived results and obtained findings of this study can be assessed through numerical simulations and experimental tests in a future study. Meanwhile, it is assumed that the wave speed in different blockage sections is constant so as to fairly compare the results of different blockage cases and to separate the influence of blockages from other factors (such as variation of wave speed induced by the changes of pipe diameter and thickness) in the system. Thus, the incident wave number (k) is constant for all blockage cases tested in this study.

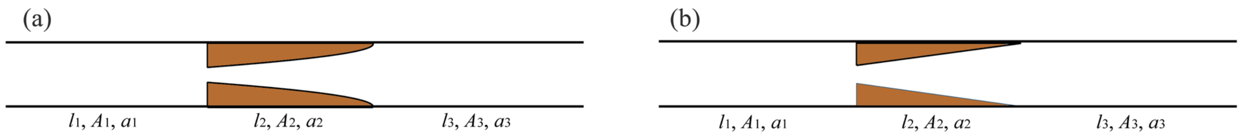

Figure 3. Irregular extended blockages used for analytical investigation, (a) exponential blockage, and (b) linear blockage.

3.1 Exponential irregular blockage

The pipe radius, $r_2(x)$ for pipe Section 2 ($-0.5l_2 < x < 0.5l_2$, note that $x = 0$ at the center of the extended blockage) in Figure 3a can be expressed as:

$$r_2(x) = C_2 e^{C_1 x} \quad [11]$$

where C_1 and C_2 are the changing rate of pipe radius and the pipe radius at $x = 0$, respectively, and $C_1, C_2 > 0$.

Then, the pipe cross-sectional area, A2(x) and its derivative, A'2(x) for pipe Section 2 can be easily calculated. Thus:

$$\frac{A_2'(x)}{A_2(x)} = 2C_1 \quad [12]$$

Substitute Eq. [12] into Eq. [10]:

$$\frac{d^2 p_2}{dx^2} + 2C_1 \frac{dp_2}{dx} + k_2^2 p_2 = 0 \quad [13]$$

To get the nontrivial solutions of Eq. [13], two assumptions are proposed herein: (i) the wave speed, a2 is constant (and thus k2 for incident wave part is constant) in the whole pipe Section 2, and (ii) solutions of p2 have the following form:

$$p_2 = \frac{e^{\alpha x}}{r_2(x)} = \frac{e^{\alpha x}}{C_2 e^{C_1 x}} = \frac{e^{(\alpha - C_1)x}}{C_2} \quad [14]$$

where α is coefficient that remains to be determined.

Substitute Eq. [14] into the wave equation Eq. [13], resulting in the following characteristic equation:

$$\alpha^2 - C_1^2 + k_2^2 = 0 \quad [15]$$

If $k_2 > C_1$:

$$\alpha_1 = ik_2', \ \alpha_2 = -ik_2' \quad [16]$$

where $k_2' = \sqrt{k_2^2 - C_1^2}$ is the group wave number of propagating wave in irregular blockage, which is modified by the changing rate of pipe radius, C_1.

Therefore, p2 has the following two special solutions:

$$\left(p_2\right)_1 = \frac{e^{ik_2^{'}x}}{C_2 e^{C_1 x}},\ \left(p_2\right)_2 = \frac{e^{-ik_2^{'}x}}{C_2 e^{C_1 x}} \tag{17}$$

In fact, the above two plane wave solutions in Eq. [17] are the incident and reflected waves propagating in opposite directions. The amplitude of these two waves is modified by the denominator, which is pipe radius, r2(x), as propagate within the blockage along axial direction. More specifically, the amplitude of transient waves in the exponential irregular blockage increases with the decrease in the pipe radius. Moreover, the wave number (in other words, spatial frequency) of these two waves is modified by the exponential changing rate of pipe radius, C1 from k2 to k2'.

Based on the rule of superposition, the general solution for Eq. [13] can be expressed as:

$$p_2 = \frac{I_2 e^{ik_2^{'}x} + R_2 e^{-ik_2^{'}x}}{C_2 e^{C_1 x}} \tag{18}$$

where I_2 and R_2 are two constant coefficients.

3.2 Linear irregular blockage

The pipe radius, $r_2(x)$ for pipe Section 2 ($-0.5l_2 < x < 0.5l_2$) in Figure 3b can be expressed as:

$$r_2(x) = C_1 x + C_2 \tag{19}$$

where C_1 and C_2 are the changing rate of pipe radius and the pipe radius at $x = 0$, respectively, and C_1, $C_2 > 0$.

Then, the pipe cross-sectional area, A2(x) and its derivative, A'2(x) for pipe Section 2 can be easily calculated. Thus:

$$\frac{A_2^{'}(x)}{A_2(x)} = \frac{2C_1}{C_1 x + C_2} \tag{20}$$

Substitute Eq. [20] into Eq. [10]:

$$\frac{\mathrm{d}^2 p_2}{\mathrm{d}x^2} + \frac{2C_1}{C_1 x + C_2}\frac{\mathrm{d}p_2}{\mathrm{d}x} + k_2^2 p_2 = 0 \tag{21}$$

To get the nontrivial solutions of Eq. [21], two assumptions are proposed herein: (i) the wave speed, a2 is constant (and thus k2 for incident wave part is constant) in the whole pipe Section 2, and (ii) solutions of p2 have the following form:

$$p_2 = \frac{e^{\alpha x}}{r_2(x)} = \frac{e^{\alpha x}}{C_1 x + C_2} \tag{22}$$

where α is coefficient that remains to be determined.

Substitute Eq. [22] into the wave equation Eq. [21], resulting in the following characteristic equation:

$$\alpha^2 + k_2^2 = 0 \tag{23}$$

As $k_2 > 0$:

$$\alpha_1 = ik_2,\ \alpha_2 = -ik_2 \tag{24}$$

Therefore, p2 has the following two special solutions:

$$\left(p_2\right)_1 = \frac{e^{ik_2 x}}{C_1 x + C_2},\ \left(p_2\right)_2 = \frac{e^{-ik_2 x}}{C_1 x + C_2} \tag{25}$$

The above two plane wave solutions in Eq. [25] are the incident and reflected waves propagating in opposite directions. Similar to Eq. [17], the amplitude of these two waves is modified by the denominator, which is pipe radius, r2(x), as propagate within the blockage along axial direction. However, the wave number, k2 of these two waves remains unchanged.

The general solution for Eq. [21] can be expressed as:

$$p_2 = \frac{I_2 e^{ik_2 x} + R_2 e^{-ik_2 x}}{C_1 x + C_2} \quad [26]$$

4 FREQUENCY RESPONSES OF PIPELINE WITH LINEAR IRREGULAR BLOCKAGE

4.1 System frequency responses

The transfer matrix of a pipeline is used to connect state vectors at two boundaries. The analytical expression of frequency response method for a single intact pipeline was derived by Chaudhry (2014) as:

$$\begin{Bmatrix} q \\ h \end{Bmatrix}^{n+1} = \begin{bmatrix} \cos(kl) & -i\frac{1}{M}\sin(kl) \\ -iM\sin(kl) & \cos(kl) \end{bmatrix} \begin{Bmatrix} q \\ h \end{Bmatrix}^{n} \quad [27]$$

where q = discharge in the frequency domain, h = pressure head in the frequency domain, $M = a/Ag$, l = pipe length, superscripts "n" = upstream boundary of n-th pipe section, and "n+1" = downstream boundary of n-th pipe section.

A similar derivation procedure can be adopted to obtain transfer matrices for both exponential and linear irregular blockages based on the wave solutions in Eq. [18] and [26]. In this study, only the following transfer matrix for the linear irregular blockage is analyzed in detail.

$$\begin{Bmatrix} q \\ h \end{Bmatrix}^{n+1} = \begin{bmatrix} U_{11} & U_{12} \\ U_{21} & U_{22} \end{bmatrix} \begin{Bmatrix} q \\ h \end{Bmatrix}^{n} \quad [28]$$

where U_{ij} are elements of the transfer matrix for the linear irregular blockage.

A pipeline system with different types of blockage, as shown in Figure 5, is adopted in this study. The overall matrix describing the whole pipeline system can be derived by the combination of matrices for each system component. It is assumed that there is no pressure head loss and no mass storage when water flow through pipe junctions (Duan et al., 2012). Therefore, the overall matrix for the pipeline system with the linear irregular blockage in Figure 5(b) can be written as:

$$\begin{aligned} \begin{Bmatrix} q \\ h \end{Bmatrix}^{\mathrm{B}} = & \begin{bmatrix} \cos(kl_4) & -i\frac{1}{M}\sin(kl_4) \\ -iM\sin(kl_4) & \cos(kl_4) \end{bmatrix} \begin{bmatrix} 1 & 0 \\ 0 & 1 \end{bmatrix} \times \begin{bmatrix} U_{11} & U_{12} \\ U_{21} & U_{22} \end{bmatrix}^3 \begin{bmatrix} 1 & 0 \\ 0 & 1 \end{bmatrix} \\ & \times \begin{bmatrix} U_{11} & U_{12} \\ U_{21} & U_{22} \end{bmatrix}^2 \begin{bmatrix} 1 & 0 \\ 0 & 1 \end{bmatrix} \times \begin{bmatrix} \cos(kl_1) & -i\frac{1}{M}\sin(kl_1) \\ -iM\sin(kl_1) & \cos(kl_1) \end{bmatrix} \begin{Bmatrix} q \\ h \end{Bmatrix}^{\mathrm{A}} \end{aligned} \quad [29]$$

where superscripts "A" = upstream boundary and "B" = downstream boundary.

Eq. [29] can be simplified into:

$$\begin{Bmatrix} q \\ h \end{Bmatrix}^{\mathrm{B}} = \begin{bmatrix} U_{11}^* & U_{12}^* \\ U_{21}^* & U_{22}^* \end{bmatrix} \begin{Bmatrix} q \\ h \end{Bmatrix}^{\mathrm{A}} \quad [30]$$

where U^*_{ij} are elements of the overall matrix for the whole pipeline system.

To obtain the head responses at the downstream boundary, a unit discharge perturbation is placed at the upstream face of the closed downstream valve (Lee et al., 2006).

$$\begin{Bmatrix} q \\ h \end{Bmatrix}^{\mathrm{B}} = \begin{bmatrix} U_{11}^* & U_{12}^* \\ U_{21}^* & U_{22}^* \end{bmatrix} \begin{Bmatrix} q \\ h \end{Bmatrix}^{\mathrm{A}} + \begin{pmatrix} 1 \\ 0 \end{pmatrix} \quad [31]$$

For the reservoir-pipe-valve system in Figure 5b, two known boundary conditions are $h_A = q_B = 0$. Substituting them into Eq. [31] leads to:

$$h^{B} = -\frac{U_{21}^{*}}{U_{11}^{*}} \qquad [32]$$

4.2 Numerical validation of the resonant condition

To validate the analytical result of Eq. [32], the classical 1D water hammer model by coupling with the method of characteristics (MOC) is adopted for comparison. The pipeline system with a linear irregular blockage, as shown in Figure 5b, is used for the numerical validation. The original intact pipeline (R = 0.25 m, L = 1000 m) is blocked by a linear irregular blockage with the minimum radius C_2 = 0.15 m and $l_2 = l_3$ = 100 m (detailed parameters can refer to T2 in Table 1). In the numerical simulation, the 1000-meter-long pipeline is discretized into 4,000 relatively small sections (that is dx = 0.025 m) to decrease the frequency shift caused by the numerical errors. The transient (pressure wave) is generated by a sudden and full closure of the downstream valve and the pressure head trace is measured at the downstream in-line valve. Then, the measured pressure head trace is transferred into the frequency domain by a Fast Fourier transform (FFT) algorithm.

The analytical and numerical frequency response results with the first 10 peaks are plotted in Figure 4a. The frequency is normalized by the fundamental frequency of the intact pipeline system $\omega_{th} = a/4L$ and is expressed as non-dimensional frequency, ω^*. In addition, the first 25 resonant peaks, m and corresponding resonant frequencies, $\omega^*_{rf,m}$ from the analytical and numerical results are extracted and plotted in Figure 4b. Figure 4a shows that the presence of the linear irregular blockage has changed the resonant frequencies of the original intact system. Moreover, both figures show good agreement between the analytical and numerical results, which confirms the validity of the analytical result of Eq. [32] and the analytical method used in this study.

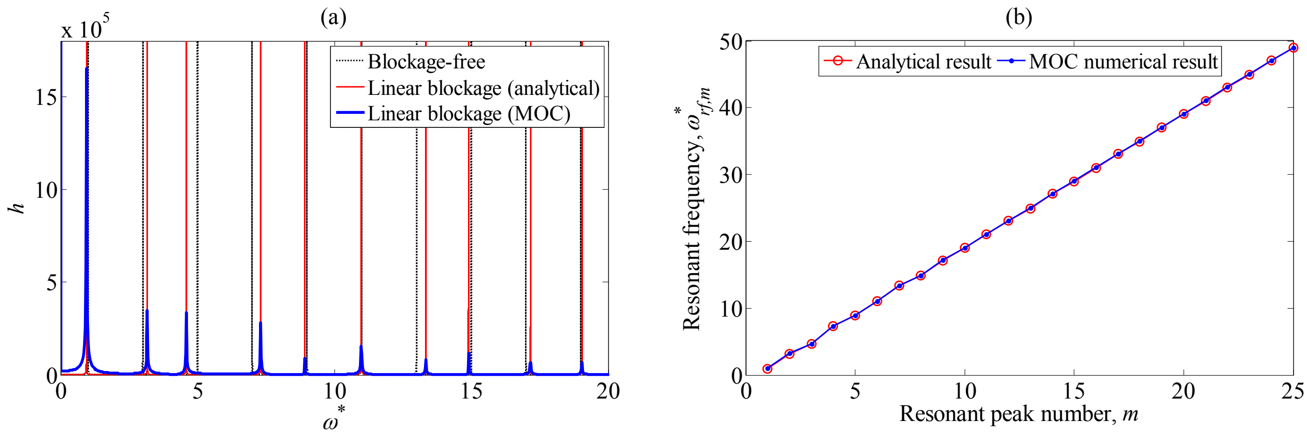

Figure 4. (a) Frequency responses for the intact pipeline and the pipeline with a linear blockage and (b) linear blockage case with first 25 resonant peaks from analytical and numerical results.

5 PRACTICAL APPLICATIONS

To study the potential influences of linear irregular blockages on the validity of the current TBBDM, three test cases, Test no. T1, T2 and T3, with different test parameters (Table 1), are investigated based on Eq. [32]. Note that Test no. T2 and T3, as shown in Figure 5, are pipelines with same volume of blockages in different shapes and Test no. T1 is the blockage-free case for convenient comparison.

Table 1. Parameters for three test cases.

Test no.	Blockage type	l_1 (m)	l_2 (m)	l_3 (m)	l_4 (m)	R (m)	C_1	C_2 (m)	a (m/s)
T1	blockage-free	300	100	100	500	0.25	0	0.25	1000
T2	uniform blockage	300	100	100	500	0.25	0	0.20	1000
T3	linear blockage	300	100	100	500	0.25	±1e-3	0.15	1000

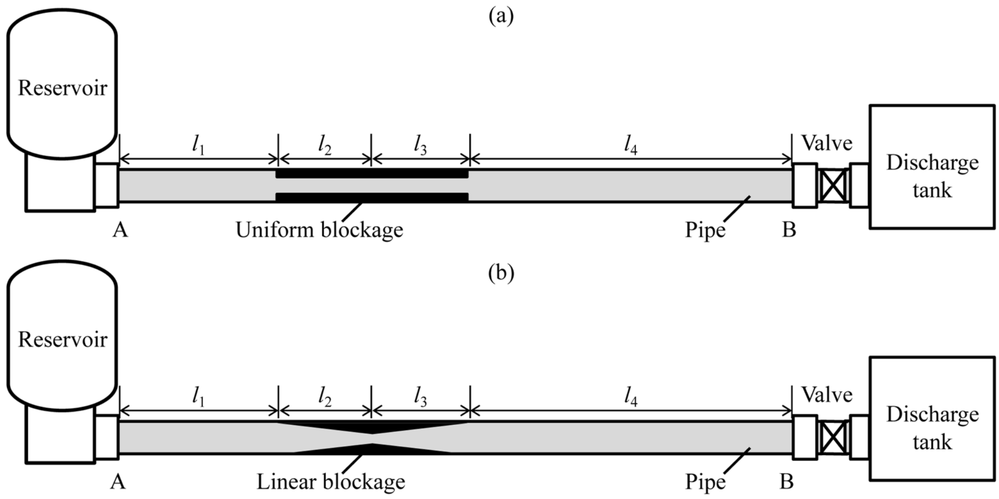

Figure 5. Sketch of a reservoir-pipe-valve test system (a) with uniform blockage and (b) with linear blockage.

The frequency response results for three test cases with low (0~20) and relative high (180~200) ω^* values are plotted in Figures 6a and 6b, respectively. The results in Figure 6a show that both linear and uniform blockages induce evident frequency shifts in the low ω^* value region. The frequency shift pattern caused by the linear irregular blockage is significantly different from that caused by the uniform blockage, even though the volume of two types of blockage is the same. However, in the relative high ω^* value region, as shown in Figure 6b, only the uniform blockage obviously alters the resonant frequencies and the resonant frequencies for linear irregular blockage almost remain the same with the original intact pipeline system.

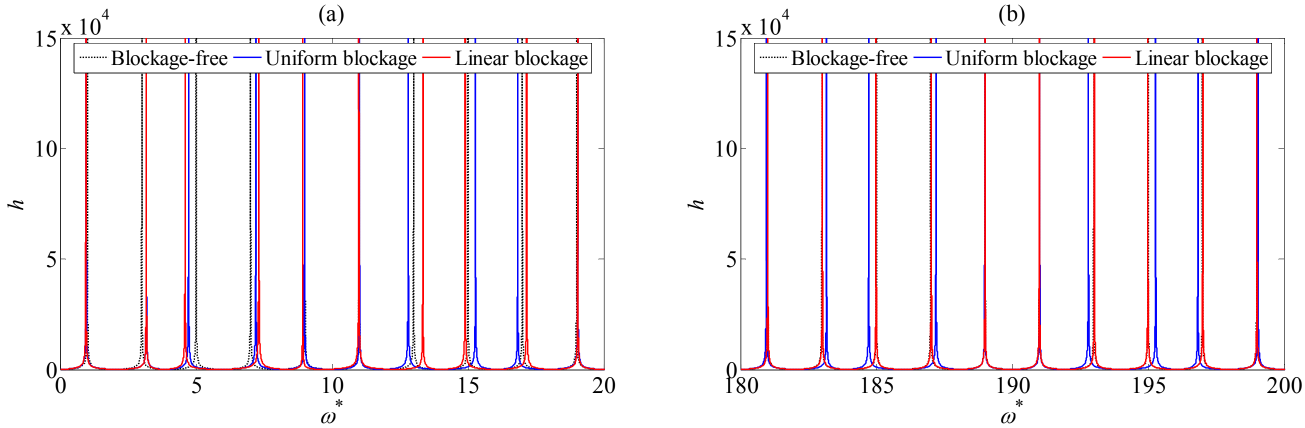

Figure 6. Frequency responses for the intact pipeline and the pipeline with a linear blockage in (a) the low frequency region and (b) the relative high frequency region.

To have an insight into the frequency shift patterns, in low and relative high ω* value regions, caused by linear and uniform blockages, the resonant peaks, m and corresponding resonant frequency shifts, δω*rf,m are extracted and plotted in Figure 7. The resonant frequency shift is defined as δω*rf,m = (ω*rf,m)blockage - (ω*rf,m)intact. It can be observed from Figure 7 that for both linear and uniform blockages, the magnitude of the frequency shift δω*rf,m varies with the peak number, m and fluctuates around zero. Moreover, in the low frequency region, as indicated in Figure 7a, the magnitude of frequency shifts caused by the linear irregular blockage and that caused by the uniform blockage are roughly in the same order. However, the results in Figure 7b show that in the relative high frequency region, the magnitude of frequency shifts caused by linear blockage is less significant than that caused by the uniform blockage. All these results indicate that the current TBBDM used for uniform extended blockage detection, which is based on the blockage-induced frequency shifts, might become inaccurate or invalid when it is applied to the detection of linear irregular blockage.

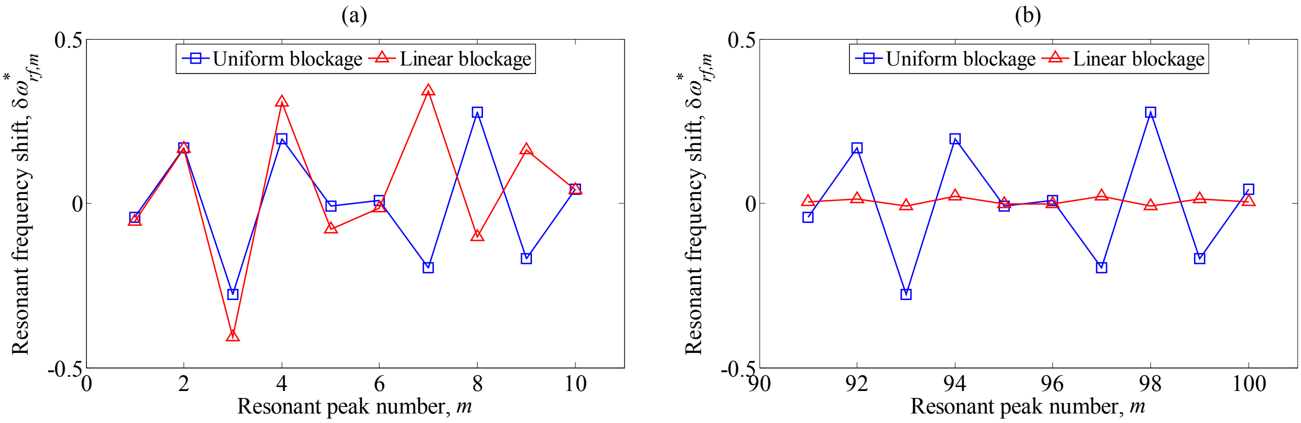

Figure 7. Resonant frequency shift patterns in (a) low frequency region and (b) relative high frequency region.

6 CONCLUSIONS

This study presents a theoretical analysis of the interaction between transient waves and different irregular blockages in water supply pipelines, by analytically solving the 1D wave equation for a conduit with varying pipe cross-sectional area. Based on these solutions, the analytical transfer matrix for the pipeline system with a linear irregular blockage is derived, which is then validated numerically. Finally, the influences of linear irregular blockage on the validity of the current TBBDM are investigated by the system frequency response method. The key conclusions are:

- Unlike the extended blockage in a regular and uniform shape, in which the wave amplitude keeps constant, the wave amplitude in irregular blockages changes as the wave propagates in the axial direction;
- In the blockage section, the linear irregular blockage does not induce a shift on the spatial frequency of the wave as provided in Eq. [25];
- The spatial frequency of the wave in the exponential irregular blockage is modified by the changing rate of the radius C1 from k2 to k2' as shown in Eq. [17];
- In a reservoir-pipe-valve system, the resonant frequency shift pattern caused by the linear irregular blockage is significantly different from that caused by the uniform blockage. This indicates that the current TBBDM may become inaccurate or invalid when it is applied to the detection of linear irregular blockages.

The results and findings promote the understanding of the influences of irregular blockages on transient waves in water supply pipelines. It may help to gain useful insights and implications for further validation and application of the current TBBDM into more practical UWSS, which will be conducted in the future study.

ACKNOWLEDGEMENTS

This paper was supported by the research grants from: (1) Hong Kong Polytechnic University (HKPU) under projects with numbers 1-ZVCD and 1-ZVGF; and (2) Hong Kong Research Grant Council (RGC) under the projects no. 25200616 and no. T21-602/15-R.

REFERENCES

Chaudhry, M.H. (2014). *Applied Hydraulic Transients*. Springer.

Duan, H.F., Lee, P.J. & Ghidaoui, M.S. (2014). Transient Wave-Blockage Interaction in Pressurized Water Pipelines. *Procedia Engineering*, 70, 573-582.

Duan, H.F., Lee, P.J., Ghidaoui, M.S. & Tung, Y.K. (2012). Extended Blockage Detection in Pipelines by Using The System Frequency Response Analysis. *Journal of Water Resources Planning and Management*, 138(1), 55-62.

Duan, H.F., Lee, P.J., Kashima, A., Lu, J., Ghidaoui, M.S. & Tung, Y.K. (2013). Extended Blockage Detection in Pipes Using The System Frequency Response: Analytical Analysis and Experimental Verification. *Journal of Hydraulic Engineering*, 139(7), 763-771.

Duan, H.F., Lee, P.J., Ghidaoui, M.S. & Tuck, J. (2014). Transient Wave-Blockage Interaction and Extended Blockage Detection in Elastic Water Pipelines. *Journal of fluids and structures*, 46, 2-16.

Duan, H.F., Lu, J., Kolyshkin, A. & Ghidaoui, M.S. (2011). The Effect of Random Inhomogeneities on Wave Propagation in Pipes. *Proceedings of the 34th IAHR Congress*, IAHR. 26 June-1 July 2011. Brisbane, Australia.

Ghidaoui, M.S., Zhao, M., McInnis, D.A. & Axworthy, D.H. (2005). A Review of Water Hammer Theory and Practice. *Applied Mechanics Reviews*, 58(1/6), 49.

Lee, P.J., Lambert, M.F., Simpson, A.R., Vítkovský, J.P. & Liggett, J. (2006). Experimental Verification of The Frequency Response Method for Pipeline Leak Detection. *Journal of Hydraulic Research*, 44(5), 693-707.

James, W. & Shahzad, A. (2003). Water Distribution Losses Caused by Encrustation and Biofouling: Theoretical Study Applied to Walkerton, ON. *Proceedings of the World Water & Environmental Resources Congress* 2003, ASCE. June 23-26, 2003. Philadelphia, Pennsylvania, United States.

Meniconi, S., Duan, H.F., Lee, P.J., Brunone, B., Ghidaoui, M.S. & Ferrante, M. (2013). Experimental Investigation of Coupled Frequency and Time-Domain Transient Test–Based Techniques for Partial Blockage Detection In Pipelines. *Journal of Hydraulic Engineering*, 139(10), 1033-1040.

Skudrzy, E. (1971). *The Foundations of Acoustics: Basic Mathematics and Basic* Acoustics. Springer-Verlag.

Stephens, M.L. (2008). Transient Response Analysis for Fault Detection and Pipeline Wall Condition Assessment In Field Water Transmission and Distribution Pipelines and Networks. *Ph.D. thesis*, Univ. of Adelaide, SA, Australia.

Wylie, E.B., Streeter, V.L. & Suo, L. (1993). *Fluid Transients in Systems (Vol. 1).* Prentice Hall Englewood Cliffs, NJ.

Proceedings of the 37th IAHR World Congress
August 13 – 18, 2017, Kuala Lumpur, Malaysia

SINGLE EXTENDED BLOCKAGE IDENTIFICATION USING A MODEL-BASED MATCHED-FIELD PROCESSING APPROACH

FEDI ZOUARI[(1)], XUN WANG[(2)], MOEZ LOUATI[(3)] & MOHAMED S. GHIDAOUI[(4)]

[(1, 2, 3, 4)] Department of Civil and Environmental Engineering, Hong Kong University of Science and Technology, Kowloon, Hong Kong
[(1)]zouari.fedi@gmail.com; [(2)]xunwang00@gmail.com; [(3)]mzlouati@gmail.com; [(4)]ghidaoui@ust.hk

ABSTRACT

A new transient-based approach for single blockage detection is proposed which requires two measurement stations at both ends of a single pipe system. The method uses the frequency response and gives satisfactory results using low frequency bandwidth. The first advantage of the proposed technique is to obtain the location and length of the blockage independently from the blockage's area. The second advantage is that the method uses information not only from the eigen-frequencies, but also from the whole frequency spectrum. This brings more accuracy, especially when the identification of the resonant frequencies and their corresponding mode number are not accurate. Moreover, the method has the ability of tolerating noise as long as it is Gaussian of zero-mean and has a well-known structure. Comparison with other blockage detection methods is given and the benefits and drawbacks of the proposed method are discussed.

Keywords: Blockage detection; transient flow; frequency response; matched-field processing; inverse problem.

1 INTRODUCTION

Extended blockages in water supply systems are ubiquitous and they cause many inefficiencies such as energy loss and increase in potential contamination and leaks. Unlike other defects in pipe, blockages are very difficult to detect as they do not have any external visible trace nor do they induce a detectable sound like leakages under steady state condition. However, researches showed that anomalies such as blockages can be detected if a transient response of a pipe system is measured (e.g. Duan et al., 2012; Meniconi et al., 2013; Louati, 2016; Ignarcio et al., 2016).

Similar inverse problems were addressed in different research fields, ranging from the identification of blockage in a sewage line (Tolstoy, 2010), and in the cooling system of nuclear reactors (Wu and Fricke, 1990) to the vocal tract shape reconstruction (Shroeder, 1967; Sondhi and Gopinath, 1970; Gopinath and Sondhi, 1970; DeSalis and Oldham, 2001) and the identification of conductivity in electrical lines (Bruckstein and Kailath, 1987).

In general, the methods for blockage detection or area reconstruction could be divided into two main categories: 1) methods that model the blockage as a step function, and therefore, the blockage is simply a pipe section with smaller diameter (see sketch in Fig. (1)), 2) other methods model the blockage with a smooth function of the longitudinal coordinate x. In both categories, the techniques/tools used for blockage detection are differentiated by whether the time domain or frequency domain signals are used. For example, in time domain wavelet analysis is applied by Meniconi et al. (2013) and reconstructive Method of Characteristics (or Layer pealing) by Gong et al. (2014). In frequency domain, Fourier decomposition and Ehrenfest theorem can be applied to write an explicit relation between the area of the pipe and its acoustic properties (e.g. Schroeder, 1967; Qunli and Fricke, 1990; DeSalis and Oldham, 2001) and recently, Duan et al. (2012) and Louati et al. (2017) combined the frequency response with the dispersion relation to determine the blockage location, length and size. So far, the frequency domain methods (Schroeder, 1967; Duan et al., 2012; Louati et al., 2017) rely on the accurate identification of several resonant frequencies and their corresponding mode number. In many practical situations, a limited number of resonant frequencies are available and their identification may be affected by the presence of noise.

In this work, a new model-based matched-field processing approach (MFP) is proposed for the detection of a single blockage in pipes. It relies on measuring the frequency response at both ends of a pipe and makes use of the transfer matrix method. In contrast to other methods in the literature, the proposed technique does not require the identification of the resonant and the anti-resonant frequencies and also tolerates the presence of noise. This approach is recently applied for leak detection in pipes by Wang and Ghidaoui (2017).

2 PROPOSED NEW METHOD FOR BLOCKAGE DETECTION

2.1 Theoretical framework

In most water supply application, the location, the length and the size of the blockage are the most critical information. Therefore, an idealized single blockage in a reservoir-pipe-valve system was considered as shown

  / ISSN 1562-6865 (Online) - ISSN 1063-7710 (Print)

in Fig. (1). The blockage had a length l_2 and an area $A_0 - \delta A$ and it was located at a distance l_1 from the reservoir. A_0 is the area of the intact pipe (before the formation of the blockage). Two measurement stations were setup at both ends of the pipe at distance $x_{m_1}$and $x_{m_2}$from the reservoir. The pipe flow was assumed frictionless and the wave speed a was assumed constant.

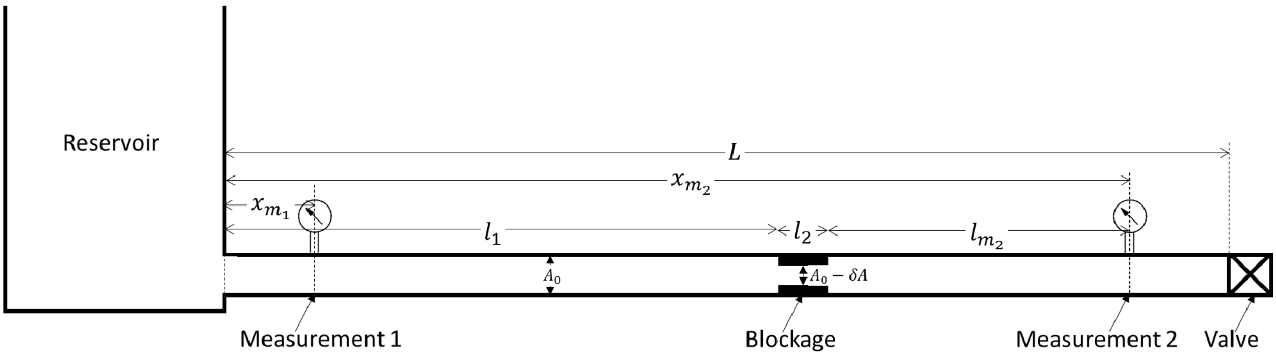

Figure 1. Pipe system layout and characteristic lengths.

In this case, for any l_1, l_2 and δA, the pressure head variations from the mean in the frequency domain at distance $x_{m_1}$and $x_{m_2}$from the reservoir ($h^c_{m_1}$ and $h^c_{m_2}$) are given from the Transfer Matrix method (Chaudhry, 2013)

$$h^c_{m_1} = -\frac{Z_0 \sin(kx_{m1})\, q_v(\omega)}{\cos(kL) + \frac{\delta A}{A_0}\cos(kl_1)\sin(kl_2)\sin(kl_3) + \frac{\delta A}{A_0 - \delta A}\sin(kl_1)\sin(kl_2)\cos(kl_3)} \qquad [1]$$

$$h^c_{m_2} = \frac{h^c_{m_1}}{\sin(kx_{m1})}\left(\sin(kx_{m2}) + \frac{\delta A}{A_0}\sin(kl_1)\sin(kl_2)\sin(kl_{m_2}) + \frac{\delta A}{A_0 - \delta A}\cos(kl_1)\sin(kl_2)\cos(kl_{m_2})\right) \qquad [2]$$

where the superscript "c" in $h^c_{m_i}$ denotes computation; $Z_0 = \mathrm{i}\; a/gA_0$ is the characteristic impedance of the intact conduit with g is the gravitational constant; $k = \omega/a$ is the wave number; $q_v(\omega)$ is a known discharge variation at the valve used to generate the transient. From Eq. (1) and (2) it can be shown that

$$-\frac{Z_0 q_v(\omega)}{h^c_{m_1}}\sin(kx_{m1}) - \cos(kL) = \frac{\delta A}{A_0}\cos(kl_1)\sin(kl_2)\sin(kl_3) + \frac{\delta A}{A_0 - \delta A}\sin(kl_1)\sin(kl_2)\cos(kl_3) \qquad [3]$$

$$\frac{h^c_{m_2}}{h^c_{m_1}}\, sin(kx_{m1}) - \sin(kx_{m_2}) = \frac{\delta A}{A_0}\sin(kl_1)\sin(kl_2)\sin(kl_{m_2}) + \frac{\delta A}{A_0 - \delta A}\cos(kl_1)\sin(kl_2)\cos(kl_{m_2}) \qquad [4]$$

With regards to blockage detection, the quantities on the left hand side (LHS) of Eqs (3) and (4) are related to the known “measured” variables; whereas the quantities on the right hand side (RHS) are related to the unknown variables. Hence, the quantities on the LHS of Eqs (3) and (4) will be referred as the “measured” synthetic signals $S^c_{m_1}$and $S^c_{m_2}$.

$$S^c_{m_1}(\omega) = -\frac{Z_0 q_v(\omega)}{h^c_{m_1}}\sin(kx_{m1}) - \cos(kL) \quad ; \quad S^c_{m_2}(\omega) = \frac{h^c_{m_2}}{h^c_{m_1}}\, sin(kx_{m1}) - \sin(kx_{m_2}) \qquad [5]$$

The main advantage of using these synthetic signals $S_{m_1}$and S_{m_2} rather than directly using the measured pressure head $h_{m_1}$and h_{m_2} is that these signals (S_{m_i}) can be written in a “quasi-linear” relation with respect to the change in area (i.e. when $l_1$and l_2 are fixed). This will allow the length and the location of the blockage to be estimated independently from its size. That is the three dimensional problem reduces to a two dimensional one.

In practice, the measured pressure head h_{m_i} will not be exactly equal to the predicted pressure head from the model (Eqs. (1) and (2)), it will rather contain noise such as environmental noise, measurement noise and many other types of noise. Therefore, the “measured” synthetic signal are given by $S_{m_i}(\omega) = S^c_{m_i}(\omega) + \text{noise}$ $i \in \{1,2\}$.

2.2 Model-based matched-field processing approach (MFP)

Given the measurements $S_{m_1}(\omega)$ and $S_{m_2}(\omega)$, for a given set of frequencies $\omega_1, \omega_2, \dots, \omega_N$, Eqs (3) and (4) can be written in a compact form as

$$\boldsymbol{S}_{\boldsymbol{m}_i} = \boldsymbol{G}_{\boldsymbol{m}_i}(l_1, l_2)\boldsymbol{\alpha}(\delta A) + \mathbf{n} \quad i = 1,2 \qquad [6]$$

where $\boldsymbol{S}_{\boldsymbol{m}_i} = \left(S_{m_i}(\omega_1), S_{m_i}(\omega_2), \dots, S_{m_i}(\omega_N)\right)^T$; $\boldsymbol{\alpha}(\delta A) = (\delta A/A_0, \delta A/(A_0 - \delta A))^T$; in which the superscript "*T*" denotes transpose operator; $\boldsymbol{G}_{\boldsymbol{m}_1}$ and $\boldsymbol{G}_{\boldsymbol{m}_2}$ are 2-by-N matrices where the elements of their j^{th} row are $(\boldsymbol{G}_{\boldsymbol{m}_1})_{\boldsymbol{1},\boldsymbol{j}} = \cos(k_j l_1)\sin(k_j l_2)\sin(k_j l_3)$; $(\boldsymbol{G}_{\boldsymbol{m}_1})_{\boldsymbol{2},\boldsymbol{j}} = \sin(k_j l_1)\sin(k_j l_2)\cos(k_j l_3)$; $(\boldsymbol{G}_{\boldsymbol{m}_2})_{\boldsymbol{1},\boldsymbol{j}} = \sin(kl_1)\sin(kl_2)\sin(kl_{m_2})$; $(\boldsymbol{G}_{\boldsymbol{m}_2})_{\boldsymbol{2},\boldsymbol{j}} = \cos(kl_1)\sin(kl_2)\cos(kl_{m_2})$; and $\mathbf{n}$ is the added noise vector.

If the noise $\mathbf{n}$ is zero-mean Gaussian white noise, then the blockage parameters can be found by minimizing the $\boldsymbol{l_2}$-norm of the difference between the "measured" signal $\boldsymbol{S}_{\boldsymbol{m}_i}$and the model $\boldsymbol{G}_{\boldsymbol{m}_i}(l_1, l_2)\boldsymbol{\alpha}(\delta A)$

$$\{\widehat{l_1}, \widehat{l_2}, \widehat{\delta A}\} = \underset{l_1, l_2, \delta A}{\arg\min} \left\|\boldsymbol{S}_{\boldsymbol{m}_i} - \boldsymbol{G}_{\boldsymbol{m}_i}(l_1, l_2)\boldsymbol{\alpha}(\delta A)\right\|^2 \qquad [7]$$

If the noise $\mathbf{n}$ is non-white Gaussian of a well-known structure (known covariance matrix) then a filter can be applied to the signals $\boldsymbol{S}_{\boldsymbol{m}_i}$and to the model $\boldsymbol{G}_{\boldsymbol{m}_i}(l_1, l_2)\boldsymbol{\alpha}(\delta A)$ to whiten the noise, and thereafter the same method can be used (Wang and Ghidaoui, 2017).

Because of the quasi-linearity between the area of the blockage and the "measured" signal, an estimate of $\boldsymbol{\alpha}(\delta A)$ which has the minimum mean square error (least square solution) is given by (for any $l_1$and l_2)

$$\widehat{\boldsymbol{\alpha}} = \left(\boldsymbol{G}_{\boldsymbol{m}_i}^{\boldsymbol{H}}\boldsymbol{G}_{\boldsymbol{m}_i}\right)^{-1}\boldsymbol{G}_{\boldsymbol{m}_i}^{\boldsymbol{H}}\boldsymbol{S}_{\boldsymbol{m}_i} \qquad [8]$$

where the superscript "*H*" denotes the conjugate transpose. Replacing $\widehat{\boldsymbol{\alpha}}$ into Eq. (7) leads to

$$\{\widehat{l_1}, \widehat{l_2}\} = \underset{l_1, l_2}{\arg\max}\, \boldsymbol{B}_{\boldsymbol{m}_i}(l_1, l_2) \qquad [9]$$

where $\boldsymbol{B}_{\boldsymbol{m}_i} = \boldsymbol{S}_{\boldsymbol{m}_i}^{\boldsymbol{H}}\boldsymbol{G}_{\boldsymbol{m}_i}\left(\boldsymbol{G}_{\boldsymbol{m}_i}^{\boldsymbol{H}}\boldsymbol{G}_{\boldsymbol{m}_i}\right)^{-1}\boldsymbol{G}_{\boldsymbol{m}_i}^{\boldsymbol{H}}\boldsymbol{S}_{\boldsymbol{m}_i}$.

Using this approach, the number of variables in the optimization problem in Eq. (7) reduced from three variables to two variables in Eq. (9). In this case, the objective function $\boldsymbol{B}_{\boldsymbol{m}_i}$ can be evaluated and plotted for all possible l_1 and l_2, and an estimate of the blockage length and location can be easily found by enumeration. This is one of the advantages of the proposed method comparing to other methods in the literature where the blockage identification involves an optimization problem with at least three variables (Duan et al., 2012; Ignarcio et al., 2016).

Once the blockage's length and location are estimated, the blockage area can be easily found by substituting the values of the estimated l_1 and l_2 into Eq. (8).

Note that the objective function $\boldsymbol{B}_{\boldsymbol{m}_2}$has a symmetry line related to the measurement location x_{m_2} given by $\boldsymbol{B}_{\boldsymbol{m}_2}(l_1, l_2) = \boldsymbol{B}_{\boldsymbol{m}_2}(x_{m_2} - l_2 - l_1, l_2)$. Whereas $\boldsymbol{B}_{\boldsymbol{m}_1}$ has a fixed symmetry line independent from the measurement location x_{m_1} given by $\boldsymbol{B}_{\boldsymbol{m}_1}(l_1, l_2) = \boldsymbol{B}_{\boldsymbol{m}_1}(L - l_2 - l_1, l_2)$. Therefore to avoid multiple solutions of l_1 and l_2 the measurement location from the valve side should not be at the valve (i.e. $x_{m_2} \neq L$). Also note that the objective functions $\boldsymbol{B}_{\boldsymbol{m}_1}$ and $\boldsymbol{B}_{\boldsymbol{m}_2}$ are not defined at the trivial solutions $l_1 = 0$, $l_2 = 0$, $l_1 + l_2 = x_{m_2}$ and $l_1 + l_2 = L$.

The procedure of the blockage identification using this approach can be summarized in the following algorithm.

Algorithm 1: Blockage identification using MFP
1: Use $\boldsymbol{h}_{\boldsymbol{m}_1}$and $\boldsymbol{h}_{\boldsymbol{m}_2}$at known locations x_{m1} and $x_{m_2} \neq L$ and $\boldsymbol{q}_{\boldsymbol{v}}$ to construct the signals $\boldsymbol{S}_{\boldsymbol{m}_1}$and $\boldsymbol{S}_{\boldsymbol{m}_2}$ (Eq. (5))
2: Construct the matrices $\boldsymbol{G}_{\boldsymbol{m}_i}$ corresponding to each signal $\boldsymbol{S}_{\boldsymbol{m}_i}$ $i \in \{1,2\}$
3: Compute the objective functions $\boldsymbol{B}_{\boldsymbol{m}_i}$ at every possible blockage location and length (l_1, l_2)
4: Find an estimate ($\widehat{l_1}$ and $\widehat{l_2}$) which correspond to the maximum of the objective function $\boldsymbol{B}_{\boldsymbol{m}_1} + \boldsymbol{B}_{\boldsymbol{m}_2}$
5: Compute two estimates of $\widehat{\boldsymbol{\alpha}}$ by substituting ($\widehat{l_1}$ and $\widehat{l_2}$) found into Eq. (8) using $\boldsymbol{G}_{\boldsymbol{m}_1}$ and $\boldsymbol{G}_{\boldsymbol{m}_2}$
6: Compute the estimates of $\widehat{\delta A}$ by $\widehat{\delta A} = A_0\widehat{\alpha_1}$ and by $\widehat{\delta A} = A_0\widehat{\alpha_2}/(1 + \widehat{\alpha_2})$

3 RESULTS AND DISCUSSIONS

To validate the proposed method, and to illustrate its advantages and limitations, a numerical case study was considered. The numerical setup consists of a reservoir pipe valve system containing a single blockage as shown in Fig. (1). The lengths of different pipe sections are $L = 2000$ m, $l_1 = 700$ m, $l_2 = 200$ m, $x_{m_1} = 50$ m, $x_{m_2} = 1950$ m. The intact pipe area is $A_0 = 0.1963\,m^2$ and the change of area due to the blockage is $\delta A = 0.1257$ m2. The wave speed was assumed to be constant $a = 1000$ m/s and the pipe was assumed to be frictionless. The pressure head response $h_{m_1}(\omega)$ and $h_{m_2}(\omega)$ at the measurement locations ($x_{m_1}$and x_{m_2}) were computed using the transfer matrix method (i.e. using Eq. (1) and (2)), where the transient was generated by an impulse (i.e. $q_v(\omega) = 1$). The frequency domain was sampled from 0 to $\omega_N = 16\omega_0$ with a step size $\Delta\omega = \omega_0/100$, where ω_0 is the fundamental frequency of the intact system $\omega_0 = 2\pi a/4L$.

Algorithm (1) was applied to compute the objective function $\boldsymbol{B}_{m_1} + \boldsymbol{B}_{m_2}$ at every point in the feasible domain discretized with $\Delta x = 2$ m. Fig. (2) shows a color plot of the objective function together with the location of the maximum. The results shows that the objective function $\boldsymbol{B}_{m_1} + \boldsymbol{B}_{m_2}$ has a single maximum which corresponds to the blockage's location and length estimates ($\widehat{l_1} = 700$ m and $\widehat{l_2} = 200$ m). This is how the method provides the blockage length and location. Regarding, the blockage area, two estimates of the change in pipe area were obtained from Eq. (8) for each signal $\boldsymbol{S}_{m_1}$ and $\boldsymbol{S}_{m_2}$. The estimates of δA are $\widehat{\delta A} = \{0.1256,\ -0.0561,\ 0.1254,\ 0.1256\}$ m^2. Note that one of the estimated values was negative, which might represent a pipe wall thinning. This negative value was ignored since it was assumed that there was only positive change in area (blockage). Hence the estimate of the area was $\widehat{\delta A} = 0.1256$ m^2.

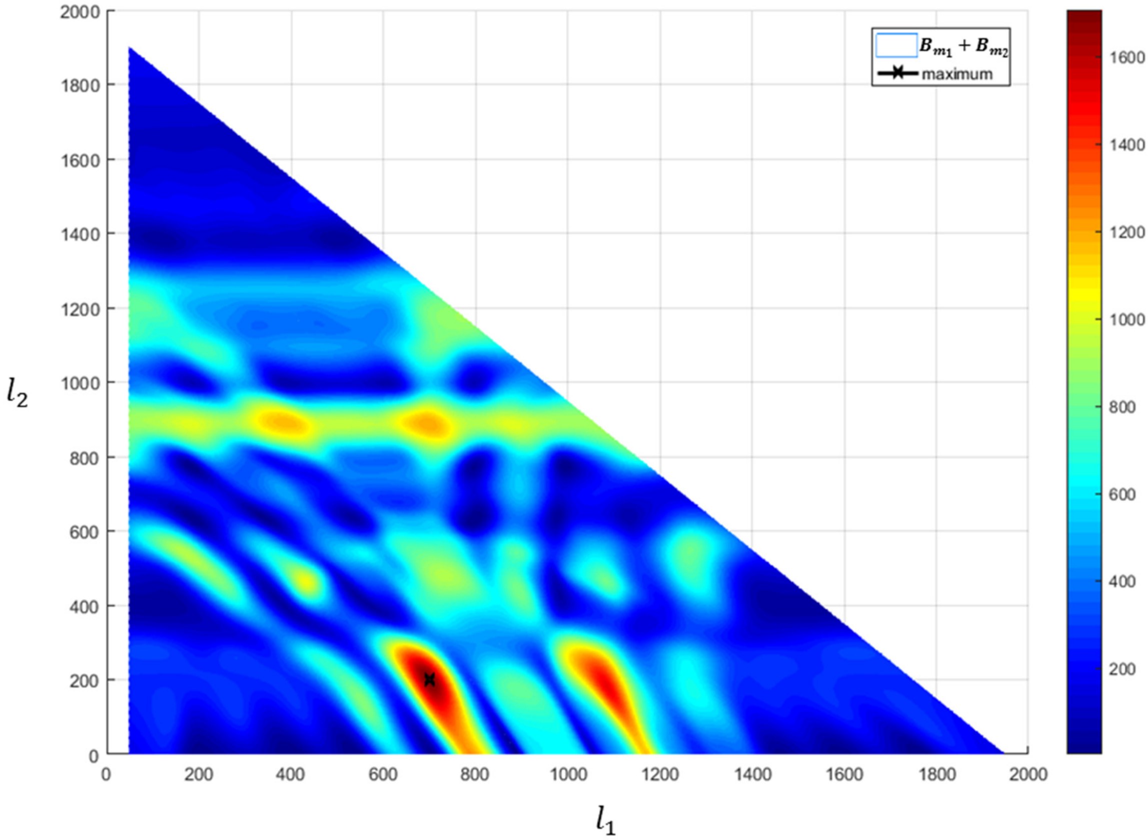

Figure 2. Objective function $\boldsymbol{B}_{m_1} + \boldsymbol{B}_{m_2}$and location of the maximum.

The above numerical example illustrates how the method can be applied to identify a single blockage in a pipe. This proposed method differs from most of the frequency domain methods for blockage detection (DeSalis and Oldham, 2001; Duan et al., 2012; Louati, 2016) by the fact that it uses the frequency response of any set of frequencies rather than using only the resonant and the anti-resonant frequencies locations. Using the frequency response at all frequencies gives more accuracy in the blockage identification especially in the cases (i) presence of noise (ii) inaccurate identification of the eigen-frequencies. These two advantages will be discussed in what follows.

3.1 Presence of noise

To illustrate the advantage of using the response of frequencies other than the resonant and anti-resonant frequencies, the results for the blockage identification were compared in the presence of noise. A zero-mean

Gaussian white noise (the noise power was the same at all frequencies) of different values of Signal-to-Noise Ratio (SNR) was added to the deterministic computed signals $\boldsymbol{S}^c_{\boldsymbol{m}_1}$ and $\boldsymbol{S}^c_{\boldsymbol{m}_2}$. The SNR is herein defined in decibel (dB) as the ratio between the power of the signals $\boldsymbol{S}^c_{\boldsymbol{m}_i}$ (i.e. $\left|\boldsymbol{S}^c_{\boldsymbol{m}_i}\right|^2$) to the power of the noise (i.e. the variance of the random variable noise σ^2). That is SNR $= 20\log_{10}\left|\boldsymbol{S}^c_{\boldsymbol{m}_i}\right|/\sigma$, where $\left|\boldsymbol{S}^c_{\boldsymbol{m}_i}\right|$ is the average of the magnitude of the signal $S^c_{m_i}$ at different frequencies.

A set of numerical simulations were conducted in which two cases were considered, the first one was the case where "all frequencies" were used for blockage identification (i.e. frequency response for the frequencies in the range $[0.01\,\omega_0, 16\omega_0]$ with a step size $0.01\omega_0$). Whereas, the second one was the case where only the "resonant and anti-resonant frequencies" were used (i.e. 8 resonant and 8 anti-resonant frequencies contained in the interval $[0.01\,\omega_0, 16\omega_0]$).

The simulation was repeated 30 times for different values of SNR from -10dB to 40dB and Algorithm (1) was again used for blockage identification. The ensemble average and the standard deviation of the estimation error in the two cases are summarized in Fig. (3). Here, the estimation error is defined by

$$\epsilon = \frac{1}{2}\left(\frac{\left|\widehat{l_1} - l_1\right| + \left|\widehat{l_2} - l_2\right|}{L} + \frac{\sum\left|\widehat{\delta A} - \delta A\right|}{nA_0}\right) \quad [10]$$

in which n is the number of feasible estimates of the change in area $\widehat{\delta A}$. The estimates $\widehat{l_1}$ and $\widehat{l_2}$ are found by enumeration of the entire feasible region with a discretization $\Delta x = 10$ m.

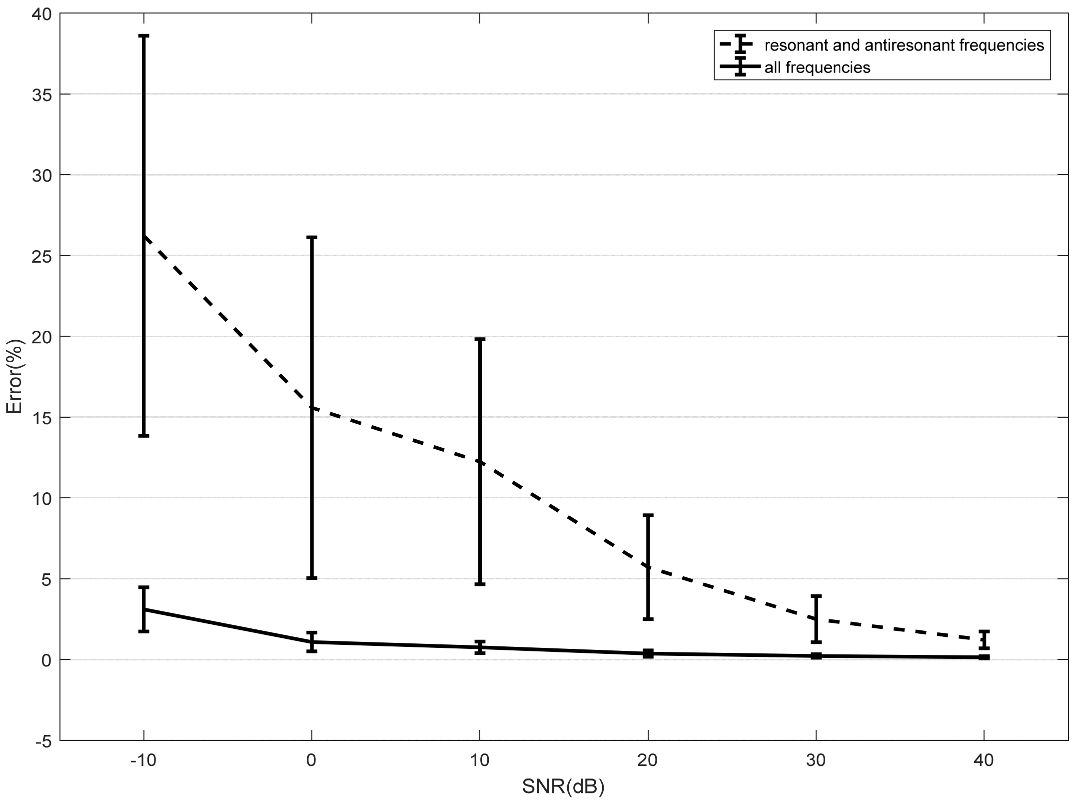

Figure 3. Error bar of the estimation error with increasing SNR.

Fig. (3) shows that the estimation error is about 5 times lower when the whole frequency bandwidth was used than for the case where only the first 8 resonant and anti-resonant frequencies are used. This shows that using more frequencies increase the accuracy of the blockage detection results. This is because, for the case of zero-mean Gaussian white noise, the matched-field processing (MFP) approach has the ability of identifying the blockage parameters which maximize the SNR (Wang and Ghidaoui, 2017). In other words, the blockage parameters are estimated such that the corresponding signal generated from the model (i.e. $S^c_{m_i}$) fits the estimated mean value of the noisy measured response (i.e. S_{m_i}). However, the mean was only well estimated if a large enough sample size was used for its estimation. Therefore, in cases where only the resonant and anti-resonant frequencies were used for blockage identification, the mean value of the "measured" signal was not well estimated because of the lack of "measurement" data. However, for the case where more frequencies

$(0.01\omega_0{:}\,0.01\omega_0{:}\,16\omega_0)$ were used for the estimation of the blockage parameters, the mean value of the measured response can be better estimated and therefore, more accurate results of the blockage parameters are obtained.

Note that, in this case the noise is added to the amplitude of the frequency response. Therefore, blockage detection methods which do not use the amplitude of the frequency response, (e.g. Duan et al., 2012; DeSalis et al., 2000), are not directly affected by the presence of such type of noise. However, the presence of noise can make the identification of the eigen-frequencies inaccurate. In this case, MFP method has advantage comparing to the methods based on the eigen-frequencies.

3.2 Inaccurate identification of the eigen-frequencies

There are several reasons which can make the identification of the resonant and the anti-resonant frequencies inaccurate, for instance, the measurement of the frequency response with a large frequency step. In this case, methods based on the eigen-frequencies identification become less accurate. However, since the MFP method does not rely on the identification of the resonant and anti-resonant frequencies. It can give more accurate results. To illustrate this, consider the same numerical example given above, the pressure heads h_{m_1} and $h_{m_2}$are simulated using the transfer matrix method (i.e. using Eqs (1) and (2)) in the frequency range $(0{:}\,4\omega_0)$ with a frequency step size $\Delta\omega = \omega_0/15$. The resonant frequencies ω_r and the anti-resonant frequencies ω_{ar} are estimated by a linear interpolation and are found to be $\omega_r = \{0.9181,\ 3.1401\}\omega_0$ and $\omega_{ar} = \{2.0825,\ 3.7208\}\omega_0$.

Under these conditions, the blockage is identified using the MFP method and results are compared with two other methods which only use the resonant and the anti-resonant frequencies. The first method used for comparison, estimates the blockage characteristics using a minimum error in the dispersion relation (MEDR) approach (Duan et al., 2012). The main advantage of this method is that it does not require the knowledge of the input signal (i.e. q_v) as it only uses the eigen-frequencies. However, this method relies on the accurate identification of the eigen-frequencies and involves an optimization problem with at least three variables. The second method used for comparison, uses an explicit area function based on the perturbation method (AFPM) (DeSalis and Oldham, 2001). The main advantages of this method comes from the fact that it does not assume the number of blockages and is independent from the type of excitation (i.e. q_v). However, the method assumes the change in area to be small. Moreover, using this method requires a large number of eigen-frequencies to guarantee an accurate area reconstruction.

The comparison between the results of the blockage identification methods in the case of inaccurate identification of the eigen-frequencies is shown in Fig. (4).

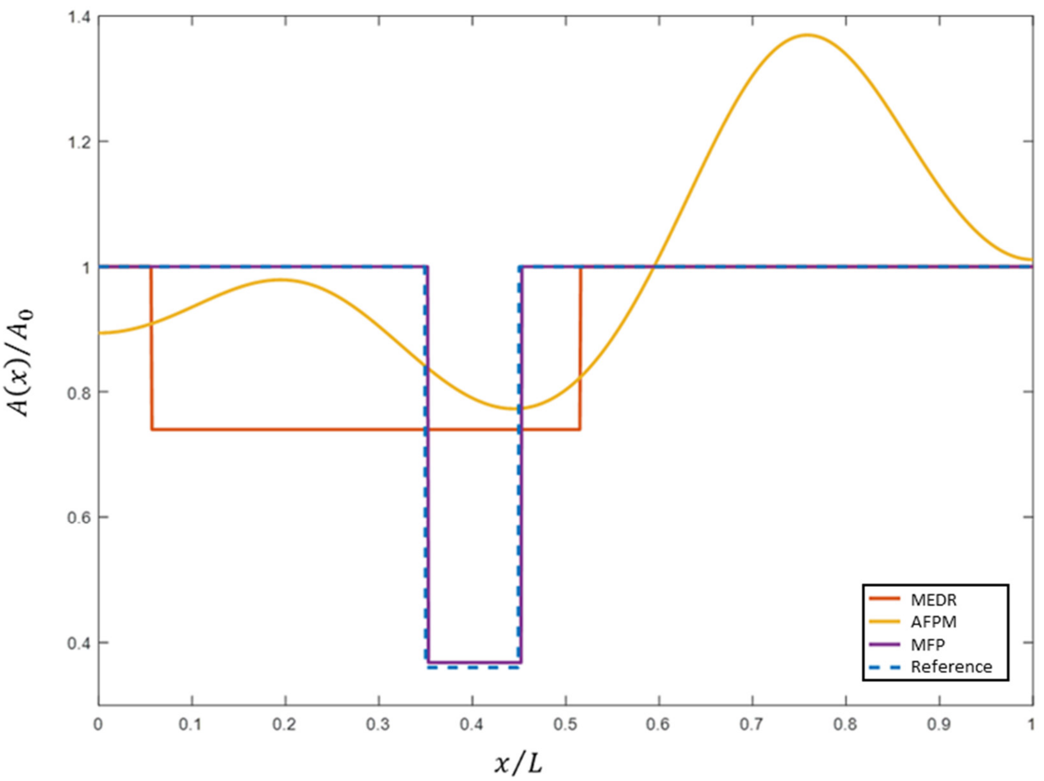

Figure 4. Comparison of the Matched-field processing with other methods in the literature.

Fig. (4) shows that the MFP method has more accurate result than the other two methods. The results found using the AFPM (DeSalis and Oldham, 2001) shows large discrepancy between the reconstructed cross-sectional area and the reference pipe's area. This is because only 3 resonant and 3 anti-resonant frequencies are used for the area reconstruction. Furthermore, the results of MEDR method (Duan et al., 2012) shows a non-accurate prediction of the blockage location and length. This is because the method is sensitive to the inaccuracy of the resonant and anti-resonant frequency identification (Duan, 2015). In contrast, the estimate of the blockage parameters was more accurate using the MFP method, this is because MFP has the ability of using frequencies other than the eigen-frequencies.

Despite the advantages of using MFP for blockage parameters estimation, this method has some limitations. The first limitation is the method requires a relatively accurate measurement of the frequency response in at least two measurement locations. It also requires a good knowledge of the input and of the boundary conditions. The second limitation is that the general form of the blockage size $\hat{\boldsymbol{\alpha}}$ used in this method (Eq. (8)), to solve for the blockage location and length independently from the blockage size, does not necessarily satisfy the feasibility condition. This is because the least square solution does not necessarily satisfy the condition $A_0\widehat{\alpha_1} = A_0\widehat{\alpha_2}/(1+\widehat{\alpha_2})$, and this is the reason why more than one estimate for the area is obtained by this method. In progress research is conducted to solve these limitations.

4 CONCLUSIONS

A new method for blockage detection is proposed. The method has the advantage of using information not only from the resonant frequencies but also from other frequencies, this is a key advantage especially when the signal is contaminated with a zero-mean Gaussian noise, and when the identification of eigen-frequencies is not accurate. The proposed MFP-based method solves for the location and the length of the blockage independently from the blockage's area. This gives the advantage of visualizing the overall objective function for all possible blockage parameters which cannot be achieved by other methods. However, an accurate knowledge of the input and the boundary conditions is required for the robustness of the proposed model-based MFP method.

ACKNOWLEDGEMENTS

This study is supported by the Hong Kong Research Grant Council (project T21-602/15R) and by the Postgraduate Studentship.

REFERENCES

Bruckstein, A. M. & Kailath, T. (1987). Inverse Scattering for Discrete Transmission-Line Models. *SIAM Review*, 29(3), 359-389.

Chaudhry, M. H. (2014). *Applied Hydraulic Transients*. Springer-Verlag New York.

DeSalis, M. & Oldham, D. (2001). The Development of a Rapid Single Spectrum Method for Determining the Blockage Characteristics of a Finite Length Duct. *Journal of Sound and Vibration*, 243(4), 625-640.

Duan, H. F., Lee, P. J., Ghidaoui, M. S. & Tung, Y.-K. (2012). Extended Blockage Detection in Pipelines by Using the System Frequency Response Analysis. *Journal of Water Resources Planning and Management*, 138(1), 55-62.

Duan, H. F. (2015). Sensitivity Analysis of a Transient-Based Frequency Domain Method for Extended Blockage Detection in Water Pipeline Systems. *Journal of Water Resources Planning and Management*, 142(4), 04015073.

Gong, J., Lambert, M.F., Simpson, A.R. & A.C. Zecchin, (2014). Detection of Localized Deterioration Distributed Along Single Pipelines by Reconstructive MOC Analysis. *Journal of Hydraulic Engineering*, 140(2), 190-198.

Gopinath, B., & Sondhi, M. M. (1970). Determination of the Shape of the Human Vocal Tract from Acoustical Measurements. *Bell System Technical Journal*, 49(6), 1195-1214.

Ignacio S. Rubio, Gildas B., and Didier G., (2016). Blockage and Leak Detection and Location in Pipelines Using Frequency Response Optimization. *Journal of Hydraulic Engineering*, 143(1).

Louati, M. (2016). In-Depth Study of Plane Wave-Blockage Interaction and Analysis of High Frequency Waves Behaviour in Water-Filled Pipe Systems. *PhD Thesis*. HKUST.

Louati M., Meniconi S., Ghidaoui M.S. & Brunone B. (2017). Experimental Study of The Eigenfrequency Shift Mechanism in Blocked Pipe System. *Journal of Hydraulic Engineering*. Accepted/In production.

Meniconi, S., Duan, H. F., Lee, P. J., Brunone, B., Ghidaoui, M. S. & Ferrante, M. (2013). Experimental Investigation of Coupled Frequency and Time-Domain Transient Test-Based Techniques for Partial Blockage Detection in Pipelines. *Journal of hydraulic engineering*, 139(10), 1033-1040.

Qunli, W. & Fricke, F. (1990). Determination of Blocking Locations and Cross-sectional Area in a Duct by Eigenfrequency Shifts. *The Journal of the Acoustical Society of America*, 87(1), 67-75.

Schroeder, M. R. (1967). Determination of the Geometry of the Human Vocal Tract by Acoustic Measurements. *The Journal of the Acoustical Society of America*, 41(4B), 1002-1010.

Sondhi, M. M. & Gopinath, B. (1971). Determination of Vocal-Tract Shape from Impulse Response at the Lips. *The Journal of the Acoustical Society of America*, 49(6B), 1867-1873.

Tolstoy, A. I. (2010). Waveguide Monitoring (such as sewer pipes or ocean zones) via Matched Field Processing. *The Journal of the Acoustical Society of America*, 128(1), 190-194.

Wang, X. & Ghidaoui, M. S. (2017). Pipeline Leak Detection Using the Matched-Field Processing Method. *Journal of hydraulic engineering*. Submitted.

Proceedings of the 37th IAHR World Congress
August 13 – 18, 2017, Kuala Lumpur, Malaysia

TIME DOMAIN INVERSE TRANSIENT ANALYSIS FOR PIPELINE LEAK DETECTION IN A NOISY ENVIRONMENT

ALIREZA KERAMAT[1], MOHAMED S. GHIDAOUI[2] & XUN WANG[3]

[1,2,3] Department of Civil and Environmental Engineering, Hong Kong University of Science and Technology, Hong Kong, China,
keramat@ust.hk

ABSTRACT

This paper addresses leak detection in the presence of measurement noise using inverse transient analysis in the time domain. The unknown leak parameters are determined by optimizing a merit function, which fits the numerically modeled pressures to measured pressures. As a result of measurement noise, the estimated parameters may correspond to some fictitious leaks whose computed pressure head best matches the noisy measurement not leak reflections. This issue is demonstrated in this research and a merit function to decline it is suggested. It is based on maximizing the signal-to-noise ratio (SNR), which is usually termed as Matched Filter in literature. This function is then compared with the conventional least square objective function and its properties subject to noise are assessed. It is found that the performance of each merit function mostly depends on the variance of noise and the system properties, which may change from case to case. It is advised to use both merit functions for localization separately and then the more reliable result corresponds to that of the objective function with lower variance.

Keywords: Leak detection; inverse problem; water hammer; noise; matched filter.

1 INTRODUCTION

Rapid excitation of fluid flow in pipe networks and collection of the resulting transient pressure response at some points in the system is widely established as a tool for leak detection in fluid-filled pipes (Colombo and Karney, 2009). Many methodologies and tools, such as leak reflection method, inverse transient analysis (ITA), impulse response analysis, transient damping method and frequency domain response analysis have been developed for solving various types of leak detection problems in recent years (Colombo and Karney, 2009).
First introduced by Liggett and Chen (1994), ITA aims at finding properties of a pipe system by means of a transient flow data. In the context of leak detection in the time domain, the method assumes that each computational node is a potential leak point. The identification then proceeds by minimizing a merit function of the measured and computed pressure time signal, which is found by a transient solver. In fact, any inverse solution should be tested for the presence of data error, such as random noise in measurements and uncertain input parameters. In the context of leak detection in conjunction with measurement noise, studies based on signal processing techniques can be addressed. Gao et al. (2005) used the cross-correlation technique to estimate time delay between measurements for leak localization. Vítkovský et al. (2007) proposed the model parsimony approach to limit the number of unknown leak candidates in the time-domain ITA. They introduced a penalty function in terms of the number of model parameters in the merit function. Guo et al. (2016) applied the empirical mode decomposition to decompose measurements into intrinsic mode functions, which in turn are used for noise cancellation. This leads to propose an adaptive time delay estimate to determine the location of a leakage in the pipe system. Ferrante et al. (2007) assessed the ability of the wavelet analysis to recognize small step variation (corresponding to small leaks) in the collected pressure signal blurred with noise. Most recently, Wang and Ghidaoui (2017) used matched field processing in the frequency domain for leak detection in the presence of measurement noise and uncertain wave speed. Although there are a couple of researches to address leak detection in a noisy environment using the other methods, the conventional method-of-characteristics-based ITA and its potential drawbacks has received less attention. The ITA in the time domain for leak detection usually employs too many decision parameters because all computational points are treated as potential leaks in the model. A large number of design parameters promote a strong alikeness between simulated pressures so that optimization procedure may arrive at non-unique optimum parameters (leak size and location). As a result, in the presence of measurement noise and when decision parameters are too many, the optimum solution may be affected by noise and provides wrong localization. In this research, to address this problem and to limit the noise effects in the localization, a Matched Filter approach is applied in the context of time-domain ITA.

  / ISSN 1562-6865 (Online) - ISSN 1063-7710 (Print)

2 LEAK DETECTION IN A NOISY ENVIRONMENT

2.1 Mathematical model

Let $h_m(t)$ defines a measured pressure at time, t at location, x_m in a pipeline, $h(t)$ defines the corresponding true model output and x_{Li}, A_{ei} denote location and effective area of leak i, respectively. Then mathematically, the problem of leak detection in the presence of measurement noise n is:

$$h_m\left(t, x_m, x_{Li}, A_{ei}, P\right) = h\left(t, x_m, x_{Li}, A_{ei}, P\right) + n\left(t\right) \quad [1]$$

in which P stands for other system parameters, *e.g.,* friction factor, wave speed, boundary condition properties, etc. Basically, noise does not contain any information about leaks and in fact, it belongs to a space that is orthogonal to the true model (neglecting any modelling errors). In practice, measurements are taken at discrete time intervals. Let M denotes the number of collected data points. Eq. [1] can be written in the vector form:

$$\mathbf{h_m} = \mathbf{h}\left(x_{Li}, A_{ei}\right) + \mathbf{n}, \quad \mathbf{h_m} = (h_{m,1}, ..., h_{m,M})^{\mathrm{T}}, \quad \mathbf{h} = (h_1, ..., h_M)^{\mathrm{T}}, \quad \mathbf{n} = (n_1, ..., n_M)^{\mathrm{T}} \quad [2]$$

The target of this paper is to study the effects of the random noise, $\mathbf{n}$ in the localization. Many papers in literature on leak detection using time-domain ITA assume $\mathbf{n} = \mathbf{0}$ (Liggett and Chen, 1994; Vítkovský et al., 2000; Kapelan et al., 2003; Jung and Karney, 2008; Haghighi and Ramos, 2012; Brunone and Ferrante, 2001; Covas, 2003).

The computed heads, $\mathbf{h}\left(x_{Li}, A_{ei}\right)$ in Eq. [2] represent model outputs, which are governed by water hammer equations solved by method of characteristics (MOC) (Chaudhry, (2014)). It is assumed that leaks can only exist at computational points so the leak detection problem reduces to find the effective area of leaks corresponding to each computational node of MOC. The simulated pressure heads then only depend on leak (node) effective area. In other words, the approximated $\mathbf{h}\left(x_{Li}, A_{ei}\right) \approx \mathbf{h}\left(x_j, A_{ej}\right), j = 1, ..., N$, and thus $A_{ej} = A_{ej}\left(x_j\right)$ applies in Eq. [2]:

$$\mathbf{h_m} = \mathbf{h}\left(A_{ej}\right) + \mathbf{n}, \quad j = 1, ..., N \quad [3]$$

in which $\mathbf{h}\left(A_{ej}\right)$ is model results assuming leaks at discrete (mesh) points and N is the number of mesh nodes.

2.2 Least square, maximum likelihood estimation

Considering Eq. [3], the process of leak detection using ITA is the fitting of M measured pressure data points to a model that is dependent on N parameters (effective leak areas). If the measured pressure heads are statistically independent and follow a Gaussian distribution with variance σ^2 around the true model pressures (Eq. [3]), the probability of the multiple measurements is the product of the probabilities of each measurement. Maximizing this likelihood corresponds to minimizing the square error between measured and modeled pressures and yields the best fit parameters (Press et al., 1992). So, the objective function of minimization becomes:

$$E_1 = \left(\mathbf{h_m} - \mathbf{h}\right)^{\mathrm{T}} \left(\mathbf{h_m} - \mathbf{h}\right) = \sum_{i=1}^{M} \left(h_i^m - h_i\right)^2. \quad [4]$$

This merit function for the leak detection using ITA was firstly suggested by Liggett and Chen (1994) and has been widely used by many researchers afterwards (see review paper by Colombo and Karney, 2009).

2.3 Matched filter, maximum signal to noise ratio

Another merit function is investigated in this research. This finds a filtering function based on computed heads such that it maximizes the energy of the signal and thus minimizes the influence of the noise. Considering Eq. [3], measured data are filtered by function $\mathbf{w}$ (Oppenheim and Schafer, 2010):

$$\mathbf{w} * \mathbf{h_m} = \mathbf{w} * \mathbf{h} + \mathbf{w} * \mathbf{n}, \quad \mathbf{w} = (w_1, ..., w_M)^{\mathrm{T}} \quad [5]$$

in which * represents a convolutional sum and $\mathbf{w}$ is assumed to be a unit vector, *i.e.,* $\|\mathbf{w}\| = 1$, to obtain a non-trivial solution. The optimal filtering function is found by maximizing the ratio of signal power to noise power, defined by signal-to-noise ratio (SNR) (Johnson and Dudgeon, 1993):

$$\mathrm{SNR} = \frac{(\mathbf{w} * \mathbf{h})^2}{\mathrm{E}\left[(\mathbf{w} * \mathbf{n})^2\right]} = \frac{\left(\sum_{k=1}^{M} w_{M-k+1} h_k\right)^2}{\sigma^2 \|\mathbf{w}\|^2} \le \frac{\left(\sum_{k=1}^{M} w_{M-k+1}^2\right)\left(\sum_{k=1}^{M} h_k^2\right)}{\sigma^2 \|\mathbf{w}\|^2} = \frac{1}{\sigma^2}\|\mathbf{h}\|^2 \quad [6]$$

in which E stands for expectation and σ^2 is the variance of the noise (measured data). Appendix A illustrates how the denominator is evaluated. The inequality in Eq. [6] is due to Schwarz's inequality, which becomes equality and thus SNR reaches maximum, if and only if w_{M-k+1} and h_k, $k = 1,...,M$ are linearly dependent, which for unit vector $\mathbf{w}$ means $w_{M-k+1} = h_k / \|\mathbf{h}\|$, $k = 1,...,M$. Based on this filter, and considering Eq. [5], a new merit function representing the highest signal power is proposed:

$$E_2 = (\mathbf{w} * \mathbf{h}_\mathbf{m})^2 = \left(\sum_{k=1}^{M} w_{M-k+1} h_{m,k}\right)^2 = \left(\sum_{k=1}^{M} \frac{h_k}{\|\mathbf{h}\|} h_{m,k}\right)^2 = \frac{1}{\|\mathbf{h}\|^2}\left(\mathbf{h}_\mathbf{m}^T \mathbf{h}\right)^2, \quad \|\mathbf{h}\|^2 = \sum_{i=1}^{M} h_i^2. \quad [7]$$

This objective function should be maximized to find the best leak parameters, which correspond to the highest filtered energy of the measured signal to the noise. Physically, this merit function is the correlation between measured and computed signals. Accordingly, this merit function is termed as Matched Filter or Matched Field Processing (MFP) in the signal processing literature (Krim and Viberg, 1996). This approach is widely used in ocean acoustics for sound source localization (Wang et al., 2016, Tolstoy et al., 2009), structural vibration (Turek and Kuperman, 1997; Tippmann and Lanza di Scalea, 2015) and ocean engineering (Baggeroer et al., 1993) by matching the modeled and measured signals or blockage detection in sewer pipes by correlations between measurements (Tolstoy, 2010).

2.4 Discussion of the two merit functions, new approach

In a noise-free condition, both objective functions [4] and [7] identify the leak parameters correctly. In a noisy environment, the global extremum point may be displaced thus leading to inaccurate localization. Here, the variances of the two merit functions are computed, which illustrates their fluctuations due to the noise and may thus signify the detection error. Assuming that the expectation of measured head (one measurement or the average of many) is equal to the computed head for actual leaks and the noise is Gaussian, the variance of Eq. [4] becomes:

$$\sigma_{E_1}^2 = 2M\sigma^4 \quad [8]$$

in which M is the number of computed (measured) head data points over time and σ is the standard deviation of measurements. The variance of Eq. [7] yields:

$$\sigma_{E_2}^2 = 2\sigma^4 + 4\sigma^2 \|\mathbf{h}\|^2, \quad \|\mathbf{h}\|^2 = \sum_{i=1}^{M} h_i^2. \quad [9]$$

The derivation of Eq. [8] and [9] is provided in Appendix B. The two variances can be compared for a fixed number of measured data (M) . They vary from one case to another, *e.g.,* different sensor and system properties including leak locations and sizes. The above variances imply the variability of the merit functions with random noise by which one can speculate the stability of leak localization. Therefore, it is well-advised to use the first approach (Eq. [4]) when the variance of Eq. [7] is relatively high and vice versa.

For the reason that leaks sizes are unknowns, the norm of the computed head for actual leaks, as observed in Eq. [9], cannot initially be found. As a result, the following procedure is suggested to select the appropriate merit function for localization. Firstly, employ the ITA with each objective function separately. Then, having estimated leaks correspond to each approach, the variance of each function is computed (using Eq. [8] and [9]). Finally, the detected leak sizes of the one with smaller variance is chosen as more reliable localization.

3 NUMERICAL RESULTS AND DISCUSSIONS

3.1 Preliminaries

A reservoir-pipe-valve system is considered to investigate the leak detection using the time-domain ITA. The system characteristics are stated in Table 1. Following Section 2.4, the selection of the appropriate merit function for the ITA depends on true model outputs, which in turn is a function of the system properties. As a result, two leak sizes according to Table 1 are defined to examine each merit function and the proposed approach to choose between them, which can eventually lead to a more stable localization.

Table 1. General specifications of the reservoir-pipe-valve system.

Pipe length	37.2 m	Number of MOC points	33
Inner diameter	22.1 mm	Mesh size	1.127 m
Steady velocity (before leak)	0.2 m/s	Leak distance from reservoir	31.56 (node 29)
Wave speed	1300 m/s	Effective leak sizes (C_d A_L)	0.2, 3 mm^2

Based on the data provided in Table 1, the forward problem is solved to find the pressure head $\mathbf{h}\left(A_{ej}\right), j=1,...,N$ at the valve. The lumped leak area is allocated at node 29 and the leak area of the other nodes are set to zero. A Gaussian white noise with zero-mean unit variance represented by a random variable $\boldsymbol{\xi}$ is used to randomly generate the noise in Eq. [3].

$$\mathbf{n}=\sigma\,\boldsymbol{\xi},\;\; \sigma=10^{-\frac{\text{SNR}}{20}}\Delta h_L \;\;\text{ or }\;\; \text{SNR}=10\log_{10}\left(\frac{\left|\Delta h_L\right|}{\sigma}\right)^2 \quad [10]$$

In this relation, SNR measured in decibel (dB) is a given number which depends on the system instrumentation and collected experimental data and $\left|\Delta h_L\right|$ corresponds to first reflection in pressure due to leak (a step pressure drop) and σ is standard deviation of noise.

In order to estimate the localization efficiency of each merit function subject to noise, an error estimation criterion is defined:

$$\varepsilon_1=\frac{\left|\hat{X}_L-X_L\right|}{L} \quad [11]$$

in which L is the pipe length, X_L is the true leak location, and $\hat{X}_L$ is the estimated leak location, which corresponds to the node with maximum effective area obtained from optimization. This criterion does not take the leakage size into account (note that in practice the reliability of localization is key to the detection exercise). A criterion that takes both leak size and location into account may be defined as follows:

$$\varepsilon_2=\frac{\left|A_eX_L-\sum_{i=1}^{N}\left(\hat{A}_{ej}\hat{X}_{Lj}\right)\right|}{A_eX_L} \quad [12]$$

In this relation, A_e is the actual leak size and $A_{ej}, j=1,...,N$ is the detected effective area for each computational point and N is the number of MOC nodes. Note that Eq. [12] is a measure of the difference in the moment of the actual leak area with respect to $X=0$ versus the moment of the identified leaks.

In the next sections, first some numerical results are presented to illustrate the noise effect in localization. It provides the motivation to use the matched filter approach as a new merit function in the time-domain ITA context to probably decline it. Then, the pipe system with the two leak cases (Table 1) is investigated in separate sections to observe the performance of the ITA while using the two merit functions.

3.2 Overfitting problem in the time-domain ITA

A noise-free signal contains the system information due to reflections from pipe system boundaries including anomalies. In the presence of noise, this information is contaminated so that the results of the transient model are not well-matched to the measured data. It means that each misfit quantity in Eq. [4] for the actual leak parameters is not necessarily zero and its expectation coincides to the estimated variance of noise.

However, some issues can lead the detection procedure to overfitting to measurements and wrong leak parameters. In other words, the global minimum is displaced and it is no longer at the actual leak parameters or at least it is not the unique global extremum. These issues are basically driven by the misfit function components being either the computed head or measured data. Adding too many parameters to the ITA decrease the sensitivity of the computed signals to the parameters (increase similarity) and can make the inverse problem non-unique. This issue which stems from assuming all nodes as potential leaks (too many parameters) in ITA is more pronounced for measurements with high noise levels.

The problem is more illustrated by Figure 1 while a noisy signal (white noise) with SNR = 0 dB in Figure 1 (a) is applied for leak localization. Typical result from an ITA is presented in Figure 1 (b) in which the actual and predicted leak sizes and locations are represented by red and blue bars respectively. Figure 1c shows the values of the least square merit function (Eq. [4]) versus optimization iterations when the starting point (initial guess) is the actual leak parameters. As seen, a set of wrong leak locations and sizes are detected. In this case, the mean square summation of the misfit is less than the noise variance. In fact, the method detects fictitious leaks to match to the white noise. As a result, the global minimum of the square fit between measured and computed signal is displaced and it corresponds to another set of leaks which differ from the actual one both in location and size. Note that this is an example with no modeling error with only leak parameters (effective leak area at each node) as decision variables of optimization. When too many decision parameters are incorporated (e.g., friction factor, viscoelastic, unsteady friction coefficients, etc.), the noise effect in the localization becomes more problematic.

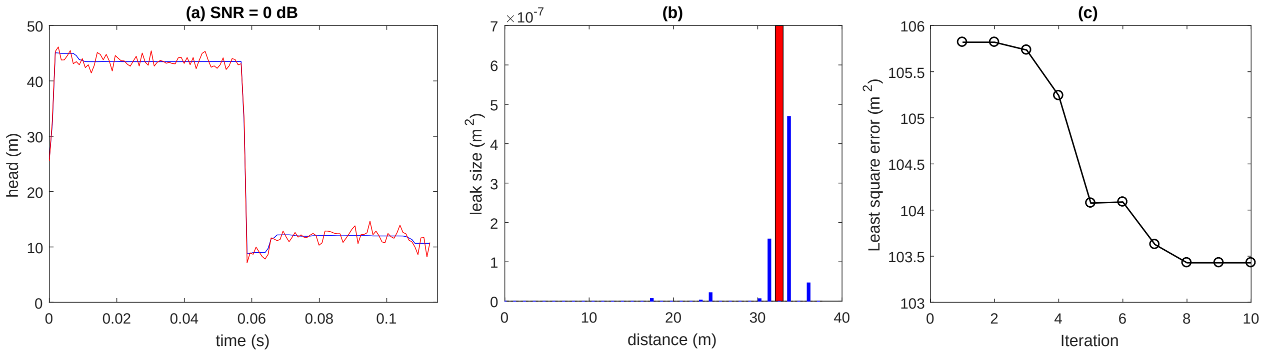

Figure 1. (a) Noisy pressure head with 0-SNR (red) and best computed fit (blue). (b) The actual (red) and detected (blue) leak parameters (location and size). (c) The convergence curve of optimization iterations.

3.3 Leak case 1

Considering the problem stated in Section 3.1, the proposed and the conventional merit functions are compared. To this aim, noisy signals are utilized for localization using ITA with the two merit functions.

Note that when there are several measurements at a location, two different approaches are possible for the localization. One way is to calculate the average signal to be used for ITA. This in fact reduces the noise variance by a constant factor corresponding to the number of measurements. One can prove that it is consistent with finding the maximum likelihood estimators of all measurements when the noise is Gaussian independent white noise. Therefore in reality, this approach has to be used while having multiple measurements. The other approach is to employ each signal for localization separately and then find the average of the results. In this paper, this is used to compare the efficiency of the two merit functions in a noisy environment to avoid making conclusions based on one single signal.

According to the data given in Table 1, the detection procedure is repeated for 10 different noisy measurements at the valve with SNR = 0 dB. The result of leak detection corresponding to each measurement is the vector of the effective leakage area ($A_{ej}, j = 1,\ldots,N$). The elements of these vectors (10 vectors corresponding to 10 measurements) are then averaged respectively and the resulting vector is presented in Figure 3 for the two merit functions. The results of this figure show that the two merit functions behave similarly. In fact, according to Eq. [12], for the matched field $\varepsilon_2^{MF} = 0.287$ and for the least square merit function, it gives $\varepsilon_2^{LS} = 0.266$. This study is repeated for SNR equal to -5 but now the average of 30 runs (to decrease the variance of identified leak area) are shown in Figure 4. Then, the evaluated errors according to Eq. [12] are $\varepsilon_2^{MF} = 0.2545$ for the matched field and $\varepsilon_2^{LS} = 0.2563$ for the least square merit function. Again, it demonstrates similar localization of the two functions though with slightly different sizes. The two figures indicate that the proposed matched-filter based objective function is capable of finding leaks. As it arrives at different results than the least square, it is conductive to employ both functions for the ITA and find the appropriate one which as discussed can be selected by their variance.

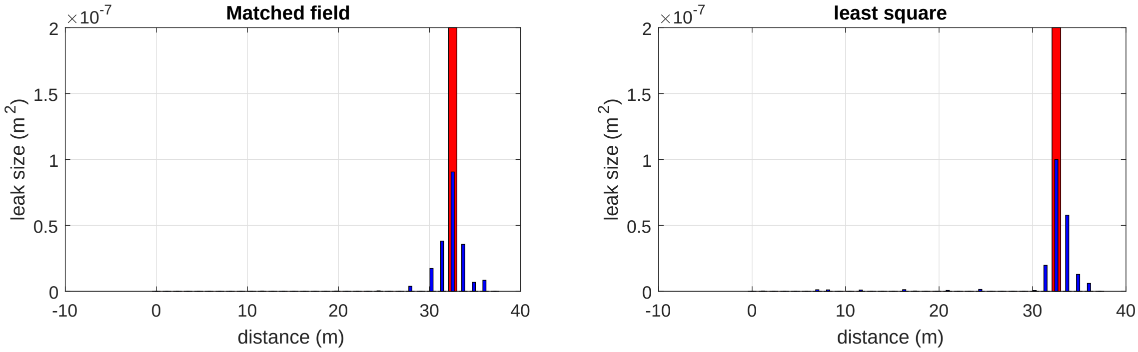

Figure 3. The actual (red) and detected (average of 10, blue) leak parameters (location and size) for the two indicated merit functions. Measurements with SNR = 0 dB are used for localization.

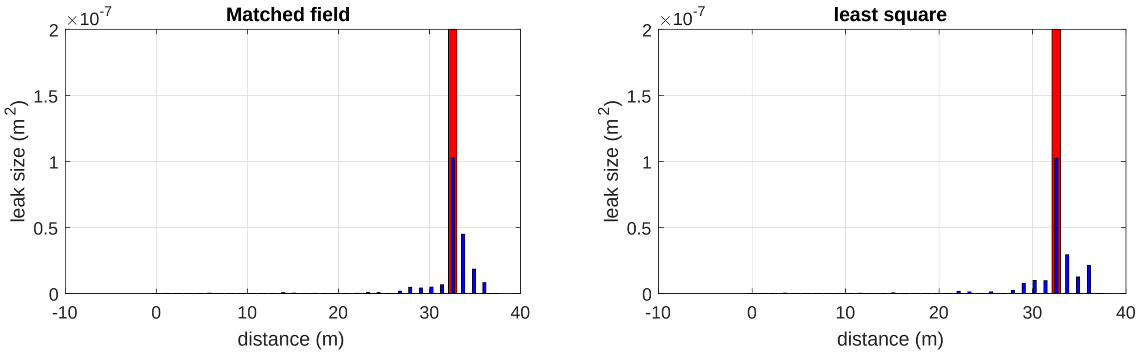

Figure 4. The actual (red) and detected (average of 30, blue) leak parameters (location and size) for the two merit functions. Measurements with SNR = -5 dB are used for localization.

To further investigate the two objective functions and the new approach in terms of localization error, the ITA is repeated for 60 times with different noisy signals. The error of each run is evaluated according to Eq. [11] to estimate the mean error. For the three methods presented in Sections 2.2 to 2.4, Figure 5 shows the mean and 95% confidence interval of error corresponding to four different SNR. As SNR decreases, the localization error increases for both methods but the least square method is clearly more accurate than the matched filter. This is due to the fact that the variance of the least square function is lower than that of the matched filter merit function (*e.g.,* for SNR = -5 dB, they are $4\times10^{2}\,\mathrm{m}^{4}$ versus $3\times10^{4}\,\mathrm{m}^{4}$, respectively). As seen in Figure 5, the localization errors for the proposed approach coincide to those of the least square objective function. In fact, since the least square function has lower deviation, the new approach chooses the localizations of this merit function in all 60 simulations.

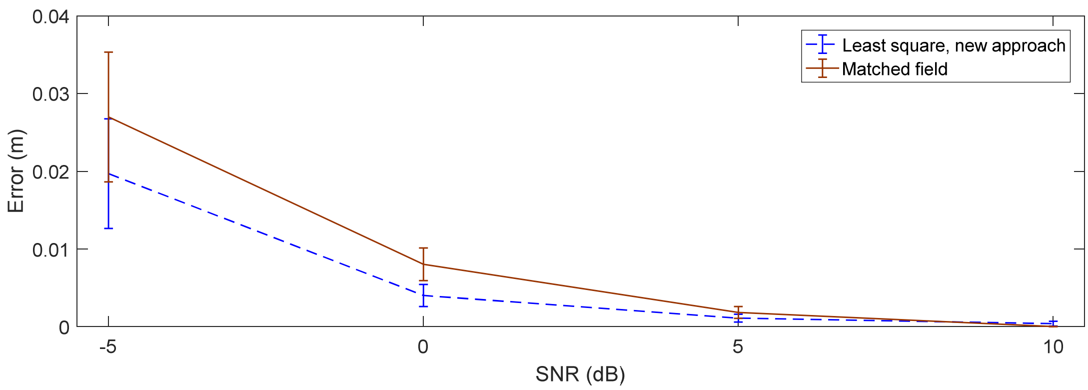

Figure 5. The mean and 95% confidence interval of localization error evaluated using Eq. [11] for 60 simulations with different SNR ($A_e = 0.2\,\mathrm{mm}^2$).

3.4 Leak case 2

A similar investigation to the previous section but now with the other leak is made. Separate ITAs are carried out for 10 signals with 0 dB white noise to arrive at 10 sets of results. The optimum leak vectors are then averaged to find the result in Figure 6, which is provided for the two merit functions. Errors evaluated based on Eq. [12] for the matched field and least square merit functions are $\varepsilon_2^{MF} = 0.146$ and $\varepsilon_2^{LS} = 0.228$, respectively. Figure 7 depicts similar results but now for 30 measurements (to decrease the variance of identified leak area) with SNR = -5 dB. The detection errors are $\varepsilon_2^{MF} = 0.222$ and $\varepsilon_2^{LS} = 0.303$. The comparison reveals that for this leak case, the matched field merit function is thus definitely preferred. This can also be anticipated from the variances of the two objective functions which will be illustrated along with the mean error of localizations corresponding to each method.

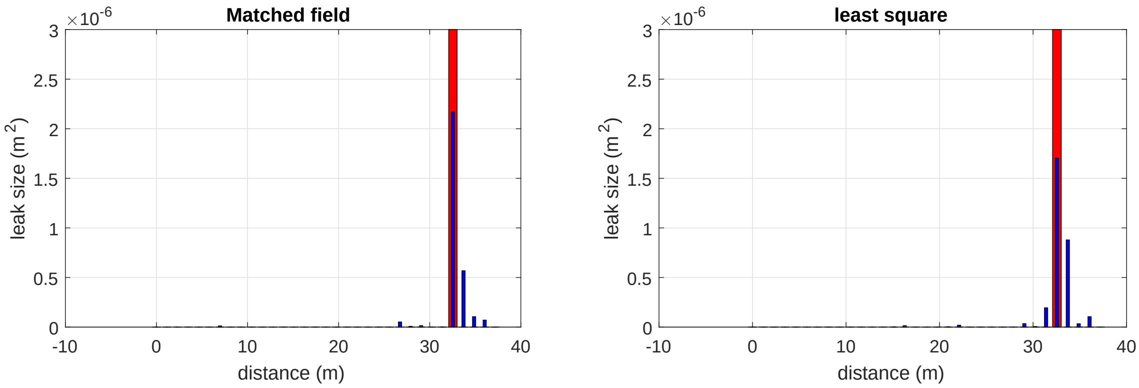

Figure 6. The actual (red) and detected (average of 10, blue) leak parameters (location and size) for the two merit functions. Measurements with SNR = 0 dB are used for localization.

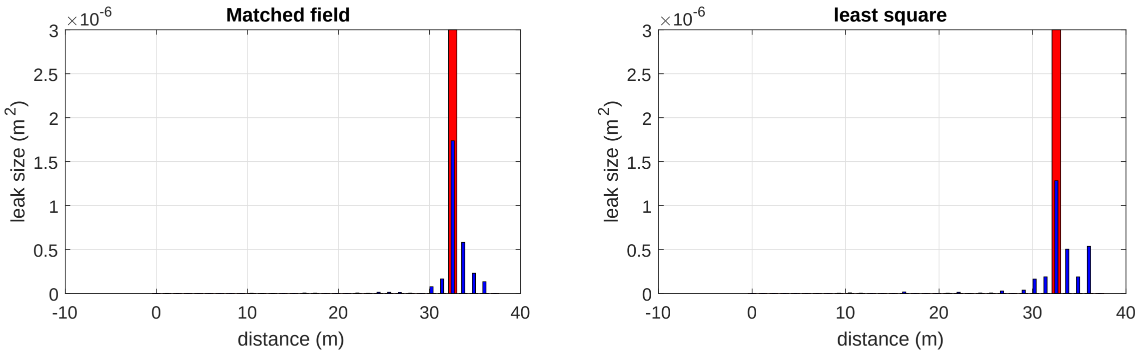

Figure 7. The actual (red) and detected (average of 10, blue) leak parameters (location and size) for the two merit functions. The results are the average of 30 measurements, each with SNR = -5 dB.

The error analysis for 60 measurements and corresponding simulations using the three schemes is carried out. Eq. [11] is utilized to estimate the error of each localization. The estimated mean and 95% confidence interval of error for each SNR is presented in Figure 8 (for the three approaches). For this leak case, the variance of the least square function is $1\times10^7\ \mathrm{m}^4$ and that of the matched filter merit function is $8\times10^5\ \mathrm{m}^4$ (for SNR = -5 dB). For the reason that the variance of the matched field merit function is lower, the average error in localization is less than that of the least square function, and thus the advantage of the proposed merit function for this leak case is confirmed. One can also expect that the proposed scheme (Section 2.4) will select the matched filter function for the localization so as it results in the same error as matched filed approach, as seen in Figure 8.

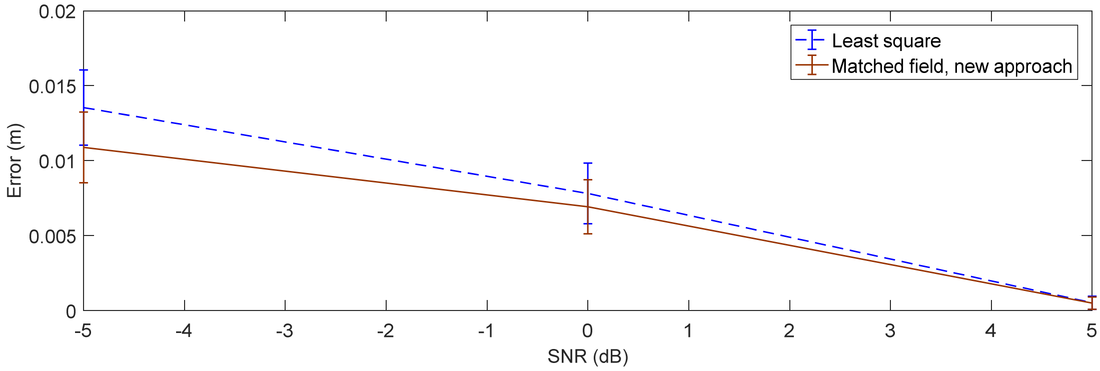

Figure 8. The mean and 95% confidence interval of localization error evaluated using Eq. [11] for 60 simulations with different SNR ($A_e = 3\,\mathrm{mm}^2$).

4 CONCLUSIONS

The leak detection based on the ITA in the time domain when measured data are contaminated with a white noise is addressed. The analysis based on maximizing signal-to-noise ratio, which is largely stablished as a successful signal processing technique is carried out. The idea is equivalent to the matched filter or Matched Field Processing (MFP), which involves correlations between the measured and modeled signals. This filter in fact adjusts the measured heads by increasing the reflections from actual leaks and decreasing noise energy. It leads to a new merit function for leak detection in the time-domain ITA instead of the conventional least square criterion. The two possible merit functions are proven to reach their global extremum at the same optimal points for localizations using noise-free signals.

The problem of non-uniqueness and over-fitting which stems from having too many decision variables (MOC nodes as leak candidates) arises for localizations with noisy signals. It is more significant under high levels of noise or equivalently in systems with very small leaks, which have reflection amplitudes of the same order or smaller than noise standard deviation. In a noisy environment, when the non-uniqueness problem in the ITA becomes a significant issue, the two objective functions behave differently. It is found in this research that the optimal variances of the two merit functions are the objective parameters to decide for the selection of each function for leakage detection. The merit function with lower variance arrives at less localization error. This finding is closely investigated by calculating the variances of the two merit functions for two case problems. The leak detection examples are solved under several measurement noise levels and on the basis of a detection-error criterion, the preference of each one to the other is demonstrated.

The incorporation of the matched field merit function in the ITA leads to an improved localization procedure in a noisy environment. The two merit functions are used for localization with a given measured signal (probably the average of several measurements at a location). If then they arrive at different results, that of merit function with lower optimal variance is supposed to be more reliable. This approach is also employed in the presented numerical case studies for the leak detection. It is demonstrated that it in fact takes the advantage of the matched field merit function when it gives less error (variance) than the other and vice versa. Consequently, the proposed approach to choose the final leak sizes from the outputs of the two merit functions is favorable.

Note that a classical solution for the raised non-uniqueness or overfitting problem is to use model parsimony, which favors a lower number of leak candidates. The proposed matched field objective function can still be used with model parsimony. The two merit functions can be applied to enumerate the domain and achieve a more reliable result. Under high noise levels, they may reach to different solutions. Discussions regarding the preferred localization can be valid herein.

ACKNOWLEDGEMENTS

This work has been supported by research grants from the Research Grant Council of the Hong Kong SAR, China (Project No. T21-602/15R). The authors would like to thank Duncan A. McInnis, Moez Louati, Fedi Zouari, Asgar Ahadpour, and Jingrong Lin for their helpful comments and discussions.

APPENDIX A EXPECTATION OF FILTERED NOISE POWER

The denominator of Eq. [6] can be estimated as follows:

$$\mathrm{E}\left[\left(\mathbf{w}*\mathbf{n}\right)^2\right]=\mathrm{E}\left[\left(\sum_{i=1}^{M} w_{M-i+1}n_i\right)\left(\sum_{j=1}^{M} w_{M-j+1}n_j\right)\right]=\sum_{i=1}^{M}\sum_{j=1}^{M}\left[w_{M-i+1}w_{M-j+1}\mathrm{E}\left(n_in_j\right)\right], \quad \text{[A1]}$$

but $\mathrm{E}\left(n_i n_j\right)=\sigma^2\delta_{ij}$, which σ^2 is the noise variance and δ_{ij} is delta di Kronecker being one if $i=j$ and zero otherwise. Therefore, Eq. [A1] reduces to:

$$\sum_{i=1}^{M}\sum_{j=1}^{M} w_{M-i+1}w_{M-j+1}\mathrm{E}\left(n_i n_j\right)=\sum_{i=1}^{M}\sum_{j=1}^{M} w_{M-i+1}w_{M-j+1}\delta_{ij}\sigma^2=\sum_{i=1}^{M} w_i^2\sigma^2=\|\mathbf{w}\|^2\sigma^2. \quad \text{[A2]}$$

APPENDIX B DERIVATION OF VARIANCES OF MERIT FUNCTIONS

To find the variance of the merit function E_1, its expectation is computed:

$$\mathrm{E}\left(E_1\right)=\mathrm{E}\left[\left(\mathbf{h_m}-\mathbf{h}\right)^T\left(\mathbf{h_m}-\mathbf{h}\right)\right]=\mathrm{E}\left[\sum_{i=1}^{M}\left(h_i^m-h_i\right)^2\right]=M\sigma^2 \quad \text{[B1]}$$

in which σ^2 is the variance of the measured pressure data. The variance of the random function E_1 is determined by:

$$\mathrm{var}\left(E_1\right)=\mathrm{E}\left(E_1^2\right)-\left[\mathrm{E}\left(E_1\right)\right]^2=\mathrm{E}\left[\sum_{j=1}^{M}\sum_{i=1}^{M}\left(h_i^m-h_i\right)^2\left(h_j^m-h_j\right)^2\right]-\left[\mathrm{E}\left(E_1\right)\right]^2. \quad \text{[B2]}$$

Since the measurement at different time points are independent, the first term of Eq. [B2] reduces to:

$$\begin{aligned}\mathrm{E}\left(E_1^2\right)&=\mathrm{E}\left[\sum_{j=1}^{M}\sum_{i=1}^{M}\left(h_i^m-h_i\right)^2\left(h_j^m-h_j\right)^2\right]=\mathrm{E}\left[\sum_{j=1,j\neq i}^{M}\sum_{i=1}^{M}\left(h_i^m-h_i\right)^2\left(h_j^m-h_j\right)^2\right]+\mathrm{E}\left[\sum_{i=1}^{M}\left(h_i^m-h_i\right)^4\right]\\&=\left(M^2-M\right)\sigma^4+3M\sigma^4.\end{aligned} \quad \text{[B3]}$$

Substituting from Eq. [B3] and Eq. [B1] in Eq. [B2], yields:

$$\mathrm{var}\left(E_1\right)=\mathrm{E}\left(E_1^2\right)-\left[\mathrm{E}\left(E_1\right)\right]^2=\left(M^2-M\right)\sigma^4+3M\sigma^4-\left[M\sigma^2\right]^2=2M\sigma^4. \quad \text{[B4]}$$

The expectation of the random function E_2 is:

$$\mathrm{E}\left(E_2\right)=\frac{1}{\|\mathbf{h}\|^2}\mathrm{E}\left[\left(\mathbf{h}_\mathbf{m}^T\mathbf{h}\right)^2\right]=\frac{1}{\|\mathbf{h}\|^2}\mathbf{h}^T\mathrm{E}\left(\mathbf{h_m}\mathbf{h}_\mathbf{m}^T\right)\mathbf{h}=\frac{1}{\|\mathbf{h}\|^2}\mathbf{h}^T\left(\sigma^2\mathbf{I}+\mathbf{h}\mathbf{h}^T\right)\mathbf{h}=\sigma^2+\|\mathbf{h}\|^2 \quad \text{[B5]}$$

and the second order moment:

$$\mathrm{E}\left(E_2^2\right)=\frac{1}{\|\mathbf{h}\|^4}\mathrm{E}\left(\left(\mathbf{h}_\mathbf{m}^T\mathbf{h}\right)^4\right). \quad \text{[B6]}$$

Define the random variable $X=\mathbf{h}_\mathbf{m}^T\mathbf{h}$ which has mean $\mathrm{E}\left(X\right)=\mu_X=\|\mathbf{h}\|^2$ and variance:

$$\sigma_X^2=\mathrm{E}\left(X^2\right)-\left[\mathrm{E}\left(X\right)\right]^2=\mathrm{E}\left(\mathbf{h}^T\mathbf{h_m}\mathbf{h}_\mathbf{m}^T\mathbf{h}\right)-\|\mathbf{h}\|^4=\mathbf{h}^T\mathrm{E}\left(\mathbf{h_m}\mathbf{h}_\mathbf{m}^T\right)\mathbf{h}-\|\mathbf{h}\|^4=\mathbf{h}^T\left(\sigma^2\mathbf{I}+\mathbf{h}\mathbf{h}^T\right)\mathbf{h}-\|\mathbf{h}\|^4=\sigma^2\|\mathbf{h}\|^2. \quad \text{[B7]}$$

Considering the following formula:

$$\mathrm{E}\left(X^4\right)=\mu_X^4+6\mu_X^2\sigma_X^2+3\sigma_X^4, \quad \text{[B8]}$$

the expectation term in Eq. [B6] is found to be:

$$\mathrm{E}\left[\left(\mathbf{h}_\mathbf{m}^T\mathbf{h}\right)^4\right]=\|\mathbf{h}\|^8+6\|\mathbf{h}\|^4\sigma^2\|\mathbf{h}\|^2+3\sigma^4\|\mathbf{h}\|^4=\|\mathbf{h}\|^8+6\sigma^2\|\mathbf{h}\|^6+3\sigma^4\|\mathbf{h}\|^4. \quad \text{[B9]}$$

Substituting Eq. [B9] in Eq. [B6] gives:

$$\mathrm{E}\left(E_2^2\right)=\frac{1}{\|\mathbf{h}\|^4}\mathrm{E}\left[\left(\mathbf{h}_{\mathbf{m}}^T\mathbf{h}\right)^4\right]=\|\mathbf{h}\|^4+6\sigma^2\|\mathbf{h}\|^2+3\sigma^4. \quad [B10]$$

Therefore, the variance of E_2 is:

$$\mathrm{var}\left(E_2\right)=\mathrm{E}\left(E_2^2\right)-\left[\mathrm{E}\left(E_2\right)\right]^2=4\sigma^2\|\mathbf{h}\|^2+2\sigma^4. \quad [B11]$$

REFERENCES

Baggeroer, A.B., Kuperman, W.A. & Mikhalevsky, P.N. (1993). An Overview of Matched Field Methods in Ocean Acoustics. *IEEE Journal of Oceanic Engineering*, 18(4), 401–424.
Brunone, B. & Ferrante, M. (2001). Detecting Leaks in Pressurized Pipes by Means of Transients. *Journal of Hydraulic Research,* 39 (5) 539–547.
Chaudhry, M.H. (2014). *Applied Hydraulic Transients, Third Edition*. Springer.
Colombo, A.F., Lee, P. & Karney, B.W. (2009). A Selective Literature Review of Transient-Based Leak Detection Methods. *Journal of Hydro-environment Research*, Vol.2(4), 212-227.
Covas, D., (2003). Inverse Transient Analysis for Leak Detection and Calibration of Water Pipe Systems Modelling Special Dynamic Effects. *Ph.D. thesis*, University of London, London.
Ferrante, M., Brunone, B. & Meniconi, S. (2007). Wavelets for The Analysis of Transient Pressure Signals for Leak Detection. *Journal of Hydraulic Engineering*. 133(11), 1274–1282.
Gao, Y., Brennan, M.J. & Joseph, P.F. (2006). A Comparison of Time Delay Estimators for The Detection of Leak Noise Signals in Plastic Water Distribution Pipes. *Journal of Sound and Vibration*, 292(3), 552-570.
Guo, C., Wen, Y., Li, P. & Wen, J. (2016). Adaptive Noise Cancellation Based on EMD in Water-Supply Pipeline Leak Detection, *Measurement*, 79, 188-197.
Haghighi, A. & Ramos, H. (2012). Detection of Leakage Freshwater and Friction Factor Calibration in Drinking Networks Using Central Force Optimization. *Water Resources Management*, 26(8), 2347-2363.
Johnson, D.H. & Dudgeon, D.E. (1993). *Array Signal Processing: Concepts and Techniques*. Prentice-Hall signal processing series.
Kapelan, Z.S., Savic, D.A. & Walters, G.A. (2003). A Hybrid Inverse Transient Model for Leakage Detection and Roughness Calibration in Pipe Networks. *Journal of Hydraulic Research*, 415, 481–492.
Krim, H. & Viberg, M. (1996). Two Decades of Array Signal Processing Research. *IEEE Signal Processing Magazine*, 13(4), 67–94.
Liggett, J.A. & Chen, L.-C. (1994). Inverse Transient Analysis in Pipe Networks. *Journal of Hydraulic Engineering.* 1208, 934–955.
Oppenheim, A.V. & Schafer, R.W. (2010). *Discrete-Time Signal Processing. Third Edition*, Pearson Education, USA.
Press, W.H., Teukolsky, S.A., Vetterling, W.T. & Flannery, B.P. (1992). *Numerical Recipes: The Art of Scientific Computing*. Cambridge University Press, Cambridge, U.K.
Strang, G. (1986). *Introduction to Applied Mathematics*. Wellesley-Cambridge Press, USA.
Tippmann, J.D., Zhu, X. & Lanza di Scales, F. (2015). Application of Damage Detection Methods Using Passive Reconstruction of Impulse Response Functions. *Philosophical Transactions of the Royal Society of London A: Mathematical, Physical and Engineering Sciences*. 373(2035)-20140070.
Tolstoy, A., Horoshenkov, K.V. & Bin Ali, M.T. (2009). Detecting Pipe Changes Via Acoustic Matched Field Processing. *Applied Acoustics*, 70(5), 695-702.
Tolstoy, A.I. (2010). Waveguide Monitoring (Such as Sewer Pipes or Ocean Zones) Via Matched Field Processing. *Journal of the Acoustical Society of America*. 128(1), 190-194.
Vítkovský, J. P., Simpson, A.R. & Lambert, M.F. (2000). Leak Detection and Calibration Using Transients and Genetic Algorithms. *Journal of Water Resources Planning and Management.*1264, 262–265.
Vitkovsky, J., Lambert, M., Simpson, A. & Liggett, J. (2007). Experimental Observation and Analysis of Inverse Transients for Pipeline Leak Detection. *Journal of Water Resources Planning and Management*, 133(6), 519-530.
Wang, X. & Ghidaoui, M.S. (2017) Pipeline Leak Detection Using the Matched-Field Processing Method. *Journal of Hydraulic Engineering*, ASCE, submitted.
Wang, X., Quost, B., Chazot, J.-D. & Antoni, J. (2016). Estimation of Multiple Sound Sources with Data and Model Uncertainties Using the EM and Evidential EM Algorithms. *Mechanical Systems and Signal Processing*, 66–67, 159–177.

MONITORING OF PIPE LEAKAGE BASED ON EMPIRICAL MODE DECOMPOSITION AND AUTOMATIC SELECTION OF INTRINSIC MODE FUNCTION

MUHAMMAD HANAFI YUSOP(1) MOHD FAIRUSHAM GHAZALI(2) MOHD FADHLAN MOHD YUSOF(3) & MUHAMMAD AMINUDDIN PIREMLI(4)

(1,2,3,4) Advanced Structural Integrity of Vibration Research (ASIVR), Faculty of Mechanical Engineering, University Malaysia Pahang, Pekan, Pahang, Malaysia,
m.hanafiyusop@yahoo.com.my; fairusham@ump.edu.my; fadhlan@ump.edu.my; aminuddin_pr@yahoo.com

ABSTRACT

Signal processing is an important tool for diagnostic of non-stationary and non-linear data. Many techniques of analysis are available to process these types of data, such as STFT, Wavelets Transform, and demodulation analysis. In the recent study, the analysis of pressure transient signal can be seen as an accurate and low-cost method for the leak and pipe feature detection in water distribution system. Transient phenomena occurred due to sudden changes in fluid propagation filled in pipelines system, which is caused by rapid pressure and flow fluctuation in a system, such as closing and opening valve rapidly or pump failure. Various method of pressure transient analysis has been applied by several groups of researcher, such as cepstrum analysis, cross-correlation, and wavelets transform. In this research, the application of Hilbert Huang Transform (HHT) was used as the method to analyse the pressure transient signal. However, this method has the difficulty in selecting the suitable IMF for the next data post-processing method, which is Hilbert Transform (HT). Previous researchers normally perform the selection of the IMF on visually basis according to user's experience and used the statistical approach that allows the automatic selection of intrinsic mode function (IMF). This paper proposed the implementation of Integrated Kurtosis-based Algorithm for z-filter Technique (I-kaz) to kurtosis ratio (I-kaz-Kurtosis) for that allows automatic selection of intrinsic mode function (IMF) should be used. This work demonstrates on 67.9 meters Medium High Density Poly Ethylene (MDPE) pipe installed with single artificial leak simulator. The analysis results using I-kaz-kurtosis ratio revealed that the method can be used as an automatic selection of intrinsic mode function (IMF), although the noise level ratio of the signal is lower. I-kaz-kurtosis ratio is recommended and advised to be implemented as automatic selection of intrinsic mode function (IMF) through HHT analysis.

Keywords: Leak detection; pressure transient; I-kaz; Hilbert Huang Transform (HHT).

1 INTRODUCTION

Water play an important role in the contribution of the economic growth of a country. In the recent decade, water is one of the major issues addressed in research worldwide due to the increase in water pollution and non-revenue water (NRW). Water Economy Network (WEN) reported that water scarcity is rapidly enhancing the number one global resource concern. Consequently, with the increase in the number of accessible clean and fresh water, the water network will increase and thus, the possibility of the increment of water issues is higher. The first global survey conducted by Lai (1991) reported that water loss for most country falling into the range of 20% – 30% and for Malaysia, the number is 43% of NRW. Non revenue water (NRW) is when the amount of water reaches to the consumer is lesser than the amount of water that has been produced. The losses are due to real losses, such as pipeline network leakage, or the apparent loss, such as through theft or bypass of water network (the water reach to the consumer not metered) and metering inaccuracies. Nowadays, minimizing of NRW during transportation process through pipeline network is very essential. The problem of water leaks in pipeline distribution system is the main cause of non revenue water (NRW). Lately, water authorities concern of leak in water distribution system, then provide some necessary incentives for investment in leak detection technology and leak reduction strategies Colombo et al. (2009).The main cause of leaks is due to the aging of pipelines, corrosion, erosion, excessive pressure of water resulting from operational error and water hammer generate by rapid opening and closing valve.

There are two types of leak detection techniques, which are an external and internal method. External method is a way to inspect pipe condition externally, such as by visually inspecting the pipe condition, whereas the internal method inspects the pipe condition internally, such as by mathematical computation and signal processing (Taghvaei et al., 2006). Signal processing is a famous method among the researchers due to its ability to detect and localize any disturbance (leak) and blockage in the pipeline system. Pressure Transient analysis is a recently developed method and attracted researchers due to cost-effectiveness. Theoretically, transient phenomena are generated due to sudden changes of fluids propagation filled in the pipeline's system caused by rapid pressure and flow fluctuation in the systems, such as rapid closing and opening valve. These phenomena generate pressure wave propagation, which travels with the speed of sound along the pipeline's system.The wave characteristic represents the pipe information and condition from various boundaries, such as pipe feature, junction outlet and the presence of the leak. Signal analysis is a way to extract the characteristics, identity, and information of pressure transient signal captured along the pipeline distribution system. A variety of pressure transient analysis method has been practiced among the researchers in order to extract information and characteristic of pressure transient signal, such as cepstrum analysis Taghvaei et al. (2006), cross-correlation Liou (1998), ortoghonal wavelets transform (OWT) Taghvaei et al. (2006), instantenous frequency analysis Ghazali (2012), and inverse transient analysis Stephens et al. (2002).

The possibility to analyse the phenomenon in both time and frequency domain has been satisfied by implementation of time-frequency signal processing techniques, such as Hilbert-Huang Transform (HHT). HHT analysis was proposed to detect and capture transient phenomena occur in the non-stationary signal. In recent years, HHT has been widely used as time-frequency analysis as signal processing method Huang et al. (1998) ,Shi and Luo (2003). HHT was proposed as newly developed and powerful method to analyze non-linear and non-stationary signal Bin et al. (2012).

However, this method has the difficulty in selecting the suitable IMF for the next data post-processing method, which is Hilbert Transform (HT). Since HHT through Empirical Mode Decomposition (EMD) will decompose the signal into the different monocomponent and symmetric component by the sifting process. The monocomponent signal is called as intrinsic mode function (IMF) (Manjula and Sarma, 2012). The main drawback of this approach is the necessity to know a priori the frequencies and level of original signal that should be analysed Ricci and Pennacchi (2011). The HHT analysis in this case is not completely automatic since the interaction of skilled user is needed to select which IMF level was suitable for further analysed. Therefore, automatic selection for better IMF was needed to overcome this problem. The mathematical computational technique and statistical value analysis were applied by the researcher to increase the degree of automation then eliminates the interaction of skilled user to select the relevant IMF.

There have been relatively few recent studies and statistical approach on measurable quality for automatic selecting relevant and appropriate intrinsic mode function (IMF). Maji et al. (2013) proposed variance and standard deviation as statistical value to differentiate each level of the decomposition of intrinsic mode function (IMF). The research was done using electrocardiogram (ECG) signal in order to detect Artificial Fibrillation (AF) rhythm and normal rhythm. Ricci and Pennacchi (2011) demonstrated Merit Index as an indicator that allows automatic selection of IMF level. The research utilizes rotary element (gear) signal to test the efficiency of merit index in selecting of relevant and appropriate IMF. The method works as a measure of periodicity degree and absolute skewness of each IMF level. In monitoring rotating machines, Kedadouche et al. (2014) introduced computation of correlation coefficient value for each level of IMF as quantifiable quality in selecting appropriate IMF level. In the research, vibration signal was captured from rolling element (bearing), then the signal was extracted using a hybrid method of Minimum Entropy Deconvolution (MED), Empirical Mode Decomposition (EMD) and Teager Energy Operator (TEO). The selected IMF is the IMF that presents the higher value of correlation coefficient as compared to the original signal. de Souza et al. (2014) presented an Energy-Based approach through mutual information (MI) coefficient as a method of selection relevant IMF. The research was done by applying the synthetic signal with embedded in white noise and real world signal. Mutual Information (MI) was also utilized as a method to select appropriate IMF in biomedical signal processing Ricci and Pennacchi (2011).

This paper proposed Integrated Kurtosis Algorithm for Z-notch filter hybrid with higher order statistical method (Kurtosis) as the automatic selection of intrinsic mode function (IMF). The Ikaz was chosen since the approach of this method was adaptive in general and detects very well any changes and uncertainties of the measured signal (Nuawi et al., 2008). Unlike the existing statistical analysis, such as variance, standard deviation, and kurtosis, I-Kaz method was capable of indicating both amplitude and frequency difference by simultaneously obtaining the I-Kaz representation and I-Kaz coefficient, $Z\sigma$. Details experimental result was discussed by Nuawi et al. (2008) and Rizal et al. (2013) using vibrational signal acquire from rotating machinery part (Bearing) and detect tool wear during turning process respectively. The research conducted by Nuawi 2014 et al, the I-kaz was compared to variance and the results are variance parameter was unable to detect both amplitude and frequency changes in the non-stationary signal. Thus, the I-Kaz method was reliable especially for monitoring purpose where the observation on the changes of the signal amplitude and frequency were commonly required (Nuawi et al., 2008).

The effectiveness and reliability of the Ikaz-kurtosis ratio as the automatic selection of IMF was done using artificial pressure transient signal and random signal generate using Matlab and the results revealed that IMF that contains the maximum value of Ikaz-kurtosis ratio coefficient was relevant and appropriate to be further analysed. The research also done by comparing the effectiveness of kurtosis compared to I-kaz as the automatic selection method for better IMF. This paper focused on the implementation of Ikaz-kurtosis ratio coefficient as the automatic selection of intrinsic mode function using real pressure transient signal captured along the 67.9 meter medium density polyethylene pipe with single artificial leak simulator attached at distanced 19.7 meter away from point of analysis. The result for real pressure transient signal shows that the IMF that contains the highest value of Ikaz-kurtosis coefficient was suitable and appropriate to be further analysed. Furthermore, the

Ikaz-kurtosis ratio was proven suitable as automatic selection method for better and relevant IMF. Therefore, the degree of automation for Hilbert Huang Transform (HHT) was improvised to detect pipe leakage in live water distribution system using pressure transient signal.

2 INTEGRATED BASED KURTOSIS ALGORITHM FOR Z-FILTER TECHNIQUE TO KURTOSIS RATIO

2.1 Integrated Based Kurtosis Algorithm for z-filter technique

Integrated Kurtosis-based Algorithm for z-filter technique (I-Kaz) is the method developed based on the concept of data scattering about its centroid. The sampling frequency of the raw signal was chosen as 2.56 referring to Nyquist number (Nuawi et al., 2008). Most of the researcher in signal analysis and processing are comfortable with the number. To avoid the aliasing effect, the maximum frequency span will be of Eq. [1]:

$$F_{\max} = \frac{fs}{2.56} \quad [1]$$

I-kaz decomposes the time domain signal into three level of the frequency range, where x-axis represents the low frequency (LF) with a range of 0 – 0.25 of f_{max}, followed by y-axis represents the high frequency (HF) with a range of 0.25 – 0.5 of f_{max}. Finally, z-axis represents the very high frequency (VF) with range 0.5 of f_{max}. The 0.25 f_{max} and the 0.5 f_{max} was selected as low and high frequency range limits, respectively by referring to the 2nd order of the Daubechies concept in signal decomposition process Daubechies (1992). Referring to the kurtosis, I-kaz method contributes three-dimensional graphical representation of the measured signal frequency distribution. The variance, σ^2 of each frequency band, σL^2 represents a low frequency band, σH^2 represents a high frequency band and σV^2 represents a very high frequency band, which was calculated as in equation 2, 3 and 4 to measure scattering of data distribution.

$$\sigma L^2 = \frac{\sum_{i=1}^{N} (x_i - \mu_L)^2}{n} \quad [2]$$

$$\sigma H^2 = \frac{\sum_{i=1}^{N} (x_i - \mu_H)^2}{n} \quad [3]$$

$$\sigma V^2 = \frac{\sum_{i=1}^{N} (x_i - \mu_V)^2}{n} \quad [4]$$

The I-Kaz coefficient, Ƶσ can be simplified in term of variance, σ as in equation 5 Rizal et al. (2013):

$$Ƶ\sigma = \sqrt{(\sigma L^2)^2 + (\sigma H^2)^2 + (\sigma V^2)^2} \quad [5]$$

2.2 Kurtosis

Kurtosis describes as a measure of spikiness and hence a good indicator of peak analysis for spikes detection in a non-stationary signal component, such as pressure transient. Kurtosis is expressed as:

$$\text{Kurtosis}(x) = \frac{E\{(x-\mu)^4\}cc}{\sigma^4} \quad [6]$$

where μ and σ represent the mean and standard deviation of time series signal, respectively. E illustrates the expectation operation. The kurtosis demonstrates the spikiness and peakedness of probability distribution associated to the instantaneous amplitudes of the time-series analysis Wang et al. (2016). Therefore, the I-kaz-kurtosis ratio expressed as Eq. [7]:

$$ZK\sigma = \frac{(\sqrt{(\sigma L^2)^2 + (\sigma H^2)^2 + (\sigma V^2)^2})(\sigma^4)}{(\mathrm{E}\ \{(\mathrm{x} - \mu)^4\})} \quad [7]$$

  / ISSN 1562-6865 (Online) - ISSN 1063-7710 (Print)

2.3 Algorithm

Automatic Selection of Intrinsic Mode Function (IMF) Based on Pressure Transient Signal:

1. Perform EMD on a pressure transient signal;
2. EMD decomposed the signal into so called level of Intrinsic Mode Function;
3. Calculate the Integrated Kurtosis Algorithm for z-filter technique to kurtosis ratio (Ikaz-Kurtosis) coefficient using Eq. [7];
4. Identified the IMF that corresponds to the largest Ikaz-kurtosis ratio coefficient;
5. Perform Hilbert Transform (HT) and Hilbert Spectrum (HS) for IMF level that contains the largest coefficient of Ikaz-Kurtosis ratio.

3 METHODOLOGY

In this paper, the signal response generated by solenoid valve was acquired using a pressure sensor. During the experiment, a solenoid valve was set to normally closed condition, and thus water hammer phenomena were induced by immediately open and close valve with three consecutive times for each of the data which then captured by MatLab Software.

3.1 Experimental setup

The experimental test was regulated in a circular loop pipeline system with 67.90 meter long. The network was constructed using Medium High-Density Polyethylene pipes (MDPE) with an outer diameter 60 millimeters, 55 millimetres of internal diameter and 2.6 millimeters mean thickness. An artificial leak simulator was installed 19.7 meters away from point of analysis in the pipeline system. The outlet of the pipe is kept connected to a free surface tank where the water from the pipe ends discharged. This is to prevent sudden expansion phenomena of the pressure waves and minimizing negative pressure wave, as it will affect the collected data from the transducer. The speed of sound calibrate from the test rig is 524.3005 m/s.

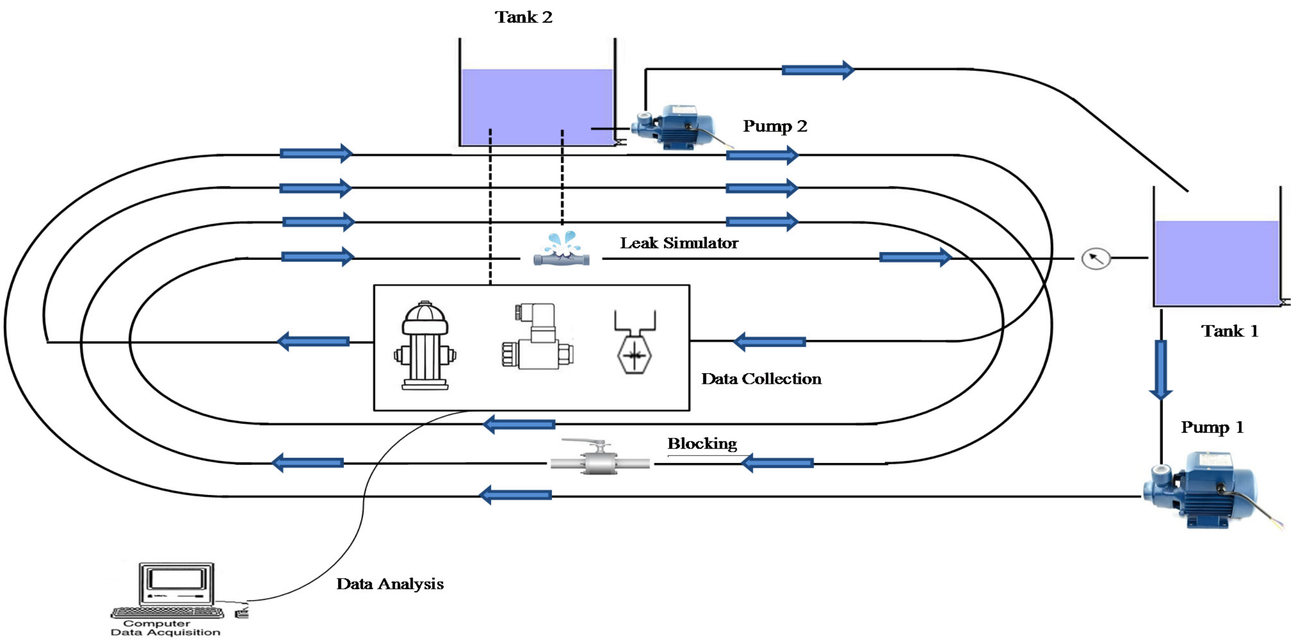

Figure 1. Schematic diagram of test rig design for laboratory and experimental test.

The schematic diagram above (Figure 1) shows the pressure sensor and solenoid valve were installed 10 meters away from the electric pump to avoid too much noise during collection the data. This is due to the wave characteristic as turbulent flow when the water exit from pump outlet, the flow is approaching laminar or steady state condition due to the distance traveled. This phenomenon generated by friction from wall pipe due to water flow and damping. Therefore, 10-meter long distance from pump to the sensor is adequate to reduce the noise. The methods used for the research mainly are pressure transient responsive. This method is commonly used as the basic technique in the pipeline leakage detection method. The idea is proposed from the usage of pressure transient flow of water in the pipeline network. Theoretically, pressure transient responds occur when there is a sudden change in the flow of water by closing or opening the valve in the pipeline network. As the phenomena happened inside the pipeline network, wave propagation of water will be created along the pipeline network and also the characteristic of wave propagation will be used as a medium to detect leak and pipe feature along the pipeline network. The wave inside the pipeline network will propagate with different signal depend on the size of the leak, a distance of leak, the type of pipe feature and distance of pipe feature.

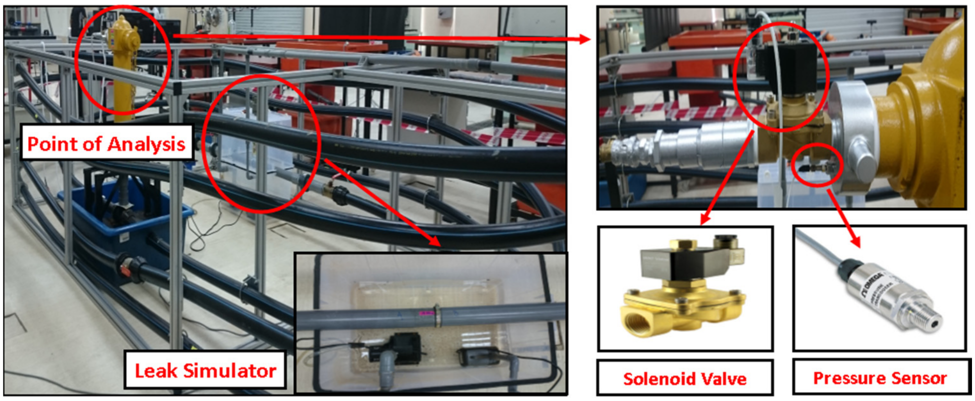

Figure 2. Experimental test rig in laboratory scale.

Figure 2 shows the experimental test rig installed in Fluid Mechanic Laboratory, University Malaysia Pahang Malaysia. The fire hydrant cap was designed and fabricated to fix the solenoid valve and pressure sensor as well as to make the system robust for a field test. Both components play an important role in each task as solenoid valve is used to generate the water hammer phenomenon and pressure sensor is used to acquire the signal. In a few cases, the system will shut down by itself due to sudden opening or closing valve and malfunction of the pump. This will generate "water hammer" on the pipeline system. This phenomenon took in all of the pressure pipe systems, frequently causing about strong vibration and destruction on pipeline system Amin et al. (2015). To generate this phenomenon, solenoid valve (Figure 2) utilized as a tool to create water hammer along the pipeline system. This situation creates the same phenomenon in real life when there is pressure disorder occur through the underground pipe.

4 RESULTS AND DISCUSSIONS

The experimental data acquired from the transducers using Matlab represents the pipeline system behavior and characteristic. The signal that acquires does retrieve the characteristic of the whole pipeline system itself. The pressure transient waves propagate along the pipeline system in both directions away from the burst origin through the speed of sound in water distribution system. In this paper, Hilbert-Huang Transform (HHT), which contains Empirical Mode Decomposition Method (EMD) as data pre-processing method and Hilbert Transform (HT) as data post-processing method, was implemented as a tool to analyze the pressure transient signal.

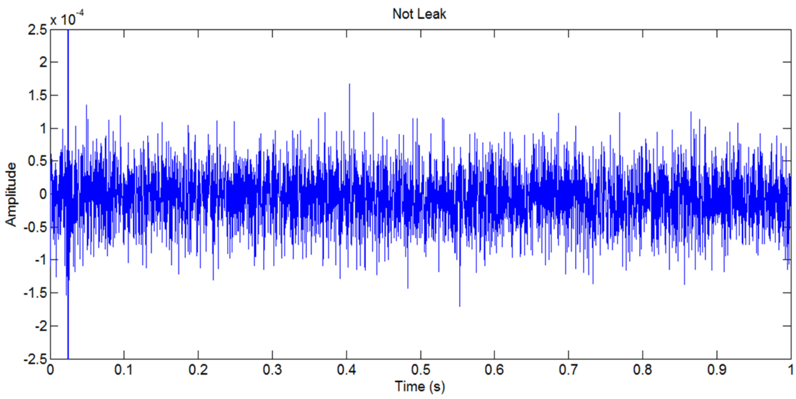

Figure 3. Signal response for no leak data.

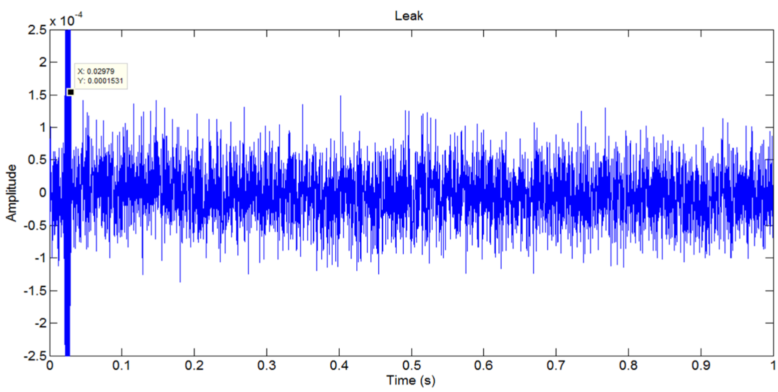

Figure 4. Signal response for leak data.

Figure 3 represents the response signal for the no leak data. Figure 4 represents the signal response for the leak data. The first maximum amplitude on the signal response presented in both Figure 3 and 4 represents the opening and closing of the solenoid valve that produces pressure transient, which is transmitted and reflected around the pipe system. The original response was recorded at three different levels of pressure: 1 bar and 2 bar. The signal captured using a different level of pressure are showing different results. The higher pressure creates a higher frequency of the signal and causes higher amplitude of the signal.

The response signal for no leak and leak data presented in Figure 3 and 4 contain the characteristic of pipeline systems, such as reflection signal from pipe fitting, blockage, outlet, and leak. From the theoretical calculation and measured distance, the reflection signal and spikes of the leak will appear at position 0.075 (amplitude time graph) second, which is equal to 19.7 meters (amplitude distance graph), while 0.152 seconds (amplitude time graph), which is equal to 39.8 meters (amplitude distance graph) for an outlet. Accordingly, for the no leak data, the presence of spikes appeared at position 0.152 seconds (amplitude time graph), which is equal to 39.8 meter (amplitude distance graph) where it is an outlet. From the observation of Figure 3 (No leak response) and Figure 4 (leak response), there were no possible spikes or transient that represent characteristic (leak, outlet, blockage, pipe fitting) of pipeline system due to the influence of surrounding noise. Thus, in order to extract the information of pipeline characteristic from the raw signal (Figure 3 and 4), the signal analysis was implemented as a tool to reveal the results.

Therefore, as presented in flow chart 1, Hilbert-Huang Transform (HHT) was implemented as signal analysis and data extraction method to reveal all of the pipeline characteristics. As we proceed on flow chart 1, the signal response will undergo the first step of data analysis and extraction method. The EMD will decompose the signal into a different level of the frequency band and amplitude called Intrinsic Mode Function (IMF).

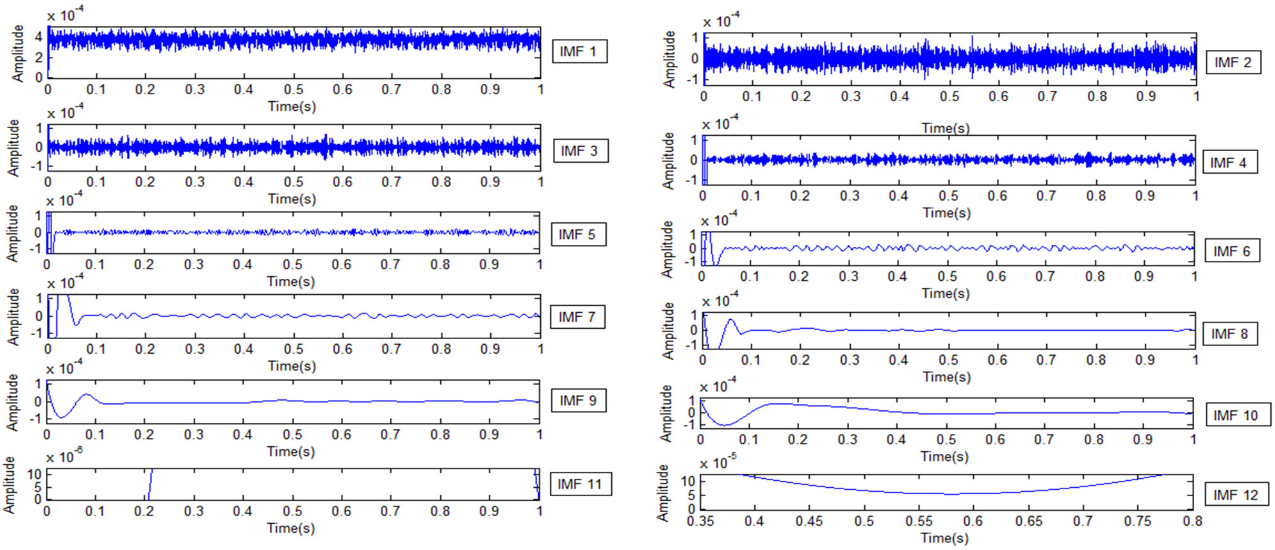

Figure 5. IMF level 1-12 for no leak data.

EMD decomposes the signal response acquired from the test rig into 13 levels of intrinsic mode function (IMF). Figure 5 shows the amplitude versus time for the first 12 levels of IMF. The first level of IMF is a group of higher frequency signals which is the noise signal. The last level was a reserve for the lower frequency signals. The first and second level of IMF was avoided for further analysis because these levels contain noise frequency signals. Meanwhile, IMF level 7 and the residue contains basic respond of the network. All these IMF were, therefore, discarded. The rest which are IMF level 3 – 6 have been recombined to produce a signal without noise Ghazali et al. (2012). Therefore, in order to identify which level of IMF is suitable for the final step of Hilbert-Huang Transform (HHT), which is Hilbert Transform (HT), Integrated Kurtosis Algorithm for Z-filter technique to kurtosis ratio (Ikaz-Kurtosis) was implemented. Since EMD decomposed the signal response into 13 levels of IMF, the Ikaz-Kurtosis ratio was utilized to compute the coefficient of each level. Therefore, each level of IMF contains the value of Ikaz-Kurtosis ratio coefficient.

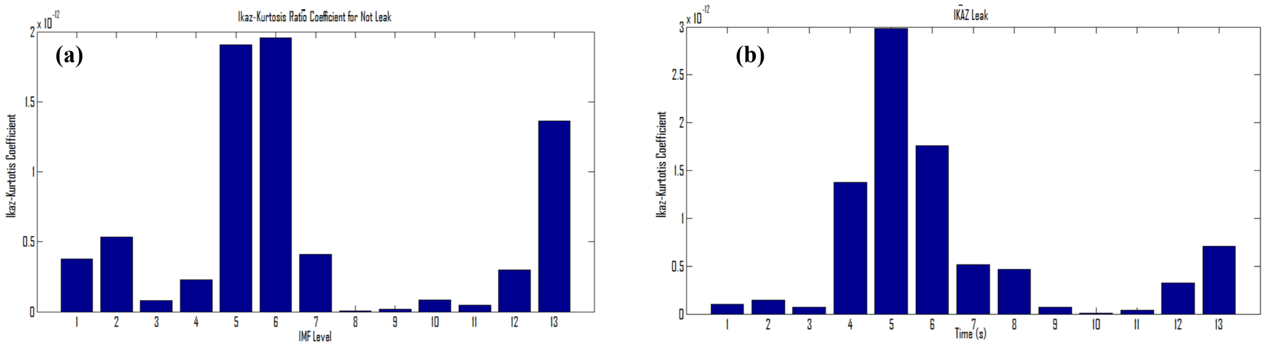

Figure 6. (a) Ikaz-Kurtosis ratio coefficient for no leak data; (b) Ikaz-Kurtosis ratio for leak data coefficient.

Figure 6a and 6b represent the Ikaz-Kurtosis ratio coefficient histogram. The X-axis shows the IMF level. Meanwhile, Y-axis shows the value of Ikaz-Kurtosis ratio coefficient. From the observation, the maximum and highest value of Ikaz-Kurtosis coefficient was the most suitable IMF level for the post-processing and the final step of Hilbert-Huang Transform (HHT) analysis, which is Hilbert Transform (HT). This is because the IMF level that contains the highest value of Ikaz-Kurtosis ratio consists of the IMF selection criterion, which is clear and narrow spikes. The lower the value of Ikaz-Kurtosis ratio, the obscure of clear and narrow spikes, which are the main selecting criterion of IMF. The first 4 IMF contains the highest value Ikaz-Kurtosis ratio coefficient was plotted in Figure 7 and 8.

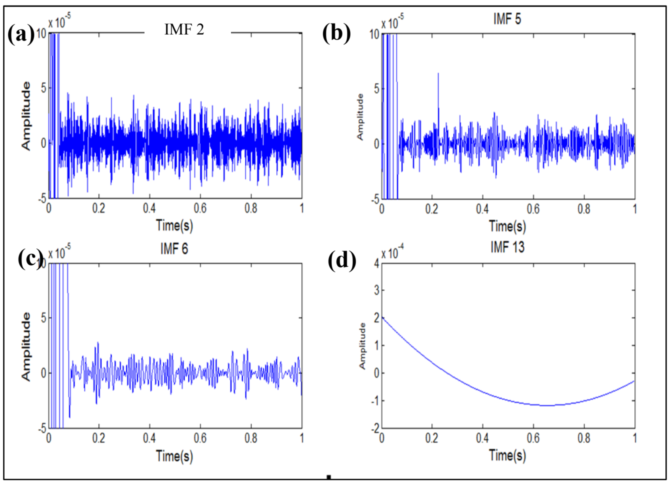

Figure 7. IMF for no leak data (a) Level 2 (b) Level 5, (c) Level 6 and (d) Level 13.

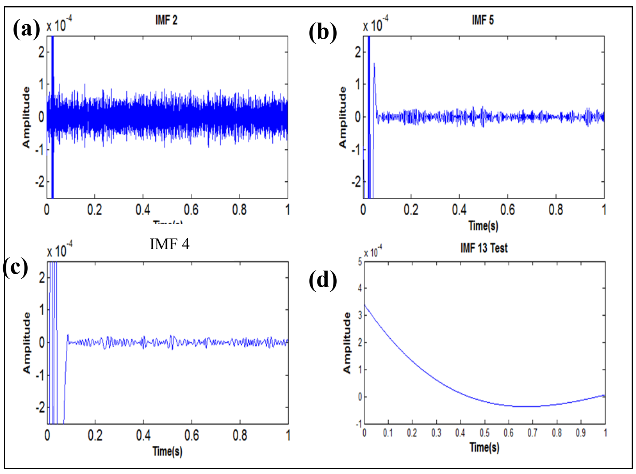

Figure 8. IMF for no leak data (a) Level 4, (b) Level 5, (c) Level 6 and (d) Level 13.

Figure 7c and 8b show the amplitude versus time graph for the IMF level that contains the highest value of Ikaz-Kurtosis ratio. From the observation, it is difficult to select visually which IMF level is suitable for further analysis. Based on IMF selecting criterion, clear spikes and lower noise frequency is presented by the IMF that contains the highest value of Ikaz-Kurtosis ratio coefficient. Therefore, these level was selected for further analysis, which is Hilbert Transform (HT). For no leak data, IMF level 6 is chosen meanwhile for leak data, IMF level 5 is chosen for further analysis. The final results of Hilbert-Huang Transform (HHT) are presented in Figure 9,10,11,and 12.

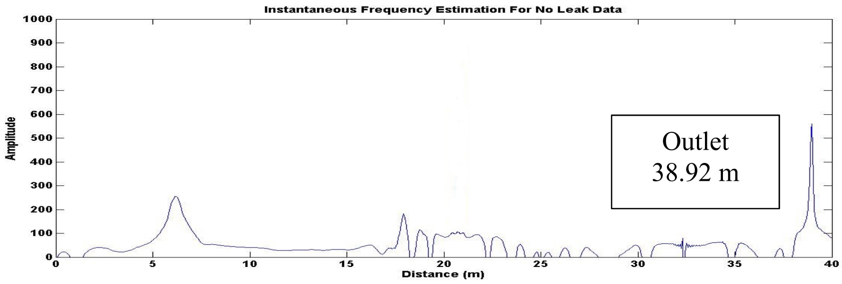

Figure 9. Instantaneous Frequency Estimation versus distance (m) graph for no leak data.

Figure 9,10,11, and 12 illustrates the final results of Hilbert-Huang Transform (HHT), which is Hilbert Transform (HT) for IMF level that contains the highest value of Ikaz-Kurtosis ratio coefficient (Ikaz-Kurtosis). The graph presented in Figure 9 and 10 is the instantaneous frequency estimation for no leak and leak data. During this phase, nonstationary signal, in which frequency value changes at any moments, is more useful to characterize a signal in term of its instantaneous frequency. Instantaneous frequency describes the frequency that locally fits the signal (Ghazali, 2012).

The consequences of the trials are from pipe systems both with the leak and without a leak. The Amplitude distance (m) graph of the processed results from the first signal response (Figure 3) using the pipe network without leak is shown in Figure 9. Due to the pipe system used as the circular pipe without fixing the pipe fitting, therefore there are two main features in the network that produce the reflection waves, being the outlet and control valve. The control valve was installed at the end (near an outlet) of the pipeline system due to control and stabilize the variation of pressure in the pipeline system. Every peak and spikes presence have seen in the analyzed results corresponded to the time that the wave takes to travel along the pipeline system from the reflection points (pipe feature/leak) and return to the point of analysis (pressure transducer). The distance (Figure 9) of reflection point from the point of analysis (pressure transducer) is acquired essentially by multiplying the time delay data corresponding to each of the peaks by speed of sound in the pipeline system (c = 524.3005 m/s) and divide by two account as return journey (Taghvaei et al., 2006).

From the observation, it can be seen that there were peaks up to about 0.03 seconds or 7 meters.These can be ignored due to a part of analysis process (these can be set to zero using liftering) Taghvaei et al. (2006).

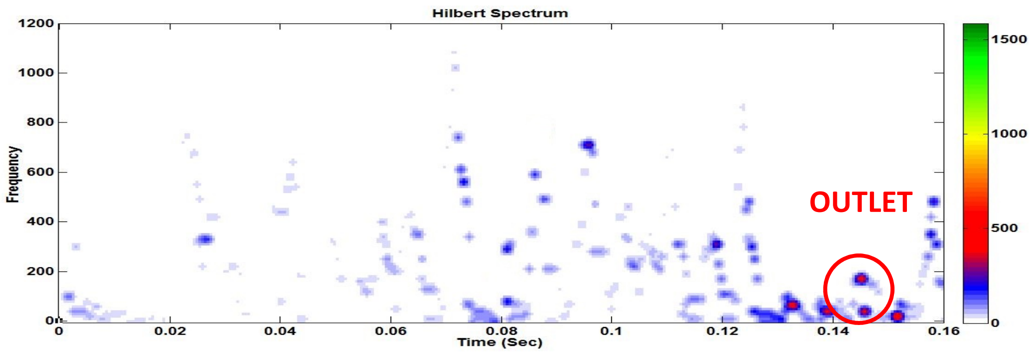

Figure 10. Hilbert Spectrum for no leak data.

For the first experiment, the water was pumped to the pipeline system without leakage with the pressure of 1 bar.The final results were shown in Figure 9 (Amplitude versus distance graph) and Figure 10 (Hilbert spectrum). Referring to Figure 9 and 10, peaks can be seen that the pipeline characteristic which is the peak/spikes appeared at 0.148 seconds (Figure 10 and 12) and 38.92 meters (Figure 9 and 11). By comparing the results with the measured distance, the presence of peaks on that time and distance represented the reflection signal from pipe outlet or control valve. Due to pipe outlet and control valve were very nearer to each other. Therefore, the reflection of both feature wasoverlapping with each other. The Hilbert spectrum was tabulated in Figure 10. It can be noticed that the position of pipe outlet reflection was same as Figure 9, but from the Hilbert spectrum graph, as presented in Figure 10, the pipe feature (leak, blockage, pipe fitting, outlet) produced new frequency response. As shown in Figure 10, from the colour map indicator illustrated on the right-hand side represent the amplitude height, we noticed that the pipe feature was produced the frequency propagation around 50 Hz to 100 Hz.

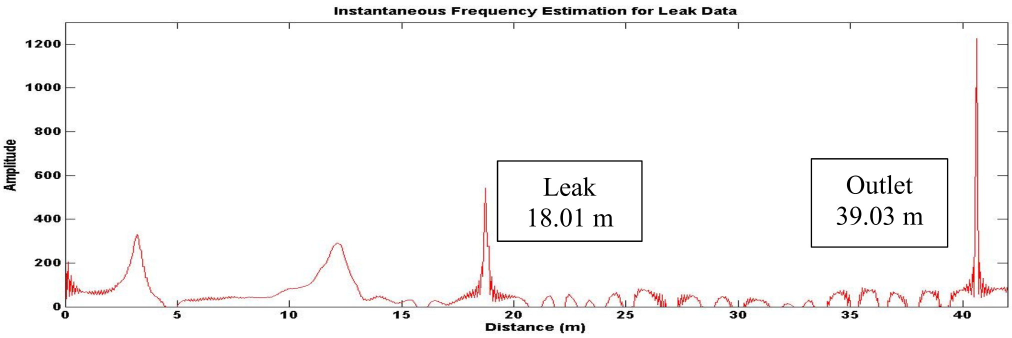

Figure 11 : Instantaneous Frequency Estimation versus distance (m) graph for leak data.

In the next experiment, artificial leak was created using a 6 millimetre whole drill at 19.7 meters away from the point of analysis (pressure transducer). The water was pumped to the pipeline's system with the pressure of 1 bar similar to the first experiment. The system was run for about 5 minutes to stabilize the flow before acquiring the data. The final results were shown in Figure 11 (Amplitude versus distance graph) and Figure 12 (Hilbert spectrum). The results were observed by comparing the measured distance of leak and pipe outlet. Referring to Figure 11 and 12, starting at 0.03 seconds or 7 meters away, peaks also can be seen that the pipeline characteristic which is the peak/spikes appeared at 0.072 seconds (Figure 12) and 18.01 meter (Figure 11) present the response of reflection signal from leak, while the peaks/spikes appeared at 0.155 seconds (Figure 12) and 39.02 meters (Figure 11) represent the response of reflection signal from pipe outlet.

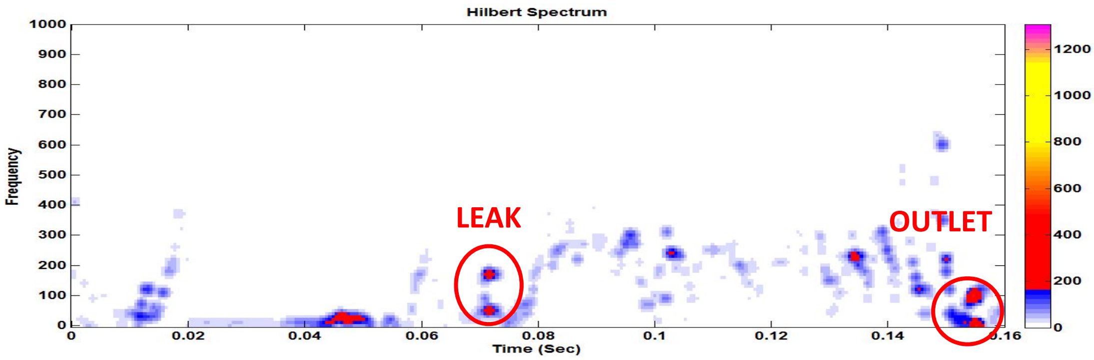

Figure 12. Hilbert Spectrum for leak data.

Figure 12 represents the Hilbert Transform for the leak data. As shown in Figure 12, the frequency response for pipe feature and the colour map indicator illustrated on the right-hand side represent the amplitude of the response. It was found that the leak was produced at the frequency propagation around 50 Hz to 200 Hz, meanwhile the pipe outlet produced the frequency response at around 50 – 100 HZ. By comparing to the results of IMF presented before, the clear spikes and transient are more clearly seen after Hilbert Transform (HT) were used in this phase. Therefore, it proves that the I-kaz-kurtosis ratio work properly as the self-decision method for IMF.

Table 1. Comparison of position spikes between measured position and experimental position.

Water Pressure	Signal Response	Pipe Feature	Measured Position (m)	Measured Position (sec)	IMF contain Maximum Ikaz-Kurtosis ratio Coefficient	Experimental Position (m)	Experimental Position (sec)	Error %
1 bar	Leak Data	Leak	19.7	0.075	6	18.01	0.072	4.00
		Outlet	39.8	0.151		39.03	0.155	1.90
	No Leak Data	Outlet	39.8	0.151	5	38.92	0.148	2.20
2 bar	Leak Data	Leak	19.7	0.075	4	18.71	0.071	1.00
		Outlet	39.8	0.151		35.91	0.137	3.89
	No Leak Data	Outlet	39.8	0.151	5	37.58	0.143	2.22

Table 1 illustrates the comparison of position spikes between the measured position and experimental position. For leak data with water pressure of 1 bar, the position of leak shows 4% error and the position of

  / ISSN 1562-6865 (Online) - ISSN 1063-7710 (Print)

outlet shows 1.9% error. Meanwhile, for no leak data presented 2.2% error for outlet position. Beside that, leak data with water pressure of 2 bar, the position of leak shows 1.0% error and the position of outlet shows 3.89% error. Meanwhile for no leak data presented 2.22% error for outlet position. From the final part of HHT analysis, it is clearly shown that the position of pipe feature, leak and pipe outlet appears at the same position as compared to each original position and measured positioned. It also proves that HHT analysis is able to detect and position the transient event occurred in the non-stationary pressure transient signal.

5 CONCLUSIONS

This paper discussed the self-decision method for IMF selection through Hibert Huang Transform (HHT) analysis. The result proves the I-kaz-kurtosis ratio is suitable and advisable self-decision method for IMF selection to implement in Hilbert-Huang Transform (HHT) analysis. The development of automated self-decision of IMF through HHT has been built and statistically analysed using I-kaz-kurtosis ratio. Therefore, this method was proposed and advised to be implemented. By efficiently utilizing I-kaz-kurtosis ratio, the issue of IMF selection was overcome. Therefore, degree of automation for Hilbert Huang Transform (HHT) was improvised to detect pipe leakage in live water distribution system using pressure transient signal..

REFFERENCES

Amin, M., Ghazali, M., Piremli, M., Hamat, A. & Adnan, N. (2015) Published. Leak detection in Medium Density Polyethylene (MDPE) Pipe Using Pressure Transient Method. *IOP Conference Series: Materials Science and Engineering*, 2015. IOP Publishing, 012007.

Bin, G., Gao, J., Li, X. & Dhillon, B. (2012). Early Fault Diagnosis of Rotating Machinery Based on Wavelet Packets—Empirical Mode Decomposition Feature Extraction and Neural Network. *Mechanical Systems and Signal Processing,* 27**,** 696-711.

Colombo, A.F., Lee, P. & Karney, B.W. (2009). A Selective Literature Review of Transient-Based Leak Detection Methods. *Journal of Hydro-environment Research,* 2**,** 212-227.

Daubechies, I. (1992). *Ten Lectures on Wavelets*, SIAM.

De Souza, D.B., Chanussot, J. & Favre, A.-C. (2014) Published. On Selecting Relevant Intrinsic Mode Functions in Empirical Mode Decomposition: An Energy-Based Approach. I*EEE International Conference on Acoustics, Speech and Signal Processing (ICASSP)*, 2014. IEEE, 325-329.

Ghazali, M., Beck, S., Shucksmith, J., Boxall, J. & Staszewski, W. (2012). Comparative Study of Instantaneous Frequency Based Methods for Leak Detection in Pipeline Networks. *Mechanical Systems and Signal Processing,* 29**,** 187-200.

Ghazali, M.F. 2012. Leak Detection Using Instantaneous Frequency Analysis*. PhD Thesis,* University of Sheffield.

Huang, N.E., Shen, Z., Long, S.R., Wu, M.C., Shih, H.H., Zheng, Q., Yen, N.-C., Tung, C.C. & Liu, H.H. (1998) Published. The Empirical Mode Decomposition and The Hilbert Spectrum for Nonlinear and Non-Stationary Time Series Analysis. *Proceedings of the Royal Society of London A: Mathematical, Physical and Engineering Sciences*, 1998. The Royal Society, 903-995.

Kedadouche, M., Thomas, M. & Tahan, A. (2014). Monitoring Machines by Using a Hybrid Method Combining MED, EMD, and TKEO. *Advances in Acoustics and Vibration,* 2014.

Lai, C. (1991). Unaccounted for Water and The Economics of Leak Detection. *Water Supply,* 9**,** 4.

Liou, C.P. (1998). Pipeline Leak Detection by Impulse Response Extraction. *Journal of Fluids Engineering,* 120**,** 833-838.

Maji, U., Mitra, M. & Pal, S. (2013). Automatic Detection of Atrial Fibrillation Using Empirical Mode Decomposition and Statistical Approach. *Procedia Technology,* 10**,** 45-52.

Manjula, M. & Sarma, A. (2012). Comparison of Empirical Mode Decomposition and Wavelet Based Classification of Power Quality Events. *Energy Procedia,* 14**,** 1156-1162.

Nuawi, M.Z., Nor, M.J.M., Jamaludin, N., Abdullah, S., Lamin, F. & Nizwan, C. (2008). Development of Integrated Kurtosis-Based Algorithm for Z-Filter Technique. *Journal of applied sciences,* 8**,** 1541-1547.

Ricci, R. & Pennacchi, P. (2011). Diagnostics of Gear Faults Based on EMD and Automatic Selection of Intrinsic Mode Functions. *Mechanical Systems and Signal Processing,* 25**,** 821-838.

Rizal, M., Ghani, J.A., Nuawi, M.Z. & Haron, C.H.C. (2013). A Comparative Study of I-kaz Based Signal Analysis Techniques: Application to Detect Tool Wear during Turning Process. *Jurnal Teknologi,* 66.

Shi, C.-X. & Luo, Q.-F. (2003). Hilbert-Huang Transform and Wavelet Analysis of Time History Signal. *Acta Seismologica Sinica,* 16**,** 422-429.

Stephens, M.L., Simpson, A.R., Lambert, M.F., Vítkovský, J. & Nixon, J. (2002) Published. The Detection Of Pipeline Blockages Using Transients In The Field. *South Australian Regional Conf.*, 2002.

Taghvaei, M., Beck, S. & Staszewski, W. (2006). Leak Detection in Pipelines Using Cepstrum Analysis. *Measurement Science and Technology,* 17**,** 367.

Wang, Y., Xiang, J., Markert, R. & Liang, M. (2016). Spectral Kurtosis for Fault Detection, Diagnosis and Prognostics of Rotating Machines: A Review with Applications. *Mechanical Systems and Signal Processing,* 66**,** 679-698.

MATCHED-FIELD PROCESSING METHOD FOR LEAK DETECTION IN A PIPE

XUN WANG[1] & MOHAMED S. GHIDAOUI[2]

[1,2] Department of Civil and Environmental Engineering, Hong Kong University of Science and Technology,
Clear Water Bay, Hong Kong, China,
xunwang@ust.hk; ghidaoui@ust.hk

ABSTRACT

This paper proposes a transient leak detection method in a pipeline system which uses head measurements in the frequency domain. A matched-field processing (MFP) approach is used to separately estimate location and size of a leak. The leak location is determined by matching the model with the measurement, more exactly by maximizing the inner product between a unit weighting vector and the measurement. This maximum occurs in the case that the weighting vector and the measurement have the same direction implying that the parameters behind are identical. Then, the leak size is estimated via least square. This MFP approach is able to use not only the resonant frequencies but also all the frequencies being invoked. Besides, the proposed method is a maximum likelihood estimation and equivalent to a matched-filter approach which maximizes the signal-to-noise ratio (SNR). Experiments on simulated data for a single pipe system illustrate the estimation efficiency of the MFP method. The simulation results justify that the proposed leak detection method is able to localize not only a single leak but also multiple leaks.

Keywords: Defect detection; leak localization; fluid transient; matched-field processing.

1 INTRODUCTION

Leakage detection in a pipeline system is an important issue in water supply systems because leaks result in financial losses, wastage of water, energy and other resources used to treat the water, and pose health risk issues since leaks are potential entry points for contaminants (Colombo et al., 2009). In Hong Kong, for example, leak water annually costs more than one billion HK dollar due to the aging water infrastructure. Therefore, a fast, accurate and low-cost leak localization method is under searching.

Fluid transients-based defect detection methodology, where a hydraulic pressure wave is introduced into the pipe system and the pressure response is measured at specified location(s), is a promising general approach for the detection of leaks and other defects. The basic premise of this approach to defect identification and characterization is that a measured wave signal in the fluid in the conduit is modified by its interaction with the physical system as it propagates and reflects throughout the system. Accordingly, it contains information of the conduit's properties and state. Examples of such approach are the (1) Transient Reflection based Method (TRM), such as Brunone (1999), Brunone and Ferrante (2001) and Covas et al. (2005b); (2) Transient Damping based Method (TDM) by Wang et al. (2002); (3) Frequency Response based Method (FRM) by Liou (1998), Mpesha et al. (2001), Ferrante and Brunone (2003), Covas et al. (2005a), Lee et al. (2003), Lee et al. (2005a), Lee et al. (2006), Sattar and Chaudhry (2008) and Taghvaei et al. (2010); and (4) Inverse Transient based Method (ITM) studied in Liggett and Chen (1994), Vítkovsky et al. (2000), Stephens (2008) and Covas and Ramos (2010).

Matched-field processing (MFP) is originally an array processing technique for the source localization problem, which generalizes the plane wave beamforming method (Krim and Viberg, 1996). It estimates the model parameter by matching the computational sound field to the measurements and is proved to be a maximum likelihood estimation (MLE) (Krim and Viberg, 1996; Wang et al., 2016a; Wang et al., 2016b). The MFP approach has been applied to the sound source reconstruction in ocean (Baggeroer et al., 1993; Kuperman and Lynch, 2004). Recently, Tolstoy et al. (2009) and Tolstoy (2010) made an initial attempt of applying MFP to blockage detection in a sewer pipe. Note that in the last two works the acoustic field in pipe is not modeled such that some of the concerned unknown parameters cannot be estimated. In the present article, the leakage detection problem is solved using the MFP approach. The leak position and size are parametrized and explicitly estimated. This method is proved to be a matched-filter approach, which maximizes the signal-to-noise ratio (SNR) and thus is robust with respect to noises. The noise can be assumed as either white or non-white noise; in the latter case a whitening filter is applied to meet the model assumption.

This paper begins with a model description. Then, the MFP method is introduced: the leak position and size estimates are explicitly given. Numerical simulation results justify the estimation efficiencies. The performance of the proposed method for multiple leaks is also discussed.

2 MODEL

This section presents the pipeline model considered in the paper. Consider a single pipeline bounded by an upstream and a downstream node, whose coordinates are $x = x^U = 0$ and $x = x^D$, respectively. A sensor is assumed to be set near the downstream node whose coordinate is denoted by x^M. Here, the model of single leak is considered, the leak location is $x^L(x^L < x^M)$, z^L denotes the elevation of the pipe at the leak, q_0^L and h_0^L stand for the steady-state discharge and head at the leak, respectively. The leak size is represented by the lumped leak parameter $s^L = C^d A^L$, where C^d is the discharge coefficient of the leak and A^L is the flow area of the leak orifice. The steady-state discharge of leak is related to the lumped leak parameter by $q_0^L = s^L\sqrt{2g(h_0^L - z^L)}$ in which g is the gravitational acceleration. The discharge and head oscillations due to a fluid transient are represented by q and h. Given the discharge $q(x^U)$ and head $h(x^U)$, the quantities at x^M can be computed in the following way (Chaudhry, 2014):

$$\begin{pmatrix} q(x^M) \\ h(x^M) \end{pmatrix} = M^{NL}(x^M - x^L)\begin{pmatrix} 1 & -\dfrac{q_0^L}{2(h_0^L - z^L)} \\ 0 & 1 \end{pmatrix} M^{NL}(x^L)\begin{pmatrix} q(x^U) \\ h(x^U) \end{pmatrix} \qquad [1]$$

in which:

$$M^{NL}(x) = \begin{pmatrix} \cosh(\mu x) & -\dfrac{1}{Z}\sinh(\mu x) \\ -Z\sinh(\mu x) & \cosh(\mu x) \end{pmatrix} \qquad [2]$$

is the field matrix, $Z = \mu a^2 / (i\omega g A)$ is the characteristic impedance, $a^{-1}\sqrt{-\omega^2 + igA\omega R}$ is the propagation function, a is the speed of sound, ω is the angular frequency, A is the area of pipeline, and R is the frictional resistance term. Note that $R = (Fq_0)/(gDA^2)$ for turbulent flows where F is the Darcy-Weisbach friction factor, q_0 is the steady-state discharge and D is the pipe diameter. If the pipe is frictionless (F=0), $\mu = ik$ where $k = \omega / a$ is the wavenumber. The transfer matrix on the right-hand side of Eq. [1] can be simplified as:

$$M^{NL}(x^M - x^L)\begin{pmatrix} 1 & -\frac{q_0^L}{2(h_0^L - z^L)} \\ 0 & 1 \end{pmatrix} M^{NL}(x^L) = M^{NL}(x^M) + s^L M^{SL}(x^L), \qquad [3]$$

in which:

$$M^{SL}(x^L) = \sqrt{\frac{g}{2(h_0^L - z^L)}} \times \begin{pmatrix} Z\sinh\left(\mu x^L\right)\cosh\left(\mu(x^M - x^L)\right) & -\cosh\left(\mu x^L\right)\cosh\left(\mu(x^M - x^L)\right) \\ -Z^2\sinh\left(\mu x^L\right)\sinh\left(\mu(x^M - x^L)\right) & Z\cosh\left(\mu x^L\right)\sinh\left(\mu(x^M - x^L)\right) \end{pmatrix} \qquad [4]$$

is a matrix related to the location of the leak, but independent of the leakage size. By combining the above equations, the head at the measurement station for a given angular frequency is:

$$h^M(\omega) = h^{NL}(\omega) + s^L G(\omega, x^L), \qquad [5]$$

wherein:

$$h^{NL}(\omega) = -Z\sinh\left(\mu x^M\right) q(x^U) + \cosh\left(\mu x^M\right) h(x^U) \qquad [6]$$

and:

$$G(\omega, x^L) = -\frac{\sqrt{g}Z\sinh\left(\mu(x^M - x^L)\right)}{\sqrt{2(h_0^L - z^L)}}\left(Z\sinh\left(\mu x^L\right) q(x^U) - \cosh\left(\mu x^L\right) h(x^U)\right). \qquad [7]$$

Let h_j^M denote the measured head at the frequency ω_j. The measurement is assumed to be contaminated by a noise n_j, i.e.:

$$h_j^M = h^{NL}(\omega_j) + s^L G(\omega_j, x^L) + n_j. \qquad [8]$$

The purpose of this work is to use the measured head at J frequencies, denoted as:

$$\mathbf{h}^M = (h_1^M, \cdots, h_J^M), \qquad [9]$$

to estimate the leak position and the leak size. Here, let us define the head difference due to leakage:

$$\Delta\mathbf{h} = (\Delta h_1, \cdots, \Delta h_J)^\top, \text{ where } \Delta h_j = h_j^M - h_j^{NL} \ (j = 1, \cdots, J), \qquad [10]$$

and:

$$\mathbf{G}(x^L) = (G(\omega_1, x^L), \cdots, G(\omega_J, x^L))^\top, \qquad [11]$$

and denote the error vector by:

$$\mathbf{n} = (n_1, \cdots, n_J)^\top, \qquad [12]$$

then the head difference is represented by:

$$\Delta\mathbf{h} = s^L \mathbf{G}(x^L) + \mathbf{n}. \qquad [13]$$

Note that since the head in the frequency domain is obtained by a discrete Fourier transform (DFT) which is the summation of a large amount of time domain signal, according to the Central Limit Theorem the noise in the frequency domain can be reasonably assumed to follow a (zero-mean) Gaussian distribution. In the next section, the leak detection problem is solved under the assumption of Gaussian white noise. For non-white noise, the measurement signal can be whitened before using the proposed leak detection method, such that the noise distribution assumption holds.

3 LEAK DETECTION USING MATCHED-FIELD PROCESSING

The leakage localization problem is solved using the matched-field processing (MFP) method. The noise vector is assumed to follow a zero-mean Gaussian distribution. The idea is to adjust a unit vector $w = (w_1, ..., w_J)^T$ ($\|w\| = 1$) to have the same direction (in the J-dimensional complex vector space) with the measurement. Here, the output function is defined by the inner product between the weighting vector w and the measured head difference Δh:

$$B \stackrel{\triangle}{=} <\mathbf{w}, \Delta\mathbf{h}> = \mathbf{w}^H \Delta\mathbf{h} \in \mathbb{C}, \qquad [14]$$

in which the superscript H stands for the conjugate transpose. When w has the same direction as Δh, i.e., $|B|^2$ reaches maximum, so that the concerned parameters behind w and Δh are the same. Therefore, the optimal weight is obtained by maximizing:

$$|B|^2 = |\mathbf{w}^H \Delta\mathbf{h}|^2 = \mathbf{w}^H \Delta\mathbf{h} \Delta\mathbf{h}^H \mathbf{w}. \qquad [15]$$

By inserting Eq. [13] into the above equation and maximizing its expectation with respect to w, the optimal weight is obtained:

$$\begin{aligned}\hat{\mathbf{w}} &= \arg\max_{\mathbf{w}} \mathbb{E}(|B|^2) = \arg\max_{\mathbf{w}} \left((s^L)^2 \mathbf{w}^H \mathbf{G}\mathbf{G}^H \mathbf{w} + \sigma^2\right) \\ &= \arg\max_{\mathbf{w}} \left(\mathbf{w}^H \mathbf{G}\mathbf{G}^H \mathbf{w}\right) = \frac{\mathbf{G}}{\sqrt{\mathbf{G}^H \mathbf{G}}},\end{aligned} \quad [16]$$

in which “arg max” represents the argument of the maximum. Then, the leakage location can be estimated by substituting $\hat{w}$ back to $|B|^2$:

$$\widehat{x^L} = \arg\max_{x^L} \frac{\Delta\mathbf{h}^H \mathbf{G}(x^L)\mathbf{G}^H(x^L)\Delta\mathbf{h}}{\mathbf{G}^H(x^L)\mathbf{G}(x^L)}. \quad [17]$$

It is remarkable that it is also a maximum likelihood estimator (MLE) of the leak position (Krim and Viberg, 1996; Wang et al., 2016a; Wang et al., 2016b). Then, by solving a least square, the leak size can be estimated by:

$$\widehat{s^L} = \frac{\mathbf{G}^H\left(\widehat{x^L}\right)\Delta\mathbf{h}}{\mathbf{G}^H\left(\widehat{x^L}\right)\mathbf{G}\left(\widehat{x^L}\right)}. \quad [18]$$

According to the property of MLE, the above two equations are consistent estimators, i.e., they converge in probability to the actual values. Furthermore, the proposed method is equivalent to a time reversal approach (Khazaie et al., 2016) and a matched-filter processing method which maximizes the signal-to-noise ratio (SNR). The latter implies that the proposed method minimizes the influence of noise.

(Lee et al., 2005b) indicated that the shape and the magnitude of the frequency response diagram (FRD) independently decide the location and the size of the leak. In the proposed approach, the estimates of location and size are separated: they reflect the information of shape and amplitude of FRD, respectively. Furthermore, the proposed method can use not only the peak frequencies but also the frequencies in between, which is not the case of the frequency response approach in (Lee et al., 2005a) and the peak-sequencing method in (Lee et al., 2005b).

4 NUMERICAL SIMULATION

In this section, numerical examples are introduced to test the MFP method. The cases of single leak and multiple leaks are respectively considered.

4.1 The case of single leak

First, the case of single leak was considered. The leakage problem in a single pipeline was numerically simulated; the setup is shown in Figure 1. Two reservoirs were connected by a pipe in a horizontal plane; the heads of the upstream and downstream reservoirs were H1=25 m and H2=20 m, respectively. The pipe length was l=2000 m and the diameter was D=0.5 m. The Darcy-Weisbach friction factor of the pipe was F=0.02 and the steady-state discharge was $q_0 = 0.0153 m^3/s$. The wave speed was 1200 m/s. A valve was located at the downstream end of the pipe and a sensor is just upstream of the valve. It is assumed that an impulse wave was generated by rapidly closing and opening the valve, thus the boundary conditions of $h(x^U) = 0$ and $q(x^U) = 1$ were applied. The wave propagation simulation in the frequency domain was realized by the transfer matrix method. The discharge at the upstream is also assumed to be obtained. Gaussian white noises with 0-mean are added to both the head at x^M and the discharge at x^u. The signal-to-noise ratio SNR=10 dB, which is defined by $SNR = 20\log_{10}(\overline{\Delta h}/\sigma)$, where $\overline{\Delta h}$ is the average head difference and σ is the standard deviation of noise.

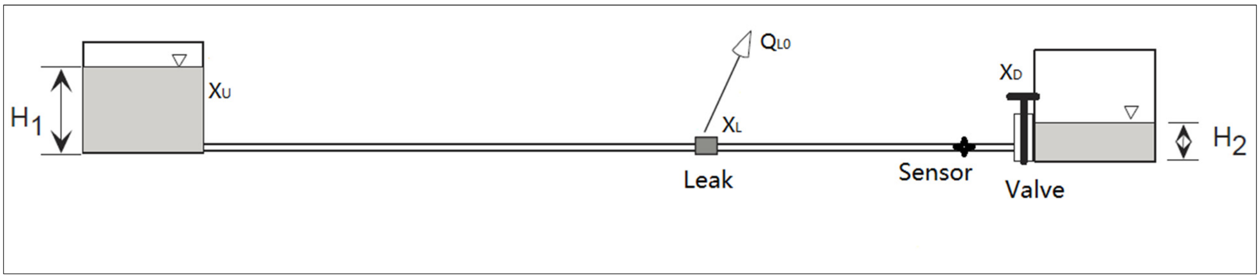

Figure 1. Setup of numerical simulation.

Here, the case of single leak was considered; the leak location was $x^L = 400$ m and the lumped leak parameter was $s^L = 1.4 \times 10^{-4} m^2$. The measurement location was at $x^M = 2000$. The first 16 peak angular frequencies were used for the leak localization. Figure 2 (a) plots the power output, which reaches maximum at the actual leak position, where is marked by the dash line. However, a symmetric maximum having the same level can be found at x=1600 m, since the boundary condition $h(x^U) = 0$ was applied (the upstream of the pipe was connected to a reservoir), such that the function $G(x^U)$ is symmetric with respect to x^M, which implies that while the objective function reaches maximum at both x^L and $x^M - x^L$. Obviously, the latter is a wrong estimate which must be excluded. The problems can be solved by using another measurement station with a different location. Figure2 (b) shows the power output for measurement station at 1800. It is clear that when the hydrophone location is changed, the peak corresponding to the actual leak stays at the same position, while the symmetric peak moves, which can therefore be excluded. Furthermore, the leak size s^L can also be estimated, which is $1.407 \times 10^{-4} m^2$ and was very close to its actual value $1.4 \times 10^{-4} m^2$.

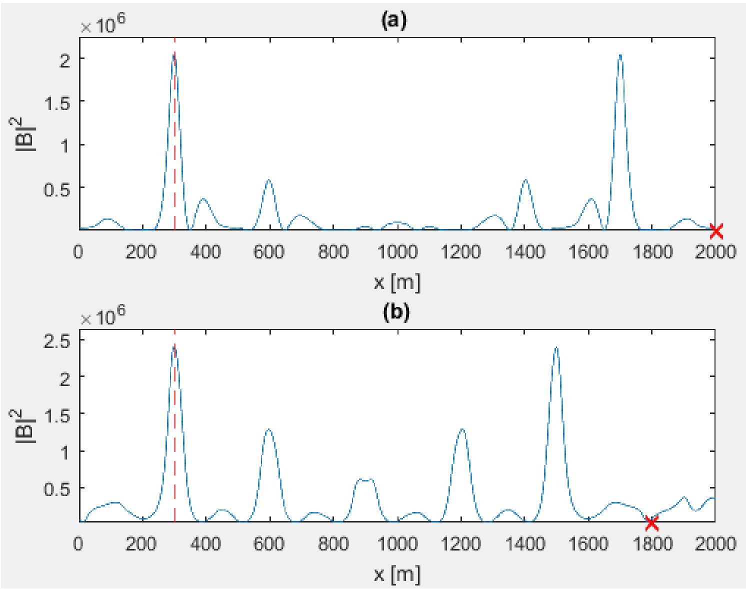

Figure 2. Localization of single leak (at 300 m) using MFP.
The dash line and the cross stand for the leak and
hydrophone locations, respectively.

4.2 The case of multiple leaks

In this section, numerical experiments for the two-leak case are considered. Two leaks located at 200 m and 700 m, and the lumped leak parameters for both leaks were $s^{L1} = s^{L2} = 1.4 \times 10^{-4} m^2$. The wave propagation and measurement were simulated and the leaks were localized using MFP based on the single-leak model. As previously, two different sensor locations were considered, the corresponding results are displayed in Figure 3. Similar to the single-leak case, a single sensor is able to localize both leaks but two symmetric maxima appear. Again, using another sensor is able to exclude the two false estimates: the two peaks corresponding to the actual leaks remains while the other two moves.

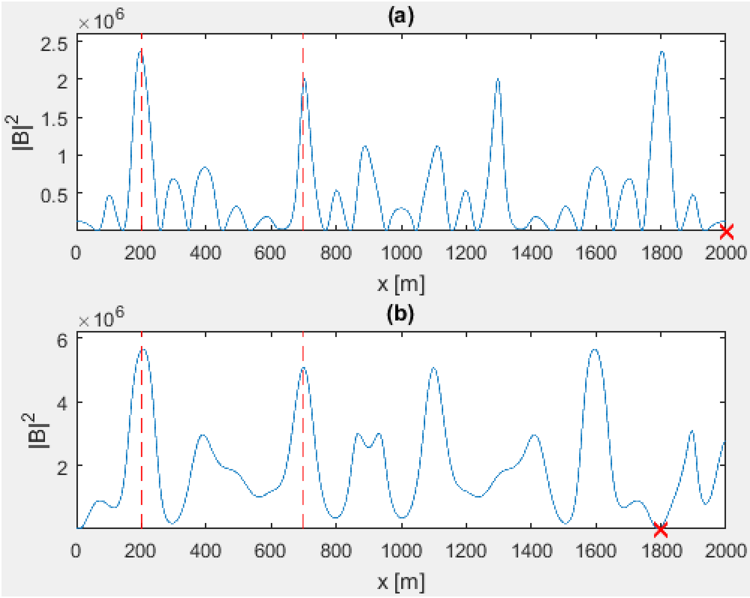

Figure 3. Localization of double leak (at 200 m and 700 m) using MFP. The dash line and the cross stand for the leak and hydrophone locations, respectively.

5 CONCLUSIONS

This paper addresses the problem of leak detection in a pipeline using a fluid transient. The leak location and size were estimated via the matched-field processing method. The model was based on the assumption of single leak but multiple leaks can still be localized. The proposed method is not limited to resonant frequencies but is able to use the head at all the frequencies.

The results obtained on simulated data illustrated the interest of the proposed method. The accuracy of the leak localization and the ability to estimate two leaks not very close to each other were demonstrated.

ACKNOWLEDGEMENTS

This work has been supported by research grants from the Research Grant Council of the Hong Kong SAR, China (Project No. T21-602/15R). The authors would like to thank Duncan A. McInnis, Bryan Karney, Fedi Zouari, Alireza Keramat, Moez Louati, and Jingrong Lin for their helpful comments and discussions.

REFERENCES

Baggeroer, A.B., Kuperman, W.A. & Mikhalevsky, P.N. (1993). An Overview of Matched Field Methods in Ocean Acoustics. *IEEE Journal of Oceanic Engineering*, 18(4), 401–424.

Brunone, B. (1999). Transient Test-Based Technique for Leak Detection in Outfall Pipes. *Journal of Water Resources Planning and Management*, 125(5), 302–306.

Brunone, B. & Ferrante, M. (2001). Detecting Leaks in Pressurised Pipes by Means of Transients. *Journal of Hydraulic Research*, 39(5), 539–547.

Chaudhry, M.H. (2014). *Applied Hydraulic Transients, Third Edition*. Springer, 35-64.

Colombo, A.F., Lee, P. & Karney, B.W. (2009). A Selective Literature Review of Transient-Based Leak Detection Methods. *Journal of Hydro-Environment Research*, 2(4), 212–227.

Covas, D. & Ramos, H. (2010). Case Studies of Leak Detection and Location in Water Pipe Systems by Inverse Transient Analysis. *Journal of Water Resources Planning and Management*, 136(2), 248–257.

Covas, D., Ramos, H. & De Almeida, A.B. (2005a). Standing Wave Difference Method for Leak Detection in Pipeline Systems. *Journal of Hydraulic Engineering*, 131(12), 1106–1116.

Covas, D., Ramos, H., Graham, N. & Maksimovic, C. (2005b). Application of Hydraulic Transients for Leak Detection in Water Supply Systems. *Water Science and Technology: Water Supply*, 4(5-6), 365–374.

Ferrante, M. & Brunone, B. (2003). Pipe System Diagnosis and Leak Detection by Unsteady-State Tests Harmonic Analysis. *Advances in Water Resources*, 26(1), 95–105.

Khazaie, S., Wang, X. & Sagaut, P. (2016). Localization of Random Acoustic Sources in an Inhomogeneous Medium. *Journal of Sound and Vibration*, 384, 75–93.

Krim, H. & Viberg, M. (1996). Two Decades of Array Signal Processing Research. *IEEE Signal Processing Magazine*, 13(4), 67–94.

Kuperman, W. A. & Lynch, J.F. (2004). *Shallow-Water Acoustics.* Physics Today, 55–61.

Lee, P., Vitkovsky, J.P., Lambert, M.F., Simpson, A.R. & Liggett, J.A. (2003). Frequency Response Coding for the Location of Leaks in Single Pipeline Systems. *The International of Conference on Pumps, Electromechanical Devices and Systems Applied to Urban Water Management, IAHR and IHRA, Valencia, Spain, April 22—25*.

Lee, P.J., Lambert, M.F., Simpson, A.R., Vítkovsky`, J.P. & Liggett, J. (2006). Experimental Verification of the Frequency Response Method for Pipeline Leak Detection. *Journal of Hydraulic Research*, 44(5), 693–707.

Lee, P.J., Vítkovsky`, J.P., Lambert, M.F., Simpson, A.R. & Liggett, J.A. (2005a). Frequency Domain Analysis for Detecting Pipeline Leaks. *Journal of Hydraulic Engineering*, 131(7), 596–604.

Lee, P.J., Vítkovsky`, J.P., Lambert, M.F., Simpson, A.R. & Liggett, J.A. (2005b). Leak Location using the Pattern of the Frequency Response Diagram in Pipelines: A Numerical Study. *Journal of Sound and Vibration*, 284(3), 1051–1073.

Liggett, J.A. & Chen, L.-C. (1994). Inverse Transient Analysis in Pipe Networks. *Journal of Hydraulic Engineering*, 120(8), 934–955.

Liou, J.C. (1998). Pipeline Leak Detection by Impulse Response Extraction. *Journal of Fluids Engineering*, 120(4), 833–838.

Mpesha, W., Gassman, S.L. & Chaudhry, M.H. (2001). Leak Detection in Pipes by Frequency Response Method. *Journal of Hydraulic Engineering*, 127(2), 134–147.

Sattar, A.M. & Chaudhry, M.H. (2008). Leak Detection in Pipelines by Frequency Response Method. *Journal of Hydraulic Research*, 46(EI1), 138–151.

Stephens, M.L. (2008). Transient Response Analysis for Fault Detection and Pipeline Wall Condition Assessment in Field Water Transmission and Distribution Pipelines and Networks, *PhD Thesis.* University of Adelaide.

Taghvaei, M., Beck, S.B.M. & Boxall, J.B. (2010). Leak Detection in Pipes using Induced Water Hammer Pulses and Cepstrum Analysis. *International Journal of COMADEM*, 13(1), 19.

Tolstoy, A., Horoshenkov, K.V. & Bin Ali, M.T. (2009). Detecting Pipe Changes via Acoustic Matched Field Processing. *Applied Acoustics*, 70(5), 695–702.

Tolstoy, A.I. (2010). Waveguide Monitoring (such as sewer pipes or ocean zones) via Matched Field Processing. *Journal of the Acoustical Society of America*, 128(1), 190–194.

Vítkovsky`, J.P., Simpson, A.R. & Lambert, M.F. (2000). Leak Detection and Calibration using Transients and Genetic Algorithms. *Journal of Water Resources Planning and Management*, 126(4), 262–265.

Wang, X., Quost, B., Chazot, J.-D. & Antoni, J. (2016a). Estimation of Multiple Sound Sources with Data and Model Uncertainties using the EM and Evidential EM Algorithms. *Mechanical Systems and Signal Processing*, 66(67), 159–177.

Wang, X., Quost, B., Chazot, J.-D. & Antoni, J. (2016b). Iterative Beamforming for Identification of Multiple Broadband Sound Sources. *Journal of Sound and Vibration*, 365, 260–275.

Wang, X.-J., Lambert, M.F., Simpson, A.R., Liggett, J.A. & Vítkovsky`, J.P. (2002). Leak Detection in Pipelines using the Damping of Fluid Transients. *Journal of Hydraulic Engineering*, 128(7), 697–711.

COMBINING OPTIMAL FILTERING WITH PUMP SCHEDULING FOR REAL-TIME ENERGY MANAGEMENT IN WATER DISTRIBUTION SYSTEMS

ERNESTO ARANDIA[(1)] & JOE NAOUM-SAWAYA[(2)]

[(1)] IBM Research, Dublin, Ireland,
ernestoa@ie.ibm.com
[(2)] Ivey Business School, London, Ontario, Canada,
jnaoum-sawaya@ivey.ca

ABSTRACT

Energy used in pumping alone can account for as much as 40% of a water utility's operational expense. Thus, an effective energy management strategy is to reduce electricity costs by optimally scheduling pump operations while using information on electricity tariffs and water network hydraulics. Real-time electricity pricing has been adopted in several countries and is increasingly becoming a policy goal as the best representation of efficient energy pricing in support of demand participation and distributed energy resources. Managing energy usage for water utilities under real-time pricing is challenging due to the volatility of energy prices. Planning the operation of pumps should rely on the most accurate forecasts of electricity tariffs using the most recent available data, which is typically updated on an hourly basis. This paper focuses first on the problem of forecasting electricity tariffs and water demands in real time using an optimal filtering technique. The paper then focuses on pump scheduling using the real-time input. The pump scheduling problem has received considerable attention and is usually formulated with the objective of minimizing energy expenditure while maintaining the system hydraulics in an acceptable range. Given the inherent nonlinearities of the system and the binary nature of the decisions, solving the problem requires computationally expensive simulations. One of the main challenges in performing pump scheduling in real time is therefore reducing the computational expense. The paper presents a methodology to combine real-time forecasting with heuristics for optimal pump scheduling. The method is applied in a case study to illustrate the challenges, potential benefits, and directions for further development in real-time energy management for water utilities.

Keywords: Energy management; real-time, pump scheduling; heuristics; optimal filtering.

1 INTRODUCTION

Energy consumption can represent 30 to 40% of the operational expenses by water utilities (Copeland and Carter, 2017; Caffoor, 2008), and is typically the second largest budget item, exceeded only by labor costs (Copeland and Carter, 2017). Therefore, energy conservation and efficiency are problems of increasing importance for utility managers. Several opportunities for increasing efficiency are available, such as upgrading to more efficient equipment, improving energy management, or even generating energy on site to offset electricity purchases. Among these strategies, energy management by means of optimized pump scheduling can be a very cost-effective measure to increase energy efficiency.

The pump scheduling optimization problem aims at minimizing the energy expense, while maintaining the water network hydraulics within an adequate range. The research literature offers many solution approaches to this problem that can be broadly classified in two categories, namely, metaheuristics and exact solution methods.

Metaheuristic methods typically consist of coupling genetic algorithms with a hydraulic simulator in search of good quality solutions (Mackle et al., 1995; Goldman and Mays, 1999; McCormick and Powell, 2004; López-Ibáñez et al., 2008, Naoum-Sawaya et al., 2015). These techniques face the computational challenge associated with the large dimensions of the solution space of potential pump schedules and the time required by the simulator to evaluate potential solutions.

Exact solution methods rely on the application of nonlinear optimization techniques (Yu et al., 1994; Sherali and Smith, 1997; Bragalli et al., 2012; Verleye and Aghezzaf, 2013; Raghunathan, 2013; D'Ambrosio et al., 2014). The main challenge for the exact methods is that the hydraulic headloss relationships in the network lead to nonlinear nonconvex optimization problems which are very difficult to solve (D'Ambrosio et al., 2014). Also, since real water networks are large, scalable optimization becomes an additional challenge.

The problem of scheduling pumps in real time has recently gained attention (Pasha and Lansey, 2009; Zheng, 2012; Jung and Kang, 2015) as a means to apply system monitoring technologies, such as SCADA (supervisory control and data acquisition) and respond to policy changes towards dynamic electricity pricing (Hogan, 2014). The computational and optimization challenges mentioned above are critical in real-time pump scheduling since fast solutions are required to update pump schedules in real time.

This paper presents a methodology to combine real-time forecasting techniques for energy price and water demand with heuristics for optimal pump scheduling. The paper focuses first on the problem of forecasting electricity tariffs and water demands in real time using an optimal filtering technique. The paper then focuses on pump scheduling using the real-time input. The method is applied in a case study to illustrate the challenges, potential benefits, and directions for further development in real-time energy management for water networks.

2 METHODOLOGY

The combined methodology applies an optimal filtering technique for the purpose of forecasting, in real time, water demands in the water network as well as electricity prices. The forecasts are used recursively by a pump scheduling algorithm in order to generate dynamically updated schedules. These individual methods and the approach to combine them are described below.

2.1 Forecasting model

Water demands and electricity prices are modeled using a seasonal multiplicative ARIMA (SARIMA) model that can be represented in state-space form for application of the optimal filtering technique. The SARIMA model is denoted as ARIMA (p,d,q)x(P,D,Q)s (Shumway and Stoffer, 2000) and is represented compactly as:

$$\Phi_P(B^s)\phi(B)\nabla_s^D\nabla^d x_t = \delta + \Theta_Q(B^s)\theta(B)\epsilon_t, \qquad [1]$$

where x_t is the observed time series, ϵ_t is a zero-mean Gaussian random error process with variance σ, t is the time index, B is the backshift operator defined by $B^k x_t = x_{t-k}$, $\mathbf{\Phi}_P(B^s) = 1 - \mathbf{\Phi}_1 B^s - \ldots - \mathbf{\Phi}_P B^{Ps}$ is the seasonal autoregressive polynomial, $\mathbf{\Theta}_Q(B^s) = 1 + \mathbf{\Theta}_1 B^s + \ldots + \mathbf{\Theta}_Q B^{Qs}$ is the seasonal moving average polynomial, $\phi(B) = 1 - \phi_1 B - \ldots - \phi_p B^p$ is the ordinary autoregressive polynomial, $\theta(B) = 1 + \theta_1 B + \ldots + \theta_q B^q$ is the ordinary moving average polynomial, P, Q, p, and q are the respective polynomial orders, s is the seasonal period, $\nabla_s^D = (1 - B^S)^D$ is the seasonal differencing operator, $\nabla^d = (1 - B)^d$ is the ordinary differencing operator, D and d are the differencing orders, $\delta = \mu(1 - \phi_1 - \ldots - \phi_p)(1 - \mathbf{\Phi}_1 - \ldots - \mathbf{\Phi}_P)$ is the intercept, and μ is the mean value of the observed time series x_t.

2.2 Optimal filtering method

By representing Eq. [1] in state-space form, it is possible to apply the optimal filtering technique known as the Kalman filter (Hamilton, 1994). The state-space model consists of the observation equation Eq. [2] and the state equation Eq. [3] below:

$$\boldsymbol{y}_t = \boldsymbol{A}^\top \boldsymbol{u}_t + \boldsymbol{H}^\top \boldsymbol{z}_t + \boldsymbol{w}_t, \qquad [2]$$

$$\boldsymbol{z}_t = \boldsymbol{F}\boldsymbol{z}_{t-1} + \boldsymbol{v}_t, \qquad [3]$$

where $\boldsymbol{y}_t$ is the vector of observed variables, $\boldsymbol{z}_t$ is the state vector that consists of variables that cannot be measured directly, $\boldsymbol{u}_t$ is a vector of exogenous variables or possibly lagged values of $\boldsymbol{y}_t$, $\boldsymbol{A}$ is a predetermined coefficient matrix, $\boldsymbol{F}$ and $\boldsymbol{H}$ are parameter matrices, and $\boldsymbol{w}_t$ and $\boldsymbol{v}_t$ are error terms assumed to be distributed as white noise with covariance matrices $\boldsymbol{W}$ and $\boldsymbol{R}$, respectively (Hamilton, 1994).

Eq. [1] is represented in state-space form by first making $\boldsymbol{y}_t = \nabla_s^D\nabla^d x_t$, *i.e.,* transforming the observed univariate variable x_t into an equivalent ARMA ($p + sP$, $q + sQ$) process (Sävås, 2013). The terms $\boldsymbol{A}$, $\boldsymbol{u}_t$, and $\boldsymbol{w}_t$ are set to zero since no exogenous variables are considered and the measurements are assumed free of noise. The rest of the terms in Eq. [2] and [3] are presented below:

$$\boldsymbol{z}_t^\top = [z_{1,t}, z_{2,t}, \ldots, z_{r,t}], \quad \boldsymbol{H}^\top = \begin{bmatrix} 1 & 0 & \ldots & 0 \end{bmatrix},$$

$$\boldsymbol{F}^\top = \begin{bmatrix} \phi_1 & \phi_2 & \ldots & \phi_{r-1} & \phi_r \\ 1 & 0 & \ldots & 0 & 0 \\ 0 & 1 & \ldots & 0 & 0 \\ \vdots & \vdots & \ldots & \vdots & \vdots \\ 0 & 0 & \ldots & 1 & 0 \end{bmatrix}, \quad \boldsymbol{v}_t = \begin{bmatrix} 1 \\ \theta_1 \\ \vdots \\ \theta_{r-1} \end{bmatrix} \epsilon_t,$$

$$\boldsymbol{W}^\top = \sigma^2 \begin{bmatrix} 1 & \theta_1 & \ldots & \theta_{r-1} \\ \theta_1 & \theta_1^2 & \ldots & \theta_1\theta_{r-1} \\ \vdots & \vdots & \ldots & \vdots \\ \theta_{r-1} & \theta_1\theta_{r-1} & \ldots & \theta_{r-1}^2 \end{bmatrix}.$$

where r = max(p + sP, q + sQ + 1) is the dimension of the vectors and matrices above. Before applying the Kalman filter, the matrices and vectors above need to be computed using previously estimated parameters of the SARIMA model.

In a real-time or online implementation, the Kalman filter allows updating the state vector of Eq. [3] every time there is a new observation of the series $\boldsymbol{y}_t$ (Harvey, 1990). The filter consists of a sequence of steps where a linear estimate $\hat{\boldsymbol{z}}_t$ is produced recursively from known values of $\hat{\boldsymbol{z}}_{t-1}$ and $\boldsymbol{y}_t$. In the initial step, the prior state $\boldsymbol{z}_1$ is computed from prior information or assumed to be zero in the absence of such information; also, the prior state's variance $\boldsymbol{P}_{1|0}$ is computed from:

!

$$vec(\boldsymbol{P}_{1|0}) = [\boldsymbol{I} - (\boldsymbol{F} \otimes \boldsymbol{F})]^{-1} \times vec(\boldsymbol{W}), \quad [4]$$

where $\boldsymbol{I}$ is the identity matrix, and vec($\boldsymbol{P}_{1|0}$) is the column vector representation of that is directly rearranged to obtain $\boldsymbol{P}_{1|0}$. The rest of the steps follow by iteratively updating the values of the state variables through recursions on the equation below:

$$\hat{\boldsymbol{z}}_{t+1|t} = \boldsymbol{F}\hat{\boldsymbol{z}}_{t|t-1} + \boldsymbol{F}\boldsymbol{P}_{t|t-1}\boldsymbol{H}(\boldsymbol{H}^\top \boldsymbol{P}_{t|t-1}\boldsymbol{H})^{-1}(\boldsymbol{y}_t - \boldsymbol{H}^\top \hat{\boldsymbol{z}}_{t|t-1}), \quad [5]$$

where $\hat{\boldsymbol{z}}_{t|t-1}$ is the forecast of the true state $\boldsymbol{z}$ based on the linear function of the past observations $\boldsymbol{y}_1$, …, $\boldsymbol{y}_{t-1}$ and $\boldsymbol{P}_{t|t-1}$ is the variance of the state forecast. To proceed to the next iteration, the forecast variance $\boldsymbol{P}_{t+1|t}$ is updated using the equation below:

$$\hat{\boldsymbol{z}}_{t+1|t} = \boldsymbol{F}\hat{\boldsymbol{z}}_{t|t-1} + \boldsymbol{F}\boldsymbol{P}_{t|t-1}\boldsymbol{H}(\boldsymbol{H}^\top \boldsymbol{P}_{t|t-1}\boldsymbol{H})^{-1}(\boldsymbol{y}_t - \boldsymbol{H}^\top \hat{\boldsymbol{z}}_{t|t-1}). \quad [6]$$

Eq. [2] to [6] above are implemented in a way that the inputs include a previously estimated SARIMA model, a segment of historical observations on the variable of interest, and a feed of measurements on this variable that is updated at every time step. The result is a sequence of optimally-filtered one-step-ahead forecasts covering the desired period of analysis (for details, see Arandia et al., 2016).

2.3 Pump scheduling

A standard pump scheduling problem consists of planning the function of pumps for the next operational time period T (usually T = 24 h) by relying on forecasts of water demand and electricity prices. The pump scheduling approach in this paper is an adaptation of the method presented by Naoum-Sawaya, et al. (2015) to the case where measurements are updated in real-time. The method consists of a Benders decomposition technique (Codato and Fischetti, 2006) where a master problem [PS1] finds potential schedules and a simulation subproblem verifies for hydraulic feasibility. The master problem is formulated as a mixed-integer linear program:

$$\begin{aligned}
\text{[PS1]:}\ \ & \min 0 && && [7]\\
\text{s.t.}\ \ & -a_{ij,t-1} + a_{ij,t} - b_{ij,t} \le 0, && \forall (i,j) \in L,\ \forall t > 0,\ t \in T, && [8]\\
& -a_{ij,t'} + b_{ij,t} \le 0, && \forall (i,j) \in L,\ \forall t \in T,\ \forall t' \in T : t \le t' \le t + \tau_1, && [9]\\
& a_{ij,t-1} - a_{ij,t} - c_{ij,t} \le 0, && \forall (i,j) \in L,\ \forall t > 0, t \in T, && [10]\\
& a_{ij,t'} + c_{ij,t} \le 1, && \forall (i,j) \in L,\ \forall t \in T, \forall t' \in T : t \le t' \le t + \tau_2, && [11]\\
& \sum_t b_{ij,t} \le N_{\max}, && \forall (i,j) \in L, && [12]\\
& a_{ij,t} \in \{0,1\},\ b_{ij,t} \in \{0,1\}, && && [13]\\
& c_{ij,t} \in \{0,1\},\ \forall (i,j) \in L, && && [14]\\
& \forall t \in T, && && [15]
\end{aligned}$$

where (i,j) represents a pair of nodes i and j connected by a link, $N_{\max}$ is the maximum number of desired of pump switches, L denotes the set of network links that contain a pump, τ_1 and τ_2 are time setting parameters, and a, b, and c are binary variables given by:

$$a_{ij,t} = \begin{cases} 1 & \text{if the pump of link } (i,j) \text{ is ON in period } t, \\ 0 & \text{otherwise,} \end{cases}$$

$$b_{ij,t} = \begin{cases} 1 & \text{if the pump on pipe } (i,j) \text{ is turned ON at period } t, \\ 0 & \text{otherwise,} \end{cases}$$

$$c_{ij,t} = \begin{cases} 1 & \text{if the pump on pipe } (i,j) \text{ is turned OFF at period } t, \\ 0 & \text{otherwise.} \end{cases}$$

Constraint [8] forces bij,t to take a value of 1 if the pump on link (i, j) is turned on at period t; constraint [9] forces the pump to remain on for at least τ1 time periods after it is switched on; constraint [10] force cij,t to take a value of 1 if the pump on link (i,j) is turned off at period t; constraint [11] forces the pump to remain off for at least τ2 time periods after it is switched off; finally, constraint [12] sets an upper bound on the maximum number of times each pump can be switched on during the planning horizon.

Given a solution of [PS1], EPANET is called to verify hydraulic feasibility. If the solution is infeasible, then it is eliminated by adding the following cut to [PS1]:

$$\sum_{(ij,t):\tilde{a}_{ij,t}=0} a_{ij,t} + \sum_{(ij,t):\tilde{a}_{ij,t}=1} (1 - a_{ij,t}) \geq 1 \qquad [16]$$

which indicates that at least one of the pumps in the current solution $\tilde{a}$ must change status in order for the solution to become feasible. Since EPANET reports the period $\tilde{T}$ at which the simulation becomes infeasible then constraint [16] can be further strengthened by forcing one of the pumps to change status before period T + 1 and thus the following cut is added instead to [PS1]:

$$\sum_{(ij,t\leq\tilde{T}):\tilde{a}_{ij,t}=0} a_{ij,t} + \sum_{(ij,t\leq\tilde{T}):\tilde{a}_{ij,t}=1} (1 - a_{ij,t}) \geq 1. \qquad [17]$$

Infeasibility is often due to tank levels going below the minimum allowed or overfilled above the maximum admissible level, therefore stronger cuts with respect to [17] can be obtained in those cases. If a tank is below the minimum allowable level by period $\tilde{T}$ then a pump must be turned on before period $\tilde{T}+1$. Similarly, if the infeasibility is due to a tank being overfilled above the allowable level by period $\tilde{T}$, then a pump must be turned off before period $\tilde{T}+1$. The following two cuts [18 and 19] deal with these two cases, respectively:

$$\sum_{(ij,t\leq\tilde{T}):\tilde{a}_{ij,t}=0} a_{ij,t} \geq 1. \qquad [18]$$

$$\sum_{(ij,t\leq\tilde{T}):\tilde{a}_{ij,t}=1} (1 - a_{ij,t}) \geq 1. \qquad [19]$$

In addition to the 0 objective Eq. [7], the method applies the two objectives below. One minimizes the distance to the currently best feasible solution $\bar{a}_{ij,t}$:

$$\min \sum_{ij,t} |a_{ij,t} - \bar{a}_{ij,t}|. \qquad [20]$$

The other favors solutions that lower the electricity costs:

$$\min \sum_{ij,t} k_t a_{ij,t}, \qquad [21]$$

where k_t is the electricity tariff at period t. Additional details about the pump scheduling method are provided by Naoum-Sawaya et al. (2015).

2.4 Combined Approach

The combined approach aims at generating pump schedules that are updated dynamically, starting from a full 24-h ahead schedule at the beginning of the operational period. There is an initial offline component that deals with the estimation of forecasting models for water demand and electricity tariff, and generates a starting pump schedule for the incoming 24-h planning horizon. Using these elements as input, the real-time pump scheduling algorithm performs the following tasks at each time step $t \in \{1, \ldots, T\}$:

- Obtain current water demand observation: x_t;
- Obtain current electricity tariff: kt;
- Forecast water demand xt+1;
- Forecast electricity tariff kt+1;
- Compute optimized pump schedule for the next time period: $\tilde{a}_{t+1}$;
- Run a hydraulic simulation with current water demands and initial tank levels;
- Get /update initial conditions (tank levels and pump status) for time period t + 1.

The next section discusses a testing implementation of the combined method.

3 RESULTS

The water network selected for the test case is C-Town (Figure 1) which comprises one reservoir, 11 pumps, 7 tanks, 388 nodes, and 432 pipes. The topology of this network is available online and its full details can be obtained from Giustolisi et al. (2013).

Figure 1. The C-Town Water Network.

3.1 Water demand forecasting

The SARIMA model estimation methodology described by Arandia et al. (2016) was applied to the available water demand data from a European water utility and the following model was identified as suitable from Eq. [1]:

$$(1-B^{168})(1-B)x_t = \delta + (1+\Theta_1 B^{168})\left(1+\sum_{i=1}^{4}\theta_i B^i\right)\epsilon_t, \qquad [22]$$

which is a SARIMA (0,1,4)x(0,1,1)$_{168}$. Output from the model is illustrated for two sample operational days in Figure 2 and 3 where the observed demands are compared with model forecasts in offline (24-h ahead forecasts) and online (optimally-filtered forecasts) modes.

The examples of Figure 2 illustrate two operational forecasts, one where the models match the water demand well, and an “unexpected” day where the forecasts deviate from the observed demands to a larger extent. The mean absolute percentage error (MAPE) of the forecasts for these examples is presented in Table 1 where it is shown that there is a larger improvement in the forecasts for the second day by applying the Kalman filter.

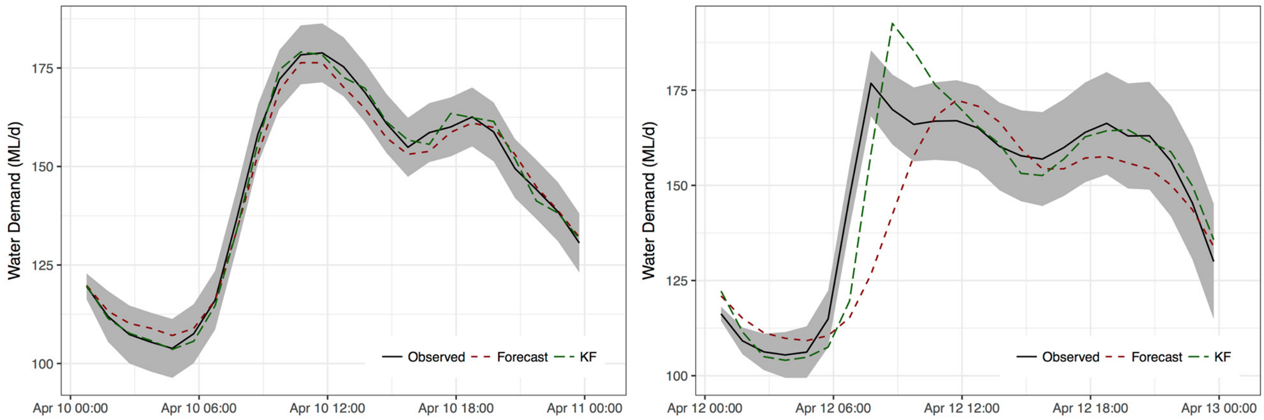

(a) (b)

Figure 2. Comparison of observed and forecasted water demands for two example operational days: (a) The 24-h ahead forecasts match the observations well and the Kalman filter improves the forecasts slightly. (b) The observed water demands follow an unexpected pattern; thus the offline forecasts deviate from the observations to a larger extent; the Kalman filter improves the forecasts.

3.2 Electricity tariff forecasting

A suitable SARIMA model (see Arandia et al., 2016) was identified for the available electricity tariffs and is shown below:

$$(1-\phi_1 B)(1-B^{72})(1-B)x_t = \delta + (1+\Theta_1 B^{72})(1+\theta_1 B)\,\epsilon_t, \qquad [23]$$

which is a SARIMA (1,1,1)x(0,1,1)$_{72}$. The model output for two sample days is presented in Figure 3 where overall, the filtered model follows more closely the variation of the electricity tariffs. It is clear also that the uncertainty in the forecasts is much larger as indicated by the gray band. In magnitude, the percent forecast deviations for these two days are presented in Table 1.

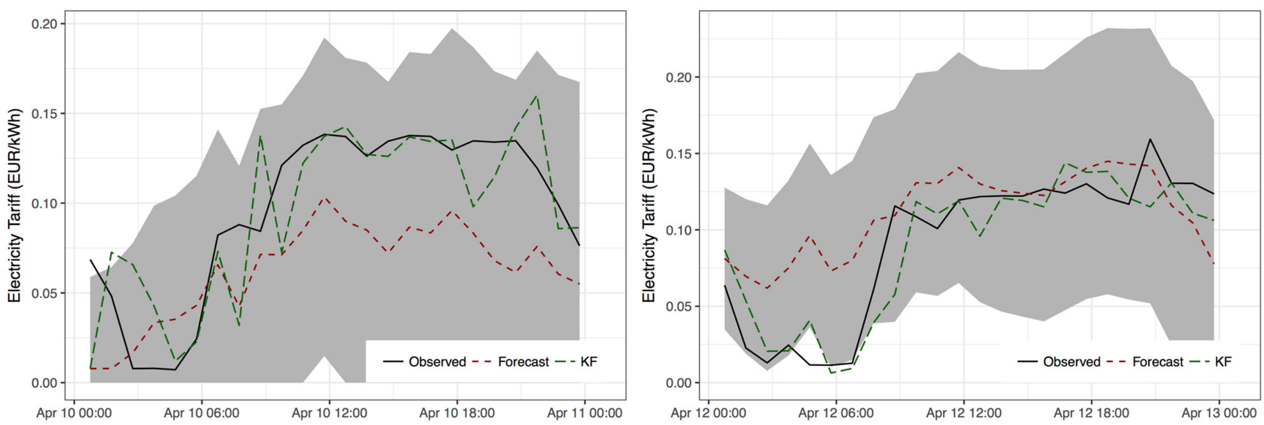

(a) (b)

Figure 3. Comparison of observed and forecasted electricity tariffs for two example operational days.

Table 1. MAPE of water demand and electricity tariff forecasts.

Day	Water Demand		Electricity Tariff	
	Forecast	KF	Forecast	KF
1	1.67	1.02	71.73	70.84
2	6.14	4.57	121.48	33.58

3.3 Pump scheduling

The pump scheduling algorithm described in Section 2.4 was used to plan the operation of pumps for the two sample days described above. For each day, the first task was to generate a schedule using the offline 24-h ahead forecasts of demand and electricity tariff. Then, a second schedule was obtained by applying the recursive method of Section 2.4. Figure 4 presents the results obtained, where for each day, the offline and online schedules are displayed alongside for comparison.

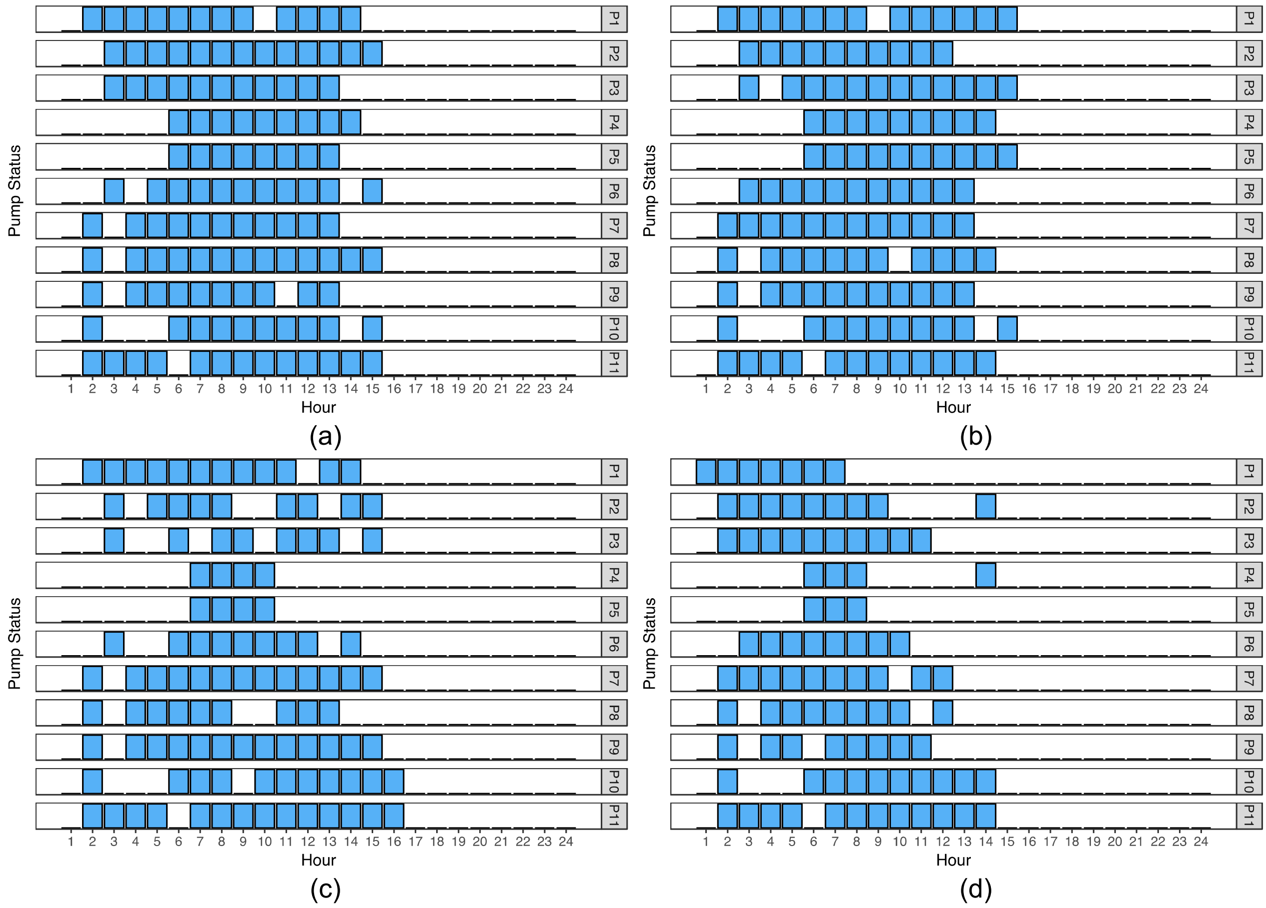

Figure 4. Solution pump schedules obtained for example operational Day 1 (April 10, 2016) and Day 2 (April 12, 2016). (a) Day 1 schedule with offline forecasts. (b) Day 1 schedule with optimally filtered forecasts. (c) Day 2 schedule with offline forecasts. (d) Day 2 schedule with optimally filtered forecasts.

In order to compare the solutions, simulations were performed for each testing day using the schedules of Figure 4. The simulations consisted of applying the solution schedule to the "real" demand conditions and electricity prices. Electricity costs were computed for each simulation hour and accumulated to obtain the values summarized in Table 2. The caveat is that the operational constraints (minimum network pressures) were relaxed to circumvent feasibility when simulating the network given water demands different to those used in optimizing the schedules.

Table 2. Daily electricity costs (€) for the optimized pump schedules.

Day	Initial	Offline	Online
1	811.38	324.57	323.12
2	758.77	240.55	134.44

With respect to the initial expenses that correspond to the extreme case of running the pumps all the time, the offline and online optimized schedules for Day 1 both produce savings of approximately 60%. The slight improvement in applying the optimal filtering technique indicates that the offline and real-time water demand and electricity price forecasts were equivalently accurate (Figure 2 and 3). In the case of Day 2, the offline and online forecasts produce savings of, respectively, 68% and 82%. For this sample day which is considered "unusual", the more accurate water demand and electricity tariff forecasts led to an additional 44% reduction of electricity costs.

4 CONCLUSIONS

This paper presents an approach to combine real-time forecasting techniques for energy price and water demand with heuristics for optimal pump scheduling. Forecasts produced by the filtering method are used recursively by a pump scheduling algorithm in order to dynamically update the pump schedules. The method is applied in a case study where for two sample days having regular and irregular demand patterns offline (24 h ahead) and online (optimally filtered) pump schedules are obtained. The results illustrate that for regular days only slight electricity savings can be obtained while for days with unexpected patterns the potential electricity savings are very significant. The preliminary implementation was performed without considerations of uncertainty in water demands and prices. Thus, the comparison of schedules generated from different water demand forecasts required relaxing the operational constraints (minimum pressures). In future research, we plan to investigate the effects of uncertainty leading to a robust optimization approach.

REFERENCES

Arandia, E., Ba, A., Eck, B. & McKenna, S. (2016). Tailoring Seasonal Time Series Models to Forecast Short-Term Water Demand. *J. Water Res. Plann. Manage.*, 142(3), 04015067.

Bragalli, C., D'Ambrosio, C., Lee, J., Lodi, A. & Toth, P. (2012). On the Optimal Design of Water Distribution Networks: A Practical MINLP Approach. *Optimization and Engineering*, 13(2), 219-246.

Caffoor, I. (2008) Energy Efficient Water and Wastewater Treatment – A Priority Technology for the UK, Treatment [Online], Available from: http://www.cost.eu/module/download/5352 [Accessed 14 March 2017].

Codato, G. & Fischetti, M. (2006). Combinatorial Benders' Cuts for Mixed-Integer Linear Programming. *Operations Research*, 54(4), 756-766.

Copeland, C. & Carter, N.T. (2017). Energy-Water Nexus: The Water Sector's Energy Use. *Congressional Research Service.* 24.

D'Ambrosio, C., Lodi, A., Wiese, S. & Bragalli, C. (2014). Mathematical Programming Techniques in Water Network Optimization. *European Journal of Operational Research*, *243*(3), 774-788.

Giustolisi, O., Brunone, B., Savic, D. & Walski, T. (2013). Battle of Background Leakage Assessment for Water Networks (BBLAWN) Detailed Problem Description and Rules. URL http://www.water-system.org/wdsa2014/sites/default/files/ WDSA2014-BWNIII-ProblemDescription 04122013 0.pdf. [Accessed date: Dec 2013]

Goldman, F.E. & Mays, L.W. (1999). The Application of Simulated Annealing to The Optimal Operation of Water Systems. In *WRPMD'99: Preparing for the 21st Century*, 1-16.

Hamilton, J.D. (1994). *Time Series Analysis (Vol. 2).* Princeton: Princeton university press.

Hogan, W.W. (2014). Time-Of-Use Rates and Real-Time Prices. *John F. Kennedy School of Government, Harvard University*.

Jung, D., Kang, D., Kang, M. & Kim, B. (2015). Real-Time Pump Scheduling for Water Transmission Systems: Case Study. *KSCE Journal of Civil Engineering*, 19(7), 1987-1993.

López-Ibáñez, M., Prasad, T.D. & Paechter, B. (2008). Ant Colony Optimization for Optimal Control of Pumps in Water Distribution Networks. *Journal of Water Resources Planning and Management*, 134(4), 337-346.

Mackle, G., Savic, G.A. & Walters, G.A. (1995, September). Application of Genetic Algorithms to Pump Scheduling for Water Supply. In *Genetic Algorithms in Engineering Systems: Innovations and Applications, 1995. GALESIA. First International Conference on (Conf. Publ. No. 414)*, 400-405. IET.

McCormick, G. & Powell, R.S. (2004). Derivation of Near-Optimal Pump Schedules for Water Distribution by Simulated Annealing. *Journal of the Operational Research Society*, 55(7), 728-736.

Naoum-Sawaya, J., Ghaddar, B., Arandia, E. & Eck, B. (2015). Simulation-Optimization Approaches for Water Pump Scheduling and Pipe Replacement Problems. *European Journal of Operational Research*, *246*(1), 293-306.

Pasha, M.F.K. & Lansey, K. (2009). Optimal Pump Scheduling by Linear Programming. In *World Environ-mental and Water Resources Congress 2009: Great Rivers*, 1-10.

Raghunathan, A.U. (2013). Global Optimization of Nonlinear Network Design. *SIAM Journal on Optimization*, 23(1), 268-295.

Sävås, F.N. (2013). Forecast Comparison of Models Based on SARIMA and the Kalman filter for inflation. *MSc thesis*, Uppsala University, Sweden.

Sherali, H.D. & Smith, E.P. (1997). A Global Optimization Approach to a Water Distribution Network Design Problem. *Journal of Global Optimization*, 11(2), 107-132.

Shumway, R. & Stoffer, D. (2000). *Time Series Analysis and Its Applications*, Springer, Berlin.

Verleye, D. & Aghezzaf, E.H. (2013). Optimising Production and Distribution Operations in Large Water Supply Networks: A Piecewise Linear Optimisation Approach. *International Journal of Production Research*, 51(23-24), 7170-7189.

Yu, G., Powell, R.S. & Sterling, M.J.H. (1994). Optimized Pump Scheduling in Water Distribution Systems. *Journal of optimization theory and applications*, 83(3), 463-488.

Zheng, Y.W. & Morad, B. (2012). Real-time Pump Scheduling Using Genetic Algorithm and Artificial Neural Network Based on Graphics Processing Unit. In *WDSA 2012: 14th Water Distribution Systems Analysis Conference, 24-27 September 2012 in Adelaide, South Australia*, 1088. Engineers Australia.

Harvey, A.C. (1990). *Forecasting, Structural Time Series Models and the Kalman filter*. Cambridge University press.

INFLUENCE OF AIR CONTENT ON TRANSIENT FLOW BEHAVIORS IN VISCOELASTIC PIPES

YAN ZHU[(1)], HUAN-FENG DUAN[(2)], FEI LI[(3)], CHEN-GUANG WU[(4)], YI-XING YUAN[(5)] & ZHEN-FENG SHI[(6)]

[(1,4,5,6)] School of Municipal and Environmental Engineering, Harbin Institute of Technology, Harbin, China,
ifengtian@126.com
[(2,3)] Department of Civil and Environmental Engineering, The Hong Kong Polytechnic University, Hung Hom, Kowloon, Hong Kong, China,
hf.duan@polyu.edu.hk

ABSTRACT

Air is easily introduced into water supply pipelines due to many factors of the system condition and operation equipment, such as air release from water under low pressure condition and air injection from devices (*e.g.,* air valve, pump). As a result, air-water mixing flows are commonly formed in pressurized water supply pipes and may cause different practical problems, such as reducing water conveyance capability, lowering pipe strength and damaging system facilities. This preliminary study aims to investigate the influence of air content on the transient behaviors of the induced air-water mixing flows in a form of homogeneous mixture fluid in viscoelastic pipes. Laboratory experiments and numerical simulations are adopted for the investigation. The numerical model based on the method of characteristics (MOC) and the discrete vaporous cavity model (DVCM) is calibrated and validated by the experimental data gained in this study, and then adopted for systematic analysis of the influence and relative importance of different factors, including unsteady friction, viscoelasticity and air content, on transient flows in viscoelastic pipes. The time-domain amplitude damping and frequency-domain frequency shifting of transient responses are examined for the effects of different influence factors in this study. The obtained results and implications are discussed for the modelling and analysis of transient flows in viscoelastic pipes.

Keywords: Air-water mixing flow; transient pipe flow; unsteady friction; viscoelasticity; air content.

1 INTRODUCTION

Modelling and analysis of transient pipe flows has become more and more important in urban water supply systems (UWSS), to the design and operation in terms of pipe strength and system safety (Duan et al., 2010a) and to the utilization and management in terms of pipe condition assessment, such as leakage and blockage detection (Duan et al., 2010b). Meanwhile, more and more plastic pipes with properties of viscoelasticity (terms as viscoelastic pipes in this study) have been applied in UWSS due to their advantages of economic investment and convenient operation. However, so far most of studies relating to transient pipe flows for both design and assessment aspects in the literature are focusing on elastic pipes (Chaudhry, 1987; Ghidaoui et al., 2005), while only very few for the viscoelastic pipes (Covas et al., 2004; 2005; Duan et al., 2012; Meniconi et al., 2014). As a result, the physical mechanism of transient wave propagation and utilization is not yet well understood in this field. From this perspective, it is worthwhile to further study and in-depth understand the transient flows in such viscoelastic pipes.

Air-water flows are easily formed in UWSS since the air is possibly introduced due to the system condition and operation equipment, such as air release from water under low pressure condition and air injection from devices (*e.g.,* air valve, pump) (Pozos et al., 2010). The existence of air in water in pipelines may cause many different problems including (but not limited to) reduction of water conveyance capacity, wastage of supply energy and increase of potential pipe leaks in the system (Wiggert and Sundquist, 1979). In particular, under transient conditions, air-water interaction may become complicated and thus affecting the prediction and analysis of the transient responses based on current models and methods (Duan et al., 2010a). At this point, it is necessary and important to study transient response of air-water flows under different system and hydraulic conditions.

It has been shown in the literature that many different factors in UWSS may affect transient responses, such as unsteady friction and viscoelasticity which have been widely studied in the literature (Duan et al., 2010c). However, another factor, air content may also have potential influence on the transient response in both amplitude damping and frequency shifting as the other two factors (Duan et al., 2010a; Soares et al., 2012). Therefore, it is essential to systematic analyze these different factors for their influences on transient flow responses, which is the scope of this study.

This paper aims to investigate the influence of air content on the relative importance of two commonly factors, unsteady friction and viscoelasticity, in complex flow systems with considering both the air-water flow and viscoelastic pipeline conditions. Laboratory experimental test system has been established and is applied for testing and calibrating the viscoelastic pipe parameters under different flow conditions. The numerical model based on the discrete vaporous cavity model (DVCM) scheme, after well validation by the experimental data obtained in this study, is then adopted for systematical analysis of transient air-water flows in viscoelastic pipes. The results of extensive numerical simulations and experimental tests are used for the analysis and discussion of the influence and relative importance of these three factors considered in this study to the transient responses, including amplitude damping in the time domain and frequency shifting in the frequency domain. Finally, the results are discussed for the model development and practical implication of transient air-water flows in viscoelastic pipes in UWSS.

2 NUMERICAL MODEL AND METHOD

In this preliminary study, the situation of air-water mixing flows with the form of uniform and small air bubbles in water flows is considered and investigated. Therefore, the air-water mixing flows can be modeled as bubbly flows with the assumption that the air-water mixture is a type of homogeneous pseudo-fluid, in which all the physical properties of this pseudo-fluid are the weighted average values of these two phases (air and water). Taking the pipe-wall viscoelasticity into consideration, the governing equations of one-dimensional (1D) transient model used for expressing such air-water mixing flows can be expressed as (Chaudhry, 1987):

$$\frac{\partial H}{\partial t}+V\frac{\partial H}{\partial x}+\frac{a^2}{g}\frac{\partial V}{\partial x}+\frac{2a^2}{g}\frac{\partial \varepsilon_r}{\partial t}=0 \qquad [1]$$

$$\frac{\partial H}{\partial x}+\frac{1}{g}\left(V\frac{\partial V}{\partial x}+\frac{\partial V}{\partial t}\right)+h_f=0 \qquad [2]$$

where H is piezometric head, x is spatial coordinate, g is gravitational acceleration, V is fluid (mixture) velocity, t is the temporal coordinate, h_f is pipe frictional loss, a is wave speed, and ε_r is retarded strain of viscoelastic pipe-wall. Since the wave speed for air-water mixing transient flow can usually be greatly affected by the air content (Duan et al., 2010a), *i.e.,* becoming much smaller than original single phase water flow, the convective terms in Eq. [1] and [2] are included for the analysis so as to improve the accuracy of the numerical results. For the numerical simulation, the traditional method of characteristics (MOC) with fixed grid interpolation scheme is applied in this study to solve the above 1D transient model (Chaudhry, 1987).

To accurately represent friction effect during transient process, the total frictional head loss (h_f) in Eq. [2] is divided into two parts (Vardy and Brown, 1995): (1) the quasi-steady friction component, which is usually modelled by Darcy-Weisbach formula, and (2) the unsteady friction component, which can be simulated by different types of unsteady friction models proposed in the literature (Ghidaoui et al., 2005), and in this study, the weighting function based unsteady friction by Vardy and Brown (1995) is used for the demonstration due to the known information of model parameters.

With regard to the retarded strain of viscoelastic pipe-wall deformation in Eq. [1], the Kelvin-Voigt (K-V) model, which derived from a conceptual model consisting of a combination of spring and dashpot elements, is adopted to mimic the viscoelastic pipe behavior during transient flow process (Covas et al., 2005; Duan et al., 2010c). The detailed expression and procedure for the implementation into MOC-based numerical model refer to these references.

Furthermore, to capture the homogeneous air-water flows, the DVCM scheme is used and implemented into the above MOC-based numerical simulation process, with the expression of wave speed (a) of air-water mixture defined as following (Soares et al., 2012):

$$a=\frac{1}{\sqrt{\rho_l\left(1-\alpha\right)\left(\frac{1}{K_l}+\frac{\alpha}{K_g}+\frac{D}{Ee}C_1\right)}} \qquad [3]$$

where ρ_l is the density of the liquid (water) phase, α is the air content (void fraction of fluid mixture), K_l is the bulk modulus of water, K_g is the bulk modulus of air, D is pipe inner diameter, e is pipe wall thickness, E is the elastic modulus of pipe material, and C_1 is a parameter related to the pipe constraints, and in this study (Chaudhry, 1987),

$$C_1=\frac{2e}{D}\left(1+\mu\right)+\frac{D}{D+e}\left(1-\mu^2\right) \qquad [4]$$

where μ is the Poisson ratio for the pipeline constraint condition.

3 LABORATORY EXPERIMENTAL TEST SYSTEM

Laboratory experimental test system has been established for this study, which consists of water supply tank, viscoelastic pipeline, discharge water tank, air compressor, and controls and measurement facilities. The schematic of the test system is shown in Figure 1. The testing viscoelastic pipeline is made of Plexiglas material with a total length of 36.0m, an inner diameter of 90mm and a wall thickness of 10mm (*i.e.,* 4-inch pipe). By testing, the elastic modulus of the testing pipe material is about 2.684GPa and the Poisson ratio for this system is about 0.358. Four pressure transducers with sample frequency of 1000Hz (see Figure 1).

For testing air-water flows, the air is compressed by the air compressor installed through a side pipe branch (as shown in Figure 1) and injected into the pipeline at the upstream of testing pipeline with its velocity (air content or air fraction) measured by the gas rotameter. During the tests, the air injected into the pipeline are fully mixed with water flow from the upstream, which results in uniformly distributed bubbly flows with different air contents in the pipeline under relatively high-pressure steady state. The transients in the test system are caused by the fast and complete closure of the butterfly valve located at the downstream of the testing viscoelastic pipeline.

The obtained experimental test data is firstly used for the validation and verification of the transient model and the K-V viscoelastic model. Then, the results of the validated model together with the experimental data are used for systematic analysis of the effects of different factors (unsteady friction, viscoelasticity and air content) on the transient responses in viscoelastic pipelines.

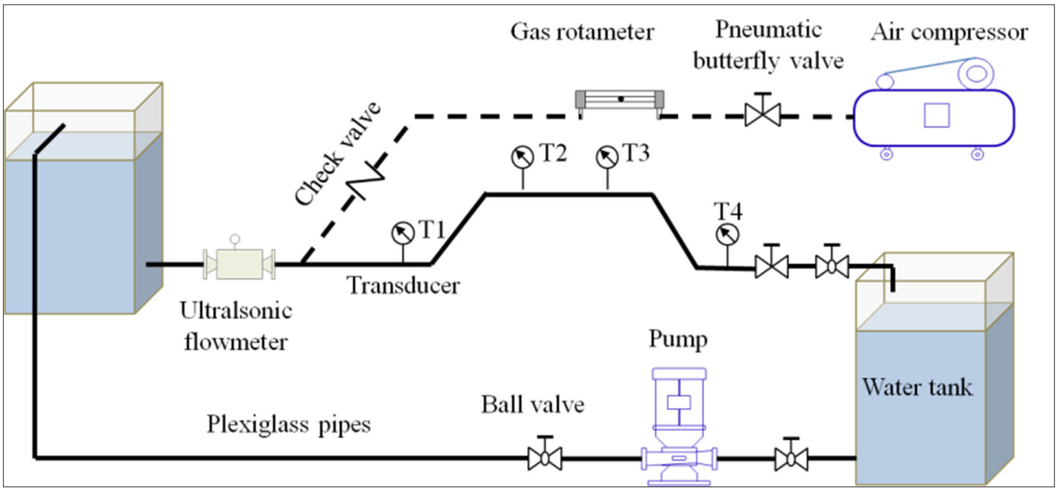

Figure 1. Schematic of the laboratory experiment test and measurement system.

4 MODEL CALIBRATION AND VALIDATION

4.1 Numerical scheme validation

The used model in Eq. [1] and Eq. [2] above based on MOC and DVCM is firstly validated for the numerical scheme and code programming through the experimental test data in the literature. One of the typical cases in Covas et al. (2005) with air content = 0 for pure water system, which was widely used in the literature, is adopted for this purpose.

The detailed parameters and settings for the test system refer to the original reference (Covas et al., 2005). The results from the experimental data in that study and numerical simulation in this study are obtained and plotted in Figure 2. The result comparison shows good agreement between the experimental and numerical data, which confirms the validity and accuracy of the proposed method and numerical scheme.

4.2 Viscoelastic pipeline calibration

With the verification of the developed method framework, the viscoelastic parameters for the pipeline condition tested in the experiment system of this study are calibrated herein by following the similar process in the literature (Covas et al., 2005; Duan et al., 2010c). The test case of initial velocity condition with V = 0.9m/s (see Figure 1) is used for this calibration process and the results are obtained as follows:

$$\tau_1 = 0.05 \text{ s},\ \tau_2 = 0.5 \text{ s and } \tau_3 = 1.5 \text{ s};$$
$$J_1 = 0.00839\times10^{-9}\ \text{Pa}^{-1},\ J_2 = 0.3504\times10^{-9}\ \text{Pa}^{-1} \text{ and } J_3 = 0.3552\times10^{-9}\ \text{Pa}^{-1}.$$

The comparative results of experimental test and numerical simulation are shown in Figure 3. The results of Figure 3 again confirm the accuracy of the developed methodology framework and numerical schemes in this study.

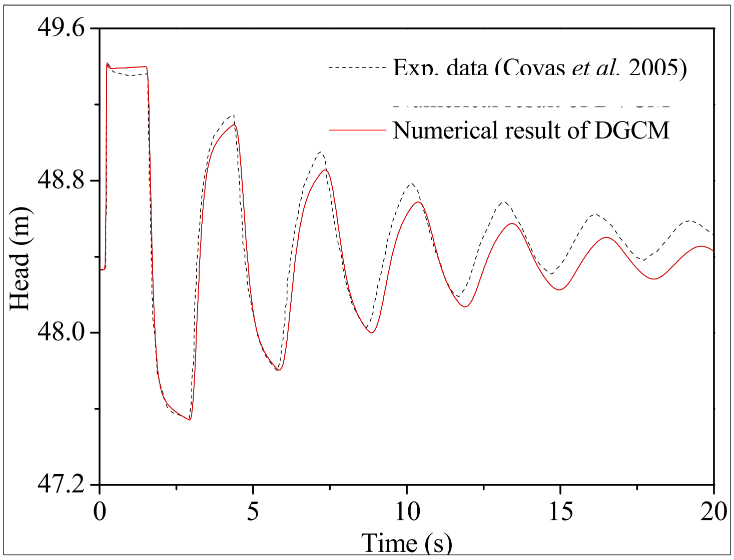

Figure 2. Model calibration by experimental data in reference.

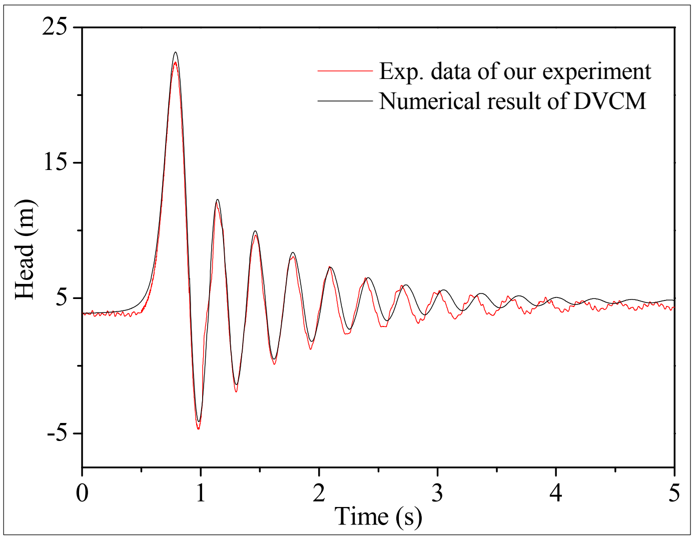

Figure 3. Comparison of calibrated numerical result and experimental data.

It is also shown in Figures 2 and 3 that the small difference is still shown between the experimental data and the numerical result, especially for the late stage of transient process (*e.g.,* after 5 wave periods in Figures 2 and 3 for the two cases). By inspection, this discrepancy may be attributed to: (i) the accuracy of calibration process of viscoelastic parameters (for both cases of Covas et al., 2005 and this study) where the initial drastic transient data may play dominant role for the fitness evaluation; (ii) the accuracy of 1D numerical model and method such unsteady friction model and MOC scheme; and (iii) the accuracy of experimental measurement, especially under the relatively small amplitude transient condition (*i.e.,* the late stage of transient histories in Figures 2 and 3). More analysis and discussion about the accuracy and reliability of these viscoelastic transient models and numerical methods are conducted later in this study.

5 NUMERICAL APPLICATIONS AND RESULTS ANALYSIS

With the validation and calibration of the used numerical models and methods by experimental data, it is necessary to further investigate the influence and important of different practical factors to the transient air-water mixing flow responses. In this study, the common factors of unsteady friction, pipe-wall viscoelasticity, and air content in UWDS are analyzed in this study. To this end, the three modelling results are defined therein: (1) inclusion of steady friction (SF), unsteady friction (UF) and viscoelasticity (VE), termed as "Model I"; (2) inclusion of SF and UF only, termed as "Model II"; and (3) inclusion of SF and VE only, termed as "Model III". For comparative analysis, the numerical tests with different system and flow conditions are listed in Table 1. Note that case no.1 is same as the experimental test case that used to calibrate the model above, while case no. 2 considers the air content influence during experiment conducted by the test system shown in Figure 1 in this study.

The wave speed from the numerical value of DVCM scheme and experimental result of test is calculated for the two test cases respectively, and listed in Table 1. The comparative results show clearly that, under both conditions of pure water (air content, α = 0m^3/h) in case no. 1 and air-water mixing (with relatively large air content, α = 0.5m^3/h), good agreements have been gained between the numerical and experimental results of wave speed, which confirms again the validity and reliability of DVCM.

Table 1. Numerical tests with different settings.

Case no.	air content, α (m^3/h)	V_0 (m/s)	Experimental result, a (m/s)	Numerical result, a (m/s)
1	0	0.90	492.19	492.81
2	0.5	1.30	79.23	78.01

The numerical results of the two cases under different conditions are obtained and plotted in Figures 4a and 4b, respectively. On one hand, the results of Figure 4a show that under pure water condition, the inclusion of SF and VE only could provide much better result than that of SF and UF only, which implies the much more important influence of the VE than the UF to the transient response of viscoelastic pipe flows. This result is consistent with the findings from previous studies in the literature (Duan et al., 2010c).

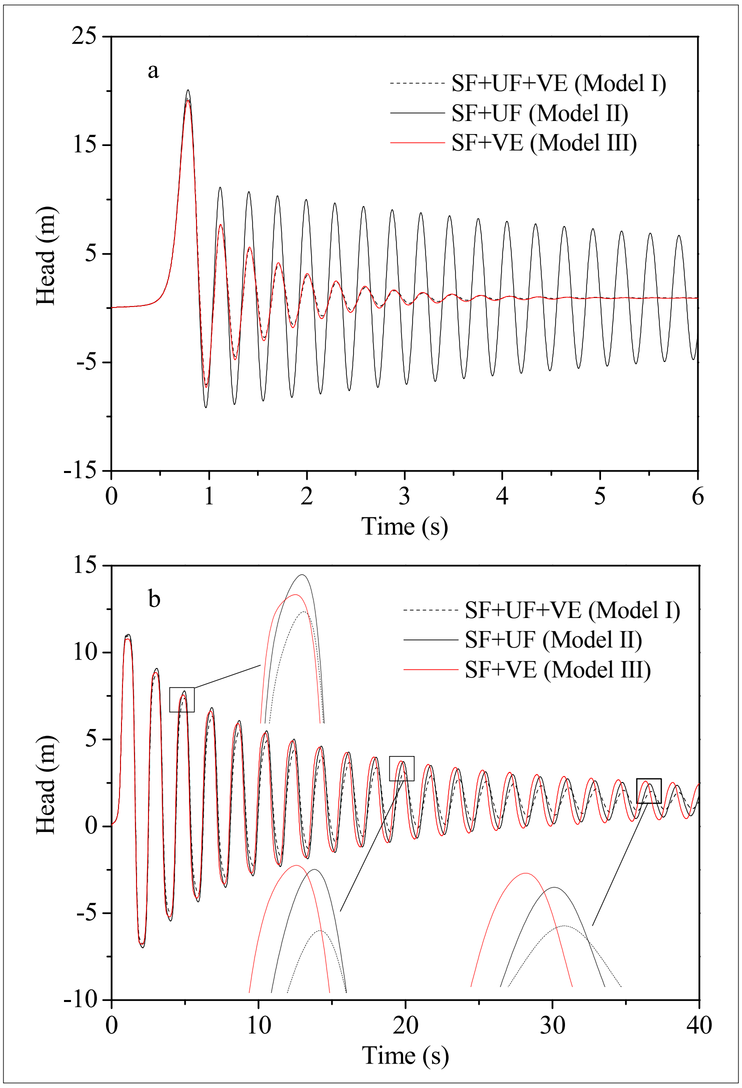

Figure 4. Numerical results with considering different influence factors for (a) case no. 1 (b) case no. 2.

On the other hand, however, the results of Figure 4) demonstrate a different extent of the influence of different factors. Specifically, with the existence of air content in pipe flows, the effect of VE on transient damping has been reduced greatly in comparison to the results of pure water situation in Figure 4a. Meanwhile, during the initial transient stage (*e.g.,* the first 10 wave cycles), the VE still has relatively larger influence than the UF to pipe fluid transients (see the first enlarged part of the amplitudes at about t = 5s in

Figure 4b), which however gradually becomes comparable to the UF effect (*e.g.,* second enlarged part at about t = 20s in the figure). Finally, during late stage of transient flows (*e.g.,* after 15 wave cycles), the VE effect becomes less dominant than the UF effect (see the third enlarged part at about t = 37s in the figure).

Furthermore, the result of Figure 4b also reveals that the frequency shifting effect of the VE can also be suppressed from the existence of air content in the pipeline (*i.e.,* through the comparison of three enlarged parts in the figure). Therefore, it can be concluded that air content in pipe flows may have significant influence on the relative importance of VE and UF effects in pipe fluid transients, which may be very different from the findings from previous studies in terms of pure water situation only (Covas et al., 2005; Duan et al., 2010c). Specifically, with the existence of air content, the relative importance and influence of the VE and the UF effects on both transient amplitude damping and frequency shifting becomes less dominant, and time-dependent (or stage-dependent) during the whole transient process.

Consequently, the results and findings above confirm again the necessity and importance of the investigation of transient air-water mixing flows in viscoelastic pipes, which may have useful insights into the theoretical model development and practical engineering application of the modelling and analysis of transient pipe flows in UWSS.

6 CONCLUSIONS

This paper investigates the influence of air content on the transient flows in viscoelastic pipes in UWSS. Laboratory experiment test system was built to collect experimental data to validate and calibrated numerical models including the viscoelastic pipe parameters in K-V model and the MOC-based DVCM numerical scheme for the simulation of the formed transient air-water mixing flows (homogeneous mixture) in viscoelastic pipes. The validated model is then used to simulate different cases of air content in viscoelastic pipes, with the aim to analyze the influence of such air content on relative importance of other two common factors (unsteady friction and viscoelasticity) on the transient behaviors (amplitude damping and frequency shifting) of viscoelastic pipe flows. In comparison to the experimental data, it is found that the proposed MOC-DVCM numeric scheme can accurately capture the transient responses of viscoelastic pipe flows, and confirm the reliability and applicability of the numerical models.

The comparative results of further numerical applications indicate that air content in pipe flows may have great impact on the relative importance of the unsteady friction and viscoelasticity effects in pipe fluid transients that have been obtained previously in the literature. Specifically, the existence of air content in water pipeline may reduce greatly the importance of both unsteady friction and viscoelasticity in terms of both amplitude damping and frequency shifting of transient responses. Moreover, the results also reveal that, the relative importance of these influence factors becomes time- or stage- dependent during the whole transient air-water mixing flow process.

The results and analysis demonstrate the necessity and importance of the study of transient air-water mixing flows, especially in viscoelastic pipes, of better modelling and analysis of UWSS. Finally, it is also noted that only the simple system and flow conditions (*e.g.,* single viscoelastic pipeline and homogeneous air-water mixing flow) are examined in this study. Consequently, based on the results and findings of current preliminary study, further investigations and validations of transient air-water flows are required for more complex system and flow conditions (*e.g.,* relatively large air pockets, column separation, multiple-pipe system and complex transient generation, etc.) in the future work.

ACKNOWLEDGEMENTS

This work was financially supported by: (1) the Hong Kong Research Grants Council (RGC) (no. 25200616 and no. T21-602/15-R); (2) the Hong Kong Polytechnic University (no. 1-ZVCD and no. 1-ZVGF); and (3) the National Natural Science Foundation of China (no. 51178141);

REFERENCES

Chaudhry, M.H. (1987). *Applied Hydraulic Transients*. Van Nostrand Reinhold, New York.

Covas, D., Stoianov, I., Mano, J., Ramos, H., Graham, N. & Maksimovic, C. (2004). The Dynamic Effect of Pipe-Wall Viscoelasticity in Hydraulic Transients. Part I—Experimental Analysis and Creep Characterization. *Journal of Hydraulic Research*, 42(5), 517-532.

Covas, D., Stoianov, I., Mano, J., Ramos, H., Graham, N. & Maksimovic, C. (2005). The Dynamic Effect of Pipe-Wall Viscoelasticity in Hydraulic Transients. Part II—Model Development, Calibration and Verification. *Journal of Hydraulic Research*, 43(1), 56-70.

Duan, H.F., Tung, Y.K. & Ghidaoui, M.S. (2010a). Probabilistic Analysis of Transient Design for Water Supply Systems. *Journal of Water Resources Planning and Management*, 136(6), 678-687.

Duan, H.F., Lee, P.J., Ghidaoui, M.S. & Tung, Y.K. (2010b). Essential System Response Information for Transient-Based Leak Detection Methods. *Journal of Hydraulic Research*, 48(5), 650-657.

Duan, H.F., Ghidaoui, M.S., Lee, P.J. & Tung, Y.K. (2010c). Unsteady Friction and Visco-Elasticity in Pipe Fluid Transients. *Journal of Hydraulic Research*, 48(3), 354-362.

Duan, H.F., Lee, P.J., Ghidaoui, M.S. & Tung, Y.K. (2012). System Response Function–Based Leak Detection in Viscoelastic Pipelines. *Journal of Hydraulic Engineering*, 138(2), 143-153.

Ghidaoui, M.S., Zhao, M., McInnis, D.A. & Axworthy, D.H. (2005). A Review of Water Hammer Theory and Practice. *Applied Mechanics Reviews*, 58(1), 49-76.

Meniconi, S., Brunone, B., Ferrante, M. & Massari, C. (2014). Energy Dissipation and Pressure Decay During Transients in Viscoelastic Pipes with an In-Line Valve. *Journal of Fluids and Structures*, 45, 235-249.

Pozos, O., Gonzalez, C.A., Giesecke, J., Marx, W. & Rodal, E.A. (2010). Air Entrapped in Gravity Pipeline Systems. *Journal of Hydraulic Research*, 48(3), 338-347.

Soares, A.K., Covas, D.I. & Ramos, H.M. (2012). Damping Analysis of Hydraulic Transients in Pump-Rising Main Systems. *Journal of Hydraulic Engineering*, 139(2), 233-243.

Vardy, A.E. & Brown, J.M. (1995). Transient, Turbulent, Smooth Pipe Friction. *Journal of Hydraulic Research*, 33(4), 435-456.

Wiggert, D.C. & Sundquist, M.J. (1979). The Effect of Gaseous Cavitation on Fluid Transients. *Journal of Fluids Engineering*, 101(1), 79-86.

Proceedings of the 37th IAHR World Congress
August 13 – 18, 2017, Kuala Lumpur, Malaysia

DEVELOPMENT AND EVALUATION OF MESHLESS PARTICLE METHODS FOR MODELLING AND ANALYSIS OF TRANSIENT PIPE FLOWS

HUAN-FENG DUAN[(1)], HEXIANG YAN[(2)], FEI LI[(3)], QINGZHI HOU[(4)], TAO TAO[(5)], KUNLUN XIN[(6)] & SHUPING LI[(7)]

[(1, 3)] Department of Civil and Environmental Engineering, The Hong Kong Polytechnic University, Hong Kong, China,
hf.duan@polyu.edu.hk
[(2, 5, 6, 7)] School of Environmental Science and Engineering, Tongji University, Shanghai, China,
hxyan@tongji.edu.cn
[(4)] School of Computer Science and Technology, Tianjin University, Tianjin, China,
qhou@tju.edu.cn

ABSTRACT

Different meshless particle methods, such as classic SPH, CSPM and MSPM, have been widely developed and used for the simulation and analysis of complex flow systems due to their advantages of computation efficiency and complexity description. However, the development and application of these methods are so far limited to free-surface or slightly pressurized flow systems, where the appropriate forms of equivalent expressions have been derived for meshless particles under different system and flow conditions. This paper aims to extend these efficient and convenient meshless particle methods to the modelling and analysis of highly pressurized transient water pipe flows, so that complex phenomena in water supply pipes could be better described and understood by these methods. The developed models and schemes are validated through the comparison with traditional methods that have been well verified by experiments in the literature. The single- and series- pipeline systems are investigated for the validity and applicability of the methods. The influences of different key parameters are then systematically examined for obtaining their most suitable values for transient pipe flows. Finally, the results of the validated models and methods are discussed for their accuracy and implications for the modelling and analysis of transient pipe flows.

Keywords: Meshless particle method; SPH; transient pipe flow; water pipe system.

1 INTRODUCTION

Water hammer (also termed as pressure surge, fluid transients) is a common phenomenon in various pressurized piping systems, which is generally caused by fast changes of pipe flowrates due to accidental or artificial factors, such as valve operation, pump startup or failure. Prediction and analysis of water hammer becomes important to the pipe design, construction and operation in engineering practice for its harmfulness to the system and associates (Duan et al., 2010a), and in the meanwhile to the pipe condition assessment such for its information reflection during wave propagation such as leakage detection (Duan et al., 2010b). Different numerical methods with appropriate mesh discretization schemes are available for the simulation of water hammer, including many classical methods such as the method of characteristic (MOC) (Wylie et al., 1993), finite volume method (FVM) (Zhao and Ghidaoui, 2004), and finite difference method (FDM) (Chaudhry and Hussaini, 1985).

In spite of the successful achievements of the mesh-based numerical methods in theory and practice, numerical difficulty and physical incapability often appear for their usage, especially in complex pipe flows, such as fluid separation, flow regime transition and multi-phase transient flows (air and water). Specifically, for the method of characteristics (MOC), interpolation has to be used for systems with different speeds of sound due to pipe complexities (e.g., variations of pipe size and material, and air content). Furthermore, if the Mach number of the flow is large enough (e.g., over 0.3 in transient pipe flows), the accuracy of MOC may suffer from a remarkable degeneration (Hwang et al., 2002). For FDMs, front tracking techniques have to be applied (Wahba, 2006), which often complicates the computation to a large extent and may also induce unacceptable numerical errors. From this perspective, traditional mesh-based methods will easily fail for solving transient problems with moving interface.

To avoid potential difficulties caused by the use of mesh schemes (e.g., convergence and accuracy), mesh-free or meshless methods are becoming popular in recent years and have attracted much attention of researchers, due to advantages of computational domain definition and construction. On this point, different mesh-free particle methods have been successfully developed and applied, including smoothed particle hydrodynamics (SPH) and its corrections, corrective smoothed particle method (CSPM) and modified smoothed particle method (MSPM), to transient flow problems with or without moving boundaries (Hou et al., 2012a; 2012b). Several useful techniques for imposing boundary conditions have been developed too (Hou et al., 2015). However, so far, these efficient and convenient meshless methods are mainly limited to free-surface flows or slightly pressurized flows in simple pipe systems (e.g., single pipeline). For highly pressurized and unsteady pipe flows and complex multi-pipe systems, their development and applicability have not yet been examined in the literature, which is the scope of this study.

This paper firstly develops and extends the meshless particle methods to transient pipe flows of both single- and series- pipeline systems, by deriving the equivalent forms of particle dynamics to the water hammer governing equations. Three types of meshless particle methods are considered for the evaluation, including the classic smoothed particle hydrodynamics (SPH) and its correction forms – corrective smoothed particle method (CSPM) and modified smoothed particle method (MSPM). Appropriate initial and boundary conditions of the used meshless methods are then proposed for typical water pipeline systems. The proposed methods and schemes are validated by the traditional numerical method (MOC) that has been well verified and validated by various experiment tests in the literature. Finally, the significance and implication of the developed methods are discussed for the future study in this field.

2 MODELS AND METHODS

2.1 Development of meshless particle methods

The one dimensional water hammer equations of the continuity and momentum equations are as follows (Wylie et al., 1993):

$$\frac{\partial p}{\partial t}+v\frac{\partial p}{\partial x}+\rho a^2\frac{\partial v}{\partial x}=0 \qquad [1]$$

$$\frac{\partial v}{\partial t}+v\frac{\partial v}{\partial x}+\frac{1}{\rho}\frac{\partial p}{\partial x}-g\sin\theta+\frac{f|v|v}{2D}=0 \qquad [2]$$

where p is pressure, v is the mean flow velocity, ρ is the density, a is the wave speed, x and t are the spatial and temporal coordinates respectively, D is the inner diameter of pipe and f is the Darcy-Weisbach friction factor, g is the gravity acceleration, θ denotes the angle of pipe with respect to the horizontal direction. When the Mach number of the pipe flow is small enough (e.g., < 0.1), then the convective terms in above equations can be neglected. In this study, the small Mach number flow is considered for water supply pipelines, and therefore the convective terms are not included in the following derivations, which, however, will not limit the extension and applicability of the method development in this study to other situations with relatively larger Mach numbers (i.e., including the convective terms).

Inspired by the idea of applying kernel approximation to a Taylor series expansion developed by Chen et al. (1999), a universal matrix formulation for different meshless particle methods is derived herein for expressing the differential terms in above equations. By examining the resulted matrix elements, the relationship between these methods becomes clear and the evolution process of them is easily appreciated. Since the meshless particle methods are relatively new (actually have never fully used) for the modelling and analysis transient pipe flows, prior to obtaining the final results of meshless models, it is good to start with the basic principle and process of the type of method development.

Expanding the Taylor series for a function $f(\xi)$ (e.g., p and v in above governing equations) around point x in a one-dimensional domain yields:

$$\begin{aligned} f(\xi)=&f(x)+(\xi-x)f'(x)\\ &+\frac{1}{2}(\xi-x)^2f''(x)+O(\xi-x)^3 \end{aligned} \qquad [3]$$

Multiplying both sides of Eq. [3] with a compactly supported function $W_1(x)$: = $W_1(\xi-x, h)$ and then integrating over the computational domain Ω gives:

$$\begin{aligned} &\int_\Omega[f(\xi)-f(x)]W_1(x)\mathrm{d}\xi\\ &=f'(x)\int_\Omega(\xi-x)W_1(x)\mathrm{d}\xi\\ &+f''(x)\int_\Omega\frac{1}{2}(\xi-x)^2W_1(x)\mathrm{d}\xi \end{aligned} \qquad [4]$$

Note that in Eq. [4] the terms with higher-order (>2) derivatives have been neglected, and the smoothing length h is a size measure of the support. Similarly, with another function $W_2(x)$: = $W_2(\xi-x, h)$, we obtain:

$$\begin{aligned}&\int_\Omega \left[f(\xi)-f(x)\right]W_2(x)\mathrm{d}\xi \\ &= f'(x)\int_\Omega(\xi-x)W_2(x)\mathrm{d}\xi \\ &+ f''(x)\int_\Omega \frac{1}{2}(\xi-x)^2 W_2(x)\mathrm{d}\xi\end{aligned} \quad [5]$$

Approximating the integrals in Eq. [4] and Eq. [5] with Riemann sum and re-writing them in a matrix form gives:

$$\mathbf{Au} = \mathbf{b} \quad [6]$$

where:

$$\mathbf{A}=(\mathrm{A}_{kl}), \mathbf{b}=(b_k), k,l=1,2,\ \mathbf{u}=(f'(x), f''(x))^{\mathrm{T}} \quad [7]$$

with:

$$\mathrm{A}_{kl}=\sum_j P_k Q_l \Delta V_j \quad [8a]$$

$$b_k=\sum_j \left[f(x_j)-f(x)\right]P_k\Delta V_j \quad [8b]$$

$$P_1=W_1(x), P_2=W_2(x) \quad [8c]$$

$$Q_1=x_j-x, Q_2=\frac{1}{2}(x_j-x)^2 \quad [8d]$$

Depending on the choice of $W_1(x)$ and $W_2(x)$, different meshless particle methods have been developed in the literature as reviewed in the introduction section. Theoretically, functions $W_1(x)$ and $W_2(x)$ can be any forms without connection, but in practice, they are often related to the same function, say $W(x)$ which is known as kernel function or kernel in the community of particle methods (Monaghan, 2012; Violeau, 2012). In this paper, we assume they are the first- and second-order derivatives of the kernel, i.e., $W_1(x) = W'(x)$ and $W_2(x) = W''(x)$. The estimated first- and second-order derivatives are obtained by solving Eq. [6], which is referred to as the modified smoothed particle method (MSPM). Only the first-order derivative estimate is given below as:

$$f'(x) = \frac{\sum_j \left[f(x_j)-f(x)\right]\left(\mathrm{A}_{22}W'(x)-\mathrm{A}_{12}W''(x)\right)}{(\mathrm{A}_{11}\mathrm{A}_{22}-\mathrm{A}_{12}\mathrm{A}_{21})/\Delta V_j} \quad [9]$$

Furthermore, depending on simplifications to the moment matrix $\mathbf{A}$ in Eq. [6], the developed MSPM estimates of the first- and second-order derivatives may degenerate to the well-known CSPM and SPH methods. Specifically, if the second-order derivative term in Eq. [4] is neglected, then kernel estimate of $f'(x)$ is obtained as:

$$f'(x)=\frac{\int_\Omega \left[f(\xi)-f(x)\right]W'(x)\mathrm{d}\xi}{\int_\Omega(\xi-x)W'(x)\mathrm{d}\xi} \quad [10]$$

or in particle summation form:

$$f'(x)=\frac{\sum_j \left[f(x_j)-f(x)\right]W'(x)\Delta V_j}{\sum_j (x_j-x)W'(x)\Delta V_j} \quad [11]$$

This is the corrective smoothed particle method (CSPM) proposed by Chen et al. (1999), which has been applied to many structural dynamic problems (Chen et al., 1999; 2001). Comparing with Eq. [9], it is easy to find out that Eq. [11] is actually a special case of Eq. [9] with A_{12} = 0. With the estimated $f'(x)$, the estimate of $f''(x)$ can be accordingly obtained from Eq. [5], which is rarely used in particle simulations. It is because high-order governing equations are usually transformed into first-order systems by introducing certain intermediate variables, e.g. heat flux and stresses (Chen et al., 1999; 2001), and then to be solved.

If $\int_\Omega [(\xi - x)\ W'(x)]\ d\xi = 1$ is further assumed and applied to Eq. [4], then the kernel estimate of $f'(x)$, in particle summation form, is

$$f'(x) = \sum_j \left[f(x_j) - f(x) \right] W'(x) \Delta V_j \qquad [12]$$

This is the most widely used estimate of the first-order derivatives in the SPH community (Monaghan, 2012; Violeau, 2012). For the estimate of the first-order derivative, the developed MSPM scheme in Eq. [9] together with the CSPM in Eq. [11] and the classic SPH in Eq. [12] can be written in a uniform way as

$$f'(x) = \sum_j \left[f(x_j) - f(x) \right] \overline{W}(x) \qquad [13]$$

where $W(x)$ can expressed based on the above developed formulas for MSPM, CSPM and SPH respectively.

In the application of meshless particle methods developed above, continuous media are partitioned into a finite number of N parts that are referred to as particles. Each particle j ~ [1, N] carries a mass m_j, density ρ_j, velocity V_j , pressure P_j and other properties depending on the specific problem. During motion, a particle is allowed to change its density and volume, but its mass $m_j = \rho_j \Delta V_j$ keeps constant. For details of standard SPH, the readers are referred to the recent review by Monaghan (2012) and the text book of Violeau (2012).

2.2 Initial and boundary conditions

The initial condition of steady-state flow in the pipeline system is calibrated by the known physical principles (such as Darcy-Weisbach friction loss and the valve orifice equation), with the aim to adjust and obtain reasonable parameters in above developed methods (e.g., artificial viscosity and particle numbers) for the studied system. Then the calibrated results and settings of the parameters based on initial flow conditions are assumed to be valid for transient flow process, with their validity and accuracy verified and discussed later in the numerical application section of this paper.

As the kernel support in boundary region is truncated, the common SPH method suffers from an inherent shortcoming known as boundary deficiency. To remedy it, two kinds of methods have been successfully proposed. The one is the image particle methods (Hou et al., 2012a; Violeau, 2012) and the other is the corrective kernel methods (Hou et al., 2012b; Zhang and Batra, 2004). The methods of defining image particles not only can remedy the boundary deficiency problem, but also provide an efficient way to enforce boundary conditions. However, it is not necessary to add image particles outside the domain in corrective kernel methods. There exist three general types of boundary conditions in transient pipe flows, including reservoir with constant pressure, fast valve closure with final zero velocity state and series-pipe junction. Enforcement of the reservoir boundary is illustrated in Figure 1a and details are found in (Hou et al., 2012a). The zero velocity (reflection boundary) can be imposed using mirror particle method (Hou et al., 2012b; Violeau, 2012), as shown in Figure 1b.

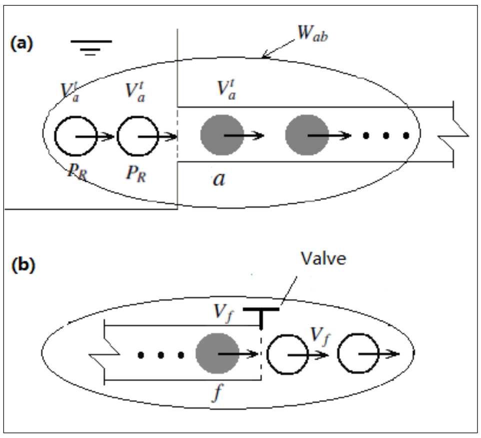

Figure 1. The image particle method for boundaries at:
(a) constant head reservoir and (b) fast closing valve.

For series-pipe junction in the multi-pipe system, the meshless particle formula can be derived for continuity and energy conservation relationships at the junction based on similar procedure above and expressed as (by assuming that no minor loss at the junction):

$$\frac{Dp_i}{Dt} = \frac{a_i^2}{A_i} \sum_{j \in S_i} m_j \left(Q_i - Q_j\right) W_{ij}\left(r_{ij}, h\right) \qquad [14]$$

$$\frac{DQ_i}{Dt} = -A_i \sum_{j \in S_i} \left[m_j \left(\frac{p_j}{\rho_j^2} - \frac{p_i}{\rho_i^2} + \Pi_{ij} \right) \right] W_{ij}\left(r_{ij}, h\right) + gA_i \sin\theta_i + \frac{f_i |Q_i| Q_i}{2D_i A_i} \qquad [15]$$

where the subscripts i and j are the indices of the particles, S_i denotes the particle set within the range of smoothing length of particle i, Π_{ij} is the artificial viscosity term for transient wave, with:

$$\Pi_{ij} = \begin{cases} \dfrac{-\alpha \bar{a} \varphi_{ij} + \beta \varphi_{ij}^2}{\bar{\rho}}, & \left(v_i - v_j\right)\left(x_i - x_j\right) < 0 \\ 0, & \left(v_i - v_j\right)\left(x_i - x_j\right) \geq 0 \end{cases} \qquad [16]$$

$$\varphi_{ij} = \frac{\bar{h}\left(v_i - v_j\right)\left(x_i - x_j\right)}{r_{ij}^2 + \eta \bar{h}^2}, \qquad [17]$$

where $\bar{a} = 0.5\left(a_i + a_j\right)$ is the average of the wave speed of particle i and j, $\bar{h} = 0.5\left(h_i + h_j\right)$ is the average smoothing length, $\bar{\rho} = 0.5\left(\rho_i + \rho_j\right)$ is the average density. For water hammer problems, α, β, and η are constant coefficients, with α = 1, β = 2, and η = 0.01 in this paper (Liu and Liu, 2003).

3 NUMERICAL VALIDATION AND APPLICATIONS

Two simple pipeline systems with different configurations, as shown in Figure 2 below, are used for the investigation in this study, with Figure 2(T1) representing for the typical single-pipeline system of reservoir-pipe-valve configuration and Figure 2(T2) representing for the multiple-pipeline system of reservoir-series-pipeline-valve configuration. Different parameters settings are as follows:

(1) For single-pipeline system in Figure 2(T1), pipe length L_a = 20 m, diameter D_a = 0.8 m, friction factor f_a = 0.02, and wave speed a_a = 1020 m/s;
(2) For series-pipeline system in Figure 2(T2), upstream pipe section (a): L_a = 30 m, D_a = 0.03 m, f_a = 0.02, and a_a = 1200 m/s; downstream pipe section (b): L_b = 37 m, D_b = 0.02 m, f_b = 0.015, and a_b = 1300 m/s.

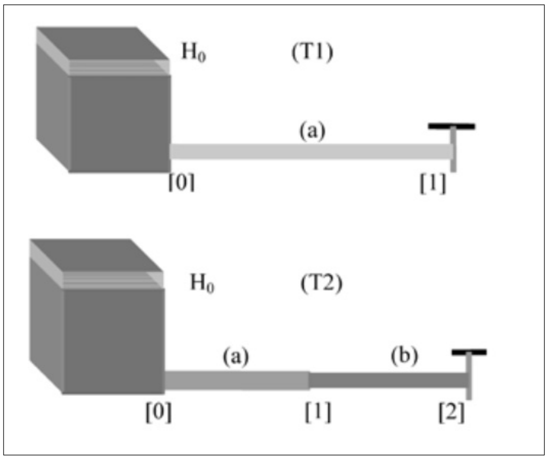

Figure 2. Schematic configuration of test pipeline systems: (T1) single-pipeline system; (T2) series-pipeline system (after Duan et al., 2009):

3.1 Single-pipeline system

The single-pipeline system in Figure 2(T1) was firstly used for the validation and comparison of different developed meshless methods in this study. Subjected to fast closure of downstream end valve at node [1] in the figure, fast transients were generated and simulated with the particle methods including SPH, CSPM and MSPM respectively. The results of typical MOC scheme were also obtained for comparison and validation. The initial steady-state velocity of pipe flow was 1.0 m/s and the reservoir pressure was constant with 1 MPa. Initially for the meshless methods, there were 201 particles evenly distributed in the pipe. The results by different methods are shown in Figure 3. All the three particle methods gave results in line with the traditional MOC solution, although SPH suffered from slightly larger numerical smearing effect. The difference between CSPM and MSPM is not distinguishable and a small oscillation occurred at the first wave front. Consequently, the comparison confirms the validity of the developed three meshless methods for the modelling and analysis of transient pipe flows, with similar accuracy of transient pressure simulations.

3.2 Series-pipeline system

Because of the similar accuracy of the developed three meshless methods shown in Figure 3, only the SPH method is applied herein for the study of series-pipeline systems in Figure 2(T2). Similar application procedures and results discussion can be conducted for other two methods. Similarly, the transients are caused by the sudden valve closure at the downstream end (i.e., noted as [2] in the figure). The results of meshless-based SPH in this study and the traditional MOC (Duan et al., 2009) were obtained and plotted in Figure 4 for comparison.

The comparison in Figure 4 clearly demonstrates that overall the meshless based SPH simulation result agree well with the traditional MOC solution. Specifically, the phases of the transient traces with complicated variations due to series-pipe junction are well predicted and in the meanwhile, relatively small differences exist for the transient amplitudes in the whole studied transient domain. It is also observed from the results that the simulated wave front by the meshless particle method is not as sharp as that by MOC due to the dissipation effect of artificial viscosity, but the difference was still relatively small. It should be noted that unlike the classical MOC algorithm, the proposed meshless based formula doesn't need to pay special numerical treatment for the series pipe junctions with regard to the temporal and spatial discretization during the simulations. Particularly, the calculation of transient flowrate and pressure is straightforward because the diameter variability has been already derived in the developed meshless method in Eq. [14] and Eq. [15], which has greatly reduce the complexities of numerical programming and the errors of mathematical interpolation.

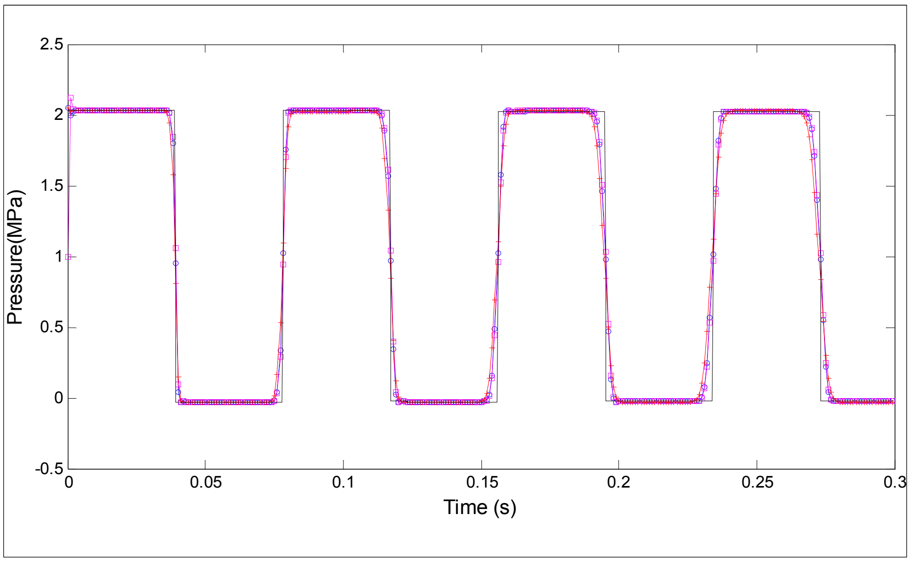

Figure 3. Simulated pressure histories at valve in the instantaneous valve closure case: solid line-MOC, solid line with plus-SPH, solid line with circle-CSPM, and solid line with square-MSPM.

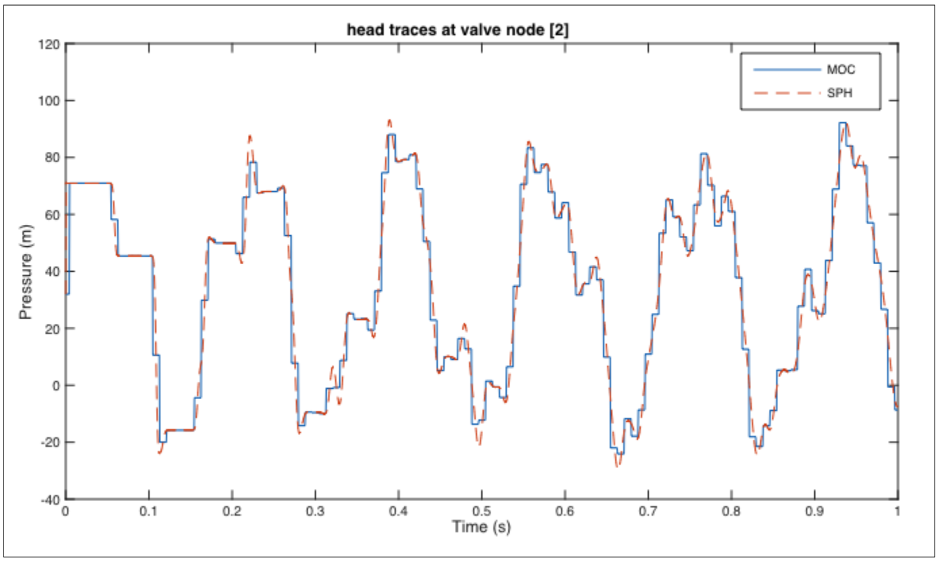

Figure 4. Simulated pressure traces at the downstream valve for the two-series-pipe system.

4 DISCUSSIONS AND IMPLICATIONS

4.1 Influence of different parameters

It is indicated in above applications that different parameters, such as the artificial viscosity coefficients of α and β in Eq. [16] and smoothing length of h in Eq. [17], was introduced and calibrated/assumed for the use of the developed meshless particle methods. Therefore, it is necessary to examine the influence of these parameters on the modelling results of these developed methods. For simplification and illustration herein, the single-pipeline system described above is taken for the investigation.

The results of transient flow modelling by applying different values of the artificial viscosity parameters (α and β) are plotted in Figure 5 and 6, respectively. From the results, it can be concluded that: (1) the artificial viscosity can suppress the numerical dispersion and maintain the numerical stability; however, (2) unsuitable (e.g., larger or smaller α) parameter set may lead to instability or less sharpness of wave front (see Figure 5). On one hand, from the test results in Figure 5, the linear term relating to parameter α in Eq. [16] plays an important role for the elimination of numerical oscillation. Specifically, it clearly reveals from Figure 5 that the case of $\alpha < 1$ leads to dispersion wiggles at the wave front, while that of $\alpha > 1$ may result in serve dissipation effect. On the other hand, from the results in Figure 6 (with only the first wave reflection shown in the figure for clear observation), the other viscosity parameter β in the artificial viscosity term also contributes to the suppression of the numerical oscillation at the sharp wave front, and the value smaller than 2 of β may not effective to eliminate the wiggles at the sharp wave front for the pipe system of interest in this study. Therefore, for the single-pipeline system studied herein, a combination of $\alpha = 1$ and $\beta = 2$ is a compromising choice for the consideration of accuracy and numerical stability in the present study.

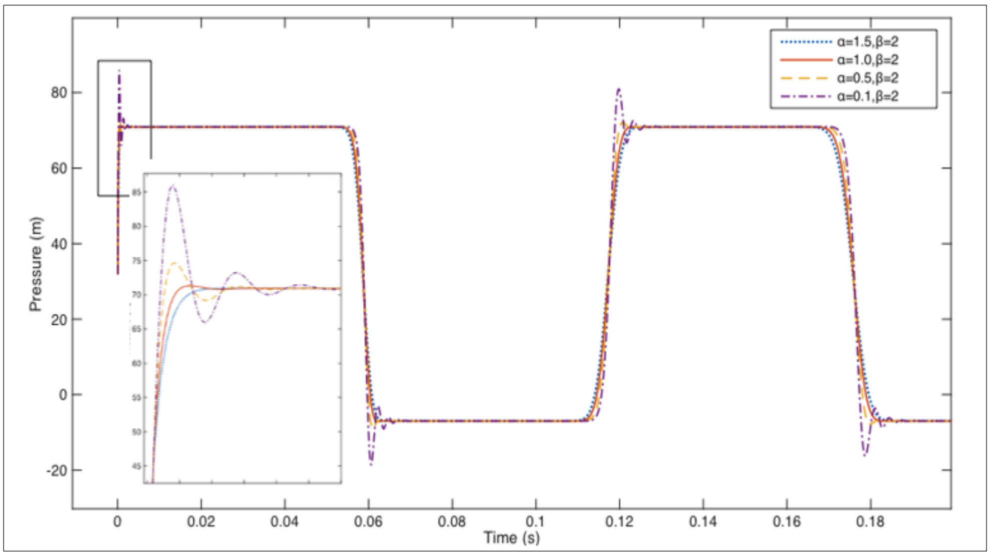

Figure 5. Effect of artificial viscosity parameter α (with fixed $\beta = 2$) on transient modelling result.

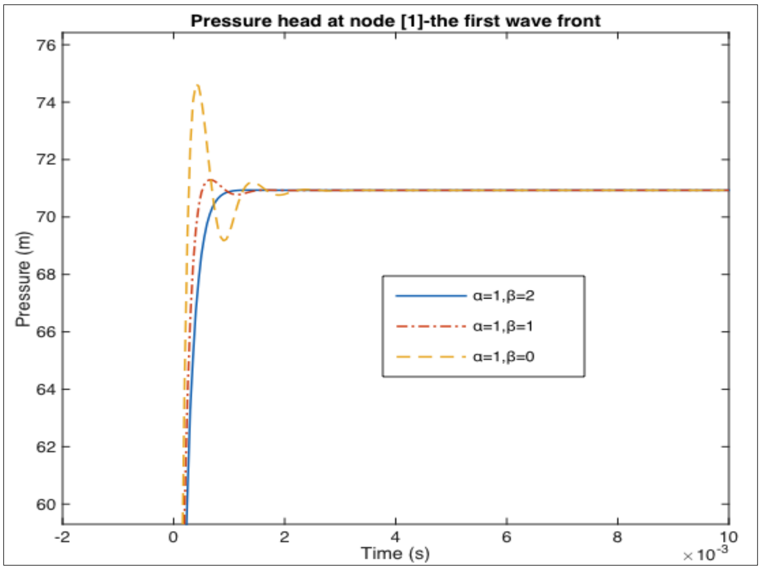

Figure 6. Effect of artificial viscosity parameter β (with fixed $\alpha = 1$) on transient modelling result.

Furthermore, the smoothing length (h) in Eq. [17] is another important parameter that may affect the validity and accuracy of the developed meshless methods in this study. This is mainly because the smoothing length defined in the meshless methods affects not only the accuracy (e.g., wave propagation and dispersion), but also the computational efficiency as well as the numerical stability (Monaghan et al., 2012; Hou et al., 2012b). Generally, in the literature, it is suggested that h = (1~2)Δx is the common choice for compromising the accuracy and efficiency. However, this criterion was proposed mainly for the free-surface flow system, which may not be suitable for transient pipe flows herein. For analysis, different choices of smoothing length h were tested for obtaining the 'best' compromising choice among accuracy, efficiency and numerical stability. The results are shown in Figure 7. From the results, it can be found that a larger smoothing length may lead to better numerical stability but with severe dissipation at the sharp wave front, while the smaller smoothing length may result in higher computational efficiency, severe dispersion and less accuracy results. With extensive tests in this study, the case of $h < 2\Delta x$ may result in numerical instability problem (with α=1, β=2 for artificial viscosity coefficients specified above), while the case of $h > 3\Delta x$ can lead to serve dissipation effect at the sharp wave front (see Figure 7). Therefore, for the studied pipe system herein, a smoothing length of h = 2.5Δx became the most suitable choice for compromising the numerical stability and computational accuracy. On this point, this tested value of smoothing length for transient pipe flows is very different from the proposed value $h \sim \Delta x$ for most cases of free-surface or slightly pressurized flows in the literature (Hou et al., 2012b; Monaghan et al., 2012; Violeau, 2012).

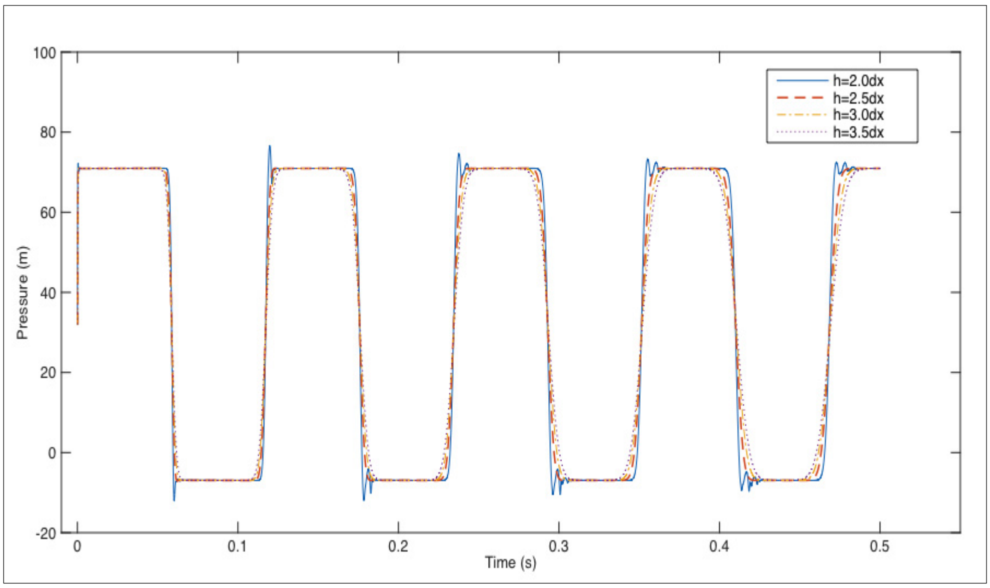

Figure 7. Effect of the smoothing length on the transient modelling result.

It is also noted that the obtained values of these important parameters (α, β, h) were mainly based on extensive tests of the pipe system inspected in this study, which require further theoretical explanation and evidence in the future work.

4.2 Practical implications

The numerical applications and results in this study indicated the feasibility and accuracy of the meshless particle methods for transient flow modelling and analysis in both single- and multiple- pipe systems. Although only the series pipe junction was considered and included in the derivation process, similar principle and procedure can be further extended and applied to more complex situations such as branched and looped junctions, which will be completed in the future work. From this perspective, the results and findings of this study may have great significance to both the theoretical development and practical applications of transient flow analysis, especially in complex pipe systems.

On one hand, the successful extension of the meshless particle based methods provides alternative approach to transient pipe flow simulations in complex pipeline systems, in addition to the classic meshed methods in the literature. On this point, with the aid of advantages of the meshless simulation scheme, the accurate capture and analysis of complex transient phenomena such as flow separation and cavitation as well as multi-phase flows (e.g., air-water flows) and flow regime transition in pipeline systems becomes probable and more convenient. On the other hand, with the successful implementation of the different meshless schemes to the complex pipe junctions, the accurate representations and simulations for the transient interactions of transient waves and system components as well as complex boundaries become feasible and relatively simple in practical applications of transient pipe flow problems.

Consequently, the development and extension of the different meshless particle based methods is necessary and significant to the modeling and analysis of transient pipe flows, which is thus worthwhile of more investigations (further extension and extensive validations) in the future.

5 CONCLUSIONS

Three different meshless particle methods (SPH, CSPM, MSPM) were extended and formulated to transient pipe flows in this study for different pipeline systems (including single- and series- pipeline systems). The developed models and methods were validated by numerical applications for two typical pipe systems with single pipeline and two-series pipelines, with comparison to the typical MOC scheme. The comparative results indicate the good agreement and accuracy of the extended meshless methods for the modelling and analysis of transient pipe flows. The concluding remarks are summarized as follows:

(1) All the three developed meshless methods could provide accurate results as the classic MOC scheme;
(2) The developed meshless methods are applicable to both single- and multiple- pipe systems for capturing accurately the evolution of transient phase and amplitude;
(3) The meshless particle methods are preferable to the application of complex systems due to their convenience of numerical treatment and calculation;
(4) The artificial viscosity term in the developed meshless particle methods is useful to eliminate the numerical oscillations, and the test results reveal that the linear term φ_{ij} in Π_{ij} may contribute more than the quadratic term φ_{ij}^2 to the suppression of the numerical oscillations;
(5) The smoothing length shows an important effect on the suppression of numerical oscillations at the shock wave, and the result of h = 2.5Δx is a most suitable choice for the studied transient pipe flow system in this paper, which is very different from the suggested value for free-surface flows in the literature.

It is also noted that only the simple pipe systems with single- and series- pipelines were considered in this preliminary study. Further extension and validation of such advantageous methods and their key parameter settings (α, β, h) to more complex system configurations (e.g., branched and looped pipe systems) and other complex flow conditions (e.g., column separation and air-water mixing flows) is necessary and significant in the future study.

ACKNOWLEDGEMENTS

This work was partially supported by the research grants from: (1) the Hong Kong Research Grants Council (RGC) under projects no. 25200616 and no. T21-602/15-R; and (2) the Hong Kong Polytechnic University under projects no. 1-ZVGF and no. 1-ZVCD.

REFERENCES

Chaudhry, M.H. & Hussaini, M.Y. (1985). Second-Order Accurate Explicit Finite Difference Schemes for Water Hammer Analysis. *Journal of Fluids Engineering – ASME*, 107, 523-529.

Chen, J.K., Beraun, J.E. & Carney, T.C. (1999). A Corrective Smoothed Particle Method for Boundary Value Problems in Heat Conduction. *International Journal of Numerical Methods in Engineering*, 46, 231-252.

Chen, J.K., Beraun, J.E. & Jih C.J. (2001). A Corrective Smoothed Particle Method for Transient Elastoplastic Dynamics. *Computational Mechanics*, 27, 177-187.

Duan, H.F., Ghidaoui, M.S. & Tung, Y.K. (2009). An Efficient Quasi-2D Simulation of Water Hammer in Complex Pipe Systems. *Journal of Fluids Engineering – ASME*, 131(8), 081105.

Duan, H.F., Tung, Y.K. & Ghidaoui, M.S. (2010a). Probabilistic Analysis of Transient Design for Water Supply Systems. *Journal of Water Resources Planning and Management – ASCE*, 136(6), 678-687.

Duan, H.F., Lee, P.J., Ghidaoui, M.S. & Tung, Y.K. (2010b). Essential System Response Information for Transient-Based Leak Detection Methods. *Journal of Hydraulic Research – IAHR*, 48(5), 650-657.

Hou, Q., Kruisbrink, A.C.H., Tijsseling, A.S. & Keramat. A. (2012a). Simulating Water Hammer with Corrective Smoothed Particle Method. *Proceedings of the 11th International Conference on Pressure Surges*, 24-26 October, 2012, Lisbon, Portugal.

Hou, Q., Zhang, L.X., Tijsseling, A.S. & Kruisbrink. A.C.H. (2012b). Rapid Filling of Pipelines with the SPH Particle Method. *Procedia Engineering*, 31(2012), 38-43.

Hou, D.Q., Wang, S., Kruisbrink, A.C.H. & Tijsseling, A.S. (2015). Lagrangian Modelling of Fluid Transients in Pipelines with Entrapped Air. Proceedings of the 12th *International Conference on Pressure Surges*, 18-20 November 2015, Dublin, Ireland.

Hwang, Y. & Chung, N. (2002). A Fast Godunov Method for the Water Hammer Problem. *International Journal of Numerical Methods in Fluids,* 40(6), 799-819.

Liu, G.R. & Liu, M.B. (2003). *Smoothed Particle Hydrodynamics: A Meshfree Particle Method*, World Scientific, Singapore.

Monaghan, J.J. (2012). Smoothed Particle Hydrodynamics and its Diverse Applications. *Annual Review of Fluid Mechanics*, 44(1), 323-335.

Violeau, D. (2012). *Fluid Mechanics and the SPH Method: Theory and Applications*. Oxford University Press, Oxford, UK, 594.

Wahba, E.M. (2006). Runge–Kutta Time-Stepping Schemes with TVD Central Differencing for the Water Hammer Equations. *International Journal of Numerical Methods in Fluids*, 52, 571-590.

Wylie, E.B., Streeter, V.L. & Suo, L.S. (1993). *Fluid Transients in Systems*. Prentice-Hall, Englewood Cliffs.

Zhang, G.M. & Batra, R.C. (2004). Modified Smoothed Particle Hydrodynamics Method and its Application to Transient problems. *Computational Mechanics*, 34, 137-146

Zhao, M. & Ghidaoui, M.S. (2004). Godunov-Type Solutions for Water Hammer Flows. *Journal of Hydraulic Engineering – ASCE*, 130(4), 341-348.

Proceedings of the 37th IAHR World Congress
August 13 – 18, 2017, Kuala Lumpur, Malaysia

DAMPING RATE OF TRANSIENT OSCILLATIONS IN PRESSURIZED CLOSED CONDUITS

SAHAD KHILQA[(1)], MOHAMED ELKHOLY[(2)], MOHAMED H. AL - TOFAN[(3)], JUAN M. CAICEDO[(4)] & M. HANIF CHAUDHRY[(5)]

[(1,3,4,5)] University of South Carolina, Columbia, South Carolina, USA,
skhilqa@email.sc.edu; maltofan@email.sc.edu; caicedo@cec.sc.edu; chaudhry@cec.sc.edu
[(2)] Alexandria University, Alexandria, Egypt,
mskhydro@gmail.com

ABSTRACT

Although the modeling of transient conditions in closed conduit has advanced significantly during the last four decades, the dissipation of transient oscillations with time is not completely understood at present, and usually, dissipation in computed results is slower than that in the actual systems. Since the first transient state peak pressure that is not affected by the dissipation of pressure oscillations is utilized for design, the dissipation is not considered important in typical situations. However, for multiple operations in a system, dissipation is important for determining the time for the second operation to reduce the severity of the subsequent transient conditions. If not done properly, the resulting transient conditions may be worse than those in a single operation. Two-dimensional models, convolution-integral and instantaneous-acceleration based methods have been used for including unsteady friction in simulations. The first two models are computationally intensive while the selection of coefficients for the latter has been challenging in addition to the requirement of the simulation for the entire system. Consequently, these methods have not been utilized for general real-life applications. In this paper, a method is presented following the methodology for the computation of the dissipation of structural oscillations initiated by impulse loading, e.g. earthquake. This method does not require simulation of the entire system, is not computationally intensive and yields reasonable results for practical applications. An empirical equation is developed for the damping ratio by using the dimensional analysis and nonlinear regression. Comparisons of the computed results for a pipeline with a constant-level upstream reservoir and a downstream control valve with the experimental measurements during 18 transient experiments show good agreement.

Keywords: Damping ratio; piping system; transient; unsteady friction.

1 INTRODUCTION

Modeling of transient conditions in closed conduits initiated by flow changes has progressed significantly during the last four decades. As long as the basic underlying assumptions on which the governing equations are based and the restrictions on the numerical procedures (*e.g.*, stability and accuracy criteria) are observed, the computed results are reliable and may be used with confidence for the design and operation of various systems. However, the dissipation of the transient oscillations with time is not completely understood at this time, and usually, the computed results show slower dissipation than that in the actual systems. This difference is mostly attributed to the use of steady state friction equation to compute oscillations during the transient state rather than using the unsteady friction in the computations. Since the first transient state peak pressure is not affected by the dissipation of pressure oscillations and this peak pressure is typically used for design, the dissipation of pressure oscillations is not considered to be very significant in typical situations. However, for multiple operations in a system, *e.g.* starting the pumps following power failure, load acceptance following load rejection on turbines or opening or closing of control valves following closing or opening operations, it becomes necessary to predict the dissipation, so that the second operation is started at a time that results in reducing the severity of the subsequent transient conditions.

Three models have been presented to simulate the dissipation of the water hammer pressures, namely the convolution integral, quasi two-dimensional and the instantaneous acceleration based models. These models (Ghidaoui et al., 2005; Adamkowski and Lewandowski, 2006; Prashanth Reddy et al., 2011; Chaudhry, 2014) require simulation of transients in the entire system and are computationally intensive. As a result, there has been limited adoption of these models for general real-life applications. In addition, there are questions about their reliability and applicability. Instantaneous acceleration-based (IAB) model, currently being used by most researchers, may be classified further as one-coefficient and two-coefficient models. The coefficients vary over a wide range, and to implement these models, a numerical solution of the governing equations is needed.

Adamkowski and Lewandowski (2006) presented a comparison between the quasi-steady friction model and the following five different models: Zielke's (Zielke, 1968),Trikha's (Trikha, 1975), Vardy and Brown (Vardy and Brown, 2003), Zarzycki's (Zarzycki, 1994), and Bruone's Brunone et al. (1991) models. They recommended studying the unsteady friction factor model for a wide range of Reynolds number (higher than 16000).

The objective of the present work is to present a model that is simple but is not computationally intensive. For illustration purposes, it is applied for the prediction of the dissipation of pressure oscillations at the valve located at the down-stream end of a simple reservoir-pipeline-valve system due to instantaneous valve closure without numerically solving the entire system.

2 EXPERIMENTAL DATA

Two data sets are used in this work: the first set is data obtained from the experiments carried out in the Hydraulic Laboratory at the University of South Carolina (USC), while the second set is data reported in the literature. Measured results for eighteen different tests are utilized in this study. To conserve space, however, results for three of such comparison are included.

The USC setup consists of a pressurized tank at the upstream end, a 158.71m long copper pipe, 0.0254m in diameter with 0.001m wall thickness and a ball valve at the downstream end of the pipe, as shown in Figure 1.

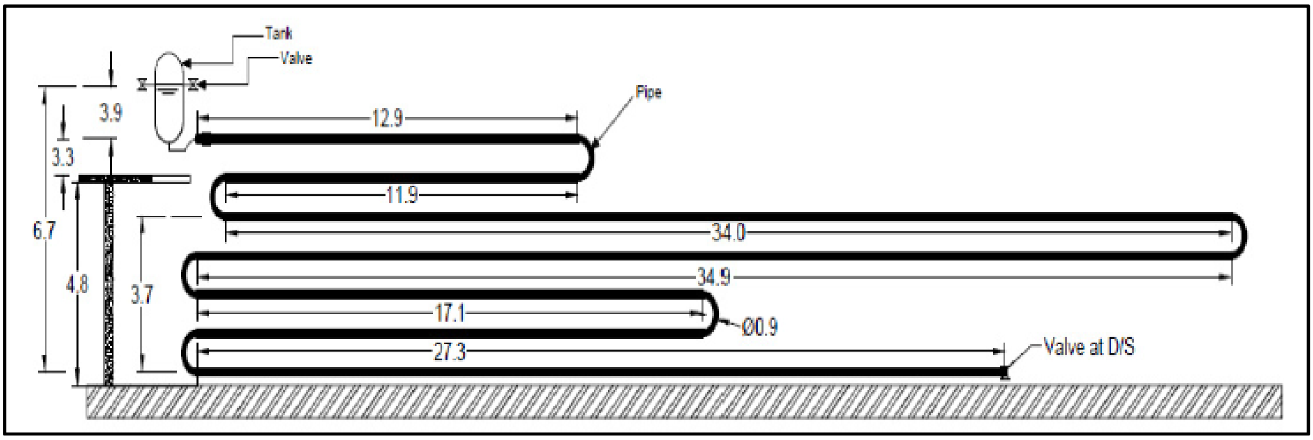

Figure 1. A layout of the experimental setup. Dimensions in meter.

A pressure transducer (manufactured by Honeywell International Inc.) is mounted on the pipe just upstream of the valve. Once the discharge and the static head become constant, the water supply to the upstream tank is cut off to keep the static head constant during the transient state. At the same time, a magnetic switch triggers a rapid valve closure to generate transient state conditions in the piping system.

The experiment is run until the flow becomes steady. Table 1 lists the system properties. Only data for three experiments are listed for which comparisons are presented in the table. Where L is the pipe length, D is the pipe diameter, H_s is the static head at the pressurized tank, V_o is the steady-state flow velocity, Re is the Reynolds number, $a_{reported}$ is the wave velocity reported in the literature, a is the wave speed.

Table 1. System properties experimental set-up.

Test No.	L (m)	D (m)	H_s (m)	V_o (m/s)	Re	$a_{reported}$ (m/s)	a (m/s)	Pipe type
1[a]	158.71	0.0254	34.36	0.309	7845	------	1197	copper
2[b]	98.11	0.016	127.5	0.34	5731	1298	1270	copper
3[c]	3000	0.40	326	0.78	311930	1000	565	steel

Note, the superscripts in the Test numbers refer to the source as follows: [a] = USC; [b] = Adamkowski and Lewandowski (2006); [c] = Ramos et al. (2004).

3 UNDER-DAMPED SYSTEM

The instantaneous closure of a valve located at the downstream end of a reservoir-pipeline-valve system results in pressure oscillations at the valve that are similar to the oscillations of the mass in a spring-mass-damper system. The mass oscillates, and the displacement of the mass exhibits an exponential decay due to viscous damping. The exponential decay may be studied by analyzing the vibration of the mass under free vibrations, i.e. there is no external force.

Similarities and differences between a vibrating spring-mass and a hydraulic system are explained in Chapter 8 of Chaudhry (2014). The current study focuses on the formulation of a model for computing the damping ratio, ξ for the pressure oscillations at the downstream end of a reservoir-pipe system following instantaneous valve closure. Similar to the motion of the mass in a spring-mass system, the normalized pressure head variation, $H = h - h_O$, may be written as:

$$m\frac{d^2H}{dt^2}+c\frac{dH}{dt}+kH=0 \qquad [1]$$

where h is the pressure head at the downstream valve and h_O is the head at the upstream reservoir; m is the mass of the spring; c is the damping constant; and k is the spring constant. The general solution of Eq. [1] for an under-damped system is:

$$H(t)=e^{-(c/2m)t}\left(c_1\cos(\omega t)+c_2\sin(\omega t)\right) \quad [2]$$

where ω is the frequency of the pressure oscillations. This equation may be simplified as:

$$H(t)=Ae^{-\xi\omega_n t}\sin(\omega_n t) \quad [3]$$

where A is the amplitude of the pressure head at t=0. The exponent term $(c/2m)$ is an unknown quantity with dimension of $(1/s)$ and it represents the rate of the decay of the pressure head with time. This term may be assumed equal to $(\xi\omega_n)$ where ω_n represents the natural frequency of the pressure oscillations at the valve.

An approximated value of the amplitude, A, may be computed using the Joukowski's formula at t=0 for an instantaneous valve closure, i.e. $A\cong\pm\Delta H$, (positive sign is for valve closure and negative sign is for valve opening) and $\Delta H=-a\Delta v/g$, where ΔH is the variation in pressure head at t=0; Δv instantaneous variation of the flow velocity at the valve. The term $e^{\xi\omega_n t}$ represents the damping of the oscillations and the head at the valve, H, approaches zero as t tends to infinity. In other words, Eq. [3] is an exponential decaying function with ξ as the damping ratio which is a function of the system boundaries, flow rate and fluid properties.

Pressure head oscillations at the downstream valve are computed by using Eq. [3] and are compared with the experimental measurements listed in Table 1. From the best fit between the computed and experimental data, the damping ratio for the experimental measurements, ξ_{exp} is determined.

The damping ratio is a function of the following system parameters:

$$\xi=\psi(L, D, V_o, \mu, \rho, \epsilon, g, K, E, e) \quad [4]$$

where μ is the dynamic viscosity of the fluid; ρ is the fluid density; ϵ is the absolute roughness of the pipe, and g is the gravitational acceleration; K is the bulk modulus of elasticity of the fluid, E is Youngs moduls of elasticity of the pipe wall material, and e is the pipe thickness. Using dimensional analysis, a relationship for the damping ratio among the parameters in Eq. [4] may be developed as:

$$\xi=\psi(Re, Ma, \frac{\epsilon}{D}, \frac{V_o^2}{Lg}) \quad [5]$$

where Re is Reynolds number $= V_oD\,\mu/a$; Ma is Mach number $= V_o/a$; ϵ/D is relative roughness of the pipe and $\left(\frac{V_o^2}{Lg}\right)$ is a dimensionless parameter defining the resistance term in the system, denoted here as S_f and a is the wave speed. In the dimensional analysis, the dimensionless group $K/\rho V_o^2$ and e represent wave speed. Therefore, it is appropriate to represent them in terms of the wave speed in Ma as in Eq. [5]. Applying non-linear regression analysis to the available experimental data for 18 tests and the dimensionless parameters of Eq. [5], a relationship is developed for the damping, ξ_{est} as a function of the dimensionless variables Eq. [5]. This may be written as:

$$\xi_{est}=Re^{0.062}\, Ma^{0.619} \left(\frac{\epsilon}{D}\right)^{0.001} S_f^{-0.033} \quad [6]$$

The correlation coefficient, R^2, between ξ_{exp} and ξ_{est} of Eq. [6] is 0.88.

It is clear from Eq. [6] that the effect of Ma and Re on the damping ratio is greater than that of ϵ/D and S_f. As shown in Figure 2, an increase in Reynolds number increases the damping ratio in general. However, this increase has a very mild gradient in the laminar region and a steep gradient for Reynolds number greater than 42,000. The experimental damping ratio varies from 0.007 to 0.021 for Reynolds number less than 42,000 and from 0.018 to 0.058, for Re greater than 42,000. It is clear from Eq. [6] that reducing the wave speed or increasing the Mach number, increases the damping ratio significantly, as shown in Figure 3.

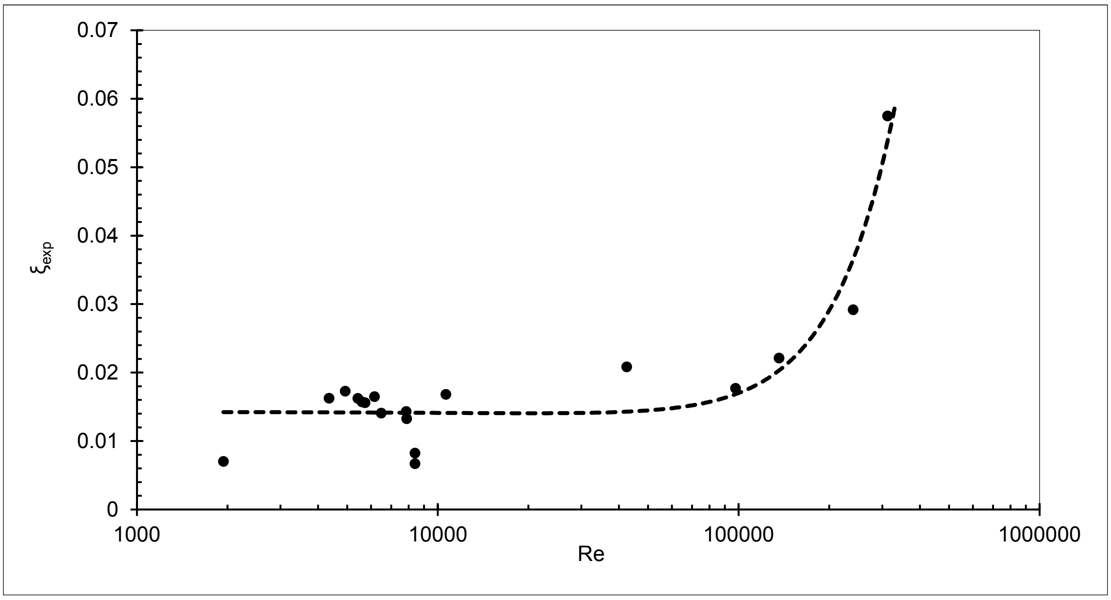

Figure 2. Variation ξ_{exp} vs. Re.

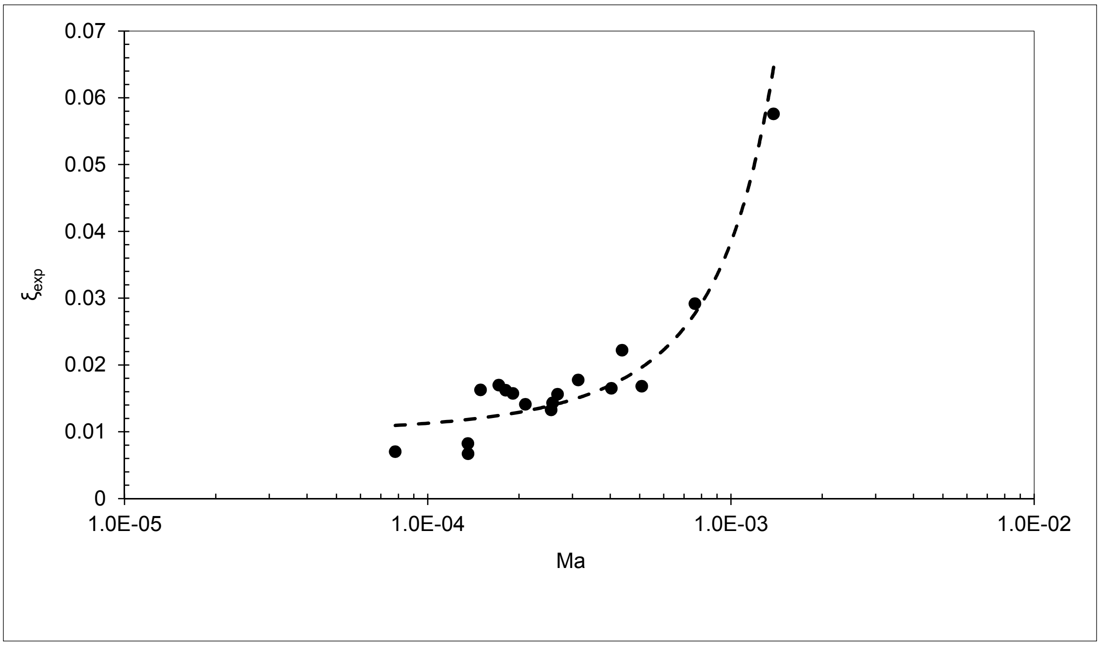

Figure 3. Variation ξ_{exp} vs. Ma.

For the effect of the relative roughness, it is noted that the damping ratio increases as the roughness increases but the effect is small and may be neglected unless the pipe has elements with large resistance, *e.g.* valves, bends, elbows, etc. In that case, their effects cannot be ignored. Other types of form resistance are not included in this analysis. The variation of S_f has a smaller effect on ξ_{exp} as compared to that due to Re and Ma. But the exponent of the resistance term is significant and shows the importance of including the pipe length.

Figure 4 - 6 show the comparison between the experimental results of the pressure head variations, H_{exp}, with time at the downstream valve and the computed, H_{comp}, from Eq. [3] based on the values of ξ_{est} estimated from Eq. [6]. These figures show that there is good agreement with the experimental measurements. It is worth mentioning that the time shift between H_{exp} and H_{comp} is almost identical. This is due to the use of the wave velocity calculated from the experimental data by averaging the wave oscillations for each $(2L/a)$. Additional experimental measurements with different boundary conditions are needed to demonstrate universal applicability of the relationship the damping ratio developed herein and to consider series pipes with different cross sections.

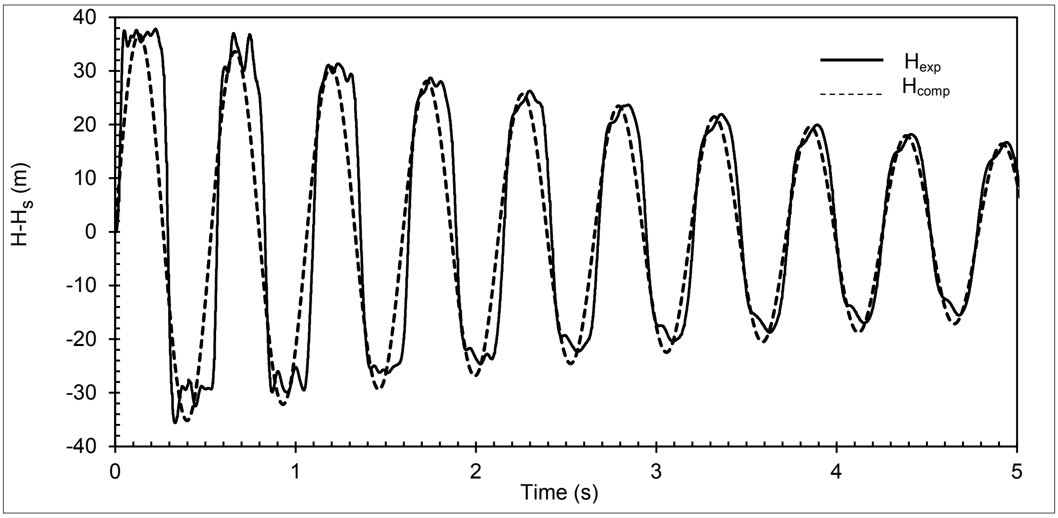

Figure 4. Comparison between H_{exp} and H_{est} of Test no.1.

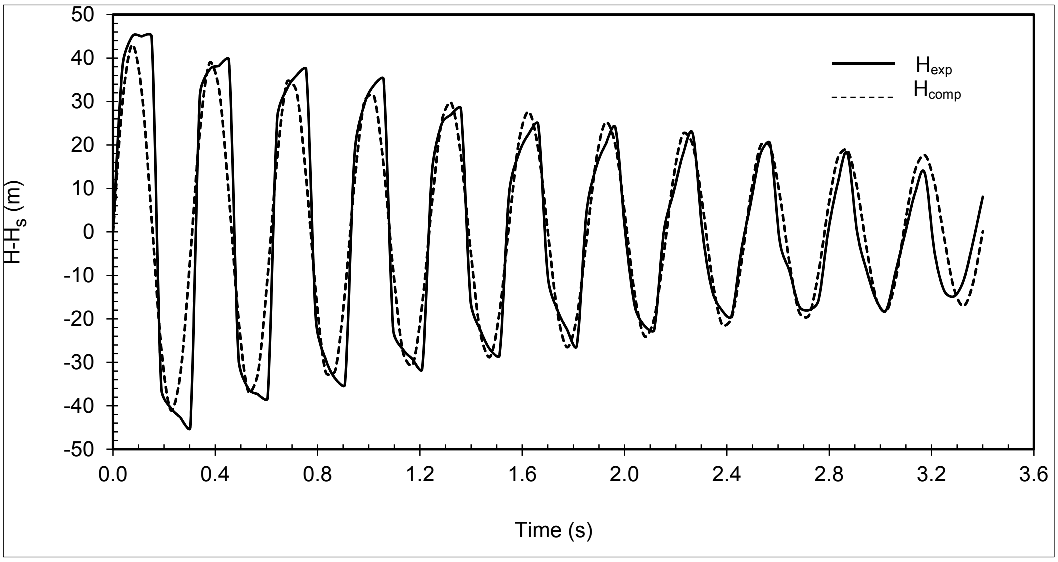

Figure 5. Comparison between H_{exp} and H_{est} of Test no.2.

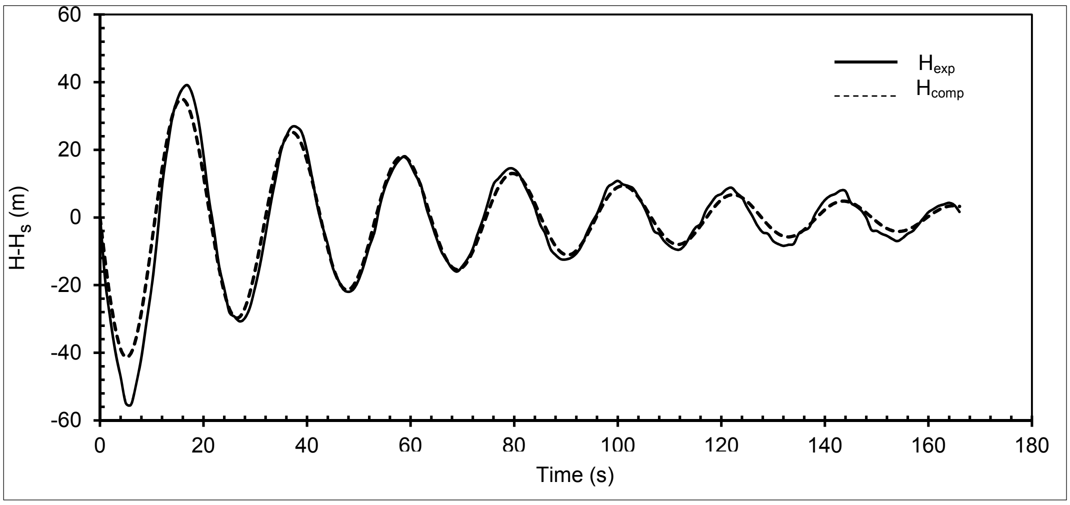

Figure 6. Comparison between H_{exp} and H_{est} of Test no.3.

4 SUMMARY AND CONCLUSIONS

The maximum and minimum transient pressures in a pipeline system are important as well as the dissipation of the transient oscillations with time to simulate multiple operations in a system properly. This study presents an expression to compute the damping of pressure oscillation in a simple piping system following the methodology for the computation of the dissipation of structural vibrations caused by impulse loading. A simple reliable model that is not computationally intensive is developed to predict the dissipation of the pressure head oscillations for the case of an instantaneous valve closure. This model does not depend on the size of the computational time step and does not require the simulation of the entire system. The damping ratio is obtained for a wide range of Reynolds numbers, Mach numbers, relative roughness of the pipe wall material and a resistance term. Both Reynolds and Mach numbers affect the damping ratio significantlly, while the effect of the relative roughness is small and may be neglected. And the effect of the length of the pipeline in the resistance term is smaller as compared to that of Reynolds and Mach numbers. The experimental damping ratio is found to vary from 0.007 to 0.021 for Reynolds number less than 42,000 and from 0.018 to 0.058 for Re >42,000.

ACKNOWLEDGEMENTS

The authors thank the Ministry of Higher Education and Scientific Research of Iraq (Mohesr), the Iraqi Cultural Office in Washington D.C., the Higher Committee for Education Development (HCED) in Iraq for providing scholarships to Khilqa and Al -Tofan to conduct this research. Financial support of National Science Foundation under Grant No. OISE 0730246 is acknowledged.

REFERENCES

Adamkowski, A. & Lewandowski, M. (2006). Experimental Examination of Unsteady Friction Models for Transient Pipe Flow Simulation. *Journal of Fluids Engineering*, 128(6), 1351-1363.

Brunone, B., Golia, U. & Greco, M. (1991). Some Remarks on the Momentum Equation for Fast Transients, *Proc. Int. Conf. on Hydr. Transients with Water Column Separation*, 201-209.

Chaudhry, M.H. (2014). *Applied Hydraulic Transients*. 3rd ed. Springer, 35-64.

Ghidaoui, M.S., Zhao, M., McInnis, D.A. & Axworthy, D.H. (2005). A Review of Water Hammer Theory and Practice. *Applied Mechanics Reviews*, 58(1), 49-76.

Prashanth Reddy, H., Silva-Araya, W.F. & Hanif Chaudhry, M. (2011). Estimation of Decay Coefficients for Unsteady Friction for Instantaneous, Acceleration-Based Models. *Journal of Hydraulic Engineering*, 138(3), 260-271.

Ramos, H., Covas, D., Borga, A., & Loureiro, D. (2004). Surge Damping Analysis in Pipe Systems: Modelling and Experiments. *Journal of Hydraulic Research*, 42(4), 413-425.

Trikha, A.K. (1975). An Efficient Method for Simulating Frequency-Dependent Friction in Transient Liquid Flow. *Journal of Fluids Engineering*, 97(1), 97-105.

Vardy, A. & Brown, J. (2003). Transient Turbulent Friction in Smooth Pipe Flows. *Journal of Sound and Vibration,* 259(5), 1011-1036.

Zarzycki, Z. (1994). Hydraulic Resistance in Unsteady Liquid Flow in Closed Conduits. *Research Reports of Tech. Univ. of Szczecin*, (516).

Zielke, W. (1968). Frequency-Dependent Friction in Transient Pipe Flow. *Journal of Basic Engineering,* 90(1), 109-115.

ANALYSIS OF PIPE TRANSIENTS IN HYDROPOWER INSTALLATIONS

GORAN PAVIĆ[(1)] & FABIEN CHEVILLOTTE[(2)]

[(1)] National Institute of Applied Science, Villeurbanne, France,
goran.pavic@insa-lyon.fr
[(2)] Matelys Research Lab, Vaulx-en-Velin, France,
fabien.chevillotte@matelys.com

ABSTRACT

Basic features of dynamics of fluid-filled pipes are summarised first. The fluid-wall coupling is discussed in some detail. Different circumferential pipe modes and the associated cut-on frequencies are addressed from theoretical as well as practical point of view. It is shown that advanced measurements require complementary analytical pipe modelling. Advantages of the use of a particular non-intrusive sensor for the detection of pressure pulsations are outlined. The sensitivity of the sensor, which depends on the frequency dependent fluid-structure coupling, is obtained by modelling. The main originality is the use of a filtering technique to reconstruct the pressure pulsation in the time domain. This in turn enables the capture of transients occurring at frequencies above 0.5 Hz. It is shown how the reconstruction of dynamic pressure along the pipeline can be obtained from a localised multi-sensor array. Several measurements done at a small hydropower plant are presented to demonstrate different techniques of multi-sensor analysis.

Keywords: Pipe dynamics; wave motion; strain sensor; transient measurement.

1 INTRODUCTION

The pressure pulsations in a fluid contained in a pipe and the vibrations of pipe wall are not independent of each other because the fluid motion couples to the wall. The coupling has been investigated since a long time ago. A simplified coupling model was developed at the end of 19th century, Korteweg (1893). Shortly after started first studies of water hammer in pipes, Zhukovsky (1899). One of the key issues was the modelling of non-rigid pipe walls. Simplified formulae of sound speed in function of pipe external conditions were published in papers (Pearsall, 1966; Halliwell, 1963), and books (Jaeger, 1977; Parmakian, 1963). Further advancement in pipe modelling was achieved by accounting for the movements of junctions which is not included in the classical pipe models, Tijsseling et al. (1990). An analysis of pipe dynamics under varying external boundary conditions aimed at diagnostics applications was recently carried out in a thesis work, Hachem (2015).

The complexity of pipe dynamics rises with frequency. One of the earliest complex pipe models has been produced by Lin et al. (1956). The pipe is modelled using thin-wall theory applied to a fluid-filled cylindrical shell. It has been shown that the dynamics of the coupled fluid-wall system can be formulated in terms of waves of different type and different speeds of propagation with wave parameters which change with frequency. A pipe model has been formulated with the cross section modelled in terms of natural modes while the wave approach was applied to the axial direction. Using such a model the excitation by a point source located in a fluid-filled elastic shell has been worked out, Merkulov et al. (1978). Similar complex modelling has been extended to the propagation of pulsation and vibration energy Fuller et al. (1982).

The present paper discusses the dynamics of large fluid-filled pipes typical of hydropower plants. The objective is to demonstrate how an external, non-intrusive strain sensor in conjunction with specific filtering of measured signals can be used to detect pressure transients.

2 DETECTION OF DYNAMIC PRESSURE VIA HOOP STRAIN MEASUREMENT

The measurement of transient pressure in a pipe is usually done using a point sensor. If the pipe is of large diameter a point pressure may not be representative enough. A way to assess the representative pressure is to measure the averaged hoop strain. This strain can be related in to the internal pressure using a model of fluid-wall coupling. The model thus represents an essential part of the measurement procedure.

2.1 The pipe model

The model discussed uses a theory of thin cylindrical shells. The model is based on general solution of shell's motion and of the associated internal pressure field. The solution is obtained analytically. The key relationship which links the hoop strain and the internal pressure is obtained in terms of a frequency-dependent relationship which in turn allows its application to strain measurement data.

  / ISSN 1562-6865 (Online) - ISSN 1063-7710 (Print)

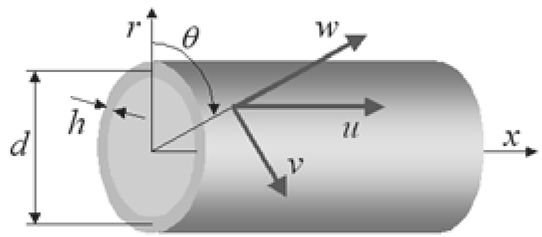

Figure 1. Geometry of cylindrical shell.

Figure 1 shows the geometry and the components of wall displacement of a cylindrical shell. The mathematical description of coupled fluid-wall motion can be put in the form where Eq. [1] and [2] are the equations of motion of the fluid and the wall respectively while Eq. [3] describes the continuity of radial motions at the fluid-wall interface.

$$\kappa \Delta p - \rho_f \frac{\partial^2 p}{\partial t^2} = 0 \qquad [1]$$

$$\left(\frac{4Eh}{d^2(1-\nu^2)} \Xi - h\rho_s \frac{\partial^2}{\partial t^2} I \right) \begin{bmatrix} u \\ v \\ w \end{bmatrix} = p_{r=d/2} \begin{bmatrix} 0 \\ 0 \\ 1 \end{bmatrix} \qquad [2]$$

$$\frac{\partial p}{\partial r} + \rho_f \frac{\partial^2 w}{\partial t^2} = 0 \qquad [3]$$

The symbols stand for: t – time, p – dynamic pressure, E, ν, ρ_s - Young's modulus, Poisson ratio and mass density of the wall, κ, ρ_f – adiabatic bulk modulus and mass density of the fluid, Ξ - differential operator of shell elasticity, I – 3×3 identity matrix. The authors use Flügge's operator Ξ, Flügge (1973).

In order to fit Eq. [2] this operator is formatted as a 3×3 matrix. Assuming harmonic motions with angular frequency $\omega = 2\pi f$ the solution to Eq. [1] and [2] can be found by factorization. This leads to a pressure distribution which is in the radial sense governed by Bessel function of order n J_n, $n \in \mathbb{Z}$, in circumferential sense by cosine function of the same order and in axial sense by exp function. For any given n the pressure reads:

$$p(r,\theta,x,t) = P J_n(k_r r)\cos(n\theta + \vartheta) e^{\mp jk_x x} e^{j\omega t} \qquad [4]$$

Here P - pressure amplitude, ϑ - polarization angle depending on circumstances while – + in the exp function denotes respectively wave direction with respect the pipe axis (x axis). The symbols k_x and k_r denote the axial and radial components of wavenumber k such to make the vector sum of the two components equal to k:

$$k_x^2 + k_r^2 = k^2 = \omega^2 / c_f^2 \qquad [5]$$

The three components of wall displacements of amplitudes U, V and W, satisfying Eq. [2] read:

$$\begin{bmatrix} u(\theta,x,t) \\ v(\theta,x,t) \\ w(\theta,x,t) \end{bmatrix} = \begin{bmatrix} U \\ V \\ W \end{bmatrix} \cos\left(n\theta + \vartheta - \begin{bmatrix} 0 \\ 1 \\ 0 \end{bmatrix} \frac{\pi}{2} \right) e^{\mp jqk_x x} e^{j\omega t} \qquad [6]$$

Upon inserting Eq. [4] – [7] into Eq. [1] – [3] and developing the Bessel function into a truncated power series a polynomial equation is obtained the roots of which provide solutions of k_r, k_x. Thus a series of wavenumbers are obtained for each circumferential order n and each frequency ω. For any particular solution

k_r,k_x the relationship between the radial displacement amplitude of the wall W and the fluid pressure amplitude P is proportional to a coefficient Γ which follows from Eq. [1] - [3] as defined by Fuller (1982):

$$\frac{P}{W} \propto \Gamma, \quad \Gamma = \frac{\Omega^2 J_n(\kappa)}{\kappa\,\partial J_n(\kappa)/\partial\kappa}, \quad \kappa = \frac{k_r d}{2}, \quad \Omega = \frac{\omega d}{\sqrt{E/\rho_s(1-\nu^2)}} \qquad [7]$$

2.2 The wave motion of a pipe

Eq. [4] - [6] show that any motion of a straight pipe can be decomposed into a number of circumferential orders n = 0,1,2… Associated to each order n is a number, theoretically infinite, of discrete wavenumber pairs $\{k_{r,n,s},k_{x,n,s}\}$, s = 1,2... These wavenumbers correspond physically to either propagating or evanescent waves in dependence of whether the axial wavenumber k_x is purely real (propagating), or not (evanescent). Figure 2 shows the circumferential pattern of first four orders, n = 0,…,3.

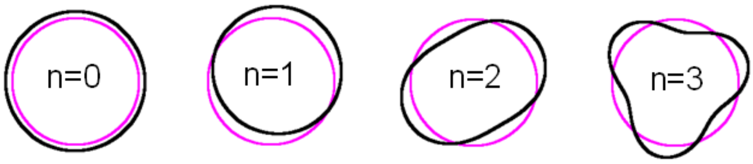

Figure 2. Circumferential orders of a pipe.

At low frequencies only four of these waves can propagate. These are pulsation wave (n=0, s=1), torsional wave (n=0, s=2), extensional wave (n=0, s=3), and flexural wave (n=1, s=1). Other waves at low frequencies are evanescent, i.e decay exponentially with distance. As the frequency increases more and more evanescent waves turn into propagating ones.

A frequency at which the conversion from an evanescent wave into a propagating one takes place is called cut-on frequency. Figure 3 shows the first cut-on frequency for waves of orders n=2 and n=3 of water-filled steel pipes. The cut-on frequency decreases with diameter increasing and thickness reducing.

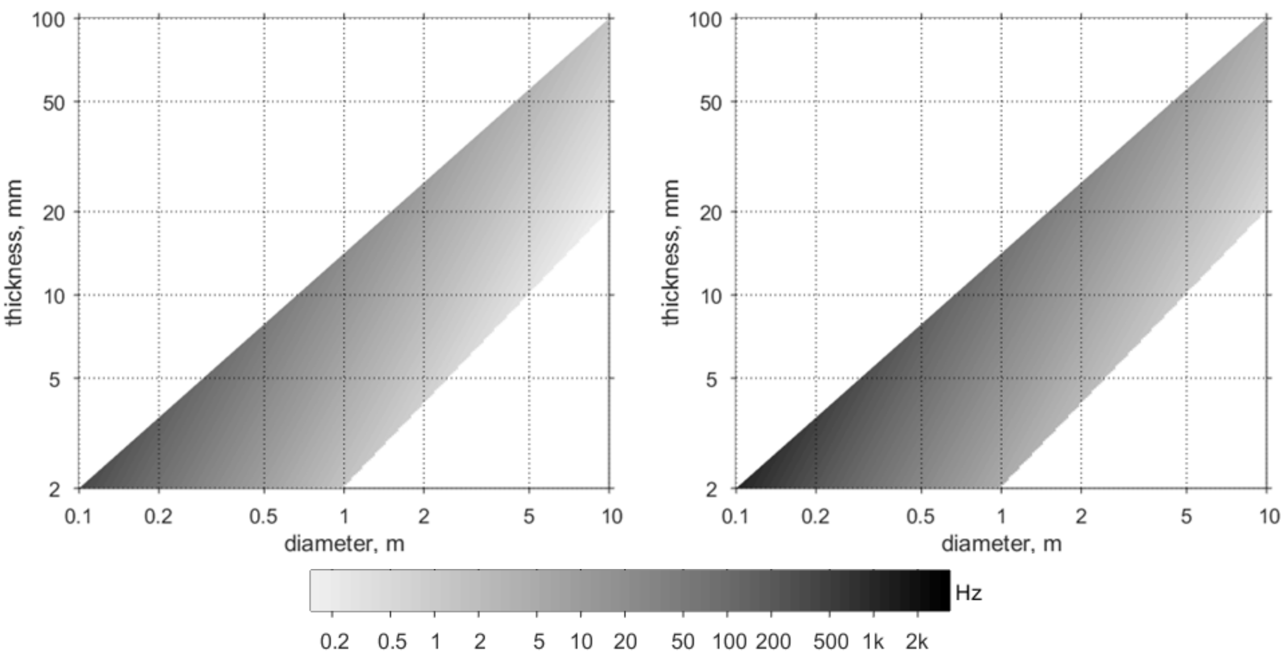

Figure 3. First cut on frequency of a water-filled steel pipe. Left: n=2; right: n=3.

Due to the fluid-wall coupling a given type of wave occurs simultaneously in the fluid and in the wall. The only exception is the torsional wave which does not exist in the (inviscid) fluid as the wall in pure torsion does not exhibit any radial motion. Each fluid-wall wave pair has the same axial wavenumber, while the radial pressure distribution in the fluid is governed by the matching radial wavenumber.

The pulsating wave is of a particular importance: to this wave is associated the largest part of pressure pulsation within a pipe. However other n=0 waves may superpose to the pulsation wave, each of these having its own wavenumber and thus its own speed. This is also true for any other order, so the total wave motion will be a complex superposition of groups of waves of different orders n = 0, 1,… with each group consisting of different wave types s = 1, 2,…. some of which may be propagating, the others evanescent.

If the flow in the fluid is non-homogeneous or of non-negligible speed compared to the speed of sound the physical picture of wave motion becomes even more complex. Turbulence makes the fluid non-homogeneous and analytical modelling becomes impossible. Effects like cavitation further worsens pertinence of analytical models However, transient phenomena in hydropower pressure pipes, like water hammer, were shown to be reasonably well modelled using the analytical approach based on the wave propagation concept.

2.3 Speed of pressure propagation

The speed of sound in a pure free (unbound) fluid $c_{f\infty}$, is given by Newton-Laplace equation depending on the bulk modulus κ and mass density ρ_f of the fluid:

$$c_{f\infty} = \sqrt{\kappa/\rho_f} \qquad [8]$$

The bulk modulus, and thus the speed of sound further depend to some extent on temperature and static pressure. E.g. the speed in pure water at 5b and 15°C is about 1467 m/s. Any presence of impurities and gas dissolved in the fluid may reduce the free sound speed, sometimes considerably – by several times.

In a pipe different waves have different propagation speeds. The notion of the speed of sound is attributed to the speed of pulsating waves. This speed is affected by the elasticity of pipe wall. The speed of sound of thick pipes of small diameter stays remains to the free sound speed. With the diameter increasing and the thickness reducing the speed of sound drops and its dependence on frequency increases.

Figure 4, left, shows the speed of sound in dependence of pipe outer diameter and thickness for a water filled steel pipe assuming the free speed of 1450 m/s. The plot refers to very low frequencies. The speed in large, relatively thin pipes is seen to be halved with respect to the free speed. The right plot shows the speed of sound as a function of frequency and of free speed. It refers to water-filled 10mm thick steel pipe of 2m diameter. The change in actual sound speed with frequency is seen to be significant.

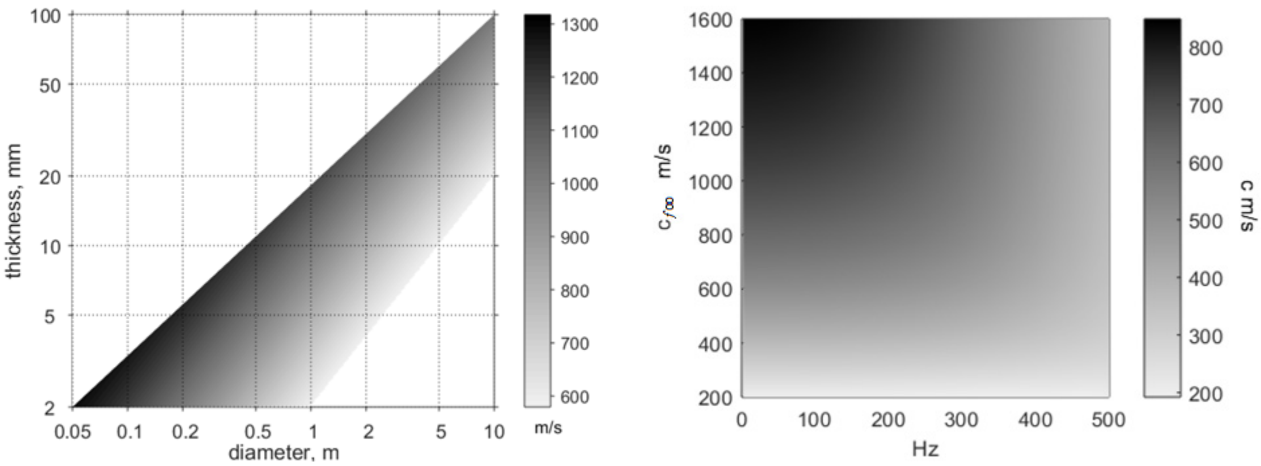

Figure 4. Speed of sound in a water-filled steel pipe.

2.4 The hoop strain

The circumferential (hoop) strain of a thin cylindrical shell reads, Flügge (1973):

$$\varepsilon_{\theta\theta} = \frac{2}{d}\left(w + \frac{\partial v}{\partial \theta}\right) \qquad [9]$$

The n=0 shell order represents the axially symmetric case, called breathing motion. In this type of motion the circumferential component of displacement is v=0. The hoop strain due to breathing becomes thus proportional to radial displacement w, $\varepsilon_{\theta\theta}=2w/d$. This allows one to employ Eq. [7] as a basis of non-intrusive pressure pulsation measurement using a hoop strain sensor.

The hoop strain can be measured by a piezoelectric wire wound around a pipe. It has been first described by Pinnington et al. (1994). Connected to a charge amplifier a signal is created by the wire proportional to the mean strain along the line on the pipe surface in contact with the sensor, Figure 5.

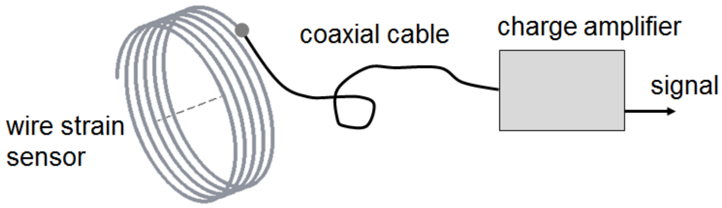

Figure 5. Wire strain sensor circuit.

3 ANALYSIS OF MEASURED DATA

The results shown herewith were obtained on a small hydroelectric power plant. The measurements were done in different operating regimes, both stable and unstable ones.

The hoop strain was measured in a number of positions along the pipe by a PDVF wire. One full turn was applied at each position. To test the influence of mounting conditions on measurements two types of wires were used: one covered by an external braid, the other painted with a conductive paint. The contact between the wire and the pipe was achieved by manual pre-tension only, either by direct mounting or by applying an adhesive tape on the pipe.

Figure 6 shows the section of pressure pipe in front of the inlet turbine valve on which three wire sensors were mounted within a close distance. The signal from an intrusive pressure sensor located just in front of the valve was used for comparison of measurements.

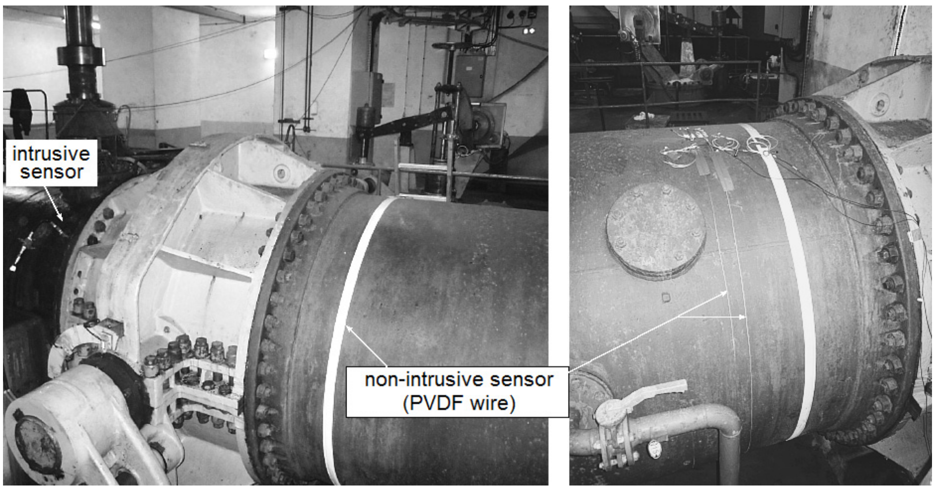

Figure 6. Pressure measurement section at the turbine inlet pipe.

Several wire sensors were mounted on the pressure pipe further upstream of the turbine hall. Mounted as well around the pressure pipe halfway from the turbine hall was an array of 6 accelerometers the role of which was to monitor the wall motion.

3.1 Measurement of dynamic pressure

Figure 7 shows the coupling coefficient Γ, defined by Eq. [5], computed for two different sections of the pressure pipe at which the measurements were done. Considerable variation with frequency in the range 0-500 Hz is noticeable. The larger the pipe diameter and the thinner its walls the stronger the frequency variation of Γ. The coefficient Γ of pressure pipes of very large hydro-power plants will exhibit much stronger variation with frequency than the one presented in Figure 7.

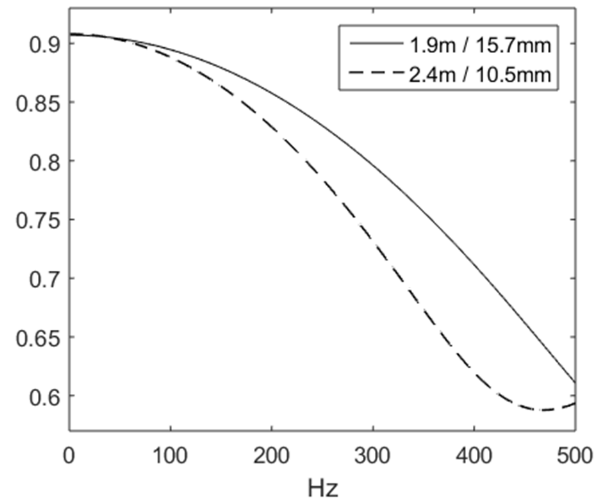

Figure 7. Coupling coefficient Γ of two water filled steel pipes.

The post-processing of stationary signals is usually carried out in the frequency domain in order to apply the required frequency weighting. RMS spectra are obtained in this way, such as shown in Figure 9 and 10. However, such type of post-processing averages the signals and the phase information is lost. In this study, a time domain filtering is employed in order to preserve the phase structure. Time domain filtering is of particular advantage where pressure transients are concerned. A finite impulse response filter (FIR) is used in order to apply the frequency dependent coefficient Γ to the measured strain signals. Time domain filters are known to introduce delays. A double sided convolution is applied in order to avoid any delay. In this way the time history of the measured hoop strain is correctly converted to the internal pressure pulsations.

Figure 8 compares the waveforms of 3 pressure signals measured by wire sensors at the turbine inlet pipe in a stable regime. In spite of different wire and mounting technologies the signals match closely. The coherence function, not plotted here, shows a good coherence between the three signals throughout 0-200 Hz range.

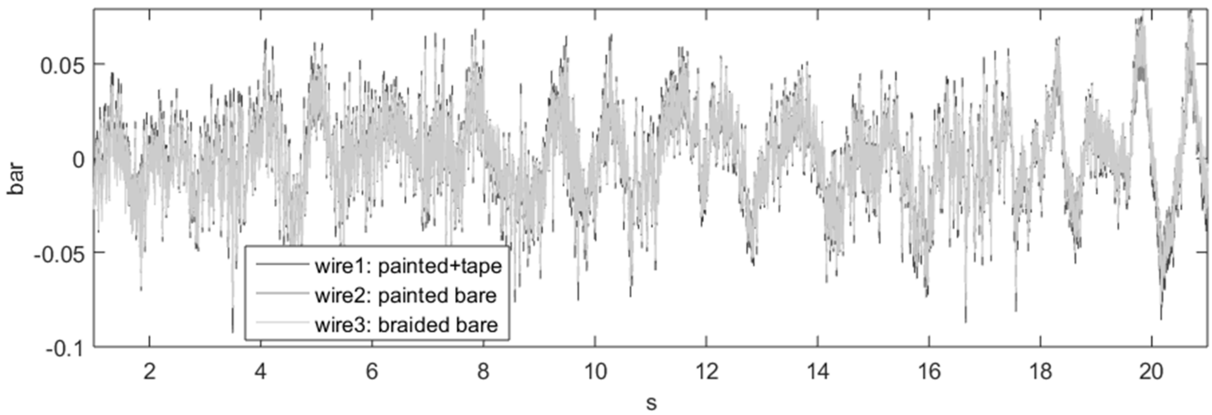

Figure 8. Waveforms of dynamic pressures measured by wire strain sensors in stable regime.

The measurement of dynamic pressure indirectly, by using strain wire sensor, cannot give the same result as the measurement of pressure in a point. The wire sensor integrates the hoop strain along its active length which in turn produces the reading of circumferentially averaged internal pressure. If the wire sensor is wound using one or several full turns, the integration effect will eliminate the contribution to strain of all orders n but n=0. On the contrary, any pressure measured in a point will be contributed by all the orders and will therefore be different than the mean (integrated) pressure. The difference between the point and integrated pressures will thus rise with frequency due to an increasing number of higher order waves which become propagating but to which the wire sensor is insensitive. In stable regime the low frequency pressure components are not pronounced; the intrusive sensor produces pressure readings where high-frequency components dominate the waveform. The wire sensor filters these components out.

Figure 9 shows the RMS spectrum of pressure measured by the intrusive point sensor and of that measured by the closest wire sensor. A good matching between the two spectra extends to around 60 Hz. At higher frequencies the difference of the two types of pressure increases as expected. The cut-on frequencies of the pipe (diameter 1.9m, thickness 15.7mm) are: n=2 – 5.8 Hz, n=3 – 18.1 Hz, n=4 – 37.6Hz, n=5 – 64.8Hz etc. The peaks at 133Hz and 266 Hz are the first and second harmonic of the passing frequency of runner blades (16 blades at 500 rpm).

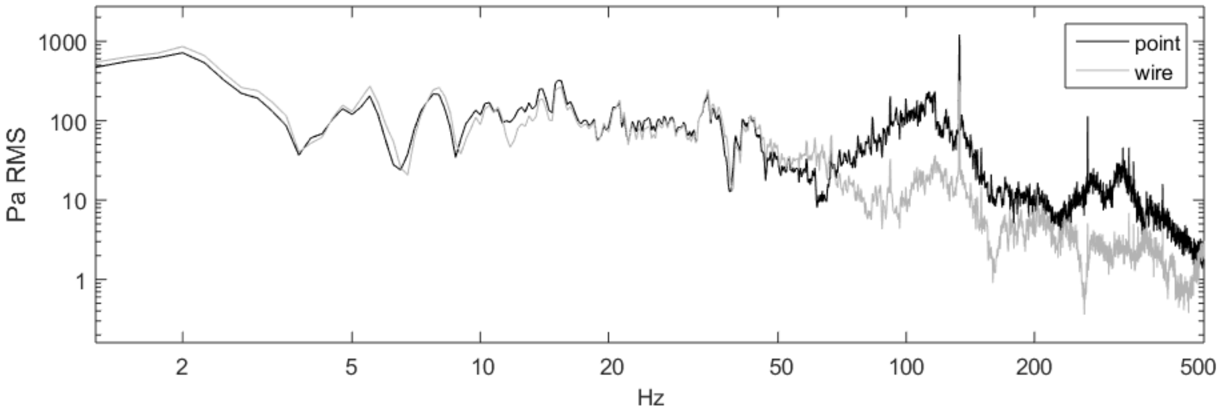

Figure 9. Dynamic pressure spectra in stable regime.

Figure 10 presents the spectra of the point and integrated pressure in an unstable regime induced by the cavitation spiral rope at the runner exit. In this regime, the dynamic pressure at low frequencies dominates, as seen on Figure 10. The matching between the waveforms of point and integrated pressure, shown in Figure 11, is fairly good.

The results show that the non-intrusive wire sensor can effectively measure the dynamic pressure in large diameter water filled pipes. The integrating feature of the sensor, which makes it insensitive to localized pressure fluctuations induced by higher-order waves can be an advantage when global transient effects, such as water hammer, are concerned.

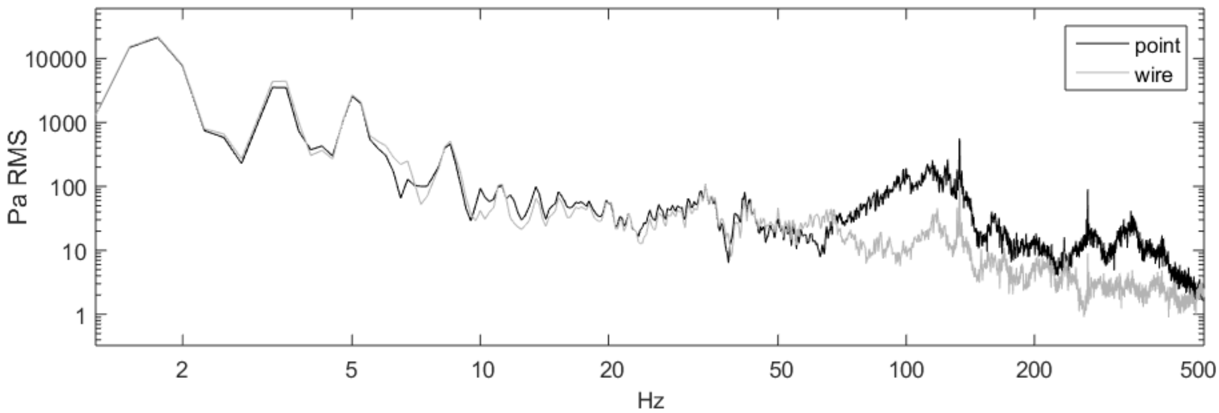

Figure 10. Dynamic pressure spectra in unstable regime.

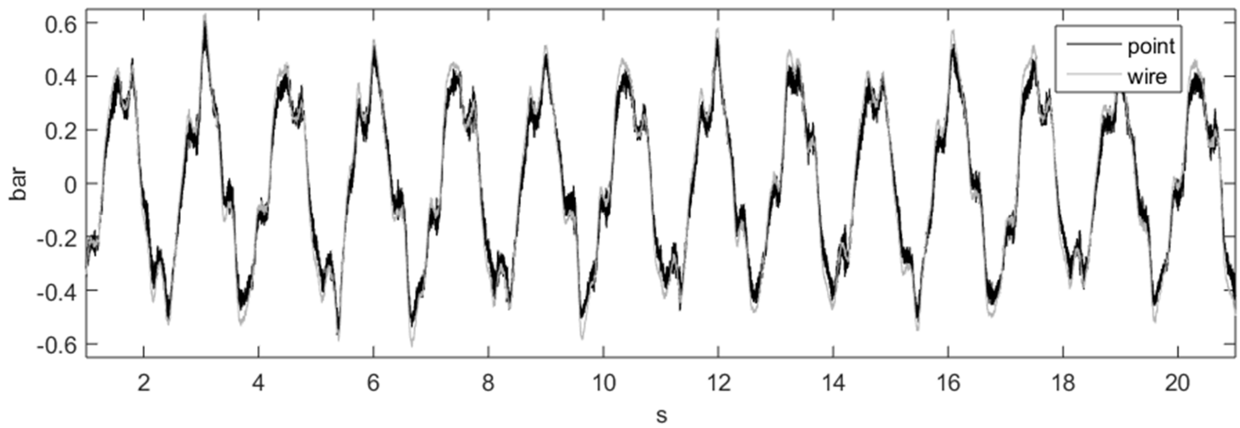

Figure 11. Waveforms of dynamic pressures in unstable regime.

3.2 Reconstruction of dynamic pressure

An important measurement parameter is the true speed of pulsation waves in a pipe, i.e. the speed of sound. The effect of the elasticity of pipe wall can be taken into account by computation providing the speed in a free fluid, which is one of computation input data, is known. As already stated the air or impurities in the fluid reduce this speed with respect to the speed in pure fluid. It is therefore useful to measure the actual speed in the pipe. One of possible techniques of speed measurement uses a specific cost function computed from the pressure pulsations at 3 points, (Pavić, 2004). The cost function is computed for a range of (unknown) speeds and its maximum value indicates the actual speed.

Figure 12 gives the cost function obtained from 3 wire sensors measured on the pressure pipe halfway from the turbine hall. A sharp peak at 740 m/s indicates the actual speed of pulsation waves. Backward computation from this value gives the free fluid speed of 1208 m/s which implies somewhat lower speed in free water than the rated value of 1450m/s.

The knowledge of true speed of pulsation waves, obtained by processing the signals from 3 wire sensors, makes it possible to compute from the same signals the amplitudes of forward and backward propagating pressure components. This in turn enables the reconstruction of dynamic pressure. at positions away from the measurement zone.

Figure 13 compares the dynamic pressures measured directly and reconstructed from 3 wire sensor array in pressure pipe upstream of the turbine hall. As the two time histories practically overlap the difference between the two is shown separately for better visualization. The reconstruction is done by separating the forward and backward propagating components and by computing the resulting pressure at the position at which the direct measurement was made. The good matching achieved is the result of correct reconstruction of all frequency components in both amplitude and phase.

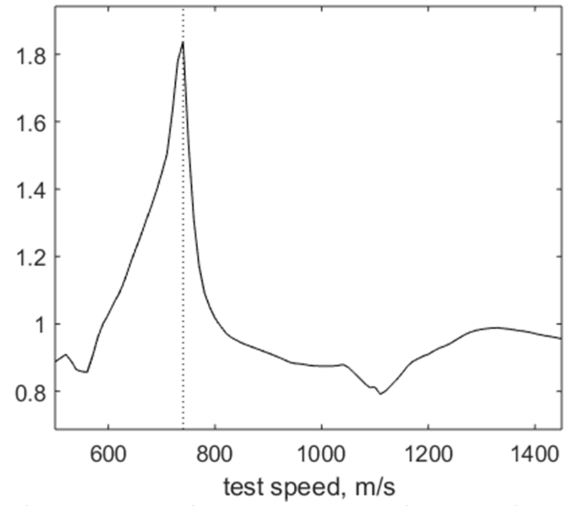

Figure 12. Cost function used for the detection of speed of sound in the pipe.

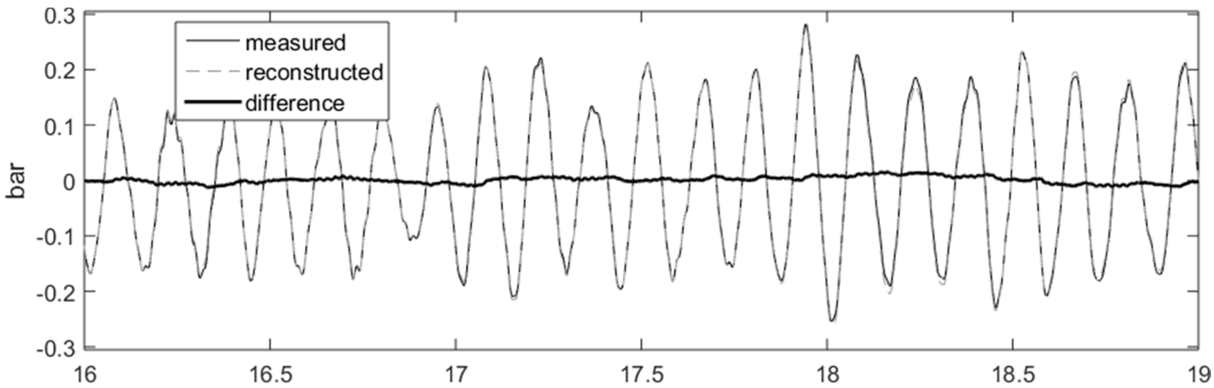

Figure 13. Dynamic pressure in the pressure pipe.

4 CONCLUSIONS

A large fluid-filled pipe exhibits complex dynamic behaviour which can be analysed in depth using multi-point measurements in conjunction with analytical modelling. The motion in any cross section of the pipe can be represented as a sum of circumferential orders n=0, 1, 2… which govern the deformation of pipe wall and the dynamic pressure distribution within the pipe. To each of these orders is associated a number of pipe waves of different kinds, propagating or evanescent, and of different wave speeds.

Particular importance in hydro applications has one of the waves of the order 0, called the pulsation wave. This wave transports most of the energy of pressure pulsations along the pipe. It has been demonstrated that an external, non-intrusive strain sensor made of piezo wire can be employed for the purpose of measurement of pressure of pulsation waves. Owing to specific filtering of wire signals the instantaneous values of dynamic pressure can be obtained directly in time domain.

It has been further shown that an array of 3 wire sensors can be successfully employed to pinpoint the true speed of pulsation waves in a pipe. The knowledge of exact speed enables the reconstruction of dynamic pressure away from the measurement zone. The results demonstrate that the developed signal data processing based on wire sensor measurement is potentially powerful tool for monitoring both stationary and transient phenomena in water-filled large pipes.

ACKNOWLEDGEMENTS

This study has been supported by General Technical Division (DTG) of the French Electricity Generating Group EDF. The authors express their gratitude to Mr. Jean Heraud of DTG for help during measurements and useful comments in the analysis stage.

REFERENCES

Flügge, W. (1973). *Stresses in Shells, 2nd edition.* Springer, 525.

Fuller, C.R. & Fahy F.J. (1982). Characteristics of Wave Propagation and Energy Distributions in Cylindrical Elastic Shells Filled with Fluid. *Journal of Sound Vibration,* 81(4), 501-518.

Hachem, F. (2011). Monitoring of Steel-Lined Pressure Shafts Considering Water-Hammer Wave Signals and Fluid-Structure Interaction, *PhD thesis.* N° 5171, Ecole Polytechnique Fédérale de Lausanne.

Halliwell, A.R. (1963). Velocity of a Water Hammer Wave in an Elastic Pipe. *Proceeding of American Society of Civil Engineers, Journal of Hydraulics Division*, 89(4), 1-21,

Korteweg, D.J. (1878). On the Velocity of Propagating Sound in Elastic Tubes. *Physics Annals*, 174, 525-542. (In German)

Jaeger, C. (1977). *Fluid Transients in Hydro-Electric Engineering Practice*. Blackie, 413.

Lin, T.C. & Morgan, G.W. (1956). Wave Propagation through Fluid Contained in a Cylindrical Elastic Shell. *Journal of the Acoustical Society of America,* 28(6), 1165-1176.

Merkulov, V.N., Prikhodko, V. Y. & Tyutekin, V.V. (1978). Excitation and Propagation of Normal Modes in a Thin Cylindrical Elastic Shell filled with Fluid. *Akusticheskii Zhurnal*, 24, 723-730. (In Russian)

Parmakian, J. (1963). *Water Hammer Analysis*. Dover Publications, 161.

Pearsall, I.S. (1966). The Velocity of Water Hammer Waves, *Proceedings of Institution of Mechanical Engineers,* 180(3E), 1965-66.

Pinnington, R.J. & Briscoe A. (1994). Externally Applied Sensor for Axisymmetric Waves in a Fluid-filled Pipe. *Journal of Sound Vibration,* 173 (4), 503-516,

Tijsseling, A.S. & Lavooij, C.S.W. (1990). Water Hammer with Fluid–Structure Interaction, *Applied Scientific Research,* 47, 273–285.

Zhukovsky, N.E. (1899). *On Hydraulic Shock in Water-Conducting Pipes.* Bulletin of Technical Society, 5, 100. (In Russian)

UNIFIED EQUATION FOR ESTIMATION OF FRICTION FACTOR

BALKRISHNA SHANKAR CHAVAN[1]

[1] Central Water and Power Research Station, Pune, India,
balkrishna0@gmail.com

ABSTRACT

Computation of head loss is required in design of water conductor systems, such as close conduit as well as open channel. Darcy Weisbach friction factor (f) plays a decisive role in designing size and shape of water conductor systems. Estimation of f has no simple solution as it is very sensitive to geometrical as well as hydraulic parameters involving implicitly related Reynolds number and relative roughness. Solution requires iterative steps to arrive at required accuracy. Many investigators proposed explicit equations for approximate estimation of friction factor. These equations have theoretical, semi-theoretical and empirical base. Solutions are for stated restricted conditions. A plot of Reynolds number vs. friction factor by Nikuradse is well known. There are several approximations to the Colebrook equation. Some of them are Wood, Swami-Jain, Churchill, Barr, Chen, Zigrang-Sylvester, Serghides, Yen, Barenblatt, McKeon, Morrison, Haaland and are briefly described. Equations proposed by researchers are applicable for stated flow conditions, underestimates friction for higher Reynolds number. Obtaining a formulation that would provide the friction coefficient with a higher accuracy and applicable to wide flow conditions is goal for present paper. Here, we seek to unify the results and to provide an explicit formula for f valid in all forms of flow viz. transition, smooth and turbulent limits. Therefore, a new equation based on published data from various journals is compiled and analyzed for arriving at unified equation. Field data collected over 25 years has been utilized to derive the equation. In present paper, proposed explicit equation removes anomaly of decreasing values of friction factor for higher Reynolds number values, which was pointed out by ASCE Task Force. At the end, simplified equation for practically useful area friction coefficient (Mannings n) is proposed.

Keywords: Friction factor; turbulent flow; laminar flow; Reynolds number; unified equation.

1 INTRODUCTION

The ASCE Task Force on Friction Factors in Open Channels (1963) highlighted usefulness of Darcy Weisbach formulation of friction factor in computing resistance to flow in open channels. Task Force noted formulation as fundamental and mentioned that the Manning equation could be used for fully rough conditions. Task Force presented figure for variation of resistance with Reynolds number, which showed with Mannings equation, there is continual decay of resistance with Reynolds number, even in the limit of large values. From this, one could deduce that Mannings equation is fundamentally flawed. The recommendations of the Task Force have almost entirely been ignored, and the Gauckler-Manning-Strickler formulation continued to dominate, even though, with the exception of the Strickler formula, there are few general research results available and use of tables/graphs continued. Even though the Task Force presented a number of experimental and analytical results, there was no simple solution path to follow for friction factor problems.

Colebrook – White (1939) equation is used extensively, covering the whole range of Reynolds numbers and relative roughness but its implicit scheme makes iterations necessary. This presents the possibility of using various equations to obtain an initial estimate of the friction factor and then use that estimate as the starting point for an iterative solution with the Colebrook equation. This process even though tedious, works quite well. Many other equations were developed, which provide the determination of friction factor explicitly. As will be shown in the following, these equations provide f with a precision for some Reynolds numbers and relative roughness values.

2 LITERATURE SURVEY

Prandtl (1925) indicated that velocity distribution in pipes is independent of radius of pipe but depends on the correlations fluid parameters, such as dynamic viscosity, mass density and average shear stress. Nikuradse presented relationship between Reynolds number and friction factor for different diameter of conduits. These graphical are globally accepted. Laminar flow represents low Reynolds numbers less than 1000 whereas turbulent flow indicates Reynolds numbers more than 4000. Reynolds numbers between these values is range of transition flow. The turbulent flow portions of the Moody friction factor diagram and the Fanning friction factor diagram are plots of the Colebrook – White equation for Darcy Weisbach friction factor f in a pipe of different flow conditions.

2.1 Colebrook – White equation (1939)

The implicit equation is:

$$\frac{1}{\sqrt{f}} = -2log\left[\frac{\frac{e}{D}}{3.7} + \frac{2.51}{Re\sqrt{f}}\right] \quad [1]$$

where e/D is the relative roughness, which is the ratio of the mean height of roughness of the pipe to the pipe diameter. As seen from Eq. [1], the friction factor is a function of the Reynolds number and pipe roughness (e). The Colebrook-White equation cannot be solved directly due to its implicit form as the value of friction factor *f.* A difficult aspect of the Colebrook-White equation in forms shown above is that it cannot be solved explicitly for the friction factor, so iterative solutions required to calculate the friction factor for known values of Re and ε/D. The parameters of this equation are determined by minimizing the approximation error and are given either in tabulated form or as mathematical expressions of roughness.

The most general equation for friction factor under turbulent flow conditions is the Colebook equation, as shown above (Eq. [1]) in its Moody friction factor form and in its Fanning friction factor form.

Various investigators given form of Colebrook White equations in general form as:

$$\frac{1}{\sqrt{f}} = -K_1 log\left[\frac{e}{K_2 R} + \frac{K_3}{4R_e\sqrt{f}}\right] \quad [2]$$

Values of K_1 and K_3 in Eq. [2] directly varies as ratio of width to depth of flow, increases if ratio increases whereas K_2 decreases.

Friction factor for turbulent flow in pipes and fixed bed channels is represented by sand roughened pipe experiments by Nikuradse (1939). Suppose a rough surface is subjected to a flow, then equivalent roughness height Eq. [1] is applicable for Re > 3000. For laminar flows, Re < 2100, Poiseuille's law (f = 16/Re) is used.

There are several approximations to the Colebrook equation some of them are Wood, Swami-Jain, Churchill, Barr, Chen, Zigrang-Sylvester, Serghides, Yen, Barenblatt, McKeon are briefly described below in its Moody friction factor forms. These equations do not agree quite as well with the friction factor diagrams over the entire turbulent flow range, but have the advantage of being explicit for the friction factor.

2.2 Wood equation

Equation proposed by Wood in (1966). Its validity region extends for Re > 10000 and 10^{-5} < (e/D) < 0.04.

$$f = 0.094\left[\frac{e}{D}\right]^{0.225} + 0.53\left[\frac{e}{D}\right] + 88\left[\frac{e}{D}\right]^{0.44} Re^{a} \quad [3]$$

$$a = -1.62\left[\frac{e}{D}\right]^{0.134} \quad [4]$$

2.3 Swami-Jain equation

Formula proposed in (1976) (For 5000 < Re < 10^7 and 0.00004 < e/D < 0.05), described as:

$$\frac{1}{\sqrt{f}} = 1.14 - 2log\left[\left[\frac{e}{D}\right] + \frac{21.25}{Re^{0.9}}\right] \quad [5]$$

2.4 Churchill equation

Correlation proposed by Churchill (1977) which is valid only for the turbulent regime and it is similar to the Swami and Jain correlation (1976). Correlation proposed by Churchill is valid for all ranges of the Reynolds numbers. (For all values of Re and e/D).

$$f = 8\left[\ (8/Re)^{12} + \frac{1}{(A+B)^{1.5}}\right]^{\frac{1}{12}} \quad [6]$$

$$A = \left\{-2.457ln\left(\frac{7}{Re^{0.9}}\right) + 0.27\frac{e}{D}\right\}^{16} \quad [7]$$

$$B = \left(\frac{37530}{Re}\right)^{16} \quad [8]$$

2.5 Barr equation

In (1979), Barr proposed following explicit equation:

  / ISSN 1562-6865 (Online) - ISSN 1063-7710 (Print)

$$f = \frac{1}{4}\left[-log\left(\frac{e}{14.8R}\right) + \frac{5.2}{(4R_e)^{0.89}}\right]^{-2} \quad [9]$$

2.6 Chen equation

Chen (1979) proposed the following equation for the friction factor covering all the ranges of the Reynolds number and the relative roughness: (For all values of Re and e/D).

$$\frac{1}{\sqrt{f}} = -2log\left[\frac{1}{3.7605}\left[\frac{e}{D}\right] - \frac{5.0452A}{Re}\right] \quad [10]$$

$$A = log\left[\frac{1}{2.8257}\left[\frac{e}{D}\right]^{1.1098} + \frac{5.8506}{Re^{0.8981}}\right] \quad [11]$$

2.7 Zigrang and Sylvester equation

Zigrang and Sylvester (1982) developed a relationship that is valid for all ranges of the Reynolds numbers and the relative roughness as follows: (For 4000 < Re < 10^8 and 0.00004 < $\frac{e}{D}$ < 0.05).

$$\frac{1}{\sqrt{f}} = -2log\left[\frac{1}{3.7}\left[\frac{e}{D}\right] - \frac{5.02A}{Re}\right] \quad [12]$$

$$A = log\left[\frac{1}{3.7}\left[\frac{e}{D}\right] - \frac{5.02}{Re}\right] + \frac{13}{Re} \quad [13]$$

2.8 Serghides equations

Serghides (1984) equation is an approximation of the implicit Colebrook–White equation. It is valid for turbulent range of the Reynolds numbers and the relative roughness' as follows. (For Re>2100 and any e/D).

$$\frac{1}{\sqrt{f}} = \left[A - \frac{(B-A)}{C-2B+A}^{2}\right] \quad [14]$$

$$A = -2log\left[\frac{\frac{e}{D}}{3.7} + \frac{12}{Re}\right] \quad [15]$$

$$B = -2log\left[\frac{\frac{e}{D}}{3.7} + \frac{2.51A}{Re}\right] \quad [16]$$

$$C = -2log\left[\frac{\frac{e}{D}}{3.7} + \frac{2.51B}{Re}\right] \quad [17]$$

2.9 Yen equation

In 1991 Yen modified Barr equation and proposed following explicit equation for wide channels for water flow with 30000 < R_e , $\frac{e}{D}$ < 0.05.

$$f = \frac{1}{4}\left[-log\left(\frac{e}{12R}\right) + \frac{1.95}{(4R_e)^{0.9}}\right]^{-2} \quad [18]$$

Barenblatt's (2003) scaling law (equation 8.29) is derived from an extended theory (incomplete similarity) of similarity (power law in the Reynolds number) to a form in which the prefactor and exponent of the power law also depend on the Reynolds number. The functional form of the prefactor and exponent are derived from theoretical assumptions. Equations are:

$$f = \frac{8}{\psi^{2(1+\alpha)}} \quad [19]$$

$$\psi = \frac{e^{\frac{3}{2}}(\sqrt{3}+5\alpha)}{2^{\alpha}\alpha(1+\alpha)(2+\alpha)} \quad [20]$$

$$\alpha = \frac{3}{2\ln(Re)} \quad [21]$$

Barenblatt power law formula estimates friction factor at the accuracy 1% for Re < 13 × 10^6, thereafter error increases rapidly.

McKeon (2005) proposed an equation based on Princeton data.

$$\frac{1}{\sqrt{f}} = 1.920 \log(\mathrm{Re}\sqrt{f} - 0.475) - \frac{7.04}{(\mathrm{Re}\sqrt{f})^{0.55}} \quad [22]$$

Eq. [22] predicts the friction factor to be within ± 1.4% of the Princeton data (± 0.6% at high Reynolds number $30*10^3 < Re < 36*10^{10}$ and within ± 2.0% of the Blasius relation at low Reynolds numbers.

Above mentioned equations deliver sufficiently accurate results for practical purposes for specified conditions only. One should be careful while using any of above equations for the flow condition beyond prescribed flow conditions and roughness range.

By using the Weisbach resistance coefficient f, Rouse (1965) expressed the resistance as the dimensionless symbolic function. Experimental data collected by university of Illinois demonstrate the turbulent zone corresponds closely to the Blasius Prandtl Von Karman curve. This indicates the law for turbulent flow in smooth pipes may be representative of smooth channels. This plot also shows that the shape of channel does not have an important influence on friction factor in turbulent flow. (Figure 1).

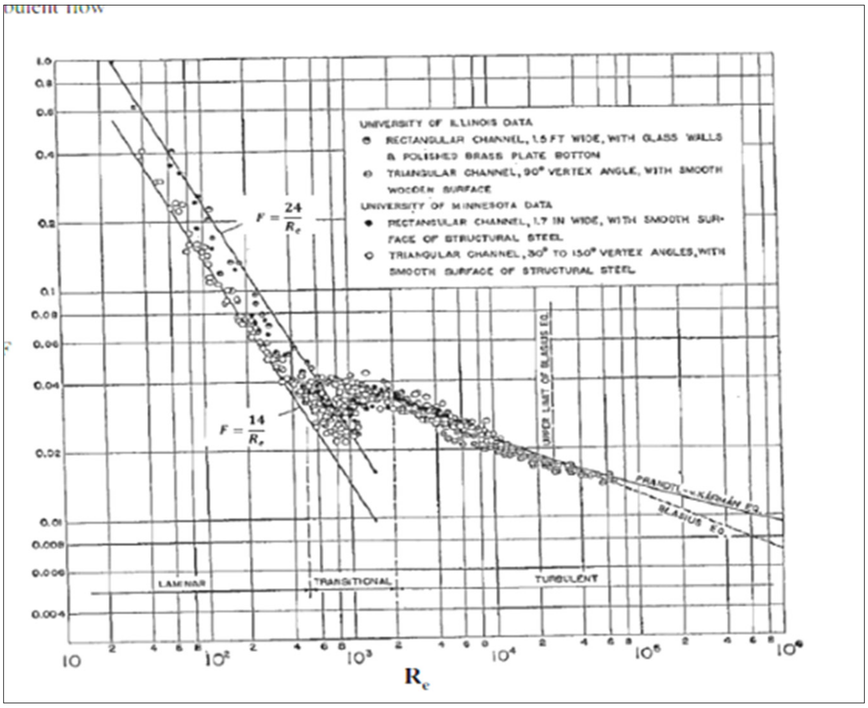

Figure 1. Friction factor - Reynolds number relationship for flow in smooth channels (Chow,1971).

For steady uniform laminar flow with Re < 500:

$$f = \frac{K_L}{R_e} \quad [23]$$

K_L= 24 for 2D wide channels
K_L= 16 for circular pipes

According to Blasius (1933) equation, for laminar flow in smooth pipes, which is often used as approximation for wide channels for 700 < Re < 25000.

Darcy Weisbach friction factor f is given by:

$$f = \frac{0.224}{\left(\frac{UD}{\nu}\right)^{\frac{1}{4}}} \quad [24]$$

3 PRESENT STUDY

Among the various explicit equations used to approximate the friction factor, f, the Haaland (1983), equation is:

$$f = \frac{0.308642}{\left[log\left|\left(\frac{e}{3.7D}\right)^{1.11} + \left|\frac{6.9}{Re}\right|\right|\right]^2} \quad [25]$$

Explicit equation suggested by Morrison (2013) for turbulent flow in smooth boundaries is:

$$f = \frac{16}{Re} + \left[\frac{0.0076\left(\frac{3170}{Re}\right)^{0.165}}{1+\left(\frac{3170}{Re}\right)^7}\right] \quad [26]$$

Analysis of published data across the globe in respect of rivers of Missouri, Ishikari, Luznice, Amazon, Orinoco, Tagus and Mississippi, collected field data from canals in Japan, Atrisco, US and Pakistan. Laboratory flume data collected by Liu, Pande, Plate Laursen, Williams, Bharat Singh, Barton and Lin, Garde. Overall 874 run of data observations analyzed in the present studies. To arrive at the results to form an explicit formula for friction factor, *f* valid in all flow conditions viz. laminar, transition and turbulent. Considering this objective, the data has been compiled and analyzed. The research work of Morrison (2013), Barenblatt (2003) and McKeon (2004; 2005) is referred for arriving at the modified formulation which will fit for field data. Optimizing the aforementioned parameters in power laws, by imposing in parallel that the error values of f for low Re and high relative roughness should be lower than 0.8%. This gave Eq. [27], where all error values, for any roughness and any Re examined, are lower than 0.8%. Equations containing Reynolds Number having two powers ranging from 0.165 to 8 were investigated. As a best fit following explicit two power equation is proposed:

$$f_f = \frac{20}{Re} + \left[\frac{0.0075\left(\frac{4000}{Re}\right)^{0.05}}{0.25+\left(\frac{4000}{Re}\right)^5}\right] \quad [27]$$

The turbulent flow data is represented by a composition of two power laws.

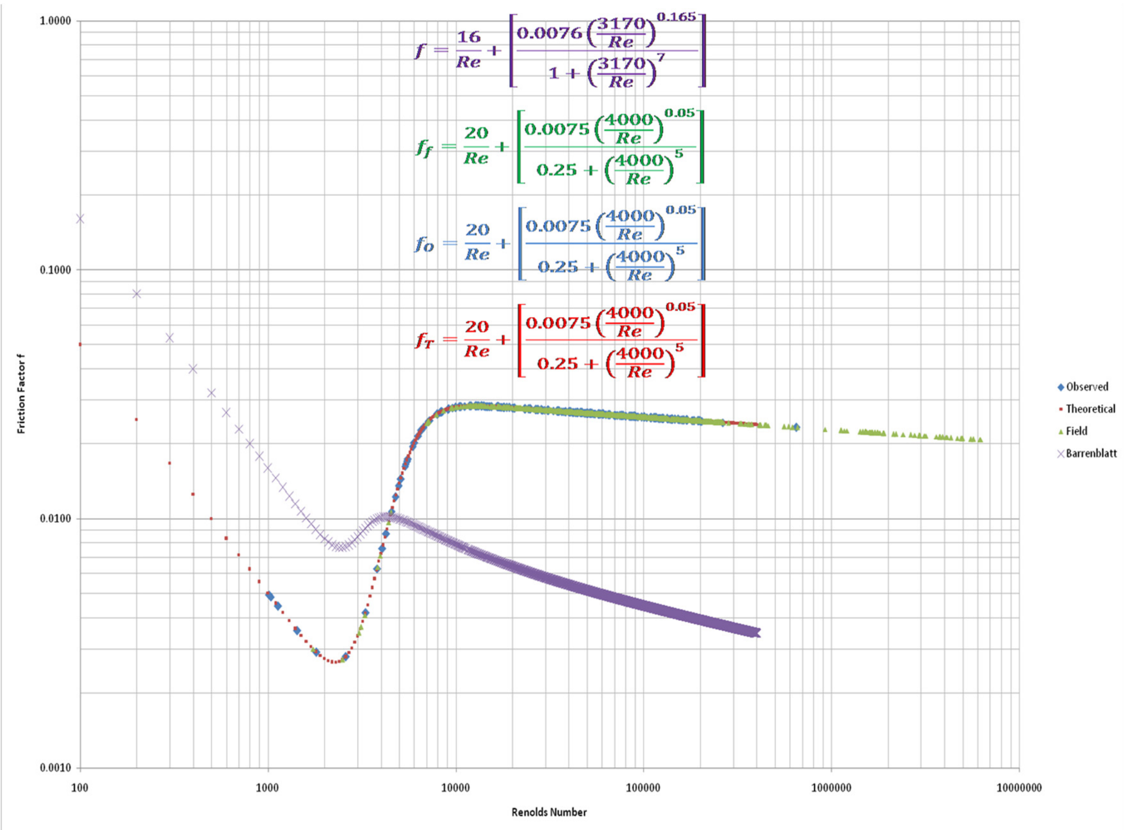

Figure 2. Comparison of explicit equations.

A plot of Eq. [27] is shown in Figure 2 along with data for smooth pipes suggested by Morisson (2013). At low Reynolds number, Eq. [27] becomes f = 20/Re. This is between 16 and 24 values, as shown in Figure 1. At high Reynolds numbers, Eq. [27] becomes the Prandtl correlation, the smooth-pipe equivalent and original source of the Colebrook-White equation (White, 2006). The unified errors are less than 1% for Re < 13 × 10^6

but the error increases rapidly thereafter. This rather sudden increase of data can be interpreted as a manifestation of the effect of roughness in an effectively smooth pipe with honed roughness. As a result, Eq. [26] predicts lower values of friction factor for higher Reynolds number (Re > 10^4) than observed values of Darcy Weisbach friction factor, f computed from field/laboratory data. An accurate formula for the full range data of Morrison et al. (2013) for pipe flow was derived as a rational fraction of power laws connected smoothly by the logistic dose function algorithm.

It can clearly be seen from Figure 1, friction factor gradually reduces as Reynolds number increases, as stated by ASCE Task Force, termed it as fundamentally flawed. Log plot of friction factor and Reynolds number for the compiled data is shown in Figure.1. According to Morrison, in the transition zone friction is overestimated. The friction factor in turbulent zone reduces from 0.038 to 0.0195 f drops by 48.68% for Reynolds number ranging from 8000 to 600000. This graph clearly separates transition zone from turbulent flow. Friction factor ranges from 0.029 to 0.021 even though f drops for the turbulent flow, which is fairly constant for Reynolds number ranging from 8000 to 600,000. Field data fairly matches with the predicted value curve.

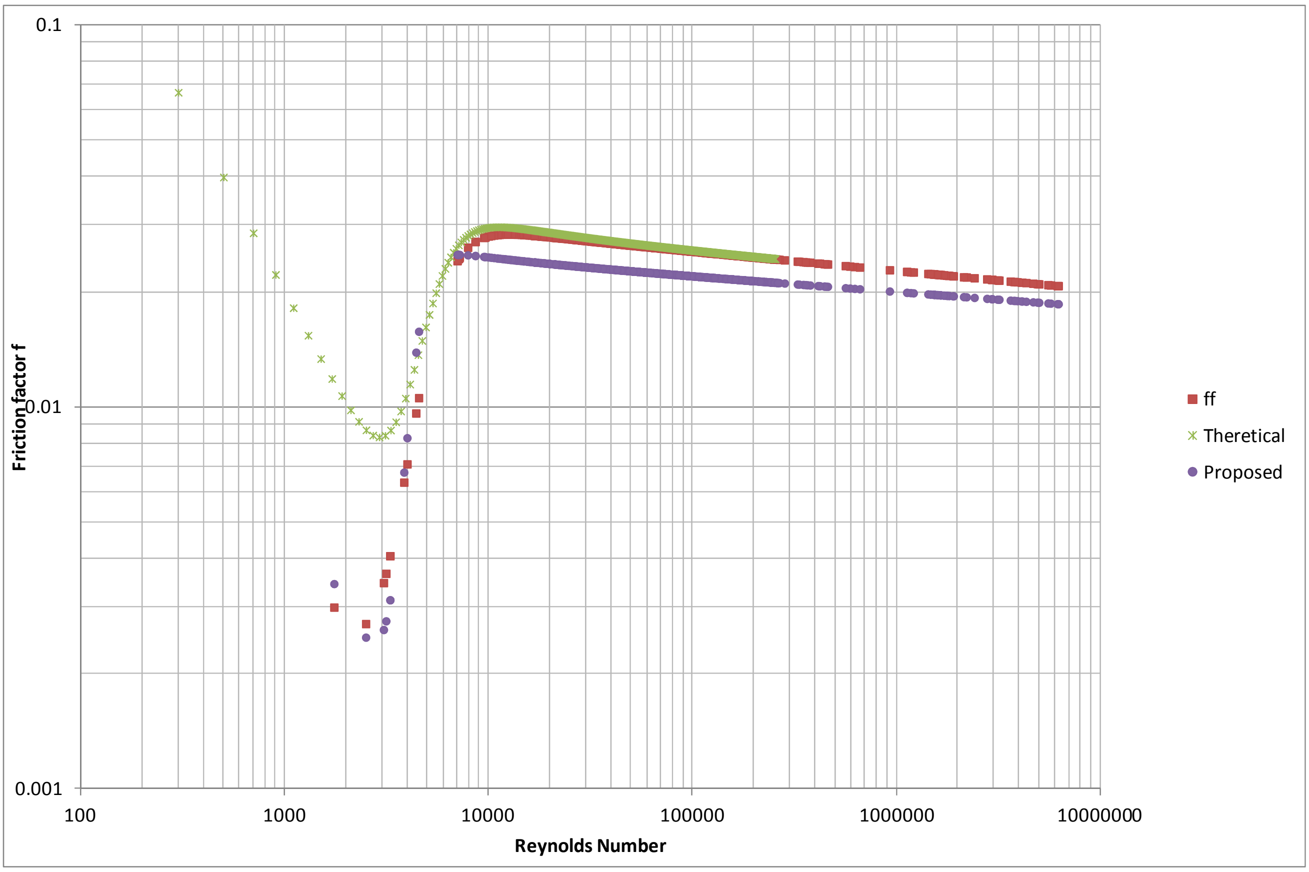

Figure 3. Comparison of Friction Factor Observed in field and Predicted by equation (27).

The correlation was computed by the proposed equation of Darcy Weisbach friction factor, f with observed data for the transition zone which has impact of 99.99 %. The result of analytical studies is plotted above shows close overall correlation of 97.7% with the observed values of friction factor in field as well as experimental data. This correlation is shown in Figure 3.

4 VALIDITY

The proposed Eq. [27] is two power, very simple explicit, has applicability over very wide range of flows. Equation reduces computation time considerably and is valid for laminar, transition and turbulent flows. Friction factor values predicted by Eq. [27] are better than values arrived through any formulation presently available, especially for flow with laminar, transition and higher values of Reynolds numbers. Accuracy of observed magnitude of f in the field and by proposed equation is considerably increased with respect to Morrison, and McKeon methods. The friction factor, f for rough boundaries practically matches with the field values. However, there is further scope to improve the formulation in turbulent range with additional data from field.

Further application of Eq. [27] could be finding area friction coefficient, *i.e.,* Mannings n:

$$f_f = \frac{8gn^2}{R^{\frac{1}{3}}} \quad [28]$$

Eq. [27] for Mannings coefficient, n becomes:

$$n = \sqrt{\frac{R^{\frac{1}{3}}}{8g}\left\{\frac{20}{Re} + \left[\frac{0.0075\left(\frac{4000}{Re}\right)^{0.05}}{0.25+\left(\frac{4000}{Re}\right)^{5}}\right]\right\}} \quad [29]$$

Table 1. Application of various friction factor formulae with validity range and values of R^2.

No	Investigator	Year	Formula	Validity Range	R^2
1	Chavan	2017	$f_f = \frac{20}{Re} + \left[\frac{0.0075\left(\frac{4000}{Re}\right)^{0.05}}{0.25+\left(\frac{4000}{Re}\right)^{5}}\right]$	Valid for wide range of Reynolds number	0.9777
2	Morrison	2013	$f = \frac{16}{Re} + \left[\frac{0.0076\left(\frac{3170}{Re}\right)^{0.165}}{1+\left(\frac{3170}{Re}\right)^{7}}\right]$	Inaccuracy crept in for higher values of Reynolds numbers	
3	Barenblatt	2005	$f = \frac{8}{\psi^{2(1+\alpha)}}$	$Re < 13\times10^6$	
4	McKeon	2005	$\frac{1}{\sqrt{f}} = 1.920\log(Re\sqrt{f} - 0.475 - \frac{7.04}{(Re\sqrt{f})^{0.55}}$		
5	Yen	1991	$f = \frac{1}{4}\left[-log\left(\frac{e}{12R}\right) + \frac{5.2}{(4R_e)^{0.9}}\right]^{-2}$	$3000<R_e$, $\frac{e}{D}< 0.05$	
6	Serghides	1984	$\frac{1}{\sqrt{f}} = \left[A - \frac{(B-A)^2}{C-2B+A}\right]$	Re>2100 and any e/D	
7	Haaland	1983	$f = \frac{0.308642}{\left[log\left(\left(\frac{e}{3.7D}\right)^{1.11} + \left\lvert\frac{6.9}{Re}\right\rvert\right)\right]^2}$		0.85096
8	Zigrang & Sylvester	1982	$\frac{1}{\sqrt{f}} = -2log\left[\frac{1}{3.7}\left[\frac{e}{D}\right] - \frac{5.02A}{Re}\right]$	$4000<Re<10^8$ and $0<\frac{e}{D}<0.04$	0.904104
9	Barr	1981	$f = \frac{1}{4}\left[-log\left(\frac{e}{14.8R}\right) + \frac{5.2}{(4R_e)^{0.89}}\right]^{-2}$		
10	Chen	1979	$\frac{1}{\sqrt{f}} = -2log\left[\frac{1}{3.7605}\left[\frac{e}{D}\right] - \frac{5.0452A}{Re}\right]$	$4000<Re<10^8$ $0.000001<\frac{e}{D}$	0.9148
11	Churchill	1977	$f = 8\left[(8/Re)^{12} + \frac{1}{(A+B)^{1.5}}\right]^{\frac{1}{12}}$		0.9066
12	Swami-Jain	1976	$\frac{1}{\sqrt{f}} = 1.14 - 2log\left[\left[\frac{e}{D}\right] + \frac{21.25}{Re^{0.9}}\right]$	$5000<Re<10^8$ $0.000001<\frac{e}{D}<0.05$	
13	Barr	1972	$f = \frac{1}{4}\left[log\left(\frac{e}{14.8R}\right) + \frac{5.76}{(4R_e)^{0.9}}\right]^{-2}$		0.9051
14	Wood	1966	$f = 0.094\left(\frac{e}{D}\right)^{0.223} + 0.53\left(\frac{e}{D}\right) + 88\left(\frac{e}{D}\right)^{0.44}(Re)^{-\psi}$	$4000<Re<5*10^8$ $0.00001<\frac{e}{D}<0.04$	0.7075
15	Moody	1947	$f = 0.0053\left[1+\left(2*10^4\frac{\varepsilon}{D} + \frac{10^6}{Re}\right)^{\frac{1}{3}}\right]$	$4000<Re<5*10^8$ $0<\frac{\varepsilon}{D}<0.01$	
16	Colebrook	1938-39	$\frac{1}{\sqrt{f}} = -2log\left[\frac{\frac{e}{D}}{3.7} + \frac{2.51}{Re\sqrt{f}}\right]$		0.90416

This is a generalized Manning equation, having two powers depend on the hydraulic radius and Reynolds number. The maximum approximation errors are much smaller than other errors resulting from uncertainty and misspecification of design and simulation quantities and also much smaller than in the original Manning and the Hazen-Willians equations. Both these equations can be obtained as special cases of the proposed generalized equation by setting the exponent parameters constant. For large Reynolds numbers, the original Manning equation improves in performance and becomes practically equivalent with the proposed generalized equation. Thus, its use particularly when the networks operate with surface flow is absolutely justified. In pressurized conditions, the proposed generalized Manning equation can be a valid alternative to the combination of the Colebrook-White and Darcy-Weisbach equations, having the advantage of simplicity and speed of calculation both in manual and computer mode.

Thus, Eq. [27] and [29] could be very useful for the design and simulation of complicated transient flows in urban water networks in predicting flow in a water supply as well as sewer pipes.

5 CONCLUSIONS

i. Proper attention has to be given to flow conditions in applying above listed formulae except Eq. [27]. Within the critical region, where 2100 < Re < 3000 and beyond specified range;
ii. Friction factor calculations with Barenblatt, McKeon and Morrison equations are very good at computing the Darcy Weisbach friction factor, *f* for turbulent flow in smooth pipe;
iii. Accuracy in computation of flow resistance by the equation of Morrison, Barenblatt for Reynolds number ranging from 8000 and above, drastically reduces when Reynolds number increases which contradicts field data;
iv. The proposed Eq. [27] in present studies involves higher roughness values and has better correlation coefficient 99.99% for data pertaining to transition, 97.6 % for turbulent and overall 97.7% with field data;
v. The proposed Eq. [29] would be of help in simulation of complicated urban water networks in predicting pressure heads and flow in a water supply and flow in sewer pipes;
vi. Mannings n as given by Eq. [29] can be easily and accurately predicts friction in river;
vii. Explicit Eq. [27] relates Friction factor, Reynolds number and relative roughness and has further scope to improve with additional parameters as pointed out by Hunter Rouse *e.g.,* Froude Number, porous bed and banks which affects friction factor after getting additional data from field.

ACKNOWLEDGEMENT

Author is indebted to Dr Sinha M.K Director and Shri Kudale M.D. Additional Director, CWPRS, Pune for constant encouragement and guidance in preparing this paper. Author is also thankful to Shri Hradaya Prakash for rendering assistance from time to time.

LIST OF SYMBOLS

e	Mean height of roughness of the pipe
K_s	Equivalent grain roughness
D	Diameter of conduit
f	Darcy Weisbach friction factor
U	Average velocity
υ	Kinematic viscosity
F	Froude number
g	Acceleration due to gravity
R_e	Reynolds number
f_f	Friction factor computed from observations

REFERENCES

Alam, A.M. & Kennedy, J.F. (1969). Friction Factor for Flow in Sand Bed Channels. *Journal of the Hydraulics Division,* 95(6), 1973-1992.

Annambhotla, V.S., Sayre, W.W. & Livesey, R.H. (1972). Statistical Properties of Missouri River Bed Forms. *Journal of the Waterways, Harbors and Coastal Engineering Division*, 98(4), 489-510.

Silberman, E., Carter, R.W., Einstein, H.A., Hinds, J. & Powell, R.W. (1963). Friction Factors in Open Channels. *J. Hydraul. Div.*, 89(2), 97-143.

Bathurst, J.C. (1978). Flow Resistance of Large Scale Roughness. *Journal of the Hydraulics Division*, 104(12), 1587-1603.

Singh, B. (1960). Transportation of Bed Load in Channels with Special Reference to Gradient and Form, *PhD Thesis*. Imperial College London, UK.

Bray, D.I. (1979). Estimating Average Velocity in Gravel Bed Rivers. *Journal of the Hydraulics Division*, 105(9), 1103-1122.

Brownlie, W.R. (1981). *Compilation of Alluvial Channel Data: Laboratory and Field,* report No. KH-R-43B, WMK Laboratory of Hydraulics and Water Resources, California Institute of Technology, Pasadena, California, USA.

Church, M. & Rood, K. (1983). *Catalogue of Alluvial River Channel Regime Data*. University of British Colombia, Canada.

  / ISSN 1562-6865 (Online) - ISSN 1063-7710 (Print)

Colosimo, C., Copertino, V.A. & Vetri, M. (1988). Friction Factor Evaluation in Gravel Bed Rivers. *Journal of Hydraulic Engineering*, 114(8), 861-876.

Joseph, D.D. & Yang, B.H. (2010). Friction Factor Correlations for Laminar, Transition and Turbulent Flow in Smooth Pipes. *Physica D: Nonlinear Phenomena*, 239(14), 1318-1328.

Garde, R.J., Prakash, H. & Arora, M. (1985). *Hydraulics of Gravel-Bed Rivers*, report prepared for Indian National Science Academy, Pune, 164.

Ghanbari, A., Fred, F.F. & Rieke, H.H. (2011). Newly Developed Friction Factor Correlation for Pipe Flow and Flow Assurance. *Journal of Chemical Engineering and Materials Science*, 2(6), 83-86.

Haaland, S.E. (1983). Simple and Explicit Formulas for the Friction-Factor in Turbulent Pipe Flow. *Journal of Fluids Engineering*, 105(1), 89-90.

Haque, M.I. & Mahmood, K. (1983). Analytical Determination of Form Friction Factor. *Journal of Hydraulic Engineering*, 109(4), 590-610.

Hey, R.D. & Thorne, C.R. (1986). Stable Channel with Mobile Gravel Beds. *Journal of Hydraulic Engineering*, 112(8), 671-689.

Prakash, H. (2014). Prediction of Flow Resistance in Gravel Bed River. *International Journal of Engineering and Technical Research*, 2(4), 155-159.

Itakura, T., Yamaguchi, Y., Shimuzu, Y., Kishi, T. & Kuroki, M. (1986). Observation of Bed Topography During 1981 Flood in the Ishikari River. *Journal of Hydro-Science and Hydraulic Engineering*, 4(2), 11-19.

McKeon, B.J., Swanson, C.J., Zagarola, M.V., Donnelly, R.J. & Smits, A.J. (2004). Friction Factors for Smooth Pipe Flow. *Journal of Fluid Mechanics*, 511, 41-44.

Milhous, R.T. (1973). Sediment Transport in Gravel-Bottomed Stream, *PhD Thesis*. Oregon State University, USA.

Morrison, F.A. (2013). *Data Correlation for Friction Factor in Smooth Pipes*, Department of Chemical Engineering, Michigan Technological University, Houghton, Michigan.

Nordin, C.F. (1971). *Statistical Properties of Dune Profiles*. US Geological Survey Professional Paper 562-F, US Government Printing Office, Washington DC.

Nordin, C.F. (1988). Sediment Studies of the Orinoco River, In *Proc. of 3rd US-Pakistan Binational Symposium on the Mechanics of Alluvial Channels,* Lahore, Pakistan, published by Water Resources Publications, Littleton, Colorado, USA, 169-186.

Papaevangelou, G., Evangelides, C. & Tzimopoulos, C. (2010). A New Explicit Relation for the Friction Coefficient in the Darcy-Weisbach Equation. In *Proceedings of the Tenth Conference on Protection and Restoration of the Environment*, 166, 1-7.

Prandtl, L. (1952). *Essentials of Fluid Dynamics*. Hafner Publication, New York.

Samide, G.W. (1971). Sediment Transport Measurement, *MSc Thesis*. University of Alberta, Canada.

Simons, D.B. (1957). Theory and Design of Stable Channels in Alluvial Materials, *PhD. Thesis.* Colorado State University, Fort Collins, USA.

Thompson, S.M. & Campbell, P.L. (1979). Hydraulics of Large Channel Paved with Boulders. *Journal of Hydraulic Research,* 17(4), 341-354.

LEAK-INDUCED FREQUENCY SHIFTS IN TRANSIENT-BASED FREQUENCY DOMAIN METHOD FOR LEAKAGE DETECTION

JINGRONG LIN[1] & MOHAMED S. GHIDAOUI[2]

[1,2] Hong Kong University of Science and Technology, Hong Kong,
jlinam@connect.ust.hk; ghidaoui@ust.hk

ABSTRACT

In recent years, an efficient and easy to apply transient-based frequency response method has been developed for pipeline leakage detection. Until now, it has been assumed that a leaking pipeline has the same resonance peaks at all the odd harmonics in its frequency response diagram as an intact pipe. However, in this research, a small but undeniable leak-induced frequency shift in a leaking pipeline is demonstrated in the frequency response diagram of the leaking pipeline in both transfer matrix method and method of characteristic simulation. The expression for this leak-induced shift is derived using Taylor series expansion together with a transfer matrix. The verification of the shift expression is given, and the factors influencing the shift are discussed. The demonstrated leak-induced frequency shift is generally quite small and therefore do not significantly affect the utility of the Frequency Domain methods. However, it is important to note that such leakage-induced frequency shifts are, in fact, real. Thus, this research and paper provide complementary knowledge and clarification to the frequency response leakage detection theory.

Keywords: Leakage detection; frequency shift; frequency response function; transient.

1 INTRODUCTION

The problem of identifying potential leaks in water supply pipelines has been an active area of both research and technology development since the 1990s. The frequency response method (FRM) has increasingly become a topic of research and pre-commercial technology development. However, in previous studies of Frequency Response Diagram (FRD) for leakage detection, the frequency response function of the leaking pipe is simplified by the assumption that no leak-induced shift in the frequency domain response occurs, and the validity of the assumption regarding the presence of leak-induced shifts in resonance frequencies still remains open.

Lee et al. (2005) considered cases in which some typical values of wave speed, leak size and driving head were chosen, (*i.e.* wave speed in the range of 1000ms^{-1}, head at the leak greater than 40m and $C_d A_l/A$ less than 5 x 10^{-3}, where $C_d A_l/A$ is a lumped parameter representing the relative size of the leak). The choice of these typical values makes a portion of the pipeline's frequency response function (FRF) so small that Lee et al. (2005) assumed that it could be neglected in their frequency response model. However, the neglected part is strongly related to leakage characteristics, and neglecting those parts of the frequency response function resulted in the loss of the corresponding leak-induced frequency shift. Based on the typical cases studied, Lee et al. (2005) modified the frequency response function of the pipeline system and proposed a simplified leakage detection model with no shift assumption.

Contrary to Lee et al. (2005) assumption, Mpesha (1999), Mpesha et al. (2001; 2002) suggested that the presence of a leak is indicated by the existence of additional resonant peaks in the experimental frequency response diagram. In their work, the amplitude of the overall resonant peaks for a leaking system are lower than that for a system with no leaks. Based on their experimental findings, Mpesha et al. (2001; 2002) developed a leakage detection method that locates and sizes the leak using the information provided by the observed additional resonant peaks. However, this method has thus far proved successful in only a few cases. Doubts regarding the validity of the method proposed by Mpesha et al. (2001; 2002) have been published as a discussion in Lee et al. (2003c), where two main areas of concern were listed. First, the FRDs generated by Mpesha et al. (2001; 2002) were significantly different from other previous researches, such as Chaudhry (1987), Ferrante et al. (2001) and Lee et al. (2002), which were based on the same methods; second, the use of a linear model for representing the nonlinear system seems inconsistent with the fundamental nature of the phenomenon.

Ferrante and Brunone (2001) presented further results on the leak-induced impact on the frequency response of the pipeline system. Ferrante and Brunone (2001) increased the size of a leak from small flows up to 80% of the pipe's base flow. The results showed that the increase in leak size leads to a change in the fundamental frequency of the pipeline.

This paper develops in theory a proof of leak-induced shift of resonance peaks in FRD for a leaking pipeline system which uses both the method of characteristics (MOC) and an analytical computation by

  / ISSN 1562-6865 (Online) - ISSN 1063-7710 (Print)

transfer matrix method. The frequency shift is analytically derived using the transfer matrix and Taylor series expansion. Following that, the accuracy of the derived expression for the leak-induced shift in wave number is verified. To highlight the effect of a leak, the following analysis is performed on the numerical pipeline (in the transfer matrix model) without the effect of pipe friction. The transient is generated by perturbing a side discharge valve located just upstream of the terminal downstream in-line valve in the simulation system.

2 TRANSIENT WAVES IN PIPELINES

2.1 Resonance wave number for an intact pipeline

A brief summary of the transfer matrix equations for the unsteady mass and conservation equation can be found in Chaudhry (1987) or Wylie and Streeter (1993), where the transfer equations are arranged in matrix forms and provide relationships between the upstream and downstream head and discharge responses for pipe segments and pipe discontinuities (leak, valve, junction, etc.).

The transfer matrix relates the discharge and head at the upstream and the downstream boundaries for an intact pipeline system. A probing transient wave is generated by a unit input discharge perturbation and is written as:

$$\begin{bmatrix} q \\ h \\ 1 \end{bmatrix}^1 = \begin{bmatrix} 1 & 0 & 1 \\ 0 & 1 & 0 \\ 0 & 0 & 1 \end{bmatrix} \begin{bmatrix} \cos(k_{NL}l) & -i\frac{1}{Z_C}\sin(k_{NL}l) & 1 \\ -iZ_C\sin(k_{NL}l) & \cos(k_{NL}l) & 0 \\ 0 & 0 & 1 \end{bmatrix} \begin{bmatrix} q \\ h \\ 1 \end{bmatrix}^0 \quad [1]$$

where q and h equal the discharge and head perturbations in the wave number domain; k_{NL} is the resonance wave number for an intact pipeline.

Solving Eq. **Error! Reference source not found.** requires the head and discharge at node 1 (node 1 represents the point at the inlet side of the downstream valve). The upstream and downstream boundary conditions are the fixed head boundary ($h_0 = 0$) upstream and the fixed discharge boundary ($q_1 = 0$) downstream. Solving Eq. [1] with these boundary conditions, gives:

$$h_1 = -iZ_C \cdot \frac{\sin(k_{NL}l)}{\cos(k_{NL}l)} \quad [2]$$

The resonance condition for an intact frictionless pipeline can be extracted from Eq. **Error! Reference source not found.** and is written as:

$$\cos(k_{NL}l) = 0 \quad [3]$$

Solving Eq. **Error! Reference source not found.** for the resonance wave number gives:

$$(k_{NL})_m = (2m-1)\frac{\pi}{2l} \quad (m = 1, 2, 3 ...), \quad [4]$$

where m is a positive integer that corresponds to the resonance peak number. Eq. **Error! Reference source not found.** indicates that an intact frictionless pipeline resonates at the odd harmonics.

2.2 Resonance wave number for a leaking pipeline

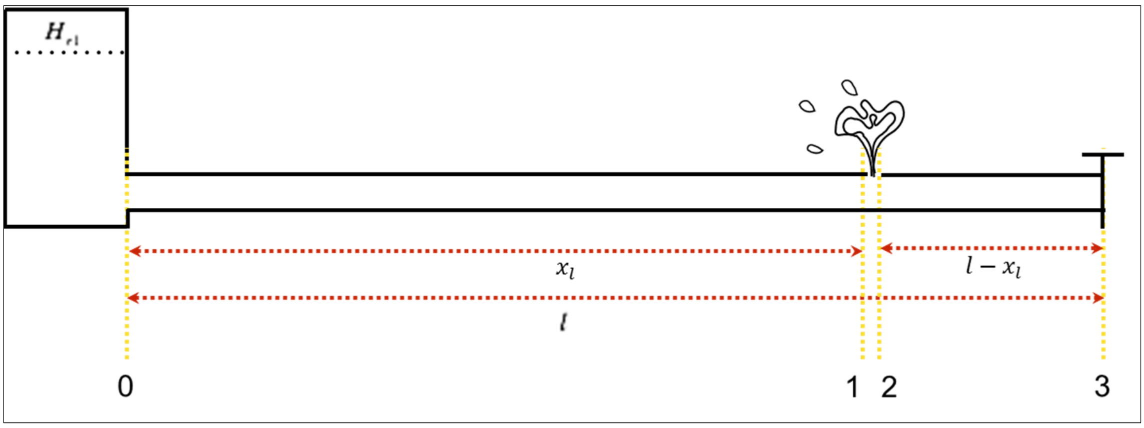

Figure 1. Single leaking frictionless pipeline layout.

A simple, leaking, frictionless pipeline layout is illustrated in Figure 1. The single pipe with a leak at distance x_l from the reservoir can be divided into two sections: the first section of length x_l goes from the upstream reservoir to the leak; the second section, of length $l - x_l$ goes from the leak to the valve. Here, 0 and 3 respectively denote the upstream and downstream nodes. The same boundary conditions as the previous intact pipeline are imposed here. The transfer matrix relating the discharge and head at the upstream and the downstream ends of the system is written as:

$$\begin{bmatrix} q \\ h \\ 1 \end{bmatrix}^3 = \begin{bmatrix} 1 & 0 & 1 \\ 0 & 1 & 0 \\ 0 & 0 & 1 \end{bmatrix} \begin{bmatrix} \cos\big(k(l-x_l)\big) & -i\frac{1}{Z_C}\sin\big(k(l-x_l)\big) & 1 \\ -iZ_C\sin\big(k(l-x_l)\big) & \cos\big(k(l-x_l)\big) & 0 \\ 0 & 0 & 1 \end{bmatrix} \begin{bmatrix} 1 & -\frac{Q_{ls}}{2H_{ls}} & 1 \\ 0 & 1 & 0 \\ 0 & 0 & 1 \end{bmatrix} \begin{bmatrix} \cos(kx_l) & -i\frac{1}{Z_C}\sin(kx_l) & 1 \\ -iZ_C\sin(kx_l) & \cos(kx_l) & 0 \\ 0 & 0 & 1 \end{bmatrix} \begin{bmatrix} q \\ h \\ 1 \end{bmatrix}^0 \quad [5]$$

Solving Eq. **Error! Reference source not found.** for the head at node 3 with the upstream boundary condition (h_0= 0) and the downstream boundary condition ($q_3 = 0$), gives:

$$h_3(k) = \frac{\left(-\frac{ia}{gA}\sin(kl)+\frac{a}{gA}\cdot\frac{Z_C}{Z_L}\sin\big(k(l-x_l)\big)\sin(kx_a)\right)\left(\cos(kl)-i\cdot\frac{Z_C}{Z_L}\cos\big(k(l-x_l)\big)\sin(kx_l)\right)}{\cos^2(kl)+\left(\frac{Z_C}{Z_L}\right)^2\cos^2\big(k(l-x_l)\big)\sin^2(kx_l)} \quad [1]$$

where $Z_L = 2H_{ls}/Q_{ls}$ is the leak impedance, Z_C/Z_L is a parameter representing the size of the leak, where the larger value of Z_C/Z_L, the bigger the size of the leak.

Since the numerator of Eq. [1] is bounded, the resonance condition for the above leaking pipeline occurs when:

$$\cos^2(kl) + \left(\frac{Z_C}{Z_L}\right)^2 \cos^2\big(k(l-x_l)\big)\sin^2(kx_l) \to 0. \quad [2]$$

Comparing the resonance condition for the intact pipeline (Eq. **Error! Reference source not found.**) with the resonance condition in the leaking pipeline (Eq. [2]), it can be found that the latter case has an additional term$\left[(Z_C/Z_L)^2\cos^2\big(k(l-x_l)\big)\sin^2(kx_l)\right]$, which represents the influence of the leak on the resonant wave number. Therefore, the solution of resonance wave number *k* for Eq. [2] is not equal to Eq. **Error! Reference source not found.**. However, when $Q_{ls}\to 0$, $Z_L\to\infty$, and the denominator converges to $\cos^2(kl) = 0$, the same resonance condition as Eq. **Error! Reference source not found.** was obtained. As can be seen from the analytical resonance condition for both the intact and the leaking pipeline, a leak in the pipeline affects the resonance wave number of the frequency response function.

In Figure 2, function $h_3(k)$ was plotted as the blue line with a discretized value of *k* = 4.1667e-05s^{-1}. Also plotted as the red asterisks in Figure 2 is a line with *k* given by Eq. **Error! Reference source not found.** using the system of Figure 1 (l = 2000m, x_l = 1500m, D = 0.3m, a = 1000m/s, and $Z_C/Z_L = 0.1355$). For comparison, the result generated numerically by the method of characteristics (MOC) was also plotted in Figure 2 as the green line under the same conditions and parameters as the leaking pipeline system, which agrees so closely with the result given by transfer matrix [function $h_3(k)$] that the curves lie practically atop one another. It should be noted that the system response $h_3(k)$ plotted with discretized k_{NL}, namely the analytical expression with no-shift assumption given by Eq. **Error! Reference source not found.**, assumes that the leak in the pipeline does not shift the resonance wave number of the system. However, when zooming in on Figure 2 at each odd normalized wave number *k** = 1, 3, 5,…, it can be seen that all the local maximum values are not located exactly at the odd normalized wave number. Instead each local maximum value of the system response is shifted slightly to the side of the odd normalized wave number.

Examples of the shift in resonance wave numbers were shown in Figure 3, which zooms in on the 3rd, 5th, 11th, 13th resonance peaks from Figure 2. Obvious leak-induced shifting can be seen from the frequency response diagram obtained from the MOC simulation and transfer matrix. The leak-induced wave-number shift (LIWNS) was located either to the left or right of the odd harmonics. Note that the slight difference in the frequency response diagram between the results of transfer matrix and MOC simulation in Figure 3 comes from the fact that the leak was linearized in the transfer matrix model compared with the complete form of leak in the MOC model. Thus, one would expect that the complete form of leak modelling in the MOC simulation should induce more damping than the transfer matrix model.

From the small but rather obvious leak-induced shift shown in Figure 3, it can be concluded that leakage in a pipeline does shift the resonance wave number of the frequency response diagram of the leaking pipeline. This fact is not currently recognized in the literature. Actually, when a leak exists in the pipeline, it constitutes discontinuity in the pipe flow condition and a change in pipeline geometry, which gives rise to a modification of the system frequency response diagram and results in the observed slight shifting of the resonance wave number together with damping the maximum value of the system response diagram. The existence of the leak-induced wave number shift showed in Figure 3 corresponds with the expectation of the resonance wave number for a leaking pipeline in Eq. [2], which also predicts the existence of the leak induced wave number shift.

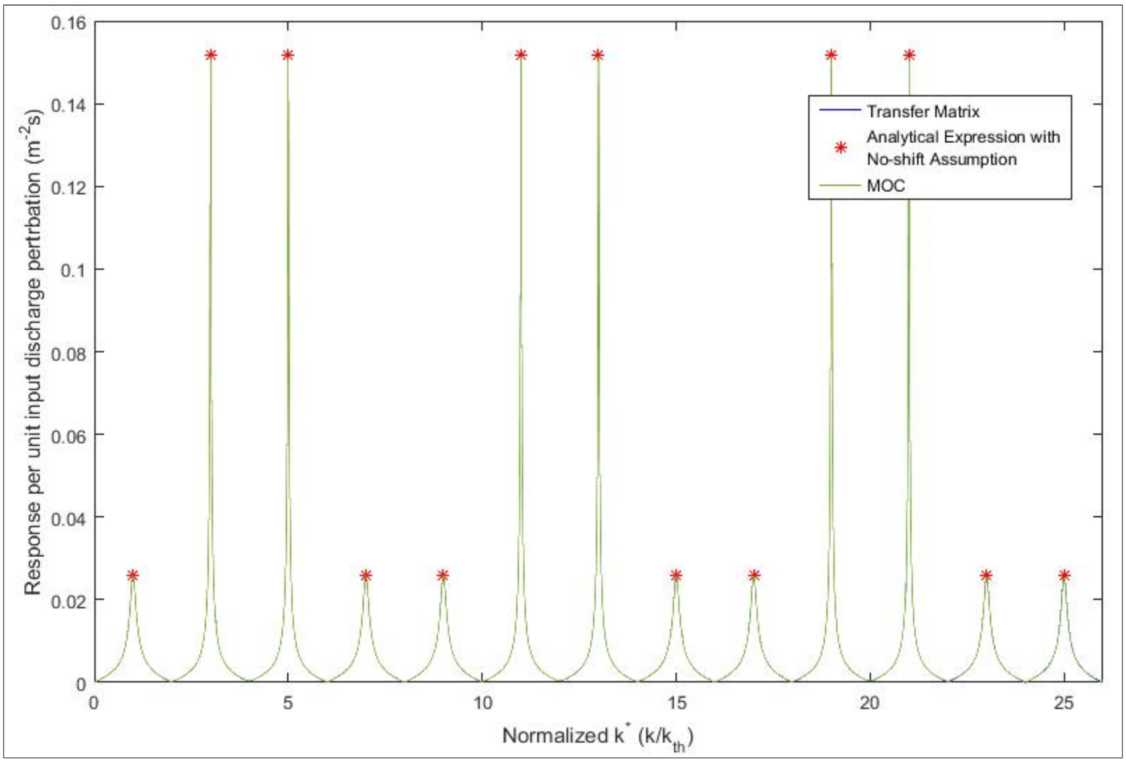

Figure 2. Response in frequency domain at the downstream end of the pipe calculated by transfer matrix and analytical expression with no-shift assumption respectively.

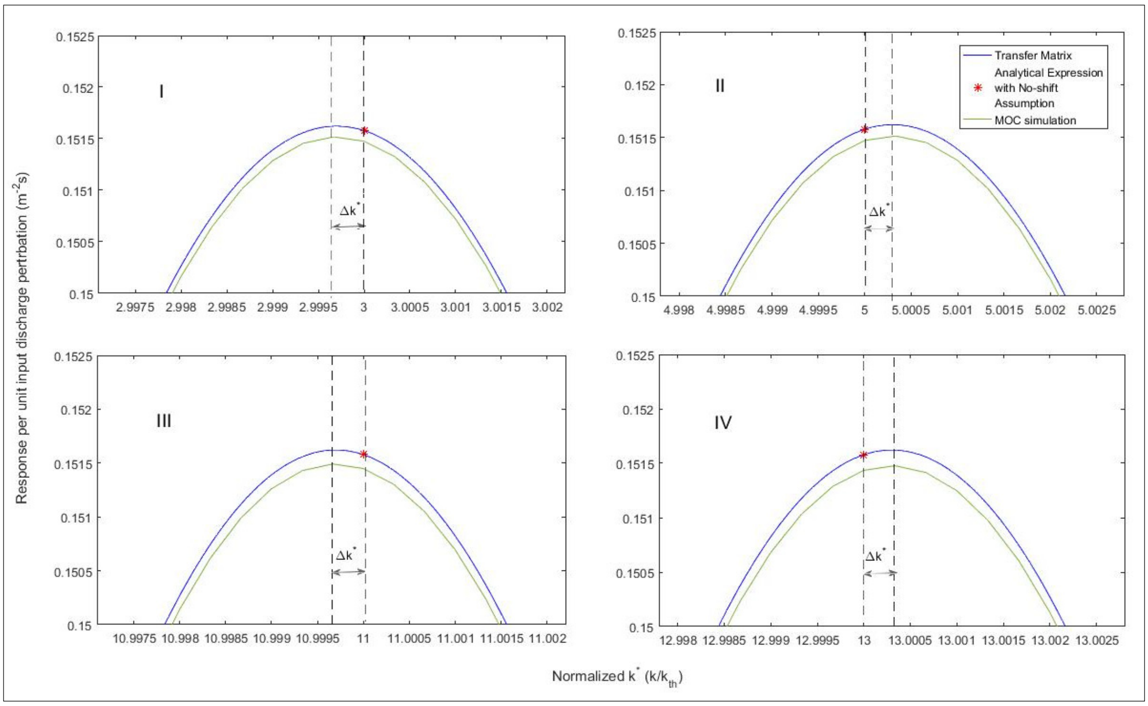

Figure 3. Zooming graph of Figure. 3 at the first resonance wave number.

3 DERIVATION OF LEAK-INDUCED SHIFT IN WAVE-NUMBER

3.1 Derivation of leak-induced shift in wave-number

Assuming the leak-induced shift in the resonance wave number is small, then the true resonance wave number of a leaking pipeline system was written as below:

$$k = k_{NL} + \Delta k \quad [3]$$

where k_{NL} stands for the resonance wave number for a pipeline with no leaks, Δk stands for the small deviation of the resonance frequency for a leaking pipeline compared to an intact pipeline. The expression containing k was approximated using a first order Taylor expansion expression, such as:

$$\sin(kx) = \sin(k_{NL}x) + x\Delta k \cos(k_{NL}x) \quad [4]$$
$$\cos(kx) = \cos(k_{NL}x) - x\Delta k \sin(k_{NL}x) \quad [5]$$

where x is the length of pipe section considered.

Since the numerator of Eq. [5] is bounded, the numerator of Eq. [5] was assumed to be a constant at the resonance wave number. Therefore, only the denominator of Eq. [2] was considered in the derivation of leak-induced shift, which was rewritten as shown below.

$$h_3(k) = \frac{\text{finite value}}{\cos^2(kl) + \left(\frac{Z_C}{Z_L}\right)^2 \cos^2\big(k(l-x_l)\big)\sin^2(kx_l)} \quad [6]$$

When a leaking pipeline resonates, the value of Eq. [1] reaches its maximum value since the denominator of Eq. [1] goes to its minimum value.

The minimum value of the denominator of Eq. [1] was given by:

$$\frac{d}{d(k)}\left(\cos^2(kl) + \left(\frac{Z_C}{Z_L}\right)^2 \cos^2\big(k(l-x_l)\big)\sin^2(kx_l)\right) = 0 \quad [7]$$

which gives:

$$2l(-\sin(kl))\cos(kl) + \left(\frac{Z_C}{Z_L}\right)^2 \Big(2(l-x_l)\big(-\sin\big(k(l-x_l)\big)\big)\cos(k(l-x_l))\sin^2(kx_l) + 2x_l\cos(kx_l)\sin(kx_l)\cos^2\big(k(l-x_l)\big)\Big) = 0. \quad [8]$$

Substituting Eq. **Error! Reference source not found.**, [4] and [5] into Eq. [8] results in the expression for the shift in wave number shown below:

$$\Delta k = \frac{-\left(\frac{Z_C}{Z_L}\right)^2\left(\left(\frac{2x_l-l}{2}\right)\left(\sin(2k_{NL}x_l) - \frac{1}{2}\sin(4k_{NL}x_l)\right)\right)}{2l^2 + \left(\frac{Z_C}{Z_L}\right)^2\Big(\big((x_l{}^2+(l-x_l)^2)\cos(2k_{NL}x_l) - (x_l{}^2+(l-x_l)^2)\cos^2(2k_{NL}x_l) - 2x_l(l-x_l)\sin^2(2k_{NL}x_l)\big)\Big)} \quad [9]$$

First, it should be noted that when $x_l = l/2$, then $\Delta k = 0$. This means that there is no shift in the resonance wave number when a leak is located at the middle of the pipeline. Secondly, within the engineering practical range of Z_C/Z_L, Δk increases as Z_C/Z_L increases. (The range of Z_C/Z_L is selected to be within 0<Z_C/Z_L<1, the reason is explained below in section 3.2) The verification for the derived leak-induced shift in wave number is discussed in the following section.

3.2 Verification of the derivation for the shift

The normalized Δk^* was obtained from:

$$\Delta k^* = \frac{\Delta k}{k_{th}} \times 100, \quad [10]$$

where $k_{th} = \pi/2l$ denotes the fundamental resonance wave number for the intact pipeline.

The normalized Δk^* was calculated for different values of Z_C/Z_L for the first 15 odd harmonics obtained from transfer matrix, MOC simulation and the analytical solution. The normalized Δk^* at $Z_C/Z_L = 0.1355, 0.7227$ and 0.9937 were plotted in Figure 4, Figure 5 and Figure 6, respectively. The value of Z_C/Z_L was selected to be 0.0 < Z_C/Z_L< 1.0. This is not a significant restriction since the value of Z_C/Z_L is usually smaller than 1.0 in practice. For example, let H_{ls} be within the range 30–60m; a be of the order of 1000m/s, and let C_dA_l/A be within the range 0.001–0.01. This leads to Z_C/Z_L being in the range 0.03–0.5. Moreover, to ensure that the transient events do not induce negative pressure in the pipeline, Z_C/Z_L should also be within the range 0–0.5. Therefore, the interval 0.0 < Z_C/Z_L < 1.0 covers a wide range of practical problems.

Let Δk_{TM} denote the leak-induced wave number shift calculated numerically by the empirical transfer matrix equation, and let Δk_{TE} denote the leak-induced wave number shift calculated analytically by the derived shift equation. The normalized error of the analytical shift solution with respect to the fundamental intact pipeline resonance wave number was defined as:

$$\Delta\varepsilon = \frac{(\Delta k_{TE} - \Delta k_{TM})}{k_{th}} \times 100. \quad [11]$$

The normalized errors of the analytical shift solution with $Z_C/Z_L = 0.1355, 0.7227$ and 0.9937 were plotted in Figure 7.

As can be seen from Figure 4, the normalized Δk calculated from the three approaches (transfer matrix, MOC simulation and the analytical solution) perfectly overlapped. And it could be read from Figure 7, under the condition of $Z_C/Z_L = 0.1355$, the normalized error $\Delta\varepsilon$ was less than one percent, which means that under the condition of $Z_C/Z_L = 0.1355$ the analytical solution can accurately predict the LIWNS. When $Z_C/Z_L = 0.7227$, the normalized Δk^* obtained from MOC simulation overlapped perfectly with that obtained from transfer matrix. The normalized Δk^* obtained from analytical shift expression slightly over-predicts the LIWNS, with an error less than 5% as can be seen from Figure 7, which is accurate enough for predicting the LIWNS. When $Z_C/Z_L = 0.9937$, the normalized Δk^* obtained from MOC simulation matches well with that obtained from transfer matrix. The normalized Δk^* obtained from analytical solution slightly over-predicts the LIWNS, with an error less than 15% as can be seen from Figure 7.

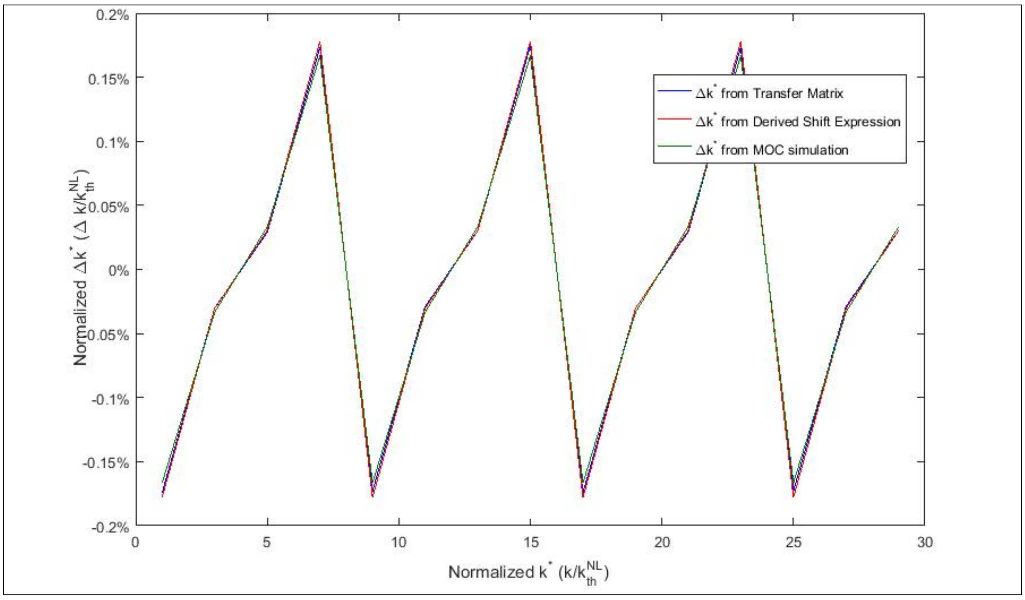

Figure 4. Comparison of Δk^* calculated from Transfer matrix, analytically derived expression, and MOC simulation respectively at $Z_C/Z_L = 0.1355$.

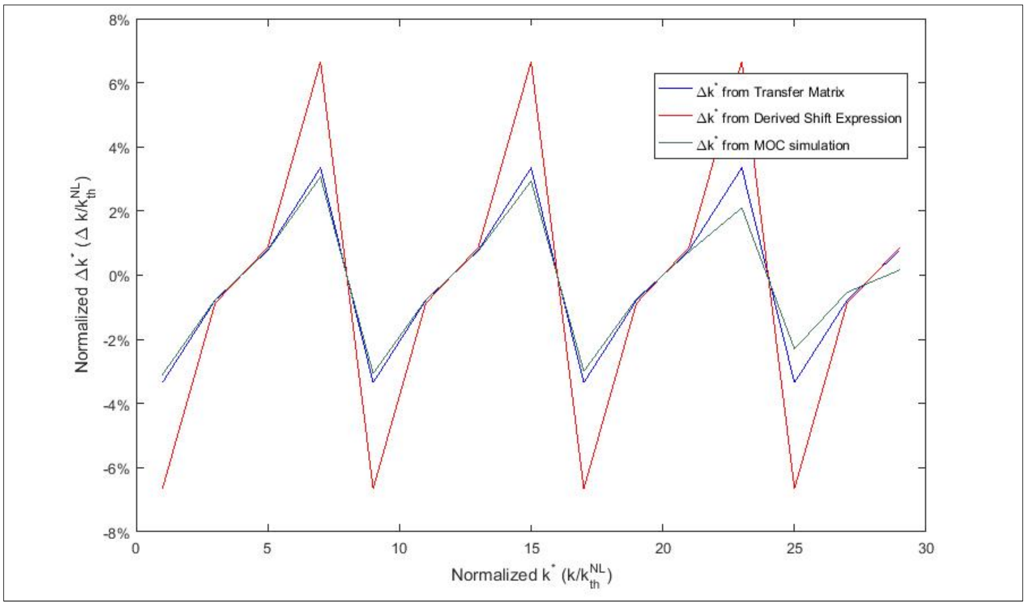

Figure 5. Comparison of Δk^* calculated from Transfer matrix, analytically derived expression and MOC simulation respectively at $Z_C/Z_L = 0.7227$.

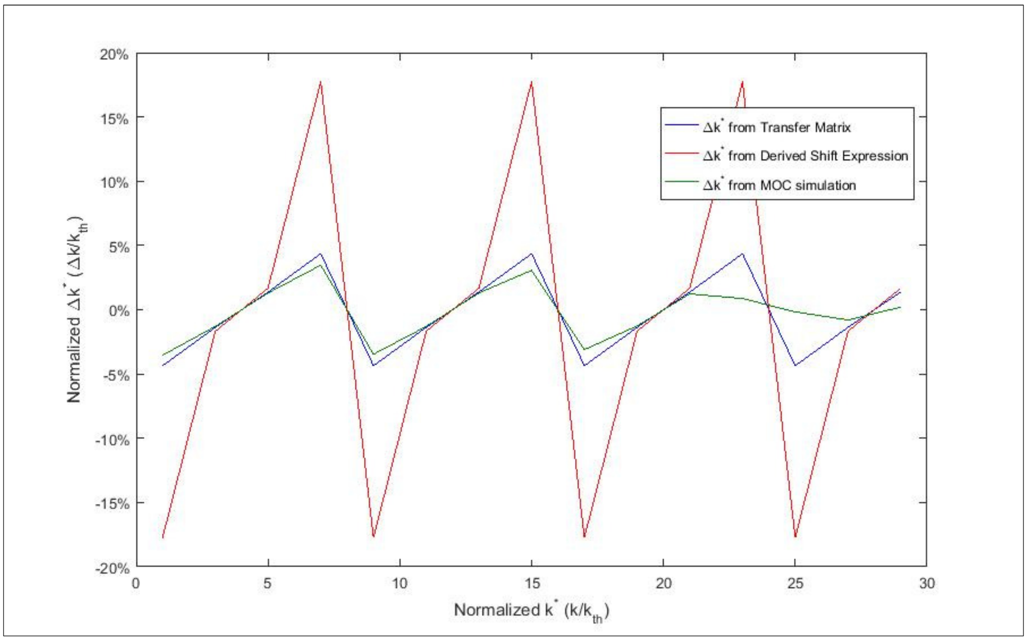

Figure 6. Comparison of Δk^* calculated from Transfer matrix, analytically derived expression and MOC simulation respectively at $Z_C/Z_L = 0.9937$.

It can be concluded from Figure 4, Figure 5 and Figure 6 that within the range of $0.0 < Z_C/Z_L < 1.0$, LIWNS increases as Z_C/Z_L increases, which corresponds to the prediction of the analytical expression of Δk in Eq. [10]. Meanwhile, the accuracy of the analytical expression for Δk increases as Z_C/Z_L decreases. As a result, the analytical solution derived using the first order Taylor expansion is a reasonable approximation and is accurate enough to estimate the LIWNS for a leaking pipeline. All methods confirmed that a leak in a pipeline does cause a shift in the resonance wave number compared with an intact pipeline.

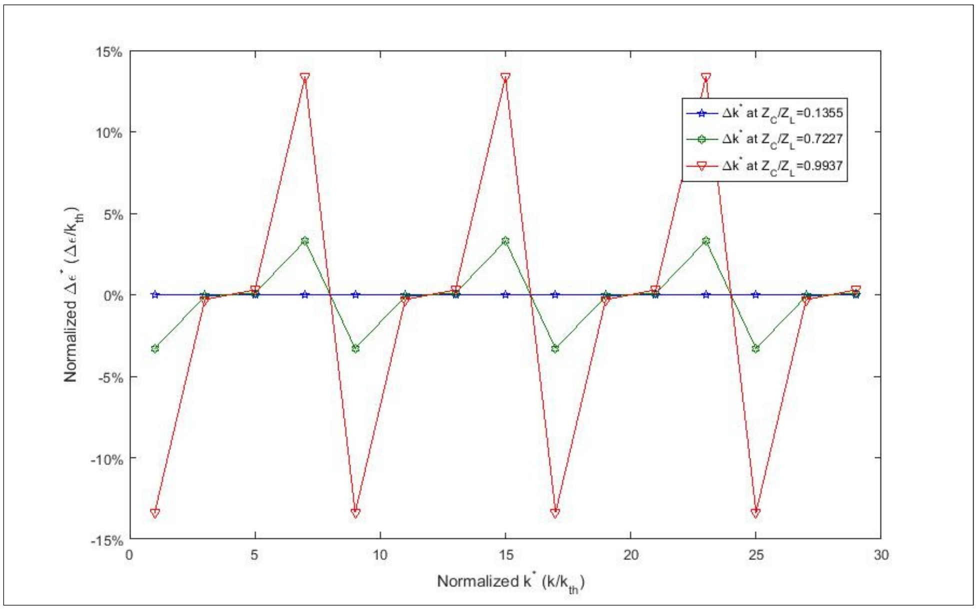

Figure 7. Comparison of Δε at three different values of Z_C/Z_L. (Curve ↲ !for $Z_C/Z_L = 0.1355$; Curve ↳ !for $Z_C/Z_L = 0.7227$; Curve ↴ for $Z_C/Z_L = 0.9937$).

4 CONCLUSIONS

A leak in a pipeline is a geometrical change as well as a change in pipe boundaries that brings about a discontinuity between adjacent pipe segments, and results in a wave number shift in the frequency response diagram of the pipeline system. The analytical expression for the shift phenomenon was derived in this paper using Taylor expansion together with a transfer matrix approach. The first order Taylor expansion expressions applied to represent the true resonance wave number for the leaking pipeline includes that small, but physical, leak-induced wave number shift. This paper provides some detailed investigations of the frequency response diagram and is concerned primarily with demonstrating the physical and theoretical existence of a leak-induced shift in wave number. An in-depth comparison of the resonance condition of the frequency response function between a leaking pipeline and an intact pipeline was given, where leak-related differences were found. The following conclusions were drawn:

i. Careful examination of the frequency response diagram obtained from transfer matrix and MOC simulation showed a small, but obvious, leak-induced wave number shift. The resonance wave number for a leaking pipeline *does* shift the resonance wave number compared with the intact pipeline. The demonstration of leak-induced frequency shift in this paper provides necessary, complementary knowledge and clarification to the existing frequency response leakage detection theory;
ii. Together with transfer matrix and Taylor expansion approaches, the analytical expression of leak-induced shift was derived and verified, and found to be sufficiently accurate to estimate leak-induced wave number shift;
iii. The effects of leak size and leak location on the leak-induced wave number shift were examined. As the leak size increases, the leak-induced wave number shift increases. However, it is worth noting that when a leak is located at the middle of the pipeline, it does not impose a shift in the resonance wave number as shown in Figure 3.

REFERENCES

Brunone, B. (1999). Transient Test-Based Technique for Leak Detection in Outfall Pipes. *J. Water Resour. Plann. Manage*., 125(5), 302–306.

Brunone, B. & Ferrante, M. (2001). Detecting Leaks in Pressurized Pipes by Means of Transients. *J. Hydraul. Res.,* 39(5), 539–547.

Chaudhry, M.H. (1987). *Applied Hydraulic Transients*. Van Nostrand Reinhold Company Inc, New York.

Ferrante, M. & Brunone, B. (2001). Leak Detection in Pressurised Pipes by Means of Wavelet Analysis, In *Proc. 4th International Conference on Water Pipeline System - Managing Pipeline Assets in an Evolving Market*, York, UK, 259-275.

Ferrante, M. & Brunone, B. (2003). Pipe System Diagnosis and Leak Detection by Unsteady-State Tests. 1. Harmonic Analysis. *Adv. Water Resour*., 26(1), 95–105.

Covas, D. & Ramos, H. (2010). Case Studies of Leak Detection and Location in Water Pipe Systems by Inverse Transient Analysis. *J. Water Resour. Plann. Manage.,* 136(2), 248–257.

Lee, P.J., Vítkovský, J.P., Lambert, M.F., Simpson, A.R. & Liggett, J.A. (2005). Frequency Domain Analysis for Detecting Pipeline Leaks. *J. Hydraul. Eng.,* 131(7), 596–604.

Lee, P.J., Duan, H.F., Ghidaoui, M.S. & Karney, B.W. (2013). Frequency Domain Analysis of Pipe Fluid Transient Behaviors. *J. Hydraul. Res.,* 51(6), 609–622.

Lee, P.J., Duan, H.F., Vítkovský, J.P., Zecchin, A. & Ghidaoui, M.S. (2013). The Effect of Time–Frequency Discretization on the Accuracy of the Transmission Line Modelling of Fluid Transients. *Journal of Hydraulic Research,* 51(3), 273-283.

Liggett, J.A. & Chen, L.C. (1994). Inverse Transient Analysis in Pipe Networks. *J. Hydraul. Eng.,* 120(8), 934–954.

Mermelstein, P. (1967). Determination of the Vocal-Tract Shape from Measured Format Frequencies. *The Journal of the Acoustical Society of America,* 41(5), 1283–1294.

Mpesha, W., Chaudhry M.H. & Gassman S.L. (2002). Leak Detection in Pipes by Frequency Response Method Using a Step Excitation. *Journal of Hydraulic Research,* 40(1), 55-62.

Mpesha, W., Gassman, S.L. & Chaudhry, M.H. (2001). Leak Detection in Pipes by Frequency Response Method. *Journal of Hydraulic Engineering*, 127(2), 134-147.

Nixon, W., Ghidaoui, M.S. & Kolyshkin, A.A. (2006). Range of Validity of the Transient Damping Leakage Detection Method. *J. Hydraul. Eng.,* 132(9), 944–957.

Qunli, W. & Fricke, F. (1990). Determination of Blockage Locations and Cross-Sectional Area in a Duct by Eigenfrequency Shifts. *Journal of the Acoustical Society of America*, 87(1), 67-75.

Schroeder, M.R. (1967). Determination of the Geometry of the Human Vocal Tract by Acoustic Measurements. *The Journal of the Acoustical Society of America*, 41(4B), 1002–1010.

Vítkovský, J.P., Simpson, A.R. & Lambert, M.F. (2000). Leak Detection and Calibration Using Transients and Genetic Algorithms. *J. Water Resour. Plann. Manage.,* 126(4), 262–265.

Wylie, E.B., Streeter, V.L. & Suo, L. (1993). *Fluid Transients in Systems*. Prentice Hall, Englewood Cliffs, New Jersey, USA.

Wang, X.J., Lambert, M.F., Simpson, A.R., Liggett, J.A. & Vítkovský, J.P. (2002). Leak Detection in Pipeline Systems Using the Damping of Fluid Transients. *J. Hydraul. Eng.,* 128(7), 697–711.